
Crystal Growth Technology

Crystal Growth Technology, Edited by H. J. Scheel and T. Fukuda
© 2003 John Wiley & Sons, Ltd. ISBN: 0-471-49059-8

Crystal Growth Technology

HANS J. SCHEEL

*SCHEEL CONSULTING, Groenstrasse, CH-3803 Beatenberg BE, Switzerland
hans.scheel@bluewin.ch*

TSUGUO FUKUDA

*Institute of Multidisciplinary Research for Advanced Materials, Tohoku
University, Sendai 980-8577, Japan
t-fukuda@tagen.tohoku.ac.jp*



Copyright © 2003

John Wiley & Sons Ltd, The Atrium, Southern Gate, Chichester,
West Sussex PO19 8SQ, England

Telephone (+44) 1243 779777

Email (for orders and customer service enquiries): cs-books@wiley.co.uk

Visit our Home Page on www.wileyeurope.com or www.wiley.com

All Rights Reserved. No part of this publication may be reproduced, stored in a retrieval system or transmitted in any form or by any means, electronic, mechanical, photocopying, recording, scanning or otherwise, except under the terms of the Copyright, Designs and Patents Act 1988 or under the terms of a licence issued by the Copyright Licensing Agency Ltd, 90 Tottenham Court Road, London W1T 4LP, UK, without the permission in writing of the Publisher. Requests to the Publisher should be addressed to the Permissions Department, John Wiley & Sons Ltd, The Atrium, Southern Gate, Chichester, West Sussex PO19 8SQ, England, or emailed to permreq@wiley.co.uk, or faxed to (+44) 1243 770620.

This publication is designed to provide accurate and authoritative information in regard to the subject matter covered. It is sold on the understanding that the Publisher is not engaged in rendering professional services. If professional advice or other expert assistance is required, the services of a competent professional should be sought.

Other Wiley Editorial Offices

John Wiley & Sons Inc., 111 River Street, Hoboken, NJ 07030, USA

Jossey-Bass, 989 Market Street, San Francisco, CA 94103-1741, USA

Wiley-VCH Verlag GmbH, Boschstr. 12, D-69469 Weinheim, Germany

John Wiley & Sons Australia Ltd, 33 Park Road, Milton, Queensland 4064, Australia

John Wiley & Sons (Asia) Pte Ltd, 2 Clementi Loop #02-01, Jin Xing Distripark, Singapore 129809

John Wiley & Sons Canada Ltd, 22 Worcester Road, Etobicoke, Ontario, Canada M9W 1L1

Wiley also publishes its books in a variety of electronic formats. Some content that appears in print may not be available in electronic books.

Library of Congress Cataloging-in-Publication Data

Scheel, Hans J.

Crystal growth technology / Hans J. Scheel, Tsuguo Fukuda.

p. cm.

Includes bibliographical references and index.

ISBN 0-471-49059-8 (pbk. : alk. paper)

1. Crystallization. 2. Crystal growth. I. Fukuda, Tsuguo. II. Title.

TP156.C7S34 2003

660'.284298 – dc21

2003050193

British Library Cataloguing in Publication Data

A catalogue record for this book is available from the British Library

ISBN 0-471-49059-8

Typeset in 10/12pt Times by Laserwords Private Limited, Chennai, India

Printed and bound in Great Britain by TJ International, Padstow, Cornwall

This book is printed on acid-free paper responsibly manufactured from sustainable forestry in which at least two trees are planted for each one used for paper production.

CONTENTS

Contributors	xix
Preface	xxv
PART 1: GENERAL ASPECTS OF CRYSTAL GROWTH TECHNOLOGY	1
1 The Development of Crystal Growth Technology	3
<i>H. J. Scheel</i>	
Abstract	3
1.1 Historical Introduction	4
1.2 The Development of Crystal-growth Methods	5
1.3 Crystal-growth Technology Now	10
1.4 Conclusion	13
References	13
2 Thermodynamic Fundamentals of Phase Transitions Applied to Crystal Growth Processes	15
<i>P. Rudolph</i>	
2.1 Introduction	15
2.2 Perfect and Real Structure of Grown Crystals	16
2.2.1 The Principle of Gibbs Free Energy Minimization	16
2.2.2 Equilibrium Point-defect Concentration	17
2.3 Thermodynamics of Phase Equilibrium	19
2.3.1 The Phase Transition	19
2.3.2 Two-component Systems with Ideal and Real Mixing	21
2.3.3 Phase Boundaries and Surfaces	23
2.4 Thermodynamics of Topical Crystal Growth Problems	25
2.4.1 Mixed Crystals with Nearly Ideal Solid Solution	25
2.4.2 Systems with Compound Formation	28
2.4.3 Compositional Modulation and Ordering in Mixed Semiconductor Thin Films	34
2.5 Deviation from Equilibrium	36
2.5.1 Driving Force of Crystallization	36
2.5.2 Growth Mode with Two-dimensional Nucleation	39
References	40

3	Interface-kinetics-driven Facet Formation During Melt Growth of Oxide Crystals	43
	<i>S. Brandon, A. Virozub and Y. Liu</i>	
	Abstract	43
3.1	Introduction	44
3.2	Model Development	46
3.2.1	Mathematical Formulation	46
3.2.2	Numerical Technique	51
3.3	Results and Discussion	52
3.3.1	Effect of Operating Parameters on Facetting	52
3.3.2	Interaction between Melt Flow and Facet Formation	55
3.3.3	Transparent Crystalline Phase	60
3.3.4	Positioning of Facets along the Interface	61
3.4	Conclusions	62
	Acknowledgments	64
	Note Added in Proof	65
	References	65
4	Theoretical and Experimental Solutions of the Striation Problem	69
	<i>H. J. Scheel</i>	
	Abstract	69
4.1	Introduction	69
4.2	Origin and Definitions of Striations	70
4.3	Homogeneous Crystals with $k_{\text{eff}} \rightarrow 1$	74
4.4	Segregation Phenomena and Thermal Striations	76
4.5	Growth of Striation-Free KTN Crystals	82
4.6	Alternative Approaches to Reduce Striations	84
4.7	Discussion	89
	References	89
5	High-resolution X-Ray Diffraction Techniques for Structural Characterization of Silicon and other Advanced Materials	93
	<i>K. Lal</i>	
5.1	Introduction	93
5.2	High-resolution X-Ray Diffraction Techniques	94
5.2.1	Theoretical Background	94
5.2.2	High-resolution X-Ray Diffraction Experiments: A Five-crystal X-Ray Diffractometer	96
5.3	Evaluation of Crystalline Perfection and Characterization of Crystal Defects	100
5.4	Accurate Determination of Crystallographic Orientation	104
5.5	Measurement of Curvature or Bending of Single-crystal Wafers	108
5.6	Characterization of Process-induced Defects in Semiconductors: Implantation-induced Damage	110

Contents	vii
5.7 Conclusions	112
5.7.1 Acknowledgement	112
References	112
6 Computational Simulations of the Growth of Crystals from Liquids	115
<i>A. Yeckel and J. J. Derby</i>	
6.1 Introduction	115
6.2 Transport Modeling in Bulk Crystal Growth	116
6.2.1 Governing Equations	116
6.2.2 Boundary Conditions	118
6.3 Computational Issues	121
6.3.1 Numerical Methods	121
6.3.2 Software: Commercial versus Research, General versus Specialty	122
6.4 Examples of One-, Two-, and Three-dimensional Models	123
6.4.1 Can we still Learn from a 1D Model?	123
6.4.2 Is 2D Modeling Routine and Accurate?	125
6.4.3 When are 3D Models Necessary?	129
6.5 Summary and Outlook	135
Acknowledgments	135
References	136
7 Heat and Mass Transfer under Magnetic Fields	139
<i>K. Kakimoto</i>	
Abstract	139
7.1 Introduction	139
7.2 Magnetic Fields Applied to Czochralski Growth	140
7.3 Numerical Modeling	141
7.4 Vertical Magnetic Field (VMF)	143
7.5 Cusp-shaped Magnetic Fields (CMF)	147
7.6 Transverse Magnetic Fields (TMF)	150
7.7 Summary	150
Acknowledgment	151
References	152
8 Modeling of Technologically Important Hydrodynamics and Heat/Mass Transfer Processes during Crystal Growth	155
<i>V. I. Polezhaev</i>	
8.1 Introduction	155
8.2 Technologically Important Hydrodynamics Processes during Crystal Growth	157
8.3 Benchmark Problem	158
8.4 Hierarchy of the Models and Codes and Summary of Benchmark Exercises	162

8.5	Gravity-driven Convection Instability and Oscillations in Benchmark Configuration	172
8.6	Convective Interaction and Instabilities in Configuration of Industrial GaAs Czoehrsalski Growth	173
8.6.1	Axisymmetrical Approach: Nonlinear Coupling Fluid Flow and Control Possibilities	174
8.6.2	Three-Dimensional Analysis	176
8.7	Conclusions	181
	Acknowledgments	182
	References	182
PART 2: SILICON		187
9	Influence of Boron Addition on Oxygen Behavior in Silicon Melts	189
	<i>K. Terashima</i>	
	Abstract	189
9.1	Introduction	189
9.2	Oxygen Behavior in Boron-doped Silicon Melts	190
9.2.1	Oxygen Solubility in Silicon Melt	191
9.2.2	Fused Quartz Dissolution Rate in Silicon Melts	196
9.2.3	Evaporation from Free Surface of Boron-doped Silicon Melts in Fused-quartz Crucible	200
9.3	Conclusion	203
	Acknowledgments	203
	References	204
10	Octahedral Void Defects in Czoehrsalski Silicon	205
	<i>M. Itsumi</i>	
10.1	Background	205
10.2	Observation Methods	206
10.3	Characterization	209
10.4	Generation Mechanism	213
10.5	Elimination	215
10.6	Oxide Defect Generation	216
10.7	Concluding Remarks	219
	References	222
11	The Control and Engineering of Intrinsic Point Defects in Silicon Wafers and Crystals	225
	<i>R. Falster, V. V. Voronkov and P. Mutti</i>	
	Abstract	225
11.1	Introduction	225
11.1.1	Vacancy-type Defects	226

11.1.2	Silicon Self-interstitial-type Defects	226
11.1.3	The Precipitation of Oxygen	226
11.2	The Control of the Agglomeration of Intrinsic Point Defects during Crystal Growth	227
11.2.1	The v/G Rule for the Type of Grown-in Microdefects	227
11.2.2	Alternative Views to the v/G Rule	228
11.2.3	Void Reaction Control	229
11.2.4	Perfect Silicon	230
11.3	The Control of Oxygen Precipitation through the Engineering of Vacancy Concentration in Silicon Wafers: Magic Denuded Zone TM Wafers	231
11.3.1	'Tabula Rasa' Silicon and the Suppression of Oxygen Precipitation in Low-Vacancy-Concentration Material	231
11.3.2	Material 'Switching' and Transfer Functions	233
11.3.3	Comparison of Conventional and Vacancy-Engineered Control of Oxygen Precipitation	233
11.3.4	The Installation of Vacancy Concentration Profiles in Thin Silicon Wafers	235
11.3.5	Advantages of the Use of Vacancies to Control Oxygen Precipitation in Wafers	236
11.3.6	The Mechanism of the Vacancy Effect on Oxygen Precipitation	236
11.4	Conclusions Drawn Regarding the Intrinsic Point-Defect Parameters taken from the Combination of Crystal Growth and MDZ Experiments	238
11.4.1	Recombination Rate	238
11.4.2	Self-interstitial Diffusivity	239
11.4.3	Vacancy Diffusivity	239
11.4.4	The Difference of Equilibrium Vacancy and Interstitial Concentrations	239
11.4.5	Formation Energies	240
11.4.6	Critical v/G Ratio	241
11.4.7	Vacancy Binding by Oxygen	241
11.5	Unified Schematic Pictures of Vacancy Control for Crystal Growth and Wafer Processing	242
	Acknowledgments	248
	References	248
12	The Formation of Defects and Growth Interface Shapes in CZ Silicon	251
	<i>T. Abe</i>	
	Abstract	251
12.1	Introduction	251
12.2	Experiments	254

12.3	Results	256
12.4	Discussion	258
12.4.1	Balance Equation	258
12.4.2	Discussion of Voronkov's Relation	262
12.4.3	Interface-shape Formation	263
12.5	Conclusions	264
	References	264
13	Silicon Crystal Growth for Photovoltaics	267
	<i>T. F. Ciszek</i>	
13.1	Introduction	267
13.2	Basic Concepts	268
13.2.1	The Photovoltaic Effect	268
13.2.2	Minority-carrier Lifetime, τ	269
13.2.3	Light Absorption	271
13.3	Silicon Source Materials	272
13.4	Ingot Growth Methods and Wafering	275
13.4.1	Single-crystal Growth	276
13.4.2	Multicrystalline Growth	277
13.5	Ribbon/Sheet Growth Methods	279
13.6	Thin-Layer Growth on Substrates	283
13.7	Comparison of Growth Methods	285
13.8	Future Trends	285
	References	287
	PART 3: COMPOUND SEMICONDUCTORS	291
14	Fundamental and Technological Aspects of Czochralski Growth of High-quality Semi-insulating GaAs Crystals	293
	<i>P. Rudolph and M. Jurisch</i>	
14.1	Introduction	293
14.1.1	Historical Background	293
14.1.2	The Importance of SI GaAs and its Performance	295
14.2	Features and Fundamental Aspects of LEC Growth of SI GaAs Crystals	297
14.2.1	The Principle of Modern LEC Technique	297
14.2.2	Correlation between Heat Transfer, Thermomechanical Stress and Dislocation Density	300
14.2.3	Dislocation Patterns	303
14.2.4	Principles of Native-defect Control	305
14.2.5	Carbon Control	310
14.3	Modified Czochralski Technologies	313
14.3.1	Vapour-pressure-controlled Czochralski (VCz) Method	313

14.3.2	Fully-Encapsulated Czochralski (FEC) Growth	315
14.3.3	Hotwall Czochralski (HWC) Technique	316
14.4	Conclusions and Outlook	317
	Acknowledgement	318
	References	318
15	Growth of III-V and II-VI Single Crystals by the Vertical-gradient-freeze Method	323
	<i>T. Asahi, K. Kainosho, K. Kohiro, A. Noda, K. Sato and O. Oda</i>	
15.1	Introduction	323
15.2	InP Crystal Growth by the VGF Method	324
15.3	GaAs Crystal Growth by the VGF Method	331
15.3.1	Growth of Undoped GaAs	331
15.3.2	Growth of Si-doped GaAs Crystals	335
15.3.3	Growth of Zn-doped Crystals	336
15.4	CdTe Crystal Growth by the VGF Method without Seed Crystals	337
15.5	ZnTe Crystal Growth by VGF without Seed Crystals using the High-pressure Furnace	344
15.6	Summary	346
	References	346
16	Growth Technology of III-V Single Crystals for Production	349
	<i>T. Kawase, M. Tatsumi and Y. Nishida</i>	
16.1	Introduction	349
16.2	Properties of III-V Materials	349
16.3	Growth Technology of III-V Materials	350
16.3.1	HB and HGF Techniques	351
16.3.2	LEC Technique	352
16.3.3	Vapor-pressure-controlled Czochralski (VCZ) Technique	353
16.3.4	VB and VGF Techniques	355
16.4	Applications and Requirements for GaAs Single Crystals	356
16.5	Growth of Large Single Crystals	357
16.6	Growth of Low-Dislocation-Density GaAs Crystal	359
16.7	Control of Quality and Yield of GaAs Crystals	361
16.7.1	Twinning	362
16.7.2	Lineage	364
16.8	Control of the Electronic Quality of GaAs	365
16.8.1	Absolute Value of Resistivity	365
16.8.2	Uniformity of Microscopic Resistivity	366
16.9	Trend of Growth Methods for GaAs	367
16.10	InP	367

16.11	Summary	369
	References	369
17	CdTe and CdZnTe Growth	373
	<i>R. Triboulet</i>	
17.1	Introduction	373
17.2	Phase Equilibria in the Cd–Te System	373
17.3	Crystal Growth versus Cd–Te Chemical Bond Characteristics	377
17.4	Crystal Growth	381
17.5	Bridgman Growth Modeling and Interface-shape Determination	388
17.6	CdZnTe Properties	393
17.6.1	Properties at Macroscopic and Microscopic Scale	393
17.6.2	Segregation	394
17.6.3	Industrial Growth	396
17.7	Properties and Defects of the Crystals	396
17.8	Purity, Contamination, Doping	399
17.9	Conclusions and Perspectives	400
	References	400
PART 4:	OXIDES AND HALIDES	407
18	Phase-diagram Study for Growing Electro-optic Single Crystals	409
	<i>S. Miyazawa</i>	
	Abstract	409
18.1	Introduction	409
18.2	Phase-relation Study of LiTaO ₃	410
18.2.1	Preliminary Studies by X-Ray Diffractometry	411
18.2.2	Determination of the Congruently Melting Composition	412
18.2.3	Optical Quality of the Congruent LiTaO ₃	415
18.2.4	Conclusion	417
18.3	Phase-relation Study of Bi ₁₂ TiO ₂₀	418
18.3.1	Re-examination of Phase Diagram	419
18.3.2	Lattice-constant Variations of the Bi ₁₂ TiO ₂₀ Phase	419
18.3.3	New Phase Diagram	422
18.3.4	Growth of Long Single Crystals	424
18.3.5	Conclusion	426
18.4	Summary	426
	Acknowledgment	427
	References	427

19	Melt Growth of Oxide Crystals for SAW, Piezoelectric, and Nonlinear-Optical Applications	429
	<i>K. Shimamura, T. Fukuda and V. I. Chani</i>	
19.1	Introduction	429
19.2	LiTaO ₃ for SAW Devices	431
19.3	Langasite-family Crystals for Piezoelectric Applications	434
19.4	Nonlinear-Optical Crystals for Blue SHG	439
19.5	Summary	441
	References	443
20	Growth of Nonlinear-optical Crystals for Laser-frequency Conversion	445
	<i>T. Sasaki, Y. Mori and M. Yoshimura</i>	
20.1	Introduction	445
20.2	Crystals Grown from Low-temperature Solutions	445
20.2.1	Growth of Large KDP (Potassium Dihydrogen Phosphate) Crystals of Improved Laser-damage Threshold	445
20.2.2	Growth and Characterization of Organic NLO Crystals	448
20.3	Crystals Grown from High-temperature Solutions	451
20.3.1	Growth and Optical Characterization of KTP (Potassium Titanyl Phosphate) Crystal [12–14]	451
20.3.2	Growth and NLO Properties of Cesium Lithium Borate CLBO	454
20.4	Conclusions	458
	References	458
21	Growth of Zirconia Crystals by Skull-Melting Technique	461
	<i>E. E. Lomonova and V. V. Osiko</i>	
21.1	Introduction	461
21.2	Physical and Technical Aspects of the Direct Radio-frequency Melting in a Cold Container (Skull Melting)	462
21.3	RF-furnaces for Zirconia Melting and Crystallization	467
21.4	Phase Relations in Zirconia Solid Solutions. Y-stabilized (YCZ) and Partially Stabilized (PSZ) Zirconia	470
21.5	Growth Processes of YCZ and PSZ Crystals	472
21.6	Structure, Defects, and Properties of YCZ and PSZ Crystals	475
21.7	Applications of YCZ and PSZ Crystals	479
21.8	Conclusion	482
	Acknowledgments	484
	References	484

22 Shaped Sapphire Production	487
<i>L. A. Lytvynov</i>	
22.1 Introduction	487
22.2 Crystal-growth Installation	487
22.3 Growing of Crucibles	488
22.4 Growth of Complicated Shapes	492
22.5 Dice	494
22.6 Group Growth	496
22.7 Local Forming	498
22.8 Sapphire Products for Medicine	499
22.9 Improvement of Structure Quality of Profile Sapphire	502
References	509
23 Halogenide Scintillators: Crystal Growth and Performance	511
<i>A. V. Gektin and B. G. Zaslavsky</i>	
23.1 Introduction	511
23.2 Modern Tendency in A ^I B ^{VII} Crystal Growth	511
23.2.1 R&D for Halogenide Crystal Perfection	511
23.2.2 Traditional Crystal Growth Methods	513
23.2.3 Automated Growth Principles and Technique	514
23.3 Modified Method of Automated Pulling of Large-size Scintillation Crystals	517
23.3.1 Principles of the Method	517
23.3.2 The Method Model and the Process Control Parameter	518
23.4 Experimental and Practical Method Realization	521
23.5 Scintillator Quality	524
23.5.1 Activated Scintillators	524
23.5.2 Undoped Scintillators	525
23.6 Conclusion	527
References	527
PART 5: CRYSTAL MACHINING	529
24 Advanced Slicing Techniques for Single Crystals	531
<i>C. Hauser and P. M. Nasch</i>	
Abstract	531
24.1 Introduction	531
24.2 Geometrical Parameters	532
24.3 Survey on Slicing Methods for Silicon Single Crystal	533
24.4 Material-removal Process	537
24.5 General Comparison of Different Slicing Methods	541
24.6 Surface Damage	542
24.7 Economics	544

24.8	Crystal Orientation	548
	References	557
25	Methods and Tools for Mechanical Processing of Anisotropic Scintillating Crystals	561
	<i>M. Lebeau</i>	
25.1	Introduction	561
25.2	Crystals	561
25.3	Machine-tools and Diamond Cutting Disks	565
25.4	Tooling for Cutting Operations	567
25.4.1	Traveling (Setting) Reference Base	567
25.4.2	Processing Reference Base	568
25.4.3	Positioning Tools	568
25.4.4	Inspection Tools	573
25.5	Tools for Lapping and Polishing Operations	575
25.6	Optical Method for Inspection of Crystal Residual Stresses	578
25.7	Conclusions and Production Forecasts	585
	References	585
26	Plasma-CVM (Chemical Vaporization Machining)	587
	<i>Y. Mori, K. Yamamura, and Y. Sano</i>	
26.1	Introduction	587
26.2	Concepts of Plasma-CVM	587
26.3	Applications of Plasma-CVM	588
26.4	Slicing	589
26.4.1	Slicing Machine	589
26.4.2	Slicing Rate	590
26.4.3	Kerf Loss	591
26.4.4	Slicing of Silicon Ingot	592
26.5	Planarization	594
26.5.1	Planarization Machine	594
26.5.2	Machining Properties	595
26.6	Figuring	598
26.6.1	Numerically Controlled Plasma-CVM System	598
26.6.2	Machining Properties	601
26.6.3	Fabrication of the Flat Mirror	605
	Acknowledgements	605
	References	605
27	Numerically Controlled EEM (Elastic Emission Machining) System for Ultraprecision Figuring and Smoothing of Aspherical Surfaces	607
	<i>Y. Mori, K. Yamauchi, K. Hirose, K. Sugiyama, K. Inagaki and H. Mimura</i>	

27.1	Introduction	607
27.2	Features and Performances	607
27.3	Atom-removal Mechanism	610
27.3.1	General View	610
27.3.2	Process Simulation and Results	611
27.4	Numerically Controlled EEM System	614
27.4.1	Requirement of Ultraclean Environmental Control	614
27.4.2	Numerically Controlled Stage System	614
27.4.3	EEM Heads	615
27.4.4	In-process Refining System of the Mixture Fluid	617
27.5	Numerical Control System	617
27.5.1	Concepts for Ultraprecise Figuring	617
27.5.2	Software for Calculating Scanning Speed	617
27.5.3	Performances of Numerically Controlled Processing	618
27.6	Conclusion	619
	Acknowledgement	620
	References	620
PART 6: EPITAXY AND LAYER DEPOSITION		621
28	Control of Epitaxial Growth Modes for High-performance Devices	623
	<i>H. J. Scheel</i>	
	Abstract	623
28.1	Introduction	623
28.2	Seven Epitaxial Growth Modes and the Role of Growth Parameters	624
28.3	Control of Growth Modes	635
28.4	Conclusions	641
	General References	642
	References	642
29	High-rate Deposition of Amorphous Silicon Films by Atmospheric- pressure Plasma Chemical Vapor Deposition	645
	<i>Y. Mori, H. Kakiuchi, K. Yoshii and K. Yasutake</i>	
	Abstract	645
29.1	Introduction	645
29.2	Atmospheric-Pressure Plasma CVD	646
29.2.1	Atmospheric Pressure, VHF Plasma	646
29.2.2	Utilization of Rotary Electrode	646
29.3	Experimental	647
29.4	Results and Discussion	648
29.4.1	Deposition Rate	648
29.4.2	Electrical and Optical Properties	648

Contents	xvii
29.5 Conclusion	651
Acknowledgements	651
References	651
Index	653

CONTRIBUTORS

Abe, Takao

Shin-Etsu Handotai, Isobe R&D Center, 2-13-1 Isobe, Annaka-shi, Gunma-ken 379-01, Japan

Asahi, T.

Central R&D Laboratory, Japan Energy Corporation, 3-17-35 Niizo-Minami, Toda, Saitama 335-8502, Japan

Brandon, Simon

Department of Chemical Engineering, Tianjin University, Tianjin 300072, P.R. China

Chani, Valery I.

Department of Materials Science and Engineering, McMaster University, 1280 Main Street West, Hamilton, Ontario, L8S 4M1, Canada

Ciszek, T. F.

National Renewable Energy Laboratory, 1617 Cole Boulevard, Golden, Colorado 80401-3393, USA

Derby, Jeffrey J.

Department of Chemical Engineering and Materials Science, Army HPC Research Center & Minnesota Supercomputing Institute, University of Minnesota, Minneapolis, MN 55455-0132, USA

Falster, R.

MEMC Electronic Materials SpA, Viale Gherzi 31, 28100 Novara, Italy

Fukuda, Tsuguo

Institute of Multidisciplinary Research for Advanced Materials, Tohoku University, 2-1-1 Katahiraa, Aoba-ku, Sendai 980 8577, Japan

Gektin, A. V.

Institute for Single Crystals, Lenin Av 60, 310001 Kharkov, Ukraine

Hauser, C. (Retired)

HCT Shaping Systems SA, 1033 Cheseaux, Switzerland

Hirose, Kikuji

Department of Precision Science and Technology, Department of Electrical Engineering, Graduate School of Engineering, Osaka University, 2-1 Yamada-oka, Suita 565-0871, Osaka, Japan

Inagaki, Kohji

Dept of Precision Science and Technology, Graduate School of Engineering, Osaka University, 2-1 Yamada-oka, Suita, Osaka 565-0871, Japan

Itsumi, Manabu

NTT Lifestyle & Environmental Technology Laboratories, 3-1 Morinosato Wakamiya, Atsugi-Shi, Kanagawa, 243-0198, Japan

Jurisch, M.

Freiberger Compound Materials GmbH, Am Junger Löwe Schacht, D-09599 Freiberg, Germany

Kainosho, K.

Central R&D Laboratory, Japan Energy Corporation, 3-17-35 Niizo-Minami, Toda, Saitama 335-8502, Japan

Kakimoto, Koichi

Institute of Advanced Material Study, Kyushu University, 6-1 Kasuga-Koen, Kasuga 816-8580, Japan

Kakiuchi, Hiroaki

Department of Precision Science and Technology, Graduate School of Engineering, Osaka University, 2-1 Yamada-oka, Suita 565-0871, Osaka, Japan

Kawase, Tomohiro

Sumitomo Electric Industries, Ltd., 1-1-1, Koya-kita, Itami, Hyogo 664-0016, Japan

Kohiro, K.

Central R&D Laboratory, Japan Energy Corporation, 3-17-35 Niizo-Minami, Toda, Saitama 335-8502, Japan

Lal, Krishnan

National Physical Laboratory, Dr K. S. Krishnan Road, New Delhi 110012, India

Lebeau, Michel

CERN, 1211 Geneva 23, Switzerland

Liu, Yongcai

Department of Chemical Engineering, Tianjin University, Tianjin 300072, P.R. China

Lomonova, E. E.

Laser Materials and Technology Research Center, General Physics Institute of the Russian Academy of Sciences, Moscow, Russia

Lytvynov, Leonid A.

Institute of Single Crystals, Lenin Av., 60, Kharkov, 61001, Ukraine

Mimura, Hidekazu

Department of Precision Engineering, Osaka University, 2-1 Yamada-oka, Suita, Osaka 565-0871

Miyazawa, Shintaro

Shinkosha Co. Ltd., 3-4-1 Kosugaya, Sakae-ku, Yokohama, Kanagawa 247-0007, Japan

Mori, Yusuke

Department of Electrical Engineering, Graduate School of Engineering, Osaka University, 2-1 Yamada-oka, Suita 565-0871, Osaka, Japan

Mori, Yuzo

Department of Precision Science and Technology, Graduate School of Engineering, Osaka University, 2-1 Yamada-oka, Suita 565-0871, Osaka, Japan

Mutti, P.

MEMC Electronic Materials SpA, Via Nazionale 59, 39012 Merano, Italy

Nasch, P. M.

HCT Shaping Systems SA, Route de Genève 42, Cheseaux Sur-Lausanne CH-1033, Switzerland

Nishida, Yasuhiro

Sumitomo Electric Industries Ltd., 1-1-1, Koya-kita, Itami, Hyogo 664-0016, Japan

Noda, A.

Central R&D Laboratory, Japan Energy Corporation, 3-17-35 Niizo-Minami, Toda, Saitama 335-8502, Japan

Oda, O.

Central R&D Laboratory, Japan Energy Corporation, 3-17-35 Niizo-Minami, Toda, Saitama 335-8502, Japan

Osiko, V. V.

Laser Materials and Technology Research Center, General Physics Institute of the Russian Academy of Sciences, Vavilov str. 38, Moscow 119991, Russia

Polezhaev, V. I.

Institute for Problems in Mechanics, Russian Academy of Sciences, Prospect Vernadskogo 101, 117526 Moscow, Russia

Rudolph, Peter

Institute for Crystal Growth, Rudower Chaussee 6, D-12489 Berlin, Germany

Sano, Yasuhisa

Department of Precision Science and Technology, Graduate School of Engineering, Osaka University, 2-1 Yamada-oka, Suita, Osaka 565-0871, Japan

Sasaki, Takatomo

Department of Electrical Engineering, Graduate School of Engineering, Osaka University, 2-1 Yamada-oka, Suita 565-0871, Osaka, Japan

Sato, K.

Central R&D Laboratory, Japan Energy Corporation, 3-17-35 Niizo-Minami, Toda, Saitama 335-8502, Japan

Scheel, Hans J.

SCHEEL CONSULTING, Groenstrasse, CH-3803 Beatenberg BE, Switzerland

Shimamura, Kiyoshi,

Kagami Memorial Laboratory for Materials Science and Technology, Waseda University, 2-8-26 Nishiwaseda, Shinjuku 169-0051, Japan

Sugiyama, Kazuhisa

Department of Precision Science and Technology, Graduate School of Engineering, Osaka University, 2-1 Yamada-oka, Suita, Osaka 565-0871, Japan

Tatsumi, M.

Sumitomo Electric Industries Ltd., 1-1-1, Koya-kita, Itami, Hyogo 664-0016, Japan

Terashima, Kazutaka

Silicon Melt Advanced Project, Shonan Institute of Technology, 1-1-1 Tsujido-Nishikaigan, Fujisawa, Kanagawa 251, Japan

Triboulet, R.

Laboratoire de Physique des Solides de Bellevue CNRS, 1, Place A. Briand, F-92195 Meudon Cedex, France

Virozub, Alexander

Department of Chemical Engineering, Tianjin University, Tianjin 300072, P.R. China

Voronkov, V. V.

MEMC Electronic Materials SpA, Via Nazionale 59, 39012 Merano, Italy

Yamamura, Kazuya

Department of Precision Science and Technology, Graduate School of Engineering, Osaka University, 2-1 Yamada-oka, Suita, Osaka 565-0871, Japan

Yamauchi, Kazuto

Department of Precision Science and Technology, Graduate School of Engineering, Osaka University, 2-1 Yamada-oka, Suita, Osaka 565-0871, Japan

Yasutake, Kiyoshi

Department of Material and Life Science, Graduate School of Engineering, Osaka University, 2-1 Yamada-oka, Suita, Osaka 565-0871, Japan

Yeckel, Andrew

Department of Chemical Engineering and Materials Science, Army HPC Research Center & Minnesota Supercomputing Institute, University of Minnesota, Minneapolis, MN 55455-0132, USA

Yoshii, Kumayasu

Department of Precision Science and Technology, Graduate School of Engineering, Osaka University, 2-1 Yamada-oka, Suita, Osaka 565-0871, Japan

Yoshimura, Masashi

Department of Electrical Engineering, Graduate School of Engineering, Osaka University, 2-1 Yamada-oka, Suita 565-0871, Osaka, Japan

Zaslavsky, B. G.

Institute for Single Crystals, Lenin Av 60, 310001 Kharkov, Ukraine

PREFACE

This volume deals with the technologies of crystal fabrication, of crystal machining, and of epilayer production and is the first book on industrial aspects of crystal production. Therefore, it will be of use to all scientists, engineers, professors and students who are active in these fields, or who want to study them. Highest-quality crystals and epitaxial layers (epilayers) form the basis for many industrial technological advances, including telecommunications, computer and electrical energy technology, and those technologies based on lasers and nonlinear-optical crystals. Furthermore, automobile electronics, audiovisual equipment, infrared night-vision and detectors for medicine (tomography) and large nuclear-physics experiments (for example in CERN) are all dependent on high-quality crystals and epilayers, as are novel technologies currently in development and planned for the future. Crystals and epilayers will gain special importance in energy saving and renewable energy. Industrial crystal and epilayer production development has been driven by the above technological advances and also by the needs of the military and a multibillion-dollar industry. From the nearly 20 000 tons of crystals produced annually, the largest fraction consists of the semiconductors silicon, gallium arsenide, indium phosphide, germanium, and cadmium telluride. Other large fractions are optical and scintillator crystals, and crystals for the watch and jewellery industries.

For most applications the crystals have to be machined, i.e. sliced, lapped, polished, etched, or surface-treated. These processes have to be better understood in order to improve yields, reduce the loss of valuable crystal, and improve the performance of machined crystals and wafers.

Despite its importance, the scientific development and understanding of crystal and epilayer fabrication is not very advanced, and the education of specialized engineers and scientists has not even started. The first reason for this is the multidisciplinary nature of crystal growth and epitaxial technology: neither chemical and materials engineering departments on the preparative side, nor physics and electrical engineering on the application side feel responsible, or capable of taking care of crystal technologies. Other reasons for the lack of development and recognition are the complexity of the multi-parameter growth processes, the complex phase transformation from the mobilized liquid or gaseous phase to the solid crystal, and the scaling problem with the required growth-interface control on the nm-scale within growth systems of m-scale.

An initial workshop, named 'First International School on Crystal Growth Technology ISCGT-1' took place between September 5–14, 1998 in Beatenberg, Switzerland, and ISCGT-2 was held between August 24–29, 2000 in Mount

Zao Resort, Japan with H. J. Scheel and T. Fukuda action as the co-chairmen. Extended lectures were given by leading specialists from industries and universities, and the majority of crystal-producing factories were represented. This book contains 29 selected review papers from ISCGT-1 and discusses scientific and technological problems of production and machining of industrial crystals for the first time. Thus, it is expected that this volume will serve all scientists and engineers involved in crystal and epilayer fabrication. Furthermore, it will be useful for the users of crystals, for teachers and graduate students in materials sciences, in electronic and other functional materials, chemical and metallurgical engineering, micro- and optoelectronics including nano-technology, mechanical engineering and precision-machining, microtechnology, and in solid-state sciences. Also, consultants and specialists from funding agencies may profit from reading this book, as will all those with an interest in crystals, epilayers, and their production, and those concerned with saving energy and in renewable energy.

In Section I, general aspects of crystal growth are reviewed: the present and future of crystal growth technology, thermodynamic fundamentals of phase transitions applied to crystal-growth processes, interface and faceting effects, striations, modeling of crystal growth from melts and from solutions, and structural characterization to develop the growth of large-diameter crystals. In Section II, the problems relating to silicon are discussed: structural and chemical characteristics of octahedral void defects, intrinsic point defects and reactions in silicon, heat and mass transfer in melts under magnetic fields, silicon for photovoltaics, and slicing and novel precision-machining methods for silicon. Section III treats problems of the growth of large, rather than perfect, crystals of the compound semiconductors GaAs, InP, and CdTe. Section IV discussed oxides for surface-acoustic-wave and nonlinear-optic applications and the growth of large halogenide scintillator crystals. Section V deals with crystal machining: crystal orientation, sawing, lapping, and polishing and also includes the novel technologies EEM and CVM. Finally, Section VI treats the control of epitaxial growth modes to achieve highest-performance optoelectronic devices, and a novel, fast deposition process for silicon from high-density plasmas is presented.

The editors would like to thank the contributors for their valuable reviews, the referees (especially D. Elwell), and the sponsors of ISCGT-1. Furthermore, the editors acknowledge the competent copy-proof reading of P. Capper, and the work from J. Cossham, L. James and L. Bird of John Wiley & Sons Ltd, the publishers: also for pleasant collaboration and their patience.

It is hoped that this book may contribute to the scientific development of crystal technologies, and that it is of assistance for the necessary education in this field.

HANS J. SCHEEL and TSUGUO FUKUDA

Part 1

General Aspects of Crystal Growth Technology

1 The Development of Crystal Growth Technology

HANS J. SCHEEL

SCHEEL CONSULTING, CH-8808 Pfaffikon SZ, Switzerland

ABSTRACT

The industrial production of crystals started with A. Verneuil with his flame-fusion growth method 1902. He can be regarded as the father of crystal growth technology as his principles of nucleation control and crystal-diameter control are adapted in most later growth methods from the melt, like Tammann, Stöber, Bridgman, Czochralski, Kyropoulos, Stockbarger, etc. The important crystal pulling from melts named after Czochralski was effectively developed by Teal, Little and Dash.

The multi-disciplinary nature of technology of crystal and epilayer fabrication, the complex multi-parameter processes – where ten or more growth parameters have to be compromised and optimized, and also the scaling problem have impeded the scientific development of this important area. Only recently has the numerical simulation of Czochralski melts started to become useful for growth technologists, the deep understanding of the striation problem allowed the experimental conditions to grow striation-free crystals to be established, and the control of epitaxial growth modes permitted the preparation of atomically flat surfaces and interfaces of importance for the performance of opto-electronic and superconducting devices.

Despite the scale of the multi-billion dollar crystal and epilayer fabrication and crystal-machining industry and the annual need worldwide of at least 400 engineers, there is so far no formation of specialists for crystal production, epitaxy technology, crystal machining and surface preparation. A special curriculum is required due to the multi-disciplinary character of crystal-growth technology (CGT) which does not fit into a single classical university discipline like chemical, mechanical, materials, or electrical engineering, or crystallography, thermodynamics, solid-state physics, and surface physics. The education scheme for CGT has to include all these disciplines and basic sciences to such an extent that the finished engineers and scientists are capable of interacting and collaborating with specialists from the various disciplines. It is up to the interested industries to request CGT engineers from the technical universities and engineering schools.

Crystal-growth technology and epitaxy technology had developed along with the technological development in the 20th century. On the other hand, the rapid advances in microelectronics, in communication technologies, in medical instrumentation, in energy and space technology were only possible after the remarkable progress in fabrication of large, rather perfect crystals and of large-diameter epitaxial layers (epilayers). Further progress in CGT and education of CGT engineers is required for significant contributions to the energy crisis. High-efficiency white light-emitting diodes for energy-saving illumination and photovoltaic/thermo-photovoltaic devices for transforming solar and other radiation energy into electric power with high yield depend on significant advances in crystal growth and epitaxy technology. Also, the dream of laser-fusion energy and other novel technologies can only be realized after appropriate progress in the technology of crystal and epilayer fabrication.

1.1 HISTORICAL INTRODUCTION

Fundamental aspects of crystal growth had been derived from early crystallization experiments in the 18th and the 19th century (Elwell and Scheel 1975, Scheel 1993). Theoretical understanding started with the development of thermodynamics in the late 19th century (Gibbs, Arrhenius, Van't Hoff) and with the development of nucleation and crystal growth theories and the increasing understanding of the role of transport phenomena in the 20th century. The phenomena of undercooling and supersaturation and the heat of crystallization were already recognized in the 18th century by Fahrenheit and by Lowitz. The corresponding metastable region, the existence range of undercooled melts and solutions, was measured and defined in 1893/1897 by Ostwald and in 1906 by Miers, whereas the effect of friction on the width of this Ostwald–Miers region was described in 1911 and 1913 by Young. Although the impact of stirring on this metastable region is important in mass crystallization of salt, sugar and many chemicals, it is not yet theoretically understood.

The rates of nucleation and crystallization in glasses were the foundation to nucleation theories. The crystal surface with steps and kinks of Kossel in 1927 allowed Stranski and Kaishew in 1934 to define the work of separation of crystal units as repeatable steps as the basis of the first crystal-growth theories. With the understanding of facet formation as a function of the entropy of fusion in 1958 by Jackson, and depending on the density of bonds in the crystal structure 1955 by Hartman and Perdok, the role of screw dislocations as continuous step sources in the formation of growth hillocks (Frank 1949), and with the generalized crystal growth theory of Burton, Cabrera and Frank 1951, many growth phenomena could be explained.

In the growth of crystals from a fluid medium (melt, solution, gas phase) the heat and mass transport phenomena also play a significant role, as was observed early by Rouelle 1745 and Frankenheim 1835. The diffusion boundary layer

defined by Noyes and Whitney 1897 was used in the growth-rate equation of Nernst 1904 and confirmed by interferometric measurements of concentration profiles around growing crystals by Berg 1938 and by others. Forced convection was recognized to be beneficial for diffusion-limited growth by Wulff 1886, Krüger and Finke 1910, and Johnsen 1915 for open systems with stirrers, whereas smooth stirring in sealed containers can be achieved with the accelerated crucible rotation technique ACRT of Scheel 1971/1972. The growth of inclusion-free crystals from the melt can be accomplished by observing the principles of “diffusional undercooling” of Ivantsov 1951 and “constitutional supercooling” of Tiller *et al.* 1953. Formation of inclusions, i.e. growth instability, can be prevented in growth from solutions by sufficient flow against or along the crystal facets: Carlson 1958 developed an empirical theory which was utilized by Scheel and Elwell 1972 to derive the maximum stable growth rate and optimized programming of supersaturation for obtaining large inclusion-free crystals.

Microscopic and macroscopic inhomogeneities in doped crystals and in solid solutions are caused by segregation phenomena, which are related to mass and heat transfer. Based on the derivation of effective distribution coefficients for melt growth by Burton *et al.* (1953) and by van Erk (1982) for growth from solutions, the theoretical and experimental conditions for growth of striation-free crystals could be established (Rytz and Scheel 1982, Scheel and Sommerauer 1983, Scheel and Swendsen 2001).

There have been remarkable developments with respect to size and perfection of crystals, with silicon, sapphire, alkali and earth alkali halides reaching diameters up to 0.5 m and weights of nearly 500 kg. These advances in Czochralski, Kyropoulos, heat-exchanger method, and Bridgman–Stockbarger growth were accompanied by numerical simulations which have become increasingly powerful to predict the optimized conditions. However, further advances in computer modelling and in the reliability of the used physico-chemical data are required in order to increase the efficiency and precision of computer simulations and to allow the prediction of the best crystal-growth technology including growth parameters for the growth of new large and relatively perfect crystals.

1.2 THE DEVELOPMENT OF CRYSTAL-GROWTH METHODS

Industrial crystal production started with Verneuil 1902 who with the flame-fusion growth process named after him achieved for the first time control of nucleation and thus single crystals of ruby and sapphire with melting points above 2000 °C. By formation of the neck and the following enlargement of the crystal diameter, not only was the seed selection achieved in a crucible-free process, but also the structural perfection of the growing crystal could be controlled to some extent.

Figure 1.1 shows the stages of Verneuil growth of high-melting oxides, and Figure 1.2 the relatively simple apparatus where powder is fed into the hydrogen–oxygen flame and enters the molten cap of first the cone and neck, and

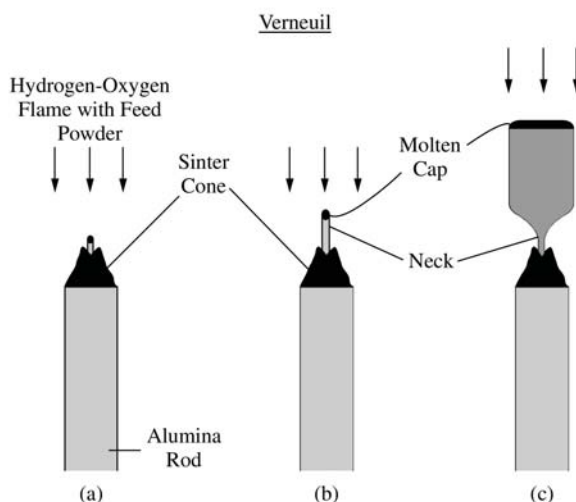


Figure 1.1 Stages of flame-fusion (Verneuil) growth of ruby, schematic: (a) formation of sinter cone and central melt droplet onto alumina rod, (b) growth of the neck by adjustment of powder supply and the hydrogen-oxygen flame, (c) Increase of the diameter without overflow of the molten cap for the growth of the single-crystal boule. (Reprinted from H. J. Scheel, *J. Cryst. Growth* **211**(2000) 1–12, copyright (2000) with permission from Elsevier Science.)

then the molten surface layer of the growing crystal. The latter is slowly moved downwards so that the surface-melting conditions remain within the observation window. Historical details of Verneuil's development were given by Nassau 1969 and Nassau and Nassau 1971. The industrialization for production of ruby watchstones and synthetic gemstones started with Verneuil's laboratory in Paris in 1910 with 30 furnaces and with the Djevahirdjian factory at Monthey VS in Switzerland where the CIBA chemical company could provide hydrogen. The annual ruby production reached 5 million carats in 1907, and 10 million carats ruby and 6 million carats sapphire in 1913. Nowadays, the production capacity of sapphire for watch windows and other applications is 250 tons (1.25×10^9 carats), the largest fraction from the Djevahirdjian factory with 2200 Verneuil furnaces, and this with the practically unchanged process.

The principles of the Verneuil method with nucleation, growth rate and diameter control have been applied in most of the growth processes described in the following years: Tammann 1914, Stöber 1925, Bridgman 1923, Stockbarger 1936, vertical-gradient-freeze growth of Ramsberger and Malvin 1927, and in the Czochralski process 1918/1950, see Figure 1.3 and Wilke-Bohm 1988. Thus, Verneuil can really be regarded as the founder of crystal-growth technology.

However, the most important method of fabrication of semiconductor and oxide crystals consists of pulling crystals from melts contained in crucibles, a method named after Czochralski. The origin of this started with the topical area

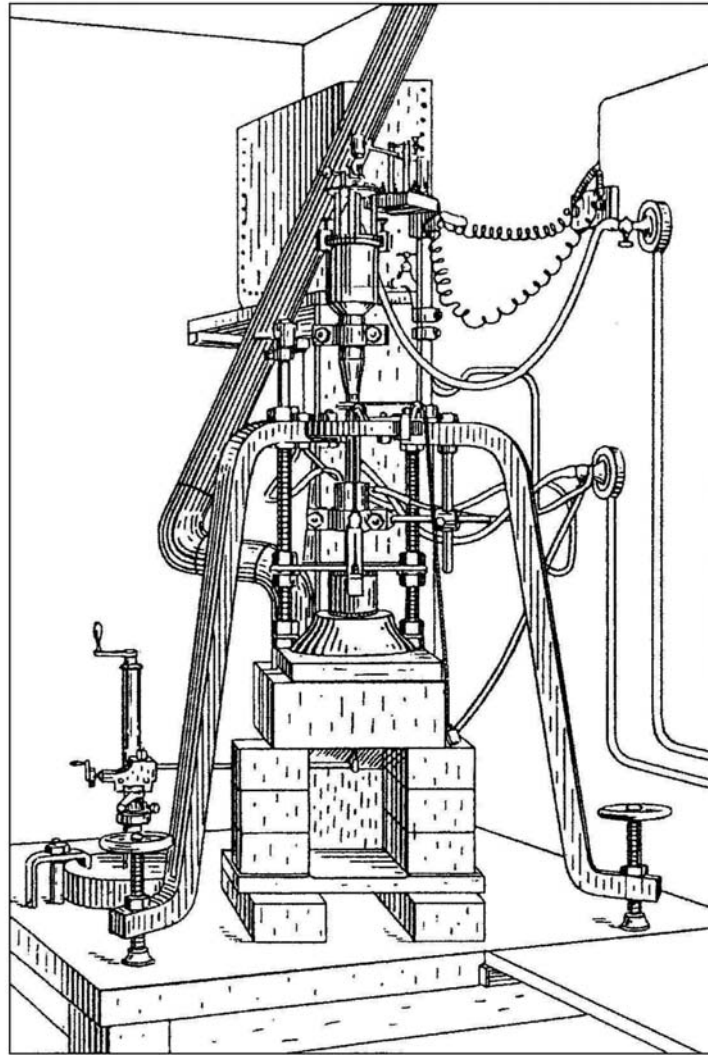


Figure 1.2 The relatively simple apparatus of Verneuil for flame-fusion growth. (Reprinted from D. T. J. Hurle (ed.) *Handbook of Crystal Growth 1, Fundamentals*, Part A, Chapter 1, 1993, copyright (1993) with permission from Elsevier Science.)

of physical chemistry for 50 years, the measurement of crystallization velocities, which was initiated by Gernez 1882, who had found a high crystallization rate of molten phosphorus. After Tammann's studies of glass crystallization, Czochralski presented in 1918 "a new method for measurement of the crystallization velocity of metals" where he pulled fibers of low-melting metals from melts. Soon after this, von Gomperz used floating dies to control the fiber diameter

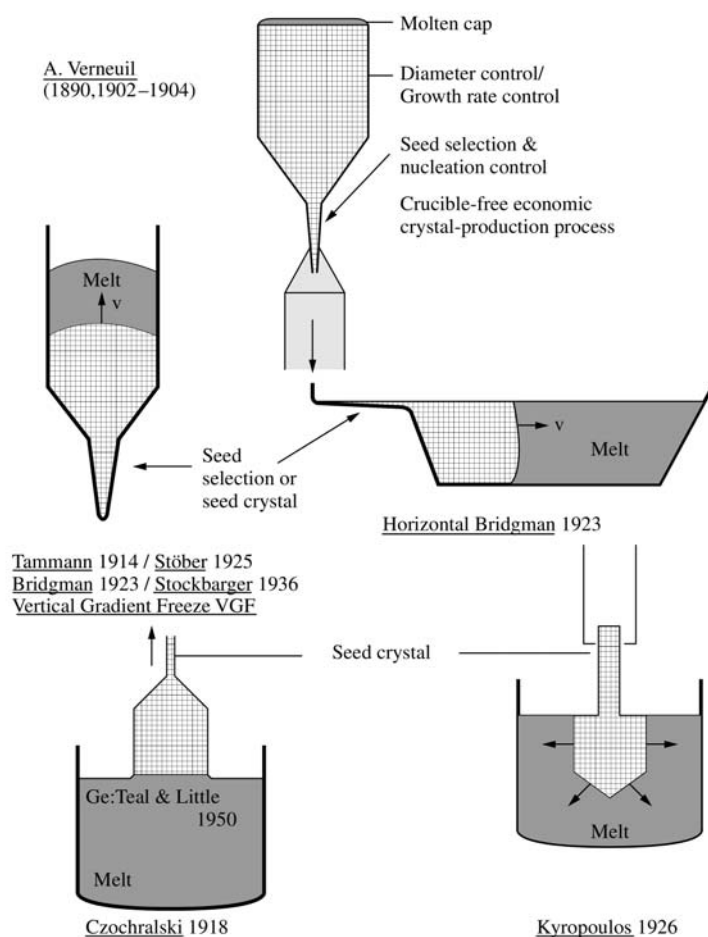


Figure 1.3 Modification of Verneuil's principles of nucleation control and increasing crystal diameters in other crystal-growth techniques. (Reprinted from H. J. Scheel, *J. Cryst. Growth* **211**(2000) 1–12, copyright (2000) with permission from Elsevier Science.)

(an early Stepanov or EFG process) 1921, and in 1928 Kapitza measured crystallization rates and prepared single-crystalline bismuth in a vertical glass tube (early zone melting).

Czochralski never considered pulling a crystal for research, although he could have adapted the inverse Verneuil principle, which was well known at that time. The metal crystals for research in Czochralski's laboratory were prepared by the Bridgman method. Therefore, it is no wonder that Zerfoss, Johnson and Egli in their review on growth methods at the International Crystal Growth Meeting in Bristol UK 1949 mentioned Verneuil, Bridgman–Stockbarger, Stöber and Kyropoulos techniques, but not Czochralski.

With the discovery of the transistor at Bell Laboratories there arose a need for single crystals of semiconductors, first of germanium. Teal and Little invented and developed crystal pulling of relatively large Ge crystals in 1950. Then it was the book of Buckley in 1951, who erroneously named pulling of large crystals after Czochralski, and this name became widespread with the fast-growing importance of crystal pulling. Possibly it is too late to change the name to Teal–Little–Dash, the latter due to his contribution to dislocation-free crystals by optimized seed and neck formation. The development of Czochralski and liquid-encapsulated Czochralski growth was discussed by Hurle 1987.

The majority of crystals is produced by pulling from the melt. Crystal dimensions have reached 10 cm for InP, LiTaO₃, sapphire and other oxide crystals, 15 cm for LiNbO₃ and GaAs, and 30 to 40 cm for silicon and for halide scintillator crystals with melt dimensions up to 1 m. Numerical modelling has assisted these developments, for instance for the optimization of the crystal and crucible rotation rates and of the temperature distribution and the design of heaters, after-heaters and heat shields. However, for the axial segregation and the striation problems the final general solution has not yet been established. The following approaches to reduce convection have been partially introduced in crystal production: double crucible for GaAs and stoichiometric LiNbO₃, magnetic fields in various configurations for semiconductors, and shallow melts or small melt volumes with continuous feeding for silicon and for halide scintillator crystals: these approaches are discussed in this volume. An alternative approach to solve, or at least minimize, the axial segregation and the striation problem is the co-rotating ring Czochralski (CRCZ) method which induces a hydrodynamic double-crucible effect: by optimized rotation rate of crystal and co-rotating ring (inserted into the melt) and counter-rotation rate of the crucible, a nearly convection-free melt fraction is achieved below the growing crystal, whereas the larger fraction of the melt is homogenized by combined forced and natural convection (Scheel 1995).

Only a few Czochralski-grown elements like silicon, germanium, and copper are produced dislocation-free by application of necking as developed by Dash in 1959. Most crystals have dislocations of typically 10^3 to 10^6 cm⁻² due to the generally large temperature gradients at the growing interface and due to the post-growth defect agglomeration behind the growth front (Völkl and Müller 1989). Attempts to grow with low-temperature gradients at the Institute of Inorganic Chemistry in Novosibirsk or to grow the crystal into the melt by the Kyropoulos method (SOI-method in St. Petersburg) have yielded low dislocation crystals of, for example, sapphire up to 40 cm diameter, but have not yet been developed for large-scale production. However, alternative technologies like Bridgman and vertical gradient freeze (VGF) have gained importance for production of semiconductor crystals of improved structural perfection like GaAs, InP, and CdTe and its solid solutions. In vertical Bridgman and in VGF growth the forced convection by the accelerated-crucible rotation technique (ACRT) of Scheel 1972 has increased homogeneity, structural perfection, and stable growth rates in the cases of halides (Horowitz *et al.* 1983) and doped CdTe (Capper 1994, 2000).

In silicon, the octahedral void defects (see Falster and Itsumi in this volume) and their distribution as well as oxygen and dopant homogeneity require further understanding (see Abe, Falster) and process optimization, otherwise an increasing fraction of silicon wafers have to be provided with epitaxial layers in order to achieve the homogeneity of surface properties required for highly integrated microelectronic circuit structures.

Examples of other remarkable developments in the growth of bulk crystals are briefly given: Hydrothermal growth of large high-quality low-dislocation-density quartz by VNIISIMS/Russia and Sawyer/USA, hydrothermal growth of large ZnO and emerald crystals, high-temperature solution growth of perovskites and garnets by top-seeded solution growth TSSG by Linz *et al.* and by the accelerated crucible rotation technique (ACRT) by Scheel and by Tolksdorf, TSSG growth of KTP and CLBO (the latter by Sasaki and Mori), aqueous-solution growth of KDP (Sasaki, Zaitseva), Bridgman–Stockbarger growth of alkali halides and of CaF_2 , float-zone growth of TiO_2 rutile by Shindo *et al.*, skull-melting growth of zirconia by Wenckus and Osiko, and Czochralski growth of numerous oxide compounds mainly in US, French, Japanese and recently Korean and Taiwan companies.

1.3 CRYSTAL-GROWTH TECHNOLOGY NOW

The world crystal production is estimated at more than 20 000 tons per year, of which the largest fraction of about 60 % are semiconductors silicon, GaAs, InP, GaP, CdTe and its alloys. As can be seen in Figure 1.4, optical crystals, scintillator crystals, and acousto-optic crystals have about equal shares of 10 %, whereas laser and nonlinear-optic crystals and crystals for jewelry and watch industry have shares of a few % only. This scale of crystal production and the fact that most

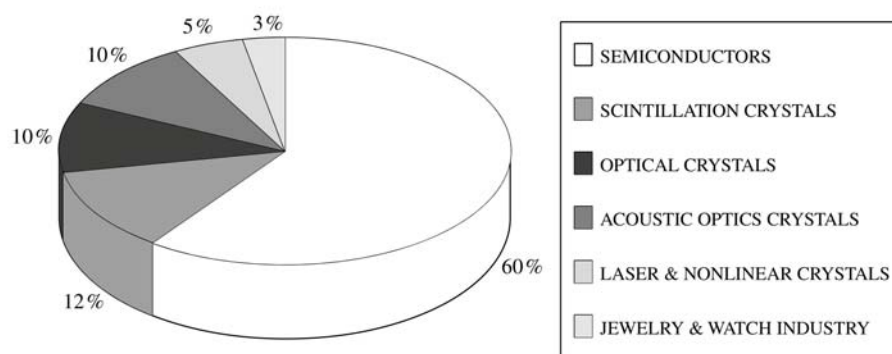


Figure 1.4 Estimated shares of world crystal production in 1999. (Reprinted from H. J. Scheel, *J. Cryst. Growth* **211**(2000) 1–12, copyright (2000) with permission from Elsevier Science.)

crystals are produced in factories specialized in silicon or GaAs or LiNbO_3 , etc. has caused an increasing degree of **specialization**. Furthermore, crystal growth has split into five major areas so that cross-fertilization and communication are more and more reduced:

1. Fundamental theoretical and experimental crystal growth studies.
2. Laboratory crystal growth for preparing research samples.
3. Industrial fabrication of single crystals and their machining and characterization.
4. Fabrication of metallic/dendritic crystals (e.g. turbine blades).
5. Mass crystallization (salt, sugar, chemicals).

Epitaxy has similarly separated from bulk crystal growth and has split into:

1. Fundamental/theoretical and experimental epitaxy studies and surface phenomena.
2. Epitaxy growth methods (VPE, MOCVD/MOVPE, MBE, ALE, LPE).
3. Materials classes (GaAs, InP, GaN, II-VI compounds, high- T_c superconductors, low-dimensional/quantum-well/quantum-dot structures, etc.).

As a consequence of these separations and splits, numerous specialized conferences, workshops and schools are established and regularly organized, new specialized journals appear, and the common language gets more and more lost, even to the extent that formerly well-defined terms are misused.

The situation is critical in research and development involving crystal growth and epitaxy. Due to a worldwide lack of education in these areas, frequently growth methods are employed for problems for which they are not well-suited or even not suited at all. It is postulated (Scheel 2002) that for a specific crystal of defined size and perfection there is only

one optimum and economic growth technology

considering thermodynamics, growth kinetics, and economic factors. This aspect is schematically shown in Figure 1.5, where the crystal performance, the crystal size, the efficiency of the growth method, and the price of crystal are shown. The shape factor may play a role when, for instance, special shapes are needed in the application, for example square, rectangular or oval watch faces of sapphire. The concept of one or maximum two optimum technologies should be considered for industrial crystal fabrication, whereas in laboratories the existing equipment or experience may determine a nonoptimum growth method. This postulate holds obviously also for epitaxial methods: for example, high- T_c compounds have been prepared by >1000 groups (after the discovery of high-temperature superconductivity, HTSC) by vapour-phase epitaxy, which cannot yield the atomically flat surfaces required for reliable HTSC tunnel-device technology. Instead only liquid

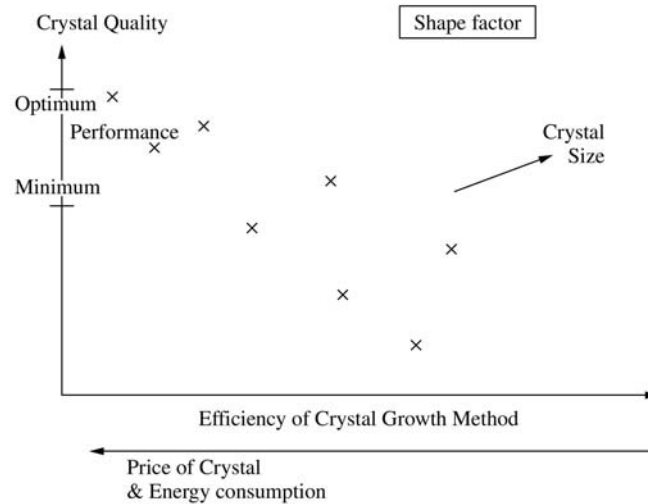


Figure 1.5 Schematic diagram of the efficiencies of various crystal-growth methods and the achieved crystal sizes and crystal quality. Note that there is normally only one optimum economic technology for the required crystal performance and size.

phase epitaxy near thermodynamic equilibrium can give atomically flat surfaces, as discussed elsewhere in this volume. Here, it could be added that the lack of recognition of the materials problems and specifically of the crystal growth and epitaxy problems have caused tremendous economic (and intellectual) losses not only in industries but also in research. As a recent prominent example, HTSC as a whole could not be properly developed, neither its physical understanding nor its many predicted applications because the chemical and structural complexity of the not very stable HTSC compounds were neglected. Most physical HTSC measurements were nonreproducible because the used crystals and layers were not sufficiently characterized for those structural and chemical defects that have an impact on these measurements or applications.

We realize that 'education' is needed for the important field of crystal-growth technology in order to achieve efficient developments in novel high technologies, in energy saving, in solar energy generation, in future laser-fusion energy and with a better approach in HTSC: in all these areas where crystal-growth technology is the progress-determining factor (Scheel 2002). However, in view of the multidisciplinary nature of crystal growth technology it will be not easy to initiate a curriculum in a classical university with the rather strict separation of disciplines in faculties or departments. In addition, the specialized education in CGT can start only after the multidisciplinary basic education and requires additional courses of 1 to 2 years. Furthermore, there are no teachers for this field as most crystal growers are specialized and experts in specific materials or specific methods only. In addition education in crystal growth technology and

Table 1.1 Complexity of crystal growth technology CGT

a. Multi-Disciplinary

- Chemistry (all fields) including Chemical Engineering
- Materials Science & Engineering
- Mechanical & Electrical Engineering (especially hydrodynamics, machine design, process control)
- Theoretical Physics (especially thermodynamics, non-equilibrium thermodynamics, statistical mechanics)
- Applied Crystallography and Crystal Chemistry
- Solid-State Physics

b. Complexity

- Phase Transformation from Fluid (melt, solution, vapour) to Crystal
- Scaling Problem: Control of surface on nm scale in growth system of $\sim m$ size, hampers numerical simulation
- Complex Structure & Phenomena in Melts and Solutions
- Multi-Parameter Processes: Optimize and compromise ~ 10 parameters

There is only one Optimum and Economic Growth Technology for a Specific Size and Performance of Crystal or Crystalline Layer!

epitaxy technology should be complemented by practical work and by periods in industries: another obstacle where, however, interested industries will collaborate. This practical work is needed in order to understand and appreciate the complexity (see Table 1.1) of crystal-growth processes in view of the involved phase transformation, of the many parameters that have to be compromised and optimized, and in view of the scaling problem, which hampers realistic numerical simulation.

1.4 CONCLUSION

Crystal-growth technology (CGT) including epilayer fabrication technology is of greatest importance for energy saving, for renewable energy, and for novel high technologies. Therefore the education of CGT engineers and CGT scientists is needed as well as significant support and publicity. Excellent students with intuition and motivation can have a great impact in crystal-growth technology and thus contribute to the energy problem and to high-technology developments of mankind.

REFERENCES

- Buckley H. E. (1951), *Crystal Growth*, Wiley, New York.
 Burton J. A., Prim R. C. and Slichter W. P. (1953), *J. Chem. Phys.* **21**, 1987.
 Capper P. (1994), *Prog. Crystal Growth Charact.* **28**, 1.

- Capper P. (2000), at second International School on Crystal Growth Technology ISCGT-2 Mount Zao, Japan August 24–29, 2000 (book in preparation).
- Elwell D. and Scheel H. J. (1975), *Crystal Growth from High-Temperature Solutions*, Academic Press, London- New York, (reprint foreseen 2003).
- Horowitz A., Gazit D., Makovsky J. and Ben-Dor L. (1983), *J. Cryst. Growth* **61**, 323 and Horowitz A., Goldstein M. and Horowitz Y., *J. Cryst. Growth* **61**, 317.
- Hurle D. T. J. (1987), *J. Cryst. Growth* **85**, 1.
- Ivantsov G. P. (1951, 1952), *Dokl. Akad. Nauk SSSR* **81**, 179; **83**, 573.
- Nassau K. (1969), *J. Cryst. Growth* **5**, 338.
- Nassau K. and Nassau J. (1971), *Lapidary J.* **24**, 1284, 1442, 1524.
- Rytz D. and Scheel H. J. (1982), *J. Cryst. Growth* **59**, 468.
- Scheel H. J. (1972), *J. Cryst. Growth* **13/14**, 560.
- Scheel H. J. (1993/1994), *Historical Introduction*, Chapter 1 in *Handbook of Crystal Growth*, editor D. T. J. Hurle, Vol. 1 Elsevier, Amsterdam.
- Scheel H. J. (1995), US Patent No. 5471943.
- Scheel H. J. (2002), Plenary lecture at Second Asian Conference on Crystal Growth and Crystal Technology CGCT-2 August 28–31, 2002 in Seoul, Korea, (proceedings in preparation).
- Scheel H. J. and Elwell D. (1972), *J. Cryst. Growth* **12**, 153.
- Scheel H. J. and Sommerauer J. (1983), *J. Cryst. Growth* **62**, 291.
- Scheel H. J. and Swendsen R. H. (2001), *J. Cryst. Growth* **233**, 609.
- Tiller W. A., Jackson K. A., Rutter J. W. and Chalmers B. (1953), *Acta Met.* **1**, 428.
- van Erk W. (1982), *J. Cryst. Growth* **57**, 71.
- Völkl J. and Müller G. (1989), *J. Cryst. Growth* **97**, 136.
- Wilke K.-Th. and Böhm J. (1988) *Kristallzüchtung*, VEB Deutscher Verlag der Wissenschaften, Berlin.

2 Thermodynamic Fundamentals of Phase Transitions Applied to Crystal Growth Processes

PETER RUDOLPH

Institut für Kristallzüchtung, Rudower Chaussee 6, 12489 Berlin, Germany

2.1 INTRODUCTION

Thermodynamics is an important practical tool for crystal growers. It helps to derive the most effective phase transition, i.e. growth method, and the value of the driving force of crystallization. From thermodynamic principles one can estimate the nucleation and existence conditions of a given crystalline phase, the width of compound homogeneity regions, and optimize the in-situ control of the crystal composition during the growth. In a word, no technological optimum can be found without considering thermodynamic relationships.

In general, crystal growth involves first-order phase transitions. This means there is the coexistence of two distinct uniform phases that are stable at the equilibrium point and separated by a phase boundary, i.e. an interface. Close to the equilibrium point the phases can still exist, one as thermodynamically stable, the other as the thermodynamically metastable phase, whereas the metastable phase is supersaturated (supercooled) with respect to the stable (equilibrium) phase. As a result, a thermodynamic driving force of crystallization will appear leading at a critical value of supersaturation to spontaneous nucleation of the crystalline phase within the metastable fluid phase. A controlled propagation of the solid/fluid phase boundary, however, takes place by providing a seed crystal or a substrate in contact with the fluid phase.

Classic thermodynamics (Guggenheim 1967, Wallace 1972, Lupis 1983) is concerned with macroscopic equilibrium states of quasiclosed systems. Such an approach for crystal growth is allowed due to the slow time scale of macroscopic processes compared with the kinetics of atoms, and due to the relatively small deviations from equilibrium. In order to describe nonequilibrium processes of quasiopen crystallization systems, characterized by continuous flows of heat and matter (i.e. entropy production), one uses linear nonequilibrium thermodynamics (de Groot and Mazur 1969, van der Erden 1993). In this work, however, we will treat only the fundamentals of classic thermodynamics.

2.2 PERFECT AND REAL STRUCTURE OF GROWN CRYSTALS

2.2.1 THE PRINCIPLE OF GIBBS FREE ENERGY MINIMIZATION

It is well known that all thermodynamic processes strive to minimize the free energy. Applied to the crystallization process this means that the single-crystalline state is a normal one because the free thermodynamic potential G (free potential of Gibbs) is minimal if the 'crystal growth units' (atoms, molecules) are perfectly packed in a three-dimensional ordered crystal structure, i.e. the atomic bonds are saturated regularly. Because the sum of the atomic bonds yields de facto the potential part H , the so-called enthalpy, of the internal crystal energy $U = H - PV$ (P = pressure, and V = volume) the process of ordering is characterized by the minimization of enthalpy ($H \rightarrow \min.$).

On the other side, however, an ideally ordered crystalline state would imply an impossible minimal entropy S . Thus, the opposite process of increasing entropy, i.e. disordering ($S \rightarrow \max.$) gains relevance with increasing temperature T . This is expressed by the basic equation of the thermodynamic potential of Gibbs

$$G = U + PV - TS = H(\downarrow) - TS(\uparrow) \rightarrow \min \quad (2.1)$$

In fact, the crystallization is composed of two opposite processes – (i) regular, and (ii) defective incorporation of the 'growth units', at which the second contribution increases exponentially with T and amounts at $T = 1000\text{ K}$ to about $10^{-3}\%$ (see Section 2.2.2).

The fundamental principle of energy minimization is also used to determine the composition of the vapour phase in equilibrium with a melt and a growing crystal in multicomponent systems. This is of the highest importance for the control of the melt chemistry and for the incorporation of foreign atoms into the crystal. For instance, in a Czochralski growth chamber the inert gas atmosphere may consist of numerous additional species produced by chemical reactions of volatile melt components with sublimates of the technological materials present (heater, crucible, insulator, encapsulant, etc.). Usually, numerous complex thermochemical reactions need to be considered. It is the aim of the material scientist, however, to determine the most stable reaction products having the lowest formation energy at given growth conditions and, thus, the highest probability of incorporation in the melt and crystal. Today, one can use powerful computer packages based on the principle of Gibbs free energy minimization (e.g. ChemSage, see Eriksson and Hack 1990, for example) in combination with thermodynamic material data bases (SGTE 1996). Examples of the thermochemical analysis of the LEC GaAs growth system are given by Oates and Wenzl (1998) and Korb *et al.* (1999), for example.

2.2.2 EQUILIBRIUM POINT-DEFECT CONCENTRATION

Considering the dialectics of ordering and disordering forces from Section 2.2.1 it is not possible to grow an absolutely perfect crystal. In reality ‘no ideal’ but only an ‘optimal’ crystalline state can be obtained. With other words, in thermodynamic equilibrium the crystal perfection is limited by incorporation of a given concentration of point defects n (as is well known, only point defects are able to exist in an equilibrium state).

Neglecting any effects of volume change, defect type and defect interplay at constant pressure the equilibrium defect concentration n can be determined from the change of thermodynamic potential by introducing the defect as

$$\Delta G = \Delta H_d - \Delta S_d T \rightarrow \min \quad (2.2)$$

with $\Delta H_d = nE_d$ the change of internal energy at incorporation of n defects, having a defect formation energy E_d , and $\Delta S_d = k \ln(N!/[n!(N-n)!])$ the accompanying change of entropy (configurational entropy) with k the Boltzmann constant and N the total number of possible sites. After substitution and application of Stirling’s approximation for multiparticle systems like a crystal [$\ln N! \approx N \ln N$, $\ln n! \approx n \ln n$, $\ln(N-n)! \approx (N-n) \ln(N-n)$] Equation (2.2) becomes

$$\Delta G = nE_d - kT[N \ln N - n \ln n - (N-n) \ln(N-n)] \quad (2.3)$$

Setting the 1st derivation of Equation (2.3) $\partial \Delta G / \partial n = 0$, which equals the energetical minimum defect concentration n_{\min} , and considering $N \gg n$ the ‘perfection limit’ of a crystal is

$$n_{\min} = N \exp(-E_d/kT) \quad (2.4)$$

exponentially increasing with temperature.

Using $N \approx N_A$ (Avogadro’s constant) $= 6 \times 10^{23} \text{ mol}^{-1}$ and $E_d = 1 \text{ eV}$ (vacancy formation energy in copper, for example) the minimum defect concentrations n_{\min} at 1000 K and 300 K are about $6 \times 10^{18} \text{ mol}^{-1}$ and 10^7 mol^{-1} , respectively.

Figures 2.1 and 2.2 show the $G(n)$ and $n(T)$ functions schematically. Due to the limitation of diffusion rate a certain fraction of high-temperature defects freezes in during the cooling-down process of as-grown crystals (broken lines) and exceeds the equilibrium concentration at room temperature markedly (Figure 2.2). In other words, in practical cases the intrinsic point-defect concentration is still far from thermodynamic equilibrium. Note, in the case of formation of vacancy-interstitial complexes (Frenkel defects) the value of $n_{\min}^{(F)}$ is somewhat modified and yields $\sqrt{n_{is}N} \exp(-E_d^{(F)}/kT)$ with n_{is} the total number of interstitial positions depending on the given crystal structure.

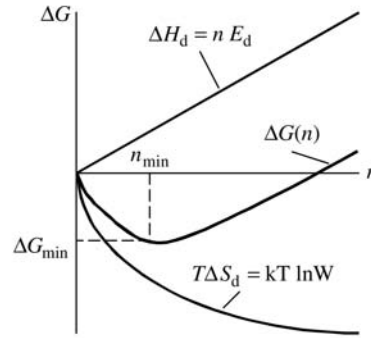


Figure 2.1 Schematic illustration of the equilibrium defect concentration ('perfection limit') n_{\min} obtained by superposition of defect enthalpy ΔH_d and entropy ΔS_d using Equations (2.2)–(2.4). (Reprinted from P. Rudolph, *Theoretical and Technological Aspects of Crystal Growth*, 1998, copyright (1998) reprinted with permission from Trans. Tech. Publications Ltd.)

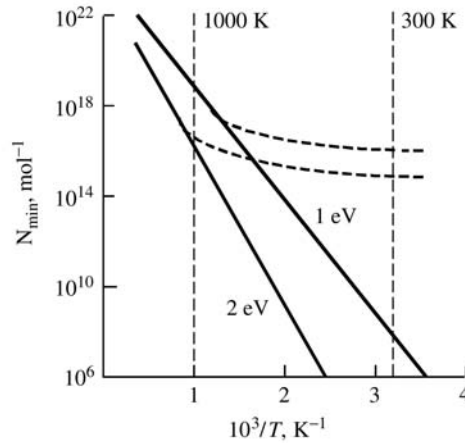


Figure 2.2 Minimum defect concentration vs. temperature at $E_d = 1$ eV (1) and 2 eV (2) after Equation (2.4). Dashed lines: the 'freezing in' courses of high-temperature defects.

Hence, depending on the device requirements the technologist has to decide the necessary purification and equilibration of a given material. For instance, semiconductor laser diodes need high-doped material ($>10^{17}$ dopants per cm^3) allowing a residual point defect level of less than 10^{16} cm^{-3} , but semi-insulating (SI) material for high-frequency devices requires the highest possible purity. Today, the standard level of residual contaminations in SI GaAs does not exceed 10^{14} cm^{-3} , for example.

2.3 THERMODYNAMICS OF PHASE EQUILIBRIUM

2.3.1 THE PHASE TRANSITION

After Landau and Lifschitz (1962) crystal growth is characterized by a first-order phase transition involving two contacting phases (1 and 2) separated by an interface. Most growth methods are carried out near equilibrium (exceptions are vapour growth processes, especially MBE and MOCVD) so that the equilibrium state, as described by phase diagrams, should serve as a useful guide to the temperature and pressure conditions.

Two phases are in equilibrium when the Gibbs potentials of the phases (G_1 and G_2) are equal so that the potential difference between the phases is zero ($\Delta G = 0$). For a single component (e.g. Si, GaAs, LiNbO₃, where stoichiometric compounds are recorded as single components), Equation (2.1) at uniform temperature and pressure becomes

$$\begin{aligned} G_1 &= U_1 - TS_1 + PV_1 \\ G_2 &= U_2 - TS_2 + PV_2 \\ G_1 - G_2 &= \Delta G = \Delta U - T\Delta S + P\Delta V = 0 \end{aligned} \quad (2.5)$$

where the change of internal energy can be expressed by $\Delta U = \Delta H - P\Delta V$. Figure 2.3 shows a three-dimensional sketch of two contacting phase planes with $G(T)$, $P(T)$ and $G(P)$ projections. Usually, a melt–solid phase transition involves relatively small volume change and hence $\Delta V \approx 0$. Then the free

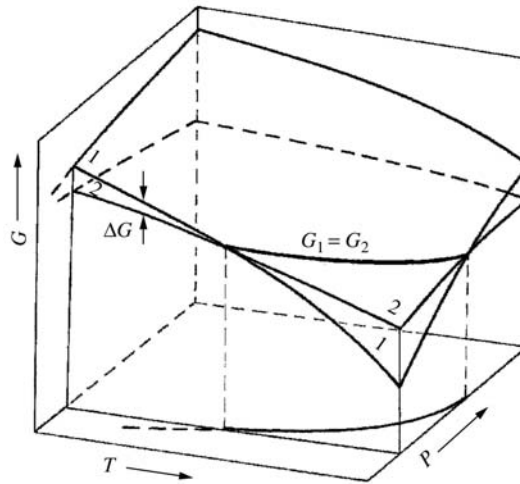


Figure 2.3 Two phase planes (1 and 2) crossing at the phase equilibrium line $G_1 = G_2$. Resulting G - T -, G - P -, and T - P -projections are demonstrated.

Helmholtz potential F can be used and at the phase equilibrium (index e) is

$$\Delta F = \Delta G_{V,P=\text{const}} = \Delta H - T_e \Delta S = 0 \quad (2.6)$$

with ΔH the enthalpy released by crystallization (latent heat of fusion), ΔS the transition (melting) entropy and T_e the equilibrium temperature (melting point). Thus, at the phase transition the enthalpy, entropy, internal energy and volume change abruptly (see Equation (2.5)) and Equation (2.6) becomes $\Delta H = T_e \Delta S$. Table 2.1 shows the parameter changes of selected materials at vapour–solid, liquid–solid and solid–solid phase transitions.

This is of practical relevance for crystal growth. For instance, the growth-rate-dependent liberated heat participates in the thermal balance at the melt–solid phase transition according to

$$k_l \frac{dT_l}{dz} - k_s \frac{dT_s}{dz} = \frac{\Delta H}{c} v \quad (2.7)$$

with $k_{l,s} = \lambda_{l,s}/(\rho_{l,s}c_{l,s})$ the thermal diffusivity (λ – heat conductivity, ρ – density, c – heat capacity), $dT_{l,s}/dz$ the temperature gradient along the growth axis z in the liquid (l) and solid (s) phase, and v the growth rate. In most cases, ΔH is conducted away through the growing crystal. For instance, at a typical value of $\Delta H/c \approx 10^3$ K (silicon) a crystallization velocity of 10 cm h^{-1} releases the heat quantity $\Delta H v/c$ (right term in Equation (2.7)) of 10^4 K cm h^{-1} . Hence, a temperature gradient greater than 20 K cm^{-1} is required to conduct this heat

Table 2.1 The abrupt change of thermodynamic parameters at first-order phase transitions of selected materials

Phase transition (1 \rightarrow 2)	Material (T, P at transit. point)	Volume change ($(V_1 - V_2)/V$ $= \Delta V/V$ (%))	Entropy change $S_1 - S_2 =$ ΔS (J/mol K)	Enthalpy change $H_1 - H_2 =$ ΔH (J/mol)
vapour–solid (v \rightarrow s)	Al (723 K, 1 atm)	>–99.9	345	250×10^3
	Si (1000 K, 1 atm)	>–99.9	304	304×10^3
liquid–solid (l \rightarrow s)	Al (933 K)	–6.0	11	11×10^3
	Si (1693 K)	+9.6	30	50×10^3
	GaAs (1511 K)	+10.7	64	97×10^3
	ZnSe (1733 K)	–19.6	7	13×10^3
	LiNbO ₃ (1533 K)	–20.9	17	26×10^3
solid–solid (s ₁ \rightarrow s ₂)	BaTiO ₃ T \rightarrow C (393 K)	0	0.5	0.2×10^3
	ZnSe _W \rightarrow ZB (1698 K)	0	0.5	1.0×10^3
	CsCl _{CsCl} \rightarrow NaCl (749 K)	–4	10	7.5×10^3
	C _{GR} \rightarrow D (1200 K, 40 atm)	–37	4.8	1.2×10^3

through the growing crystal with thermal diffusivity of $5 \times 10^2 \text{ cm}^2 \text{ h}^{-1}$ (note no temperature gradient is assumed in the melt).

In the case of vapour growth the heat of vaporization is released during condensation (i.e. deposition) of the solid phase. For instance, in the layer-by-layer growth mode, assisted by a discontinuous two-dimensional nucleation mechanism, the liberated thermal impulse is $I_T = (\Delta H/c)\Delta z$ with Δz the crystallizing step width. Assuming a spacing between layers $\Delta z = 6.5 \times 10^{-8} \text{ cm}$ and $\Delta H/c \approx 6 \times 10^3 \text{ K}$ (ZnSe at 1000°C) the heat I_T of about $4 \times 10^{-4} \text{ K cm}$ per layer has to dissipate through the growing crystal (i.e. substrate) and ambient.

2.3.2 TWO-COMPONENT SYSTEMS WITH IDEAL AND REAL MIXING

In addition to the variables T, P, V in a material system consisting of two (or more) chemical components $i = A, B, C \dots$ the free potential of Gibbs is also determined by the chemical phase composition, i.e. the component quantity n_i (number of gram-atomic weights, for example) so that $G = f(T, V, P, n_i)$. Hence, at constant T, V and P the change of the free Gibbs potential depends on the variation of n_i only and the partial derivative is named chemical potential μ_i

$$\frac{\partial G}{\partial n_i} = \mu_i \quad (2.8)$$

In a solution, the composition can be expressed by the mole fraction x_i yielding, in a two-component system

$$x_A = \frac{n_A}{n_A + n_B}; \quad x_B = (1 - x_A) \quad (2.9)$$

It proves to be convenient to write the chemical potential of a component i in a particular phase as

$$\mu_i = \mu_i^\circ(T, P) + RT \ln(\gamma_i x_i) \quad (2.10)$$

with R the universal gas constant, γ_i the *activity coefficient* and μ_i° the chemical *standard potential*. If the solution phase is a liquid, then μ_i° is the Gibbs energy per gram-atom of pure liquid i . If the solution is a solid with a particular crystal structure α , then μ_i° is the chemical potential of pure i with α crystal structure. For an ideal solution with completely mixing the activity coefficients are all equal to unity.

Using the dimensionless atomic fraction of the components x_i one has to translate the extensive thermodynamic functions of G, H and S in intensive (molar) values as $g = G/n, h = H/n$ and $s = S/n$. At fixed T, P and V Euler's Theorem can be applied to obtain the molar free Gibbs potential

$$g = \frac{G}{n} \Big|_{T, P, V} = \sum_{i=A}^C \mu_i \frac{n_i}{n} = \sum_{i=A}^C \mu_i x_i \quad (2.11)$$

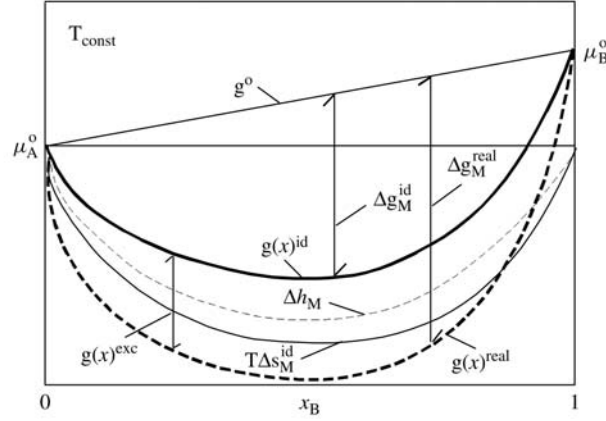


Figure 2.4 Energy composition curves for ideal [$g(x)^{\text{id}}$ with $\Delta h_{\text{M}} = 0$] and real solutions [$g(x)^{\text{real}}$ with $h_{\text{M}} < 0$]. (Reprinted from P. Rudolph, Theoretical and Technological Aspects of Crystal Growth, 1998, copyright (1998) reprinted with permission from Trans. Tech. Publications Ltd.)

so that in a two-component phase the molar free potential depends on the composition as

$$g(x) = g^{\circ} + \Delta g_{\text{M}} = (\mu_{\text{A}}^{\circ} x_{\text{A}} + \mu_{\text{B}}^{\circ} x_{\text{B}}) + (\Delta h_{\text{M}} - T \Delta s_{\text{M}}) \quad (2.12)$$

with g° and g_{M} the standard and mixing term, respectively (Figure 2.4).

In the case of ideal mixing there is no interaction between the particles of the different constituting components ($\gamma_i = 1$), i.e. there is no mixing enthalpy ($\Delta h_{\text{M}}^{\text{id}} = 0$). However, due to the disordering by mixing, the configurational entropy can be enlarged in the mixture by the amount

$$\Delta s_{\text{M}}^{\text{id}} = -R(x_{\text{A}} \ln x_{\text{A}} + x_{\text{B}} \ln x_{\text{B}}) \quad (2.13)$$

and the free molar mixing potential (bold-lined curve in Figure 2.4) is then

$$\Delta g_{\text{M}}^{\text{id}}(x) = -T \Delta s_{\text{M}}^{\text{id}}(x) = RT(x_{\text{A}} \ln x_{\text{A}} + x_{\text{B}} \ln x_{\text{B}}) \quad (2.14)$$

However, only very few systems yields $\gamma_{\text{A}} \approx \gamma_{\text{B}} \approx 1$ over the whole composition ($\text{CCl}_4\text{-SnCl}_4$, chlorobenzene-bromobenzene, n-hexane-n-heptane; see Rosenberger 1979).

For real solutions ($\gamma_i \neq 1$) the term Δh_{M} is no longer more zero and deforms the $g(x)$ course as shown by the broken-lined curve in Figure 2.4. Now the real mixing potential consists of an ideal and a so-called excess term as

$$\begin{aligned} g(x)^{\text{real}} &= g(x)^{\text{id}} + g(x)^{\text{exc}} \\ (g^{\circ} + RT \ln \gamma x) &= (g^{\circ} + RT \ln x) + (RT \ln \gamma) \end{aligned} \quad (2.15)$$

In many cases the regular-solution model with randomly mixed alloy ($\Delta s_M^{\text{exc}} = 0$) can be applied. Then the variation of the excess potential is $\Delta g^{\text{exc}} = RT \ln \gamma = \Delta h_M^{\text{exc}} = \Omega x(1 - x)$ where Ω is the interaction parameter related in the regular solution model of a binary A–B system to the relative energies of AB, AA and BB bonds in the alloy. A positive interaction parameter indicates that AB bonds have a higher energy than the average of AA and BB and phase separation may occur. On the other side, a negative value of Ω indicates that A and B atoms are attracted to each other with a tendency of compound formation. Using the quasichemical equilibrium (QCE) model of Panish (1974) the interaction parameter can be expressed as

$$\Omega = ZN_A [E_{AB} - \frac{1}{2}(E_{AA} + E_{BB})] \quad (2.16)$$

with Z the coordination number, N_A the Avogadro number, and E_{ij} the bond energy between nearest neighbours. In the more physical delta-lattice-parameter (DLP) model of Stringfellow (1972) the enthalpy of mixing is related to the effect of composition on the total energy of the bonding electrons. In this case the interaction parameter depends on the lattice parameters of the constituents only

$$\Omega = 4.375K(\Delta a)^2/\bar{a}^{4.5} \quad (2.17)$$

with Δa the lattice-parameter difference, \bar{a} the average lattice parameter, and K an adjustable constant (being the same for all III–V alloys, for example). A major prediction of the DLP model is that the values of Ω are always greater than or equal to zero. This means in the regular-solution the solid alloys may cluster and phase-separate, but they will not order (Stringfellow 1997). However, ordering is also observed, especially in thin films of semiconductor alloys consisting of atoms of markedly different size. For such cases one has to apply the Hume-Rothery model (1963), which predicts in systems with large difference of atomic size the evolution of large macroscopic strain energies that drive short- and long-range ordering rather than clustering (see Section 2.3.3).

The following typical cases can be distinguished at liquid–solid crystallization, for example:

$$\begin{array}{llll} \gamma < 1 & \Delta h_M^{\text{exc}} < 0 & \Delta g(x)_s < \Delta g(x)_l & \text{system with } T_{\text{max}} \\ \gamma > 1 & \Delta h_M^{\text{exc}} > 0 & \Delta g(x)_s < \Delta g(x)_l & \text{system with } T_{\text{min}} \end{array} \quad (2.18)$$

The extreme cases of both types lead to the appearance of intermediate phase (systems with compound; see Section 2.3.2) or eutectic composition, respectively. Further numerous transitive variants (i.e. systems with miscibility gap) are possible (see Lupis 1983 and Rosenberger 1979, for example).

2.3.3 PHASE BOUNDARIES AND SURFACES

The surface of a crystal is a cross discontinuity and has a free energy associated with it. The value of this free energy depends on the orientation of the face

and on the other phase in contact (vacuum, liquid). After Brice (1987) a first approximation of the surface free energy is

$$\gamma = (1 - w/u)\Delta H N_A^{-1/3} \quad (2.19)$$

where u is the number of nearest neighbours for an atom inside the crystal and w is the number of nearest neighbours in the crystal for an atom on the surface ($w < u$). N_A is the Avogadro number and ΔH the enthalpy of fusion (i.e. vaporization). A plot of γ against face orientation is shown in Figure 2.5 schematically. Energetic minima appear at atomically smooth, so-called singular faces. Faces corresponding to less-sharp minima are not flat on the atomical scale. Some values of γ for solid/vapour, solid/liquid and liquid/vapour interfaces of selected materials are compiled in Table 2.2. The equilibrium shape of a crystal consists of a set of singular faces by using the principle of surface potential minimization (Wulff construction)

$$G = \sum_{(100)}^{hkl} \gamma_{hkl} A_{hkl} \rightarrow \min \quad (2.20)$$

with A the surface area and hkl indicating the crystallographic orientation. Hence, the change of the Gibbs potential is also determined by the surface-area variation, i.e. $\partial G / \partial A = \gamma$, and the complete thermodynamical function is now $G = f(T, P, V, n_i, A)$.

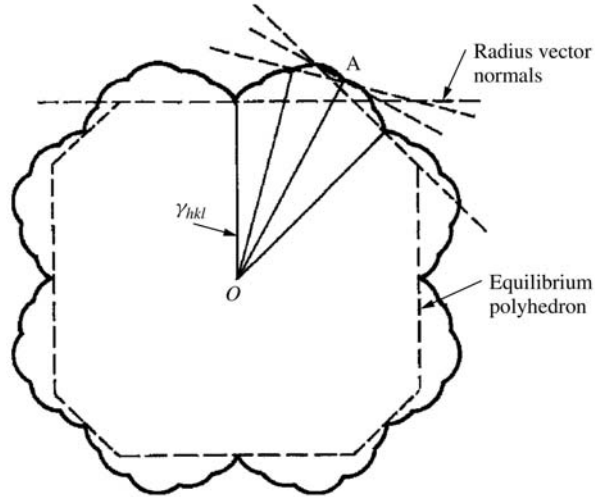


Figure 2.5 Wulff plot (bold contour) showing the variation of the free surface energy γ_{hkl} (radius vector) with orientation. The dotted contour gives the cross section of the equilibrium crystal shape.

Table 2.2 Surface tensions (γ_v), solid/vapour and solid/liquid interface energies (γ_{sv} , γ_{sl}) of selected materials (in $\text{J cm}^{-2} \times 10^4$)

Material	γ_{sv}	(<i>hkl</i>)	(<i>T</i>)	γ_v	γ_{sl}
Cu	1.70	(100)	(300 K)	1.35	0.14
Ag	1.20	(111)	(300 K)	0.93	0.11
Si	1.24	(111)	(300 K)	0.74	0.57
	1.08	(111)	(1683 K)		
Ge	0.76	(111)	(1209 K)	0.63	0.24
GaAs	0.50	(111)	(1511 K)	0.70	0.19
LiNbO ₃	0.10	(0112)	(1533 K)	0.18	0.15

Such a theoretical estimation is of special interest for the overcritical nucleation state where first stable crystallites with equilibrium shape may exist. Usually, however, large real crystals contain numerous defects (dislocations, for example) and grow under specific kinetic conditions that modify the equilibrium shape.

The surface energy also plays a role for diameter control in crystal-pulling methods (Czochralski, floating zone, EFG). For instance, the equilibrium between the three interface energies γ_{sv} , γ_{sl} and γ_v controls the capillary condition (stable meniscus height) by the characteristic growth angle (Tatartchenko 1994)

$$\psi_o = \arccos[(\gamma_v^2 + \gamma_{sv}^2 - \gamma_{sl}^2)/2\gamma_v\gamma_{sv}] \quad (2.21)$$

ψ_o values of 11° for silicon, 13° for germanium, 25° for indium antimonide and 17° for Al_2O_3 were reported (Hurle and Cockayne 1994). Hence, to pull a crystal with constant diameter in the vertical direction, the meniscus angle at the three-phase boundary (between the line tangent to the meniscus and the horizontal) of $\alpha_o = 90^\circ - \psi_o$ needs to be held constant.

In systems of two (and more) components like solutions, the composition at the interface differs from that of the bulk (effect of adsorption). In this case the specific free interface energy depends on the concentration x and is a function of the chemical potential μ^i (Lupis 1983). If a solute is enriched at the interface then it is a surface (interface) active one ($\partial\gamma/\partial x < 0$), passive surface (interface) components ($\partial\gamma/\partial x > 0$) are rejected.

2.4 THERMODYNAMICS OF TOPICAL CRYSTAL GROWTH PROBLEMS

2.4.1 MIXED CRYSTALS WITH NEARLY IDEAL SOLID SOLUTION

Mixed bulk crystals are of increasing importance, especially as suitable substrates for epitaxial layers of pseudobinary semiconductor-alloys like $\text{Ge}_{1-x}\text{Si}_x$, $\text{In}_{1-x}\text{Ga}_x\text{As}$, $\text{Cd}_{1-x}\text{Zn}_x\text{Te}$, for example. In such cases, monocrystals with high

compositional homogeneity (x uniformity) are required. On the other hand, mixed crystals with linear variation of the ‘lattice constant’ (delta-crystals) have enhanced mechanical stability (Ginzburg–Landau theory) and, after Smither (1982) are applicable as lenses in X-ray optics. The difficulty of this concept is to achieve the linear variation of the lattice constant with high accuracy and without loss of single crystallinity. In both areas, mixed crystals with nearly ideal solution behavior are under investigation.

An ideal solution means a system with complete miscibility in both the liquid and solid phase within the whole composition range $0 < x < 1$. In the low-pressure T – x -projection of such a phase diagram there are three fields, liquid, liquid + solid, and solid, separated by two boundaries known as the liquidus L and solidus S (Figure 2.6).

The liquidus and solidus lines of an ideal system can be calculated analytically. With respect to the component $i = B$ the equilibrium between solid and liquid phases is given by (compare Equations (2.8)–(2.10))

$$\begin{aligned}\mu_{Bs}(x_{Bs}, T) &= \mu_{Bl}(x_{Bl}, T) \\ \mu_{Bs}^0 + RT \ln x_{Bs} \gamma_{Bs} &= \mu_{Bl}^0 + RT \ln x_{Bl} \gamma_{Bl} \\ RT \ln \left(\frac{x_{Bs} \gamma_{Bs}}{x_{Bl} \gamma_{Bl}} \right) &= \Delta \mu_B^0 = \Delta h_B^0 - T \Delta s_B^0 = 0\end{aligned}\quad (2.22)$$

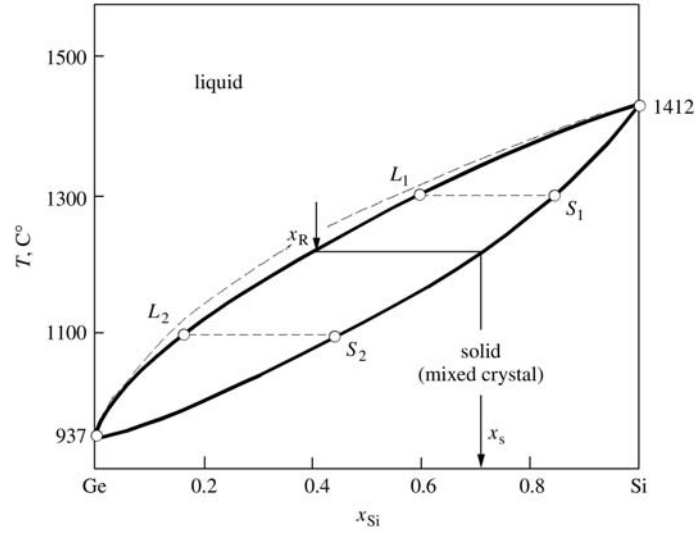


Figure 2.6 T – x -Projection of the near ideal system Ge–Si. Full lines were calculated, dashed line is experimental. The equilibrium distribution coefficient k_0 is given by x_s/x_l with subscripts s, l for solid and liquid phase, respectively. (Reprinted from P. Rudolph, Theoretical and Technological Aspects of Crystal Growth, 1998, copyright (1998) reprinted with permission from Trans. Tech. Publications Ltd.)

with h_B^0 and $s_B^0 = h_B^0/T_{mB}$ the intensive standard enthalpy and entropy of the pure component B with melting temperature T_{mB} . Hence, Equation (2.22) becomes

$$\ln \left(\frac{x_{Bs} \gamma_{Bs}}{x_{Bl} \gamma_{Bl}} \right) = -\frac{\Delta h_B^0}{R} \left(\frac{1}{T} - \frac{1}{T_{mB}} \right) \quad (2.23)$$

Since the solutions are ideal, the activities $\gamma_{Bs,l}$ may be replaced by mole fractions and Equation (2.23) yields the *van Laar equation*

$$\frac{x_{Bs}}{x_{Bl}} = k_o = \exp \left[-\frac{\Delta h_B^0}{R} \left(\frac{1}{T} - \frac{1}{T_{mB}} \right) \right] \quad (2.24)$$

with k_o the (thermodynamic) *equilibrium distribution coefficient* of component B (in the case of Ge–Si is $k_{oSi} > 1$, as demonstrated in Figure 2.6). Using $x_{As,l} + x_{Bs,l} = 1$ the equation of the *solidus* is

$$x_{As} \exp \left[-\frac{\Delta h_A^0}{R} \left(\frac{1}{T} - \frac{1}{T_{mA}} \right) \right] + x_{Bs} \exp \left[-\frac{\Delta h_B^0}{R} \left(\frac{1}{T} - \frac{1}{T_{mB}} \right) \right] = 1 \quad (2.25)$$

and, the equation of the *liquidus* is

$$x_{Al} \exp \left[\frac{\Delta h_A^0}{R} \left(\frac{1}{T} - \frac{1}{T_{mA}} \right) \right] + x_{Bl} \exp \left[\frac{\Delta h_B^0}{R} \left(\frac{1}{T} - \frac{1}{T_{mB}} \right) \right] = 1 \quad (2.26)$$

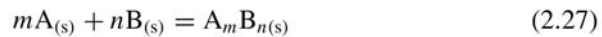
Figure 2.6 shows the T – x -projection of the Ge–Si phase diagram calculated after Equations (2.25) and (2.26) using $\Delta h_{Ge}^0 = 32 \text{ kJ mol}^{-1}$, $\Delta h_{Si}^0 = 50 \text{ kJ mol}^{-1}$, $T_{mGe} = 1210 \text{ K}$ and $T_{mSi} = 1685 \text{ K}$. Since the experimental and calculated curves agree quite well, one can say the Ge–Si system exhibits nearly ideal mixing behavior. This is also reflected in the near linear variation of the lattice constant with composition (Vegard's rule). At present, one is interested to obtain (i) high-quality $\text{Ge}_{1-x}\text{Si}_x$ substrates with fixed homogeneous composition for homoepitaxy of Si–Ge MQWs expanding the area of Si technology (high-speed bipolar transistors, photodetectors), (ii) high-efficiency solar cells, and (iii) crystals with linear composition gradient, i.e. linear gradient of the lattice constant, for application in X-ray focusing systems. Looking at the phase diagram one can show that for homogeneous compositions a diffusion-controlled growth regime with $k_{\text{eff}} = 1$ is favored (Figure 2.6). Further successful measures are the double-crucible Czochralski technique and conventional Czochralski growth with in-situ recharging (Abrosimov *et al.* 1997). For growth of 'delta' crystals one has to find a well-defined program of monotonous variation of k_{eff} from k_o to 1, e.g. by convection damping applying an increasing magnetic field (as was proposed by Johnson and Tiller 1961, 1962), or one uses the travelling-solvent-zone growth in a positive temperature gradient (Penzel *et al.* 1997). However, due to the concave solidus (Figure 2.6) a slightly concave axial temperature gradient needs to be established during the zone run.

The growth of ternary bulk mixed crystals ($\text{Ga}_{1-x}\text{As}_x\text{P}$ and $\text{Ga}_{1-x}\text{In}_x\text{As}$) by using of the liquid-encapsulated Czochralski technique was reported by Bonner (1994). These pseudobinary III-V materials form solid solutions with significant separation between liquidus and solidus. This results in strong compositional segregation, associated supercooling effects, and potential for interface breakdown resulting in polycrystalline growth. The problem was solved by intensive mechanical stirring of the melt. Also, $\text{InP}_{1-x}\text{As}_x$ ternary monocrystals with diameter of 2–3 cm, length up to 8 cm and x values up to 0.14 have been grown by the same method. With improved radial composition uniformity these crystals still exhibit a moderate x variation along the length of the boule due to the separation between liquidus and solidus lines. As a result, individual wafers cut normal to the growth direction of a given crystal may be of uniform composition, but there are still wafer-to-wafer composition variations that have to be eliminated in future (Bonner 1997). The first encouraging R&D results of MQW epitaxy on lattice-matched pseudobinary III-V substrates demonstrate the potential for a number of devices, particularly for 1.3- μm laser structures grown on $\text{InGa}_{1-x}\text{As}_x$ (Shoji *et al.* 1997).

2.4.2 SYSTEMS WITH COMPOUND FORMATION

2.4.2.1 Thermodynamic fundamentals

The tendency to form intermediate phases arises from the strong attractive forces between unlike atoms ($\gamma < 1$, $\Delta h_{\text{M}}^{\text{exc}} < 0$, $\Delta g(x)_{\text{s}} < \Delta g(x)_{\text{l}}$; see Equation (2.18)). In intermediate phases the bonds have a much stronger ionic or covalent character than in the metallic ordered solution. Therefore, the free energy, i.e. entropy and enthalpy, of such phases are typically low leading to their high stability. The following chemical reaction takes place



As example, Figure 2.7 shows the T - x -projection of the Ga-As system with GaAs compound at $m = n = 1$ after Wenzl *et al.* (1993). Due to the relatively narrow stability region the compound is shown as a single vertical line of exact stoichiometry. If the solid and liquid phases are of identical composition in equilibrium at a given melt temperature, the compound melts congruently (as in the case of GaAs with a congruent melting point at 1513 K).

In compounds, two elements A and B mix to form an ordered structure where the atoms occupy well-defined lattice sites. Such completely ordered structure exists only if the ratio of the numbers of atoms A and B is equal to the ratio of relatively small integers ν_A and ν_B . The mixture is then designated by the formula $A_{\nu_A}B_{\nu_B}$. Hence, the compounds AB or A_2B are related to $\nu_A = \nu_B$ or $\nu_A = 2\nu_B$, respectively. Deviation from such formulas ($\nu \pm \delta$) corresponds to nonstoichiometric compositions with misarrangements or vacancies. As discussed

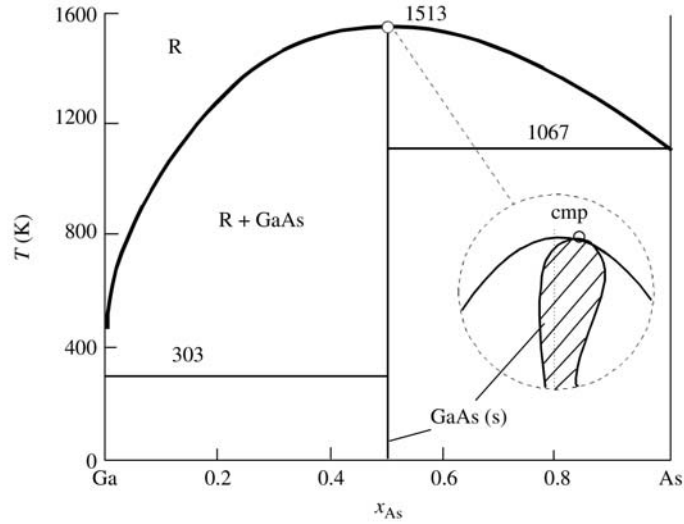


Figure 2.7 The T - x -projection of the Ga-As phase diagram with congruent melting point (cmp) on the arsenic-rich side after Wenzl and Oates (1993).

already in Section 2.2.2, at $T > 0$ K, in thermodynamic equilibrium the materials always contain a certain number of intrinsic point defects. This follows also from the plot of the free energy curves vs. composition (Figure 2.8) where the narrowness and steepness of the compound branch g_{AB} as well as the minimum positions of the g_A and g_B branches indicate the deviation from stoichiometry by the tangent intersection points. The region between these points (bold lines in Figure 2.8) is called the *range of existence* or *region of homogeneity*.

If its width is very small, i.e. the two tangents $A - A_A B_B$ and $A_A B_B - B$ touch the AB curve close to the minimum (Figure 2.8(a)), then its structure is referred to as a stoichiometric compound. If the range of stability is not negligible, i.e. the tangent contact points are markedly separated, the phase corresponds to a non-stoichiometric compound (Figure 2.8(b)). The width of the homogeneity region increases with T and depends on the formation enthalpies of nonstoichiometry-related defects.

Table 2.3 compiles some $\Delta\delta$ of selected compounds. Near stoichiometric situations with widths between 10^{-5} to 10^{-2} mole fraction are typical for semiconductor compounds with typical formation enthalpies of point defects between 1 and 4 eV.

2.4.2.2 Nonstoichiometry-correlated growth defects

Today, the deviation from stoichiometry is a key problem in growth of compound crystals. The side and degree of deviation influences the intrinsic point

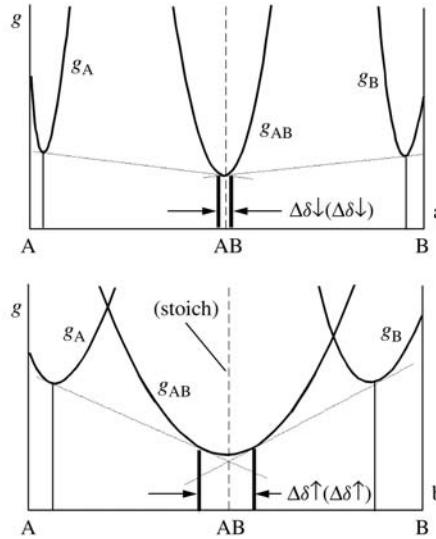


Figure 2.8 Thermodynamic derivation of the width of existence region ($\Delta\delta$) using the tangent construction of (a) near-stoichiometric compound AB and (b) nonstoichiometric compound AB.

Table 2.3 Maximum widths of the existence region $\Delta\delta$ of selected compound materials

Compound	GaAs	Cr ₃ S ₄	CdTe	PbTe	MnSb	Fe ₃ O ₄	Cu ₂ S	LiNbO ₃
$\Delta\delta$ (mole fraction)	$\sim 10^{-4}$	10^{-4}	3×10^{-4}	10^{-3}	10^{-3}	3×10^{-3}	3×10^{-2}	5×10^{-2}

defect concentration, i.e. electrical and optical parameters of such crystals, very sensitively. Thus, the control of stoichiometry during the growth process or by post-growth annealing is important. But in certain cases nonstoichiometry is required. For instance, the prerequisite for semi-insulating behavior of GaAs is a critical As excess. Therefore, such crystals are exclusively obtained from As-rich melt resulting in off-stoichiometric, i.e. arsenic-rich compositions and As-antisite defects known as double donors EL2, which are of crucial importance for compensation by doping control.

The generation of stoichiometry-related structural defects will be explained by the $T-x$ phase projection of the system Cd–Te. CdTe single crystals are of interest for photo-refractive devices and X-ray detectors. Figure 2.9 shows the region of homogeneity of this compound after Rudolph (1994). Three coupled growth problems can arise if the melt composition is not controlled: (i) the incongruent evaporation of the melt at the congruent melting point, therefore, (ii) segregation effects (i.e. constitutional supercooling) from the excess component on both sides

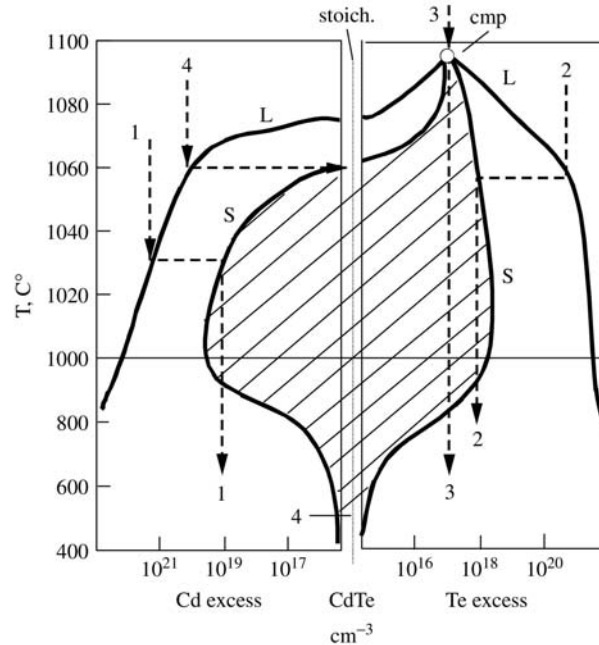


Figure 2.9 Sketched T - x -phase projection with region of homogeneity (hatched) of CdTe demonstrating the genesis paths of inclusions and precipitates in dependence on deviation from stoichiometry in the melt. 1,2 – formation of Cd (1) or Te (2) inclusions and precipitates; 3,4, – growth conditions of near inclusion- and precipitate-free solid composition, respectively (after Rudolph 1994).

of the congruent melting point, and (iii) the precipitation of the excess component during cooling of the as-grown crystal due to the retrograde behavior of the solidus lines. Here, one should distinguish between precipitates, generated by point-defect condensation in the solid, and inclusions that are formed by melt droplet capture from the diffusion boundary layer in front of the growing interface and enriched by the excess component (case (i)).

Second-phase precipitates and inclusions are common defects in melt-grown compound semiconductors (II-VI, III-V, IV-VI) and in several oxide systems. A sensitive dependence of the density of inclusions and also of the carrier concentration on deviation from stoichiometry was detected by Rudolph *et al.* (1995a) and is demonstrated in Figure 2.10. Under microgravity conditions an increased content of Te inclusions has been observed in CdTe due to the absence of convection in the melt. Variable magnetic fields (Salk *et al.* 1994) or accelerated crucible rotation techniques (Capper 1994, adapted from Scheel and Schulz-DuBois 1971) were used to prevent the enrichment at the interface and inclusion capture. Also post-growth annealing of bulk and wafers in active gas atmosphere (Cd saturated) was used by Ard *et al.* (1988) to remove inclusions. However, in this case

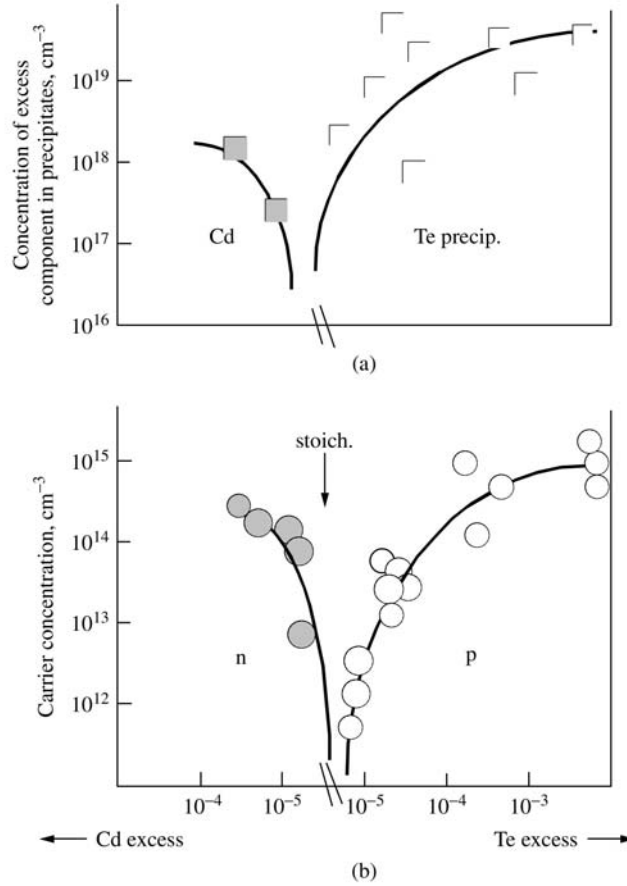


Figure 2.10 Concentration of excess component measured in (a) second-phase particles and (b) as carrier concentration vs. deviation from stoichiometry in CdTe. The results were obtained by vertical and horizontal Bridgman growth (after Rudolph *et al.* 1995).

the dissolution process of inclusions during annealing can promote the release of residual impurities by diffusion. Moreover, mechanical stress and dislocation multiplication at the site of inclusions were reported. Therefore, the best way is the in-situ control of stoichiometry during the crystal growth process.

2.4.2.3 The use of the P - T - x phase diagram to control the stoichiometry

As can be seen from Figure 2.9 (path 4) the growth of stoichiometric crystals requires an off-stoichiometric melt composition (in CdTe and GaAs a Cd- or Ga-rich melt, respectively). In order to achieve constant conditions the melt composition with a given excess component must be kept constant during the whole

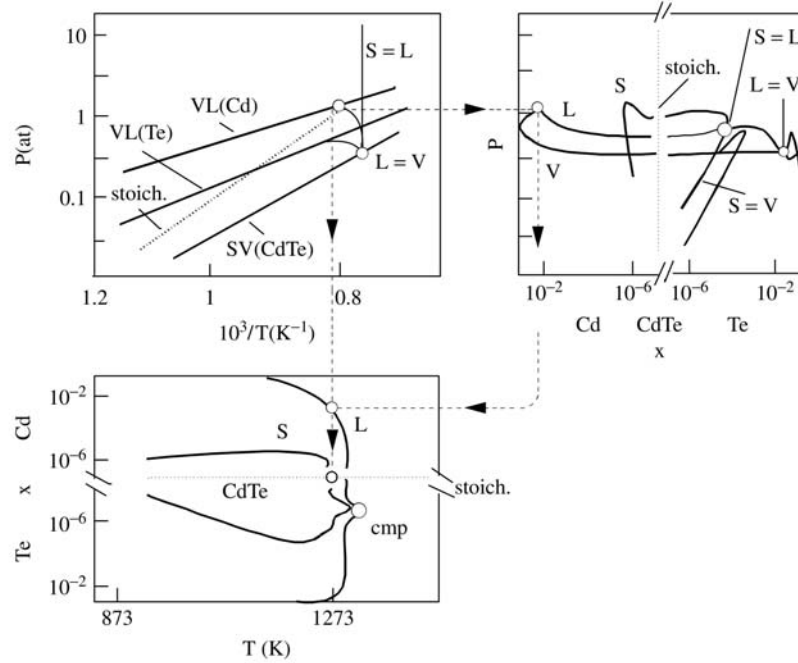


Figure 2.11 P - T -, P - x -, and T - x -projections of the system Cd-Te in three-phase equilibrium. Dashed lines mark the $P_{\text{Cd}} = P_{\text{CdTe}}$ (melt) equilibrium pressure for the growth of near stoichiometric crystals from the melt. As can be seen a marked Cd-excess in the melt is required to fix stoichiometric growth. (Reprinted from P. Rudolph, *Theoretical and Technological Aspects of Crystal Growth*, 1998, copyright (1998) reprinted with permission from Trans. Tech. Publications Ltd.)

growth run by accurate control of the gas atmosphere (Nishizawa 1990). Hence, the use of the p - T and P - x -projections in combination with the traditional T - x -projection of the phase diagram is necessary (Figure 2.11).

If both elements A and B are volatile, like in II-VI compounds, and the melt evaporates incongruently with vapour species A and B₂ (whereas $P_A > P_{B_2}$), the expression for the temperature of an additional source of the A component is approximately given by Rudolph *et al.* (1994)

$$T_A[\text{K}] = \frac{c_1}{c_2 - \log \left[\frac{a P_{AB}}{(1/x_1) + (a - 1)} \right]} \quad (2.28)$$

with P_{AB} – total pressure above the melt, $a = P_A/P_{B_2}$ – relative volatility (ratio of partial pressures of components), x_1 – melt composition for stoichiometric growth, and $c_{1,2}$ – constants of the partial function $\log P_A(\text{atm}) = -c_1/T + c_2$. Rudolph (1994) and Rudolph *et al.* (1994) introduced this formula to estimate

the source temperature of Zn ($T_{\text{Zn}} = 1000^\circ\text{C}$) and Cd ($T_{\text{Cd}} = 850^\circ\text{C}$) for stoichiometry-controlled Bridgman growth of ZnSe ($a = 5$, $P_{\text{ZnSe}} = 2 \text{ atm}$, $c_1 = -6678.4$, $c_2 = 5.491$) and CdTe ($a = 35$, $P_{\text{CdTe}} = 2 \text{ atm}$, $c_1 = 5317$, $c_2 = 5.119$), respectively. A good agreement with experimental values ($T_{\text{Zn}}^{\text{exp}} = 986^\circ\text{C}$ and $T_{\text{Cd}}^{\text{exp}} = 848^\circ\text{C}$) was found.

Today it is standard to grow well-controlled semiconductor crystals of III-V and II-VI compounds by using the vertical or horizontal Bridgman method with an in situ source of the volatile component (As at GaAs, Cd at CdTe, for example) the partial pressure (i.e. temperature) of which is selected after the P - T and P - x projections of the phase diagram.

2.4.3 COMPOSITIONAL MODULATION AND ORDERING IN MIXED SEMICONDUCTOR THIN FILMS

In the following, a phenomenon of surface thermodynamics occurring in modern thin-film technology will be discussed (see MRS Bulletin Vol. 22, No. 7, 1997). Almost all semiconductor devices are based on the control and manipulation of electrons and holes in thin-film structures. These structures are often produced in mixed semiconductor alloys ($\text{Ga}_{1-x}\text{In}_x\text{As}$, $\text{Ga}_{1-x}\text{In}_x\text{P}$), which become increasingly important because the electronic properties can be tailored by varying the composition. In addition, the use of very thin alloys allows the production of special structures such as quantum wells with abrupt changes in bandgap energy. Due to the microscopic scale of the layer thickness the energetical surface, i.e. the interface state becomes dominant for atom arrangement within the film "volume". In fact, recent studies of epitaxial growth of mixed semiconductor alloys showed interesting materials-growth phenomena that are driven mainly by surface thermodynamics. The well-known effect of surface reconstruction causes an atomistic ordering of the alloy components within the thin layer. First, the discovery of this phenomenon was surprising because for many years it was believed that when two isovalent semiconductors are mixed, they will form a solid solution at high temperature or separated phases at low temperature, but they will never produce ordered atomic arrangements. It was assumed that the mixing enthalpy $\Delta h(x)$ of an alloy depends on its global composition x only and not on the microscopic arrangement of atoms. However, thermodynamic analysis (Stringfellow 1997, Zunger 1997) has shown that certain ordered three-dimensional atomic arrangements within the layer minimize the strain energy resulting from the large lattice-constant mismatch between the constituents, while random arrangements do not (see also Section 2.3.2). In particular, there are special ordered structures α that have lower energies than the random alloy of the same composition x , that is

$$\Delta h(\alpha, \text{ordered}) < \Delta h(x, \text{random}) \quad (2.29)$$

where $\Delta h(\alpha, \text{ordered}) = E(\alpha, \text{ordered}) - xE(\text{A}) - (1-x)E(\text{B})$ and $\Delta h(x, \text{random}) = E(x, \text{random}) - xE(\text{A}) - (1-x)E(\text{B})$ with $E(\alpha, \text{ordered})$ the total

energy of a given arrangement α of A and B atoms on a lattice with N sites, $x = N_B/N$, $E(A)$ and $E(B)$ the total energies of the constituent solids.

Thus, ordered and disordered configurations at the same composition x can have different excess enthalpy $\Delta h^{\text{exc}}(x)$. In particular, the thermodynamically stable arrangement near the surface will be qualitatively different from the thermodynamically stable arrangement in an infinite bulk solid. Obviously, the surface has an important role in ordering of very thin films.

The most frequently observed form for these alloys grown epitaxially on (001) oriented substrates is the rhombohedral CuPt structure, with ordering on one or two of the set of four $\{111\}$ planes (MRS Bulletin Vol. 22, No. 7, 1997). In its turn the CuPt structure is stable only for the surface reconstruction that forms $[110]$ rows of $[110]$ group-V dimers on the (001) surface. These group-V-dimer rows form to reduce the energy due to the large number of dangling bonds at the surface.

Figure 2.12 shows the lowest-energy configuration of a (100) film of $\text{Ga}_{0.5}\text{In}_{0.5}\text{P}$ on a GaAs (100) substrate illustrating the relation between surface reconstruction, surface segregation, and subsurface ordering (MRS Bulletin Vol. 22, No. 7, 1997). When the reconstruction is $\beta(2 \times 4)$, In segregation and CuPt-B ordering (alternating $\{111\}$ planes of In and Ga) exist. CuPt-B ordering implies that there is Ga under the dimer (site A) and In between dimer rows (site C).

This thermodynamically driven effect of ordering has extremely important practical consequences. An interesting order-induced property of thin-film alloys is the reduction of the bandgap energy compared to that of bulk alloys of the same composition (Stringfellow 1997), thus moving the wavelength further into

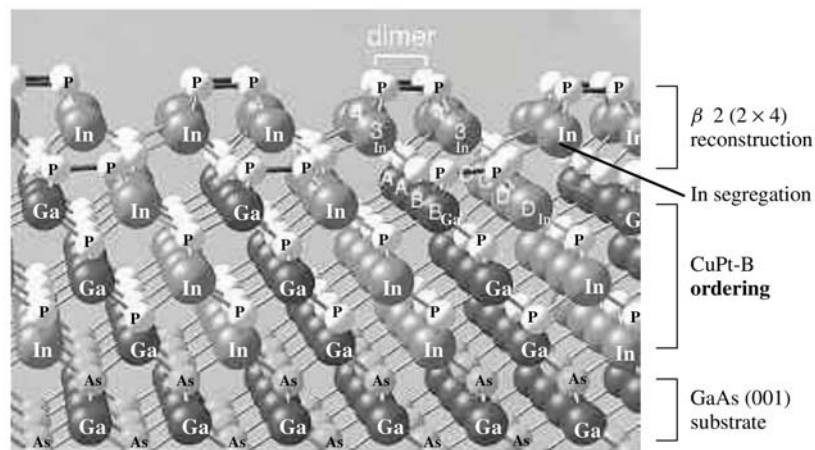


Figure 2.12 The lowest energy configuration of a (100)-oriented thin layer of $\text{Ga}_{0.5}\text{In}_{0.5}\text{P}$ on a GaAs (100)-substrate, illustrating the relation between surface reconstruction, surface segregation and subsurface ordering. (Reprinted from A. Zunger, MRS Bull. **22/7** (1997) cover image, copyright (1997) reprinted with permission from MRS Bulletin.)

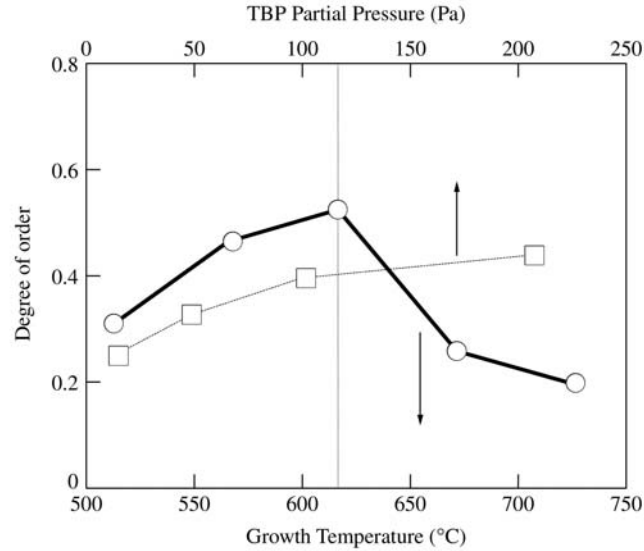


Figure 2.13 Degree of order as function of the growth temperature (for growth at a constant tertiarybutylphosphine (TBP) partial pressure of 50 Pa) and TBP partial pressure (for growth at constant temperature of 670 °C) in OMCVD-grown (Ga, In)P layers (after Stringfellow 1997).

the infrared. Hence, ordered III-V structures may become useful for IR detectors for which, so far, complicated II-VI materials ($\text{Cd}_{1-x}\text{Hg}_x\text{Te}$) were used. But for that the materials engineer must be able to control ordering over the entire surface of a wafer, to replace the spontaneous ordering by a precisely controlled one. Figure 2.13 shows a successful result to control the ordering in MOCVD grown $\text{Ga}_{1-x}\text{In}_x\text{P}$ layers as a function of the growth temperature after Stringfellow (1997).

2.5 DEVIATION FROM EQUILIBRIUM

2.5.1 DRIVING FORCE OF CRYSTALLIZATION

The prerequisite for crystallization of a stable solid phase within a metastable fluid phase is the deviation from the thermodynamic equilibrium, i.e. the crossing of coexistence conditions between the phases. In Figure 2.14 the $\mu(T)$ function in the neighborhood of a first-order phase transition is sketched. It can be seen, that μ (i.e. the Gibbs potential G) has a different dependence from the intensive variables in the two phases. Only at equilibrium are these potentials equal (Equation (2.5)). But away from equilibrium the potentials of the solid μ^s and fluid (mother phase) μ^f are different. The difference in temperatures

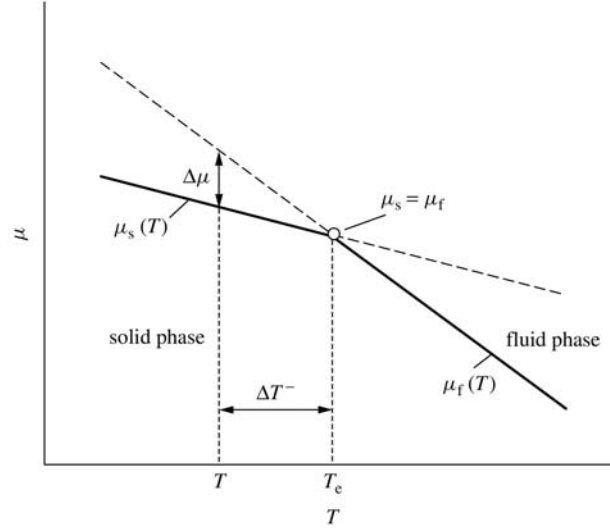


Figure 2.14 $\mu(T)$ function near the two-phase equilibrium. Solid lines: stable phases, dashed lines: metastable phases, T_e – equilibrium temperature, $\Delta\mu$ – driving force of crystallization. (Reprinted from P. Rudolph, Theoretical and Technological Aspects of Crystal Growth, 1998, copyright (1998) reprinted with permission from Trans. Tech. Publications Ltd.)

$\Delta T = T_e - T$ (Figure 2.14) denotes the *driving force of crystallization* or growth affinity as

$$\Delta\mu = \mu_f - \mu_s \quad (2.30)$$

In practical operations, several terms are used. One differs between *supersaturation*, expressing the pressure or concentration relationships at vapour–solid or solution–solid transition, and temperature-related *supercooling* used mainly in the case of crystallization from melt. Most convenient expressions are

$$\begin{aligned} \Delta P &= P - P_e && \text{total supersaturation} \\ \Delta P / P_e &= (S - 1) = \sigma && \text{relative supersaturation} \\ \Delta P / P_e \cdot 100 (\%) &&& \text{percentage of relative supersaturation} \end{aligned} \quad (2.31)$$

with P and P_e the actual and equilibrium pressure, respectively, and $S = P/P_e$. For small values of σ the energetic relation $\Delta\mu/kT = \ln(P/P_e) \approx \sigma$, i.e. $\ln S = \ln(1 + \sigma) \approx \sigma$, is used.

The supercooling at liquid–solid transition ($l \rightarrow s$)

$$\Delta T = (T_m - T) \quad (2.32)$$

is related to the driving force by

$$\mu_{l \rightarrow s} = \Delta h - T \Delta s = \Delta h - T(\Delta h/T_m) = (\Delta h/T_m)(T_m - T) = \Delta h \Delta T/T_m \quad (2.33)$$

where T – actual temperature, T_m – melting point, $\Delta h, \Delta s$ – enthalpy and entropy of melting, respectively. The melt-growth processes are characterized by relatively low driving forces. Values of $\Delta h/T_m$ usually fall within the range of 10 to $100 \text{ J K}^{-1} \text{ mol}^{-1}$, and values of ΔT are typically 1–5 K. Hence, $\Delta\mu_{l \rightarrow s}$ is about $10\text{--}100 \text{ J mol}^{-1}$.

In Figure 2.15 the metastable regions of supersaturation and supercooling in a sketched P – T -projection are demonstrated. As can be seen, below the triple point T_3 the v–s phase transition can begin with the unstable intermediate stage of fluid nuclei due to the smaller supersaturation (lower nucleation work) for generation of molten droplets than for solid nuclei. Only after that do the droplets translate into the stable crystalline phase. This phenomenon has been observed in various vapour-growth situations and is an example of *Ostwald's step rule*.

Comparing the various methods of epitaxy the relative supersaturation σ differs considerably. As 'rule of thumb', we have

liquid phase epitaxy (LPE):	$\sigma_{\text{LPE}} \approx 0.02\text{--}0.1$
vapour phase epitaxy (VPE):	$\sigma_{\text{VPE}} \approx 0.5\text{--}2$
molecular beam epitaxy (MBE):	$\sigma_{\text{MBE}} \approx 10\text{--}100$
metal organic chemical vapour deposition (MOCVD):	$\sigma_{\text{MOCVD}} \approx 40$

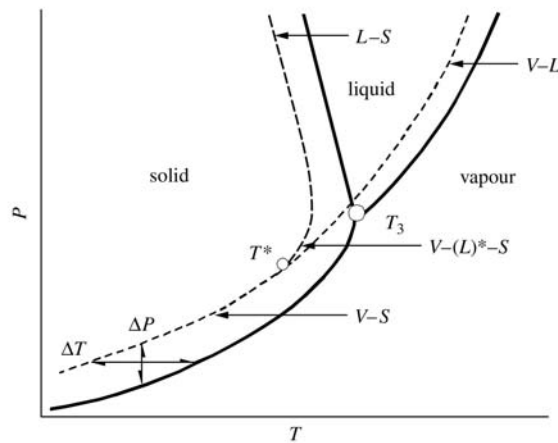


Figure 2.15 Schematic drawing of a P – T -projection with metastable regions of supersaturation ΔP and supercooling ΔT (dashed lines). T_3 – equilibrium triple point, T^* – intersection point between the metastable regions of vapour–solid ($V \rightarrow S$) and vapour–liquid ($V \rightarrow L$) transitions, i.e. non-equilibrium triple point.

Because at melt growth and LPE the crystals and layers are grown in near-equilibrium situations, the actual equilibrium states as described by the phase diagrams can be used as good approximation. At high deviations from equilibrium, however, the equilibrium phase diagrams are a rough tool only. For such cases, nonequilibrium phase diagrams considering additionally the growth kinetics are under theoretical investigations (Cherepanova and Dzelme 1981).

2.5.2 GROWTH MODE WITH TWO-DIMENSIONAL NUCLEATION

In the practice of bulk and thin-film crystal growth one starts with artificial seed crystals or single-crystalline substrates, respectively. Therefore the case of homogeneous three-dimensional nucleation in a metastable fluid phase, quite important for industrial mass crystallization, here omitted. In this work the special case of two-dimensional (2D) nucleation will be discussed which plays not only an important role in thin-film deposition processes (including homoepitaxy) but also reflects the bulk crystal growth at atomically flat phase boundaries. It is well known that after the 2D-nucleus is formed, the whole interface plane is then rapidly completed by lateral growth.

The change of the free Gibbs potential at the generation of a disc-shaped nucleus is expressed by the energy balance

$$\begin{aligned}\Delta G_{2D} &= \Delta G_V + \Delta G_{IF} \\ \Delta G_{2D} &= -\pi r^2 a \Delta \mu / \Omega + 2\pi r a \gamma\end{aligned}\quad (2.34)$$

where ΔG_V associates with increasing volume of the nucleus (being negative due to the energy gain) and ΔG_{IF} denotes the energy required for increase of nucleus surface (r – radius of the nucleus disc, a – lattice constant, Ω – molecular volume, γ – surface energy, $\Delta \mu$ – driving force). The maximum, i.e. critical value of ΔG_{2D} , at which the nucleus is stable, can be obtained by $\partial(\Delta G)/\partial r = 0$. Then the critical of the nucleus radius becomes

$$r^* = \frac{\gamma \Omega}{\Delta \mu} \quad (2.35)$$

Combining Equation (2.34) with Equation (2.35) the critical nucleation energy becomes

$$\Delta G_{2D}^* = \frac{\pi \Omega \gamma^2 a}{\Delta \mu} \quad (2.36)$$

For instance, in the melt growth of the atomically smooth and dislocation-free {111} face of Si crystals a supercooling of $\Delta T \approx 4$ K was ascertained experimentally (Chernov 1985). Inserting this value in Equation (2.33) together with the heat of fusion $\Delta h = 50 \text{ kJ mol}^{-1}$ and melting point $T_m = 1693$ K a driving force of $\Delta \mu = (\Delta h/T_m)\Delta T = 118 \text{ J mol}^{-1}$ can be deduced. Taking from

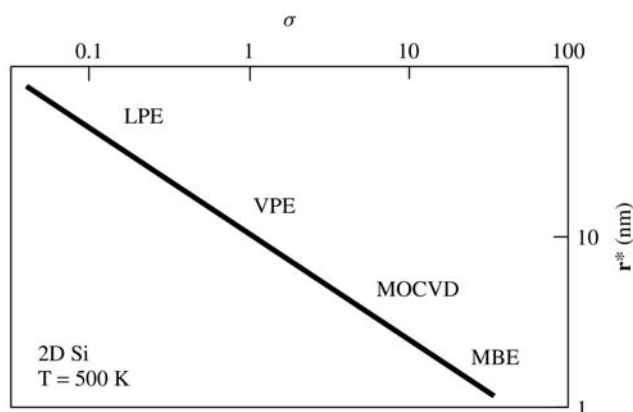


Figure 2.16 2-D nucleus radius vs. supersaturation for different thin-film deposition techniques estimated from Equation (2.35).

Table 2.2 the value of $\gamma_s = 0.57 \times 10^{-4} \text{ J cm}^{-2}$ and for $\Omega = 12 \text{ cm}^3 \text{ mol}^{-1}$ after Equation (2.35) the critical nucleus radius yields about 60 nm.

Figure 2.16 shows the critical radius of disc-shaped 2D-nucleus versus supersaturation for different methods of homoepitaxy of silicon at 500 K using Equation (2.35). As can be seen in the case of highly supersaturated growth from the vapour (MOCVD, MBE) the nucleus dimension yields only a few nm, comparable to a cluster consisting of a few atoms only.

Crystal growth from the melt occurs mainly under conditions of an atomistically rough interface (metals, semiconductors), which are growing without nucleation generation and, hence, under very small supercooling (i.e. driving force). In certain cases, however parts of the interface grow with atomically smooth interface-forming facets. On such face a discontinuous nucleation mechanism, as discussed above, takes place. As a result, in semiconductor compounds, twins can form (Hurle 1995). Furthermore typical sawtooth-like facet seams generate along the melt-grown boule surface, being a reliable indication of single crystallinity.

In epitaxial processes, where mainly atomically smooth interfaces occur, the growth mode of 2D-nucleation can be prevented by using slightly off-oriented substrates (few degrees) in order to achieve a continuous step-flow mechanism.

REFERENCES

- Abrosimov, N. V., Rossolenko, S. N., Thieme, W., Gerhardt, A., Schröder, W. (1997), *J. Cryst. Growth* **174**, 182.
 Ard, C. K., Jones, C. L., Clark, A. (1988), *Proc. SPIE* **639**, 123.

- Bonner, W. A. (1997), *Compound Semiconductor July/August*, p. 32 [see also (1994), *Proc. SPIE* 2228, 33].
- Brice, J. C. (1987), in: *Ullmann's Encyclopedia of Industrial Chemistry*, Vol. A8, VHC: Weinheim, p. 99.
- Capper, P. (1994), *Prog. Cryst. Growth Charac.* **28**, 1.
- Cherepanova, T. A., Dzelme, J. B. (1981), *Crystal Res. Technol.* **16**, 399.
- Chernov, A. A. (1985) in: *Crystal Growth of Electronic Materials*, Kaldis, E. (ed.). Elsevier: Amsterdam, p. 87.
- de Groot, S. R., Mazur, P. (1969), *Non-Equilibrium Thermodynamics*, North-Holland: Amsterdam.
- Eriksson, G., Hack, G. (1990), *Metall. Trans* **B12**, 1013.
- Guggenheim, E. A. (1967), *Thermodynamics*, 5th edition, North-Holland: Amsterdam.
- Hume-Rothery, W. (1963), *Electrons, Atoms, Metals, and Alloys*, 3rd. edition, Dover: New York.
- Hurle, D. T. J., Cockayne, B. (1994), in: *Handbook of Crystal Growth*, Vol. 2b, Hurle, D. T. J. (ed.), North-Holland: Amsterdam, p. 99.
- Hurle, D. T. J. (1995), *J. Cryst. Growth* **147**, 239.
- Johnston, W. C., Tiller, W. A. (1961), *Trans AIME* **221**, 331 and **224**, 214.
- Korb, J., Flade, T., Jurisch, M., Köhler, A., Reinhold, Th., Weinert, B. (1999), *J. Cryst. Growth* **198/199**, 343.
- Landau, L. D., Lifschitz, E. M. (1962), *Statistical Physics*, Chap. 14, Pergamon Press: London.
- Lupis, C. H. P. (1983), *Chemical Thermodynamics of Materials*, North-Holland: New York.
- Nishizawa, J. (1990), *J. Cryst. Growth* **99**, 1.
- Oates, W. A., Wenzl, H. (1998), *J. Cryst. Growth* **191**, 303.
- Panish, M. B. (1974), *J. Cryst. Growth* **27**, 6.
- Penzel, S., Kleessen, H., Neumann, W. (1997), *Cryst. Res. Technol.* **32**, 1137.
- Rosenberger, F. (1979), *Fundamentals of Crystal Growth I*, Springer: Berlin.
- Rudolph, P. (1994), *Prog. Cryst. Growth and Charac.* **29**, 275.
- Rudolph, P., Rinas, U., Jacobs, K. (1994), *J. Cryst. Growth* **138**, 249.
- Rudolph, P., Engel, A., Schentke, I., Grochocki, A. (1995a), *J. Cryst. Growth* **147**, 297.
- Rudolph, P., Schäfer, N., Fukuda, T. (1995b), *Mater. Sci. Eng.* **R15**, 85.
- Salk, M., Fiederle, M., Benz, K. W., Senchenkov, A. S., Egorov, A. V., Matioukhin, D. G. (1994), *J. Cryst. Growth* **138**, 161.
- Scheel, H. J., Schulz-DuBois, E. O. (1971), *J. Cryst. Growth* **8**, 304.
- SGTE *Pure Substance Database*, Version 1996 and *SGTE Solution database*, Version 1994, distributor: GTT-Technologies mbH, Herzogenrath.
- Shoji, H., Otsubo, K., Kusunoki, T., Suzuki, T., Uchida, T., Ishikawa, H. (1996), *Jpn. J. Appl. Phys.* **35**, L778. [see also Moore, A. (1997), *Compound Semiconductor July/August* 34].
- Smither, R. K. (1982), *Rev. Sci. Instrum.* **53**, 131.
- Stringfellow, G. A. (1972), *J. Phys. Chem. Solids* **33**, 665.
- Stringfellow, G. B. (1997), *MRS Bull.* **22**, 27.
- Tatartchenko, V. A. (1994), in: *Handbook of Crystal Growth*, Vol. 2b, Hurle, D. T. J. (ed.), North-Holland: Amsterdam, p. 1011.

- van der Eerden, J. P. (1993), in: *Handbook of Crystal Growth, Vol. 2b*, Hurle, D. T. J. (ed.), North-Holland: Amsterdam, p. 307.
- Wallace, D. C. (1972), *Thermodynamics of Crystals*, Wiley: New York.
- Wenzl, H., Oates, W. A., Mika, K. (1993), in: *Handbook of Crystal Growth, Vol. 1a*, Hurle, D. T. J. (ed.), North-Holland: Amsterdam, p. 105.
- Zunger, A. (1997), *MRS Bull.* **22**, 20.

3 Interface-kinetics-driven Facet Formation During Melt Growth of Oxide Crystals

**SIMON BRANDON, ALEXANDER VIROZUB,
YONGCAI LIU¹**

*Department of Chemical Engineering, Technion-Israel Institute of Technology
32 000 Haifa, Israel*

ABSTRACT

Facetting of crystals during their growth from the melt may lead to unwanted phenomena, adversely impacting the quality of the final crystalline product. In addition, substantial facet formation may significantly influence details of melt flow and other transport phenomena in the growth system. We present a computational method for combining the prediction of transport phenomena with interface-attachment-kinetics-driven faceting during the melt growth of single crystals; this method is applied in the analysis of vertical gradient solidification growth of oxide slabs. Calculations showing the sensitivity of faceting to changes in crystal-growth rate and furnace temperature gradient are reviewed. Results are compared with predictions based on a simple algebraic relation derived in the literature. In addition, the effects of melt convection and a transparent crystalline phase on faceting are examined. Melt flow is shown, in the bottom-seeded configuration, to enhance faceting at the center of the interface. Center facets on top-seeded crystals are, on the other hand, decreased in size due to the inverted melt flow pattern. A severely deflected, partially faceted melt/crystal interface in the case of a transparent crystalline phase demonstrates the difficulties associated with calculations of this type. Finally, semiquantitative agreement is achieved between facet positions predicted according to our calculations and those due to experiments shown in the literature. Discrepancies are most probably due to differences between the geometries studied (cylinders versus slabs) as well as inaccurate estimates of the degree of internal radiative transport within the crystalline phase.

¹ Current address: Department of Chemical Engineering, Tianjin University, Tianjin 300072, P. R. China.

3.1 INTRODUCTION

Facet formation during melt growth of single crystals is a phenomenon commonly seen in many systems. One may observe facets appearing on the melt/crystal interface as well as, in some cases (e.g. Czochralski (CZ) growth of several oxides), along the sides of the solidified crystalline material. Both anisotropy in interfacial-attachment kinetics and anisotropy in surface energy are the primary causes of facetting. In addition, transport phenomena within the growth system play a major role in controlling details of facet formation, size and position.

Understanding facetting phenomena, in particular understanding how to incorporate facetting into existing algorithms for modeling crystal-growth,² is of utmost importance. Achieving a capability for the prediction of facet formation is an important step towards learning how to control and minimize adverse effects resulting from facetting. Moreover, this approach is invaluable in systems involving severely faceted crystals; calculation of transport phenomena using existing algorithms may, in these systems, be erroneous due to inadequate prediction of the crystal geometry, which affects details of heat, mass and momentum transport.

Several problems related to facetting are recorded in the literature. The rapid step motion associated with growth of a faceted melt/crystal interface is often shown to be accompanied by nonequilibrium incorporation of a solute along the facet. Examples of this so, called 'facet effect' (Hurle and Cockayne, 1994) are numerous. Noteworthy is the case of Te incorporation during the CZ growth of InSb in the $\langle 111 \rangle$ direction, which was shown to exhibit an eight-fold difference in the effective segregation coefficient when comparing a $\langle 111 \rangle$ facet ($k_{\text{eff}} = 4.0$) to regions off the facet ($k_{\text{eff}} = 0.5$) (Hulme and Mullin, 1962). Of particular relevance to the results presented here is the facet effect in garnet crystals (Cockayne, 1968; Cockayne *et al.*, 1973), which has been linked to the appearance of a low-quality strained inner core along the axis of certain CZ grown crystals. An additional adverse effect of facetting involves twin formation associated with facets connected to the three-phase tri-junction during CZ and encapsulated vertical bridgman (VB) growth of certain semiconductor materials (e.g. InP). Discussions and examples of this phenomenon are given in (Hurle, 1995; Amon *et al.*, 1998; Chung *et al.*, 1998) and references within.

In a recent publication (Liu *et al.*, 1999) we presented a method for incorporating modeling of facet formation along the melt/crystal interface into existing algorithms for computation of transport phenomena during crystal-growth. This approach is strictly valid only in the case where facetting is caused by anisotropy of the interfacial attachment kinetics coefficient. The system studied in (Liu *et al.*, 1999) loosely corresponds to the VB growth experiments of Nd:YAG reported in (Petrosyan and Bagdasarov, 1976). Facetting, in these experiments, was shown to exhibit a sensitivity to thermal gradients and crystal-growth velocity in a manner suggesting kinetics as the dominant cause of facet formation.

² Large-scale modeling of bulk crystal-growth (see, e.g. Dupret and van den Bogaert, 1994) has traditionally focused on transport phenomena while ignoring facetting effects.

Two classical kinetic mechanisms (see, e.g. Flemings, 1974) linking the growth rate normal to the melt/crystal interface (V_n) to the driving force for crystallization (the undercooling ΔT) are of relevance to the work presented in (Liu *et al.*, 1999). These are growth by screw dislocations, which is characterized by a dependence of growth rate on undercooling raised to the second power ($V_n \propto \Delta T^2$), and two-dimensional nucleation limited growth, which requires a relatively large undercooling value and is associated with an exponential growth rate dependence on undercooling ($V_n \propto \exp(-A/\Delta T)$). In (Liu *et al.*, 1999) we described calculations obtained using a model kinetic relation that is consistent both with the experimental results of Petrosyan and Bagdasarov (1976) and with a dislocation-driven growth mechanism. In addition, we showed an approach compatible with a two-dimensional nucleation growth mechanism.

In the early 1970s, Brice (1970) and Voronkov (1972) proposed simple geometric theories, relating the facet size (b) to the maximum undercooling (ΔT_0) along the facet, the radius of curvature of the melting point isotherm (R) as well as the temperature gradient at the melt/crystal interface (g). According to these the size of the facet is given by

$$b = \sqrt{8\Delta T_0 R/g} \quad (3.1)$$

where, following (Voronkov, 1972),

$$g = \frac{k_m g_m + k_s g_s}{k_m + k_g}; \quad (3.2)$$

here g_m and g_s are the temperature gradients normal to the interface in the melt and solid phases, respectively. Assuming facet formation does not significantly affect transport phenomena, it is possible to use results of large-scale models of crystal-growth (which do not account for faceting) as a tool for obtaining the values of R and g necessary for the prediction of faceting via Equation (3.1).

In (Liu *et al.*, 1999) we compared results from our new approach for simultaneously calculating faceting and transport phenomena with predictions based on Equation (3.1). In this chapter we review these comparisons as well as present new calculations involving effects of melt flow, internal radiation through a transparent growing crystal, and more.

Convective heat transport in the melt of VB (or vertical gradient solidification) systems has been extensively studied in the literature (e.g. Chang and Brown, 1983; Adornato and Brown, 1987; Kim and Brown, 1991; Brandon *et al.*, 1996; Yeckel *et al.*, 1999). It has been shown that this mode of heat transport may or may not be of importance depending on the system studied. In the case of oxide growth (relevant to results presented here), melt convection has been demonstrated to be of importance in relatively large crucibles placed in substantial furnace gradients (Derby *et al.*, 1994).

Internal radiation within the crystalline phase of oxides is known to be of importance, mainly due to the high growth temperatures and optical properties

associated with these materials (see, e.g. Brandon *et al.*, 1996, and references within). In the results presented in (Liu *et al.*, 1999) as well as in most of the results shown here we use an enhanced thermal conductivity in the crystalline phase, therefore (in some sense) assuming the crystal to be an optically thick medium. This assumption is compatible with certain doped (see, e.g. Petrosyan, 1994) or undoped (see, e.g. Cockayne *et al.*, 1969) oxide systems. In addition, in this chapter, we briefly consider the growth of crystals whose optical properties render them almost transparent to infrared radiation.

This chapter is organized as follows. An outline of the model system and equations as well as the numerical approach is given in Section 3.2. Results of our calculations are presented in Section 3.3. These include a short review of the effects of crystal-growth rates and furnace gradient values on facet formation, calculations of convective effects and internal radiation (in a transparent crystalline phase) coupled with interface facetting, as well as an attempt at predicting the position of facets along the melt/crystal interface in the context of the experimental results of Petrosyan and Bagdasarov (1976). Finally, our conclusions are presented in Section 3.4.

3.2 MODEL DEVELOPMENT

We employ the same idealized model system, for the growth of oxide slabs, described in our previous work (Liu *et al.*, 1999). The system consists of a translational symmetric rectangular-shaped molybdenum crucible placed in a vertical furnace whose linear temperature profile is slowly reduced with time, thus inducing directional solidification. In (Liu *et al.*, 1999) we presented both a transient and a quasi-steady-state version of our model. The transient analysis showed that after a short time the thermal field and partially faceted melt/crystal interface shape reached a steady-state form, thereby justifying the use of a quasi-steady-state approach. Therefore, most of the calculations presented in (Liu *et al.*, 1999) as well as all of those presented here are based on a quasi-steady-state formulation. Details of the transient analysis as well as further information on the model system can be found in (Liu *et al.*, 1999).

3.2.1 MATHEMATICAL FORMULATION

A two-dimensional slab-shaped system is modeled. The equations describing heat transport in this system result from a quasi-steady-state formulation involving conduction, radiation and convection heat transport mechanisms. Note, however, that convective and certain aspects of the radiative effects are not accounted for in all of the results presented here. Deviations from the model equations presented in this section are clearly described where relevant (in Section 3.3).

The temperature distribution T is governed by

$$\begin{aligned}\rho_m C_{pm} \mathbf{v} \cdot \nabla T - \nabla \cdot k_m \nabla T &= 0 \quad \text{in the melt} \\ \nabla \cdot k_s \nabla T &= 0 \quad \text{in the crystal} \\ \nabla \cdot k_c \nabla T &= 0 \quad \text{in the crucible,}\end{aligned}\tag{3.3}$$

where \mathbf{v} describes the melt velocity field, k , ρ , C_p are the thermal conductivity, density, and heat capacity respectively, ∇ is the gradient operator and the subscripts m, s, c denote properties of melt, crystal, and crucible, respectively.

Melt convection, which was not accounted for in (Liu *et al.*, 1999), is included in the current formulation through the term on the left-hand side of Equation (3.3) (applied in the melt). This equation is coupled with the Navier–Stokes equation with the Boussinesq approximation,

$$\rho_m \mathbf{v} \cdot \nabla \mathbf{v} = \nabla \cdot \mathbf{T} + \rho_m \beta_T \mathbf{g}(T - T_{mp})\tag{3.4}$$

as well as the continuity equation in the melt,

$$\nabla \cdot \mathbf{v} = 0.\tag{3.5}$$

In Equation (3.4) the gravity vector is denoted by \mathbf{g} , T_{mp} is the material's melting point temperature, β_T is the melt thermal expansion coefficient, and the stress tensor \mathbf{T} , which is composed of the viscous stress together with the deviation of the pressure from the hydrostatic value P (i.e. dynamic pressure), is given by

$$\mathbf{T} = -P\mathbf{I} - \boldsymbol{\tau} = -P\mathbf{I} + \mu(\nabla \mathbf{v} + \nabla \mathbf{v}^T),\tag{3.6}$$

where \mathbf{I} is the unit tensor, and μ is the melt viscosity.

Assumptions of no-slip and no-penetration on the melt/crystal and crucible/melt interfaces are the basis for the boundary condition for velocity at these surfaces,

$$\mathbf{v} = \mathbf{0};\tag{3.7}$$

note that implicit in this boundary condition is the assumption that melt and crystalline densities are identical.

External boundaries of the crucible exchange heat with an idealized furnace thermal profile according to

$$-k_c \nabla T \cdot \mathbf{n}_{ce} = h(T - T_f) + \varepsilon \sigma (T^4 - T_f^4),\tag{3.8}$$

where \mathbf{n}_{ce} is the unit normal vector along the crucible's external boundary pointing away from the system, h is the convective heat transfer coefficient, ε is

the crucible wall's emissivity, and σ is the Stefan–Boltzmann coefficient. The furnace temperature, T_f is given by

$$T_f = T_{co} + Gy, \quad (3.9)$$

where G is the furnace temperature gradient, y is the spatial coordinate in the vertical direction, and T_{co} is the cold zone temperature, positioned (in the furnace) at the same height as the bottom of the crucible.

Continuity of heat flux along the inner crucible boundaries is enforced through the boundary condition:

$$(-k_c \nabla T)_c \cdot \mathbf{n}_{ci} = \mathbf{q}_i \cdot \mathbf{n}_{ci}, \quad (3.10)$$

where the subscript c denotes a term evaluated on the crucible side of the boundary, \mathbf{n}_{ci} denotes a unit vector normal to the crucible's inner boundaries (i.e. crucible/melt and crucible/crystal interfaces), and \mathbf{q}_i is the heat flux along the inner boundaries of the crucible on the melt ($i = m$) or crystalline ($i = s$) sides of the boundary.

Along the melt/crystal interface two conditions must be satisfied, the first represents a balance of thermal energy across the interface:

$$[(-k_m \nabla T)_m - \mathbf{q}_s] \cdot \mathbf{n}_{ms} = \Delta H_v V_n, \quad (3.11)$$

and the second gives the temperature distribution along the interface:

$$T = T_{mp} - f(V_n). \quad (3.12)$$

Here, \mathbf{n}_{ms} is a unit vector normal to the melt/crystal interface (pointing into the melt), the subscript m denotes a term evaluated on the melt side of the interface, ΔH_v is the heat of solidification per unit volume of crystalline material, and $f(V_n)$ is the interfacial undercooling whose form is defined and discussed in Section 3.2.1.1 below. The growth velocity normal to the interface (V_n) is assumed (in this quasi-steady-state formulation) to correspond to

$$V_n = \frac{G^*}{G} (\mathbf{n}_{ms} \cdot \mathbf{e}_y), \quad (3.13)$$

where $G^* = -dT_f/dt = -dT_{co}/dt$ is the rate at which the furnace temperature is reduced (thereby inducing solidification) and \mathbf{e}_y is the unit vector pointing in the vertical direction.

The form of the heat flux \mathbf{q}_i in Equation (3.10) depends on the dominant heat transport mechanisms acting in phase i at the interface. In the case where $i = m$ (i.e. melt), regardless of the presence or absence of convection, this flux is given by Fourier's law,³

$$\mathbf{q}_m = -k_m \nabla T. \quad (3.14)$$

³ This is a result of the no-penetration and no-slip conditions given by Equation (3.7).

The increase in heat transport through the crystalline phase due to thermal radiative effects is represented, in this study, either by an enhanced thermal conductivity, an approach strictly valid only for optically thick media, or by looking at the opposite limit where the crystal is transparent to infrared radiation. In the first instance the heat flux \mathbf{q}_s appearing in Equations (3.10) and (3.11) is given by Fourier's law,

$$\mathbf{q}_s = -k_s \nabla T, \quad (3.15)$$

while in the case where the crystal is transparent to infrared radiation the flux is given by

$$\mathbf{q}_s = -k_s \nabla T + \mathbf{q}_R, \quad (3.16)$$

where the radiative heat flux at the surfaces of the crystal, within the crystalline phase (\mathbf{q}_R), is obtained as described in Section 3.2.1.2 below.

3.2.1.1 Interfacial Kinetics

Equation (3.12) can be rearranged to give the undercooling at the interface which, assuming a single-component system with a planar melt/crystal interface, is the driving force for crystal growth,

$$\Delta T = T_{mp} - T = f(V_n) \quad (3.17)$$

whose functional dependence on V_n can be inverted to give a general kinetic relation of the form

$$V_n = \beta \Delta T, \quad (3.18)$$

where the kinetic coefficient β may be a function both of ΔT and of the local crystallographic orientation.

Due to surface-energy effects, nonplanarity of the melt/crystal interface leads to modifications in the definition of the driving force for crystal-growth. In the problem studied here, surface-energy effects are assumed unimportant. However, as described in (Liu *et al.*, 1999), including a small amount of artificial surface energy in the formulation is numerically beneficial. Results presented here were obtained with this slightly modified formulation that, in the interest of brevity, is not described here.

The undercooling is typically negligible on nonfacetted regions of the melt/crystal interface. Therefore, the dependence of β on θ (the angle denoting the crystallographic orientation in this two-dimensional model) can be ignored for all values of θ except for those that are close in magnitude to singular orientations (corresponding to surfaces that tend to facet). The most important parameters in this case are the β value corresponding to the singular orientation, the parameters determining the dependence of β on ΔT , and the range of θ values over which β significantly varies.

In this study, similar in spirit to ideas used by other authors (Yokayama and Kuroda, 1990), the kinetic coefficient (β) is modeled as a piecewise linear function of the surface slope relative to the singular orientation according to (see Figure 3.1),

$$\beta = \begin{cases} \beta^* + \frac{\beta_0 - \beta^*}{\tan(\Delta\theta_0)} \tan |\theta - \theta_0| & |\theta - \theta_0| < \Delta\theta_0 \\ \beta_0 & |\theta - \theta_0| \geq \Delta\theta_0, \end{cases} \quad (3.19)$$

where β_0 is the temperature-independent kinetic coefficient off the facet, θ_0 is the crystallographic angle corresponding to the singular orientation along which a facet will develop, and $\Delta\theta_0$ is the maximum deviation from θ_0 beyond which the interface behaves as a nonfaceted surface. The coefficient β^* , given by

$$\beta^* = (\beta_0 - \Delta\beta_0) \Delta T_0^{n-1}, \quad (3.20)$$

is the temperature-dependent kinetic coefficient on parts of the facet where the crystallographic orientation exactly equals the singular direction ($\theta = \theta_0$). In Equation (3.20) n is the exponent of this power-law kinetic equation, ΔT_0 is the undercooling on regions of the facet where $\theta = \theta_0$, and $\beta_0 - \Delta\beta_0$ is the kinetic coefficient corresponding to these regions in the special case where $\Delta T_0 = 1$ (in units corresponding to those used for V_n/β).

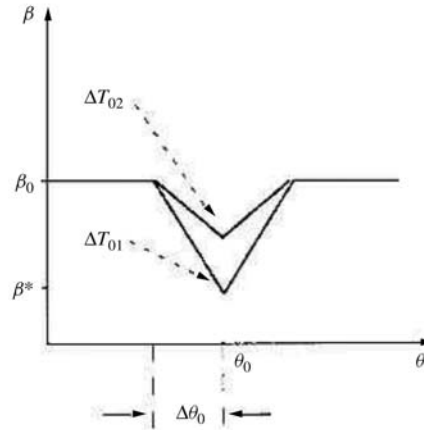


Figure 3.1 The kinetic coefficient (β) as a function of crystallographic orientation (θ) and undercooling. Here ΔT_{01} and ΔT_{02} (where $\Delta T_{01} < \Delta T_{02}$) are two different values of the maximum undercooling that correspond to melt/crystal interface orientations coinciding with the singular orientation (i.e. $\theta = \theta_0$). The lower curve corresponds to $\beta(\theta)$ for $\Delta T_0 = \Delta T_{01}$ and the upper curve corresponds to $\beta(\theta)$ for $\Delta T_0 = \Delta T_{02}$; both curves coincide for $|\theta - \theta_0| \geq \Delta\theta_0$. The β^* value appearing in this figure corresponds to $\Delta T_0 = \Delta T_{01}$. The curves are schematically plotted as piecewise linear since it is assumed, in this figure, that $\Delta\theta_0 \ll 1$. (Reprinted from Liu *et al.*, *J. Cryst. growth*, **205** (1999) 333–353, copyright (1999) with permission from Elsevier Science.)

Values of important parameters of the model, namely β^* , n , and $\Delta\theta_0$, were chosen as follows. The value of the kinetic coefficient β^* and the exponent n were derived to be consistent with the experimental observations in (Petrosyan and Bagdasarov, 1976), i.e. $\Delta T_0 \approx 1$ K and $n = 2$. Estimated values of $\Delta\theta_0$ can be deduced from (Bauser and Strunk, 1984). Due to numerical considerations we employ larger values of this parameter though, as described in (Liu *et al.*, 1999), these differences in $\Delta\theta_0$ values do not affect the results as long as $\Delta\theta_0$ is small enough. Finally, note that if β_0 is large enough it should yield negligible undercooling off the facet thereby rendering its exact value unimportant.

3.2.1.2 Radiative Flux Formulation

Formulation of the internal radiative heat flux appearing in Equation (3.16) is given by

$$\mathbf{q}_R \cdot \mathbf{n}_b = -\varepsilon_b \left[\tilde{n}^2 \sigma T_b^4 - \int_{\Omega=0}^{2\pi} i'(\Omega) \cos(\psi) d\Omega \right], \quad (3.21)$$

where \mathbf{n}_b represents the direction normal to the crystal's surface pointing away from the crystal, ε_b is the emissivity of the surface, \tilde{n} is the crystalline refractive index, σ is the Stefan–Boltzmann constant, $i'(\Omega)$ is the radiation intensity directed along the solid angle Ω , and ψ represents the angle between the direction of $i'(\Omega)$ and \mathbf{n}_b .

The intensity of radiation leaving the surface of the crystal towards its interior along the solid angle Ω , with the assumption of gray and diffuse boundaries, is given by

$$i'(\Omega) = \frac{1}{\pi} \left(\left\{ \tilde{n}^2 \sigma T_b^4 - \frac{1 - \varepsilon_b}{\varepsilon_b} [\mathbf{q}_R \cdot (-\mathbf{n}_b)] \right\} \Big|_{\text{surface}} \right). \quad (3.22)$$

For detailed discussions of radiative heat flux formulations in the context of crystal-growth from the melt see (Dupret *et al.*, 1990; Brandon and Derby, 1992a; Brandon and Derby, 1992b). In the case of the present work, please see (Virozub and Brandon, 1998) for a study of a similar system, albeit without kinetic effects.

3.2.2 NUMERICAL TECHNIQUE

A full account of the techniques employed here can be found in (Brandon *et al.*, 1996; Brandon, 1997; Virozub and Brandon, 1998; Liu *et al.*, 1999) and references within. In particular, see (Liu *et al.*, 1999) for details pertaining to application of Equation (3.12) including the introduction of artificial surface energy into the formulation.

Our algorithm is based on a standard Galerkin finite element method (GFEM), using biquadratic basis functions⁴ for all variables except the pressure, which is

⁴ A recent study (Virozub and Brandon, 2002) discusses the application of incomplete Hermite or complete Lagrangian cubic elements versus complete Lagrangian quadratic elements (which were used here).

represented by 2-D linear basis functions. An elliptic mesh generation technique was employed; the method is based mostly on the work described in (Christodoulou and Scriven, 1992), though in cases where the crystal was assumed transparent to infrared radiation the mesh-generation technique was modified to correspond to work presented in (Tsiveriotis and Brown, 1992).

The nonlinear Galerkin weighted residual equations associated with the temperature, velocity, pressure and nodal position unknowns were solved using the Newton–Raphson technique (Dahlquist and Björck, 1974). The mesh used in the calculations presented here included 988–1368 two-dimensional, nine-node, Lagrangian quadrilateral elements. Between 2 and 8 Newton–Raphson iterations were required for a fully convergent solution with 2–50 CPU minutes needed per iteration on a 32-processor Cray J932 supercomputer.⁵ The convergence criterion was set in the L-2 norm as $\|\delta\|_2 < 10^{-6}$, where δ represents the update vector for the Newton–Raphson iteration.

3.3 RESULTS AND DISCUSSION

A number of issues are investigated in this study. First we review the effect of two important operating parameters, the crystal-growth rate and the furnace gradient, on facetting in a system in which melt convection is unimportant and internal radiative effects can be approximated by an enhanced thermal conductivity in the crystalline phase. The second set of results focuses on the effects of melt flow on facetting phenomena, while the third part of this section is concerned with modeling the growth of transparent crystals prone to facet formation along the melt/crystal interface. Finally, an attempt is made to reproduce and understand the positioning of facets as observed in the experiments of Petrosyan and Bagdasarov (1976).

Physical properties and operating parameters vary according to the subject studied. In general, the system, which is loosely based on the experiments described in (Petrosyan and Bagdasarov, 1976), was modeled using the same properties and parameters applied in our previous report (Liu *et al.*, 1999). All deviations from the parameters given in (Liu *et al.*, 1999) or application of additional data (e.g. necessary for modeling melt convection), are accounted for in the text.

3.3.1 EFFECT OF OPERATING PARAMETERS ON FACETTING

Two important operating parameters existing in melt growth systems are the furnace temperature gradient and the crystal axial growth rate ($V_g = G^*/G$).⁶

⁵ The exact CPU time requirement and number of elements used depend on the transport mechanisms considered in the calculation.

⁶ As indicated in Section 3.2.1, we assume that the growth rate in the vertical direction (V_g) is equal to that induced by the furnace operator (see Equation (3.13)).

Understanding how these parameters can be used to control facet size and position is most important in the event that adverse phenomena (e.g. the appearance of strain in garnets) is associated with faceting in the system under consideration.

At slow enough growth rates, the kinetic relation (Equation (3.18)) yields a negligible value for undercooling ($\Delta T = f(V_n) \approx 0$) which, when neglecting surface-energy effects, leads to an interface conforming to the shape of the melting-point isotherm. This is generally the case for regions of the interface that support a large enough value of β . However, in the vicinity of singular orientations, β may be small enough so that the undercooling $\Delta T = V_n/\beta$ (Equation (3.18)) is not negligible even for the relatively small growth rates typically employed in systems of interest. In this case, the melt/crystal interface may exhibit visible facets corresponding to singular orientations.

In Figure 3.2 we present results showing the sensitivity of interface shapes and their corresponding undercooling profiles to the axial growth rate for two different singular orientations ($\theta_0 = 0^7$ and $|\theta_0| = \pi/4$). In both cases partially faceted surfaces are predicted with facets corresponding to orientations defined as singular. In addition, an increase in facet size with increasing growth rate is obtained in these calculations. Finally, the maximum undercooling is consistent with Equations (3.18)–(3.20) (with $n = 2$); for a given singular orientation the maximum undercooling obtained is proportional to the square root of the growth rate.

Interface shapes and undercooling profiles are next shown (Figure 3.3) for different values of the furnace temperature gradient G , for the same two singular orientations considered in Figure 3.2. Here, as expected, the maximum undercooling does not vary with G (for a given orientation). However, it is evident that facet sizes (which are probably easier to estimate by looking at the undercooling profiles), grow with decreasing furnace temperature gradient.

Following Chernov (1973) we combine the Brice–Voronkov theory given by Equations (3.1) and (3.2) with the kinetic relation Equations (3.18)–(3.20) (with $\theta = \theta_0$ and $n = 2$) yielding:

$$b = [V_n/(\beta_0 - \Delta\beta_0)]^{0.25} \sqrt{8R/g} \quad (3.23)$$

This equation predicts a linear relation between the facet size b and $V_g^{0.25}$ (for a given singular orientation $V_g \propto V_n$) as well as a linear relation between b and $g^{-0.5}$. It is conceivably possible to use crystal-growth models that ignore faceting (e.g. our model with $\beta \rightarrow \infty$) to obtain predictions of g and R that, together with Equation (3.23), can be employed in the estimation of the facet size b .

Facet sizes were obtained from the results shown in Figures 3.2 and 3.3 by relating facet edges to points along the melt/crystal interface at which $\theta = \theta_0 + \Delta\theta_0$ and $\theta = \theta_0 - \Delta\theta_0$. See Figure 3.4 for a comparison of these values of b with those calculated via the Brice–Voronkov theory Equation (3.23). It is

⁷ Corresponding to a singular orientation coinciding with the direction of growth.

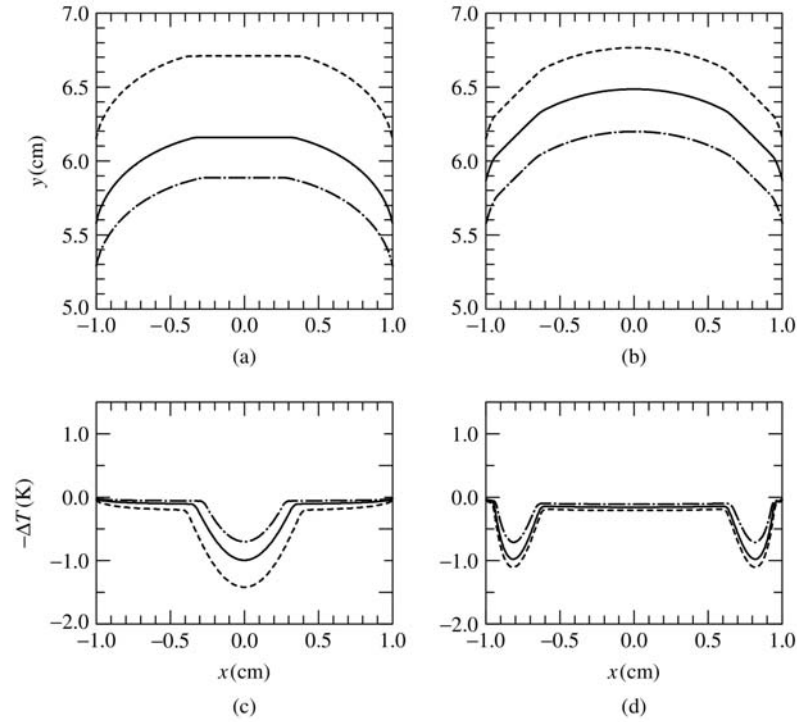


Figure 3.2 The effect of growth rate on interface shapes and interfacial undercooling for $G = 50$ K/cm. Interface shapes for (a) $\theta_0 = 0$ (singular orientation aligned with growth direction); (b) $|\theta_0| = \pi/4$ (singular orientation at an angle $\pi/4$ radians away from the growth direction). Undercooling profiles for (c) $\theta_0 = 0$; (d) $|\theta_0| = \pi/4$. In the case where $\theta_0 = 0$ (a,c) dashed curves correspond to $V_g = 0.4$ cm/h, continuous curves correspond to $V_g = 0.2$ cm/h, and dashed-dotted curves correspond to $V_g = 0.1$ cm/h. In the case where $|\theta_0| = \pi/4$ (b,d) dashed curves correspond to $V_g = 0.4$ cm/h, continuous curves correspond to $V_g = 0.3$ cm/h, and dashed-dotted curves correspond to $V_g = 0.2$ cm/h. For the sake of clear presentation, interface shapes are plotted at a vertical distance from each other that is proportional to their growth rates (assuming 2.9 h have elapsed since growth was initiated). (Reprinted from Liu *et al.*, *J. Cryst. growth*, **205** (1999) 333–353, copyright (1999) with permission from Elsevier Science.)

evident that the Brice–Voronkov theory gives predictions of b that are linear with $V_g^{0.25}$, indicating that R and g are almost unaffected by changes in V_g . A linear relation is also found between facet sizes, estimated via Equation (3.23), and $G^{-0.5}$. Consistent with this interesting observation we found that a linear relation exists between g and G . In addition, these last results also indicate that R is not significantly affected by changes in G . Finally, facet sizes obtained with (Equation (3.23)) are close to but different from those calculated by our model. Most significant are differences obtained for low values of G .

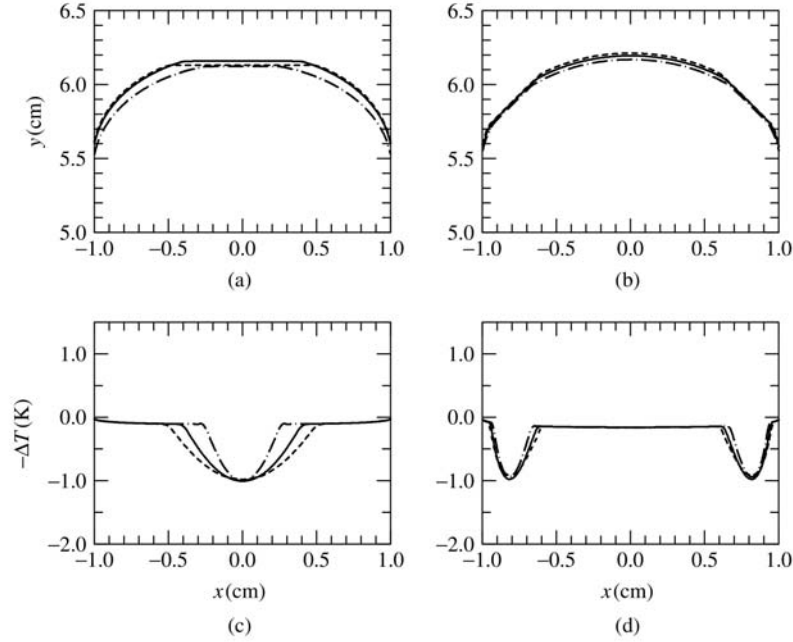


Figure 3.3 The effect of furnace temperature gradient on interface shapes and interfacial undercooling. Interface shapes for (a) $\theta_0 = 0$; (b) $|\theta_0| = \pi/4$. Undercooling profiles for (c) $|\theta_0| = 0$; (d) $|\theta_0| = \pi/4$. In the case where $\theta_0 = 0$ (a,c) $V_g = 0.2 \text{ cm/h}$, dashed curves correspond to $G = 20 \text{ K/cm}$, continuous curves correspond to $G = 34 \text{ K/cm}$, and dashed-dotted curves correspond to $G = 90 \text{ K/cm}$. In the case where $|\theta_0| = \pi/4$ (b,d) $V_g = 0.3 \text{ cm/h}$, dashed curves correspond to $G = 34 \text{ K/cm}$, continuous curves correspond to $G = 50 \text{ K/cm}$, and dashed-dotted curves correspond to $G = 70 \text{ K/cm}$. (Reprinted from Liu *et al.*, *J. Cryst. growth*, **205** (1999) 333–353, copyright (1999) with permission from Elsevier Science.)

3.3.2 INTERACTION BETWEEN MELT FLOW AND FACET FORMATION

It is reasonable to assume that heat transport in the small-scale system studied in (Liu *et al.*, 1999), as well as in Section 3.3.1 of this chapter, is only marginally affected by melt convection. However, as shown for a similar (though cylindrical) system in (Derby *et al.*, 1994) it is expected that increasing the size of the crystal will lead to increased natural-convective flows that, beyond a certain system size, will significantly affect heat transport and therefore facet formation. This enhancement in flow is due to the fact that the dimensionless driving force for flow is proportional to a characteristic length of the system (e.g. crystal width) raised to the third power (see, e.g. Landau and Lifshitz, 1959).

In this section we present calculations that account for melt flow. Properties employed here, not used in (Liu *et al.*, 1999), are the melt viscosity

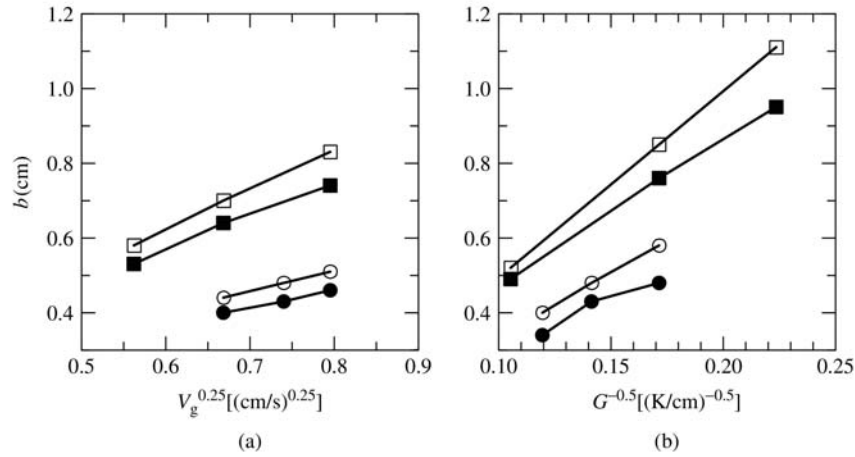


Figure 3.4 Facet size as a function of (a) growth rate and (b) furnace temperature gradient. Open symbols depict values predicted based on the Brice–Voronkov approach using calculations with $\beta \rightarrow \infty$ together with Equation (3.23). Filled symbols represent results from our calculations (shown in Figures 3.2 and 3.3) accounting for coupling between kinetics and thermal field calculations (i.e. using finite values for β). Squares and circles represent results for $\theta_0 = 0$ and $|\theta_0| = \pi/4$, respectively. (Reprinted from Liu *et al.*, *J. Cryst. growth*, **205** (1999) 333–353, copyright (1999) with permission from Elsevier Science.)

($\mu = 0.0426 \text{ Pa s}$) and thermal expansion coefficient ($\beta_T = 1.8 \times 10^{-5} \text{ K}^{-1}$) both of which are based on measurements of Fratello and Brandle (1993).

Melt/crystal interface shapes as well as interfacial undercooling profiles are plotted in Figure 3.5 for a variety of crystal widths both with and without accounting for melt flow. Increasing the crystal width (B^*) leads to a strengthening of convection characterized by fluid rising along the hot crucible walls and descending along the centerline towards the melt/crystal interface. This flow pattern (as can be seen in Figure 3.5) promotes the appearance of facet sizes larger than those calculated without taking melt convection into account.

In an attempt to better understand the results shown in Figure 3.5 we plot, in Figure 3.6 data corresponding to calculations using our model without accounting for kinetic effects (i.e. $\beta \rightarrow \infty$). This data includes values of the thermal gradient in the melt (g_m) normal to the melting-point isotherm and the curvature (R) of the melting-point isotherm, both calculated at the position on the melting-point isotherm whose orientation corresponds to θ_0 . Results shown in Figure 3.6 were calculated both with and without accounting for melt convection, as a function of the width of the crystal B^* .

Considering the simple Brice–Voronkov approach Equations (3.1) and (3.23), it is apparent that the facet size is sensitive to the ratio R/g . When convection is not considered, increasing the system size leads to a decrease in g , and an increase

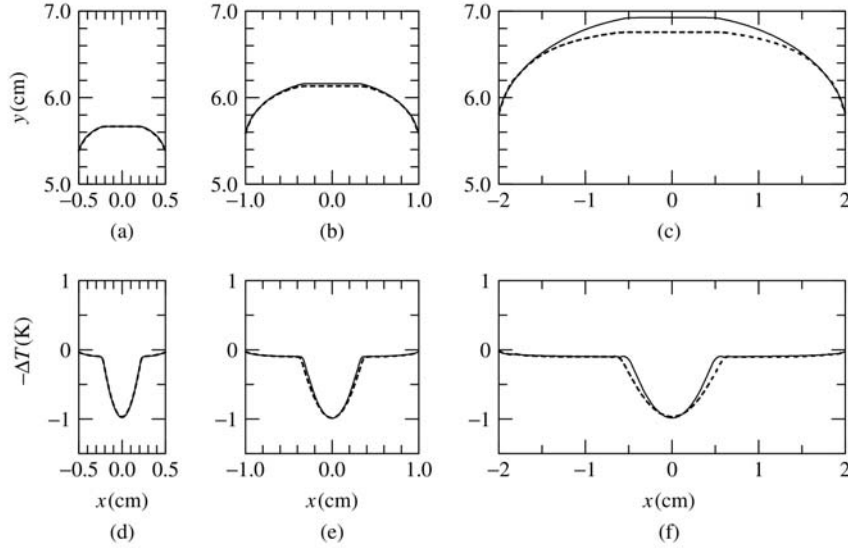


Figure 3.5 The effect of melt convection (and crystal width B^*) on interface shapes and interfacial undercooling for $\theta_0 = 0$, $G = 50$ K/cm and $V_g = 0.2$ cm/h. Interface shapes for (a) $B^* = 1$ cm, (b) $B^* = 2$ cm, (c) $B^* = 4$ cm. Undercooling profiles for (d) $B^* = 1$ cm, (e) $B^* = 2$ cm, (f) $B^* = 4$ cm. Dashed curves were obtained while accounting for melt convection and continuous curves were calculated while neglecting convection (i.e. $\beta_T = 0$).

in R , which promotes⁸ an increase in facet size. In the (more realistic) event that melt convection is considered, increasing the system size leads to an increase both in g_m and in R . In this case even though R/g_m can be shown to increase with increasing system size, it is not obvious at first glance if the rapid increase in R (compared to the case where convection is ignored) is significant enough to cause widening of facets (for a given system size) due to convective effects. The convection-induced increase in g_m , compared to the case where convection is ignored, may conceivably offset the increase in R . However, looking at Figure 3.5 and at Figure 3.7 it is evident that changes in R dominate and that, for a given system size, convective effects lead to an increase in facet size. Moreover, it is interesting to note (see Figure 3.7) that for $B^* = 4$, convective effects are strong enough to cause an increase in the discrepancy between the predictions based on Equation (3.23) and calculations obtained using our approach. These discrepancies are, as in the cases shown in Figure 3.4, most serious for low values of G .

⁸ Note that although we consider g_m rather than g , conservation of energy across the interface in this type of system (in which latent heat effects are most probably unimportant) renders $g_s \propto g_m$ and therefore $g \propto g_m$.

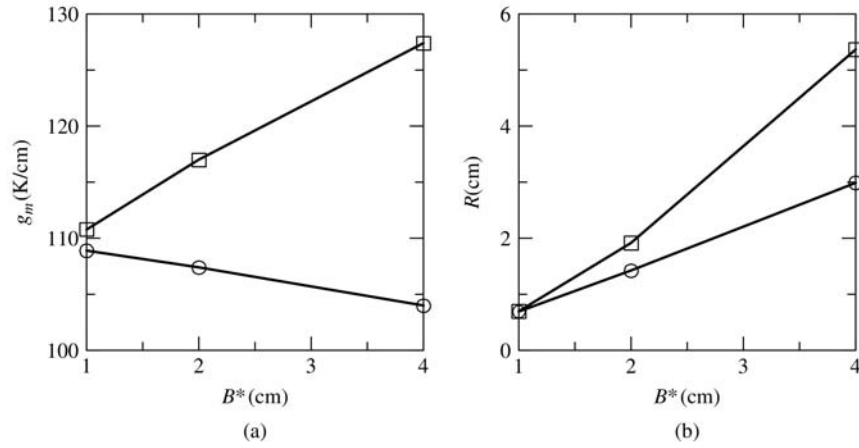


Figure 3.6 (a) The thermal gradient in the melt normal to the melting point isotherm (g_m , defined in the text) and (b) the curvature of the melting point isotherm (R), as a function of crystal width (B^*). Squares correspond to values calculated while accounting for melt convection and circles represent values calculated while neglecting melt convection (i.e. $\beta_T = 0$). All data points were evaluated at a position on the melting-point isotherm for which $\theta = \theta_0 = 0$, in the case where $G = 50$ K/cm, $V_g = 0.2$ cm/h and kinetic effects are unimportant ($\beta \rightarrow \infty$).

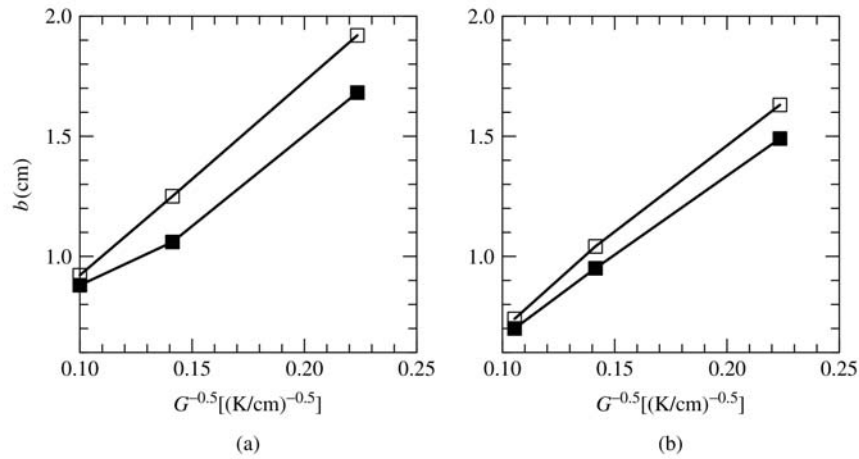


Figure 3.7 Facet size as a function of furnace temperature gradient calculated (a) with convection in the melt and (b) without convection in the melt ($\beta_T = 0$). Here $G = 50$ K/cm, $V_g = 0.2$ cm/h, $\theta_0 = 0$, $B^* = 4$ cm. Open symbols depict values predicted based on the simplified approach using calculations with $\beta \rightarrow \infty$ together with Equation (3.23). Filled symbols represent results from our calculations accounting for coupling between kinetics and thermal field calculations (i.e. a finite β value).

Our analysis is limited to the particular vertical gradient solidification system described here. It is interesting to consider many different variations of the parameters used in the calculations shown in Figure 3.5. Unfortunately, a comprehensive study of these is beyond the scope of our work. We do, however, consider one permutation of the system parameters. Results shown in Figure 3.8 exhibit melt/crystal interface shapes and undercooling profiles calculated without taking convection into account, taking convection into account and taking convection into account with the gravity vector pointing in the opposite direction. This last situation describes a top-seeded vertical growth system in which the crystal is placed above the melt into which it is growing (i.e. the gravity vector is directed from the cold zone of the furnace towards the hot zone, in the y direction).

Melt flow, in the case of top seeding, is considerably more vigorous than in the previous calculations. This is evident when observing the significant shift in the melt/crystal interface position due to flow in the case of inverted gravity compared to the usual situation. Of relevance is the direction of flow near the melt/crystal interface, which, due to inversion of gravity, is similar to the direction of natural-convective-dominated flows often observed in Czochralski systems (see Müller and Ostrogorsky, 1994, and references within). Here, melt flows towards the interface near its periphery, towards the centerline along the interface, and away from the interface near its center. This inverted flow pattern tends, in the absence of facetting, to sharpen the interface near its center thereby increasing its curvature in this region; a similar effect was observed in natural-convective dominated flow calculations during the growth of oxides via the Czochralski technique (Xiao and Derby, 1993). When facetting is considered (see Figure 3.8),

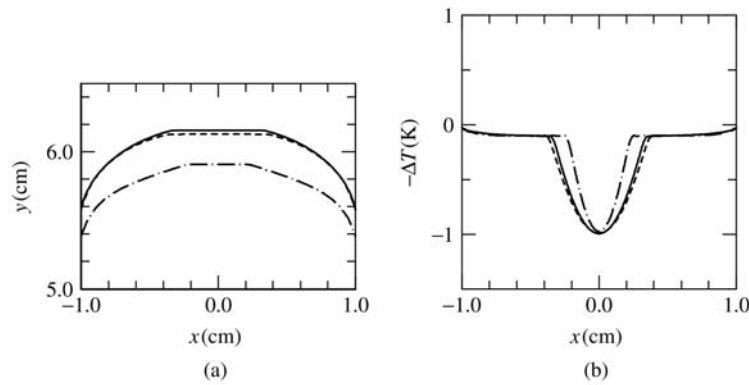


Figure 3.8 (a) Interface shapes and (b) undercooling profiles for different convective driving forces. Continuous curves correspond to calculations without a convective driving force ($\beta_T = 0$), dashed curves correspond to calculations with melt convection in the thermally stabilized, base-case configuration (bottom seeding), and dashed-dotted curves correspond to calculations with melt convection in a top-seeded configuration. Here $G = 50$ K/cm, $V_g = 0.2$ cm/h, and $\theta_0 = 0$.

the facet size is reduced in comparison to the calculation that does not account for melt convection. The decrease in facet size is most probably due to the reduction in R near the center of the system.

3.3.3 TRANSPARENT CRYSTALLINE PHASE

In (Liu *et al.*, 1999) and in most of the results shown here, radiative transport within the crystalline phase was modeled using an enhanced thermal conductivity. This approach, which in some sense approximates internal radiation in optically thick media, has difficulty predicting the deep interfaces associated with optically thin or transparent crystals (Brandon and Derby, 1992a). In this section the crystal is approximated as a medium completely transparent to infrared radiation. Here, system parameters remain the same as before except for: (a) the crucible height, which was set to $L = 20$ cm, thus allowing for full exploration of severe deflections in interface shapes; (b) the hot and cold zone temperatures, which were modified to allow for the same base-case gradient as before ($G = 50$ K/cm); (c) the growth rate, which was chosen to be 0.55 cm/h due to numerical limitations briefly mentioned below. Physical parameters remain the same except for the thermal conductivity in the crystalline phase, which without artificial radiative enhancement is given by $k_s = 0.08$ W/cm K. Emissivities of the crucible/crystal boundaries, the melt/crystal interface and the crystal's refractive index were chosen according to the properties used in our previous study of a similar system (Virozub and Brandon, 1998).

In (Virozub and Brandon, 1998) we showed that slab-shaped geometries, in comparison with cylindrical systems, may exhibit severely deflected melt/crystal interface shapes due to effects associated with radiative cooling through the transparent crystal. Radiative transport is, in some sense, enhanced by relatively large viewing angles between the interface and the cold end of the crucible in this slab-shaped system. The large deflection in the interface leads to difficulties in achieving closure of energy balances; this problem was solved by optimizing mesh-generation parameters. In attempting to model facetting phenomena in this system, numerical difficulties associated with the combination of radiative transport, resultant deep interfaces, and facet formation lead to the requirement of relatively intensive computational resources. For this reason we have limited the study to a case involving a relatively large value of the crystallographic orientation $|\theta_0| = 1.2$ (smaller values of $|\theta_0|$ require additional mesh refinement). However, obtaining significant facetting using $|\theta_0| = 1.2$ requires a relatively large value for V_g .⁹ This is a result of the relation $V_n = V_g(\mathbf{n}_{ms} \cdot \mathbf{e}_y) = V_g \cos(|\theta|)$, which for $|\theta| = |\theta_0| = 1.2$ yields a value of V_n significantly smaller than V_g .

A sample interface shape is shown in Figure 3.9. Notice the severe deflection of the interface (due to the crystal's transparency), which is shaped in a

⁹ Here we use $V_g = 0.55$ cm/h.

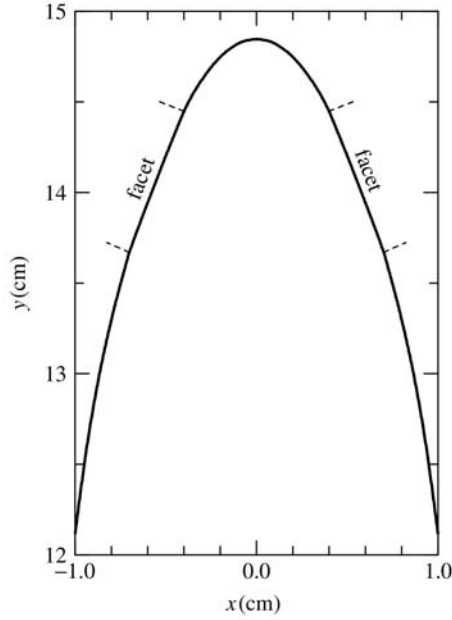


Figure 3.9 Partially faceted interface of a transparent crystal grown at $V_g = 0.55$ cm/h with $G = 50$ K/cm and $\theta_0 = 1.2$. Facet boundaries are marked by small dashed lines perpendicular to the facet.

manner where curvature is significant near the center. Facets, whose boundaries are marked by small dashed lines, appear where expected.

3.3.4 POSITIONING OF FACETS ALONG THE INTERFACE

Growth of $\langle 111 \rangle$ axis garnet crystals using the Czochralski method often yields a crystal with a strained inner core bounded by three $\{211\}$ facets (see, e.g. Zydzik, 1975); $\{110\}$ facets are also known to appear in this case at larger radial positions (see, e.g. Cockayne and Roslington, 1973).

Application of the vertical bridgman technique to the growth of YAG in several different crystallographic directions is shown to be characterized by a variety of facet distribution patterns depending on the growth orientation (Petrosyan *et al.*, 1978). Using this technique to grow Nd:YAG along the $\langle 221 \rangle$ direction yields $\{211\}$ and $\{110\}$ facets positioned near the periphery of the melt/crystal interface (Petrosyan and Bagdasarov, 1976).

In Figure 3.10 we present results attempting to reproduce the growth conditions reported in (Petrosyan and Bagdasarov, 1976) with the aim of better understanding causes of facet positioning along the interface. Parameters were chosen to closely follow those used by Petrosyan and coworkers. These are the

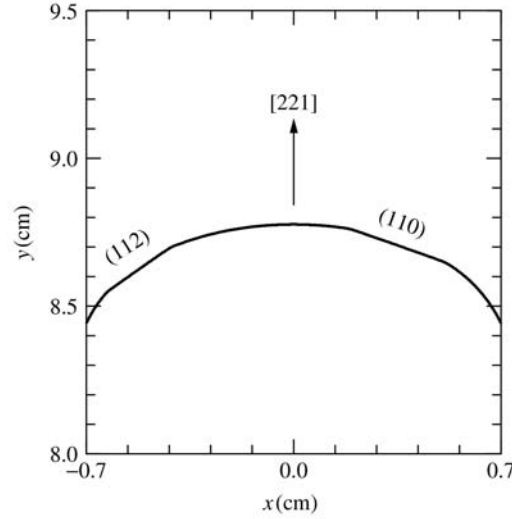


Figure 3.10 Partially faceted interface of a crystal grown under conditions (detailed in the text) closely following those used by Petrosyan and Bagdasarov (1976).

same as base-case values used in (Liu *et al.*, 1999) and in the present study except for the crucible inner half-width, the crucible inner length, and crucible wall thickness, which were estimated to be $B^* = 0.7$ cm, $L^* = 15$ cm, and $d = 0.03$ cm, respectively (Petrosyan, 1998). In addition, in these calculations, $G = 100$ K cm and $V_g = 0.26$ cm/h (Petrosyan and Bagdasarov, 1976). Here the crystal is grown along the $[221]$ direction and the two singular surfaces considered, whose orientations are coplanar with this growth orientation, are (112) ($|\theta_0| = 0.615$) and (110) ($|\theta_0| = 0.340$).¹⁰ Finally, note that in this small-scale system, convection was not taken into account and radiative transport within the crystalline medium was modeled using an enhanced thermal conductivity.

Facet positions shown in Figure 3.10 are semiquantitatively consistent with the experimental results of (Petrosyan and Bagdasarov, 1976). The (112) facet shown on the left is close to the crucible wall (consistent with Petrosyan and Bagdasarov, 1976), though the (110) facet shown on the right is not so obviously positioned along the periphery of the crystal surface.

3.4 CONCLUSIONS

Facetting during the growth of single crystals from the melt can cause unwanted phenomena.¹¹ In addition, using standard computational algorithms for the analysis

¹⁰ Note that, in this asymmetric case, each singular orientation appears only on one side of the growth axis; Figure 3.10 is consistent with $\theta_0 = 0.615, -0.340$.

¹¹ See (Cockayne and Roslington, 1973) for a situation where facets are beneficial.

of melt growth may lead to inaccuracies in the prediction of thermal, solute and flow fields, all of which may be significantly affected by the presence of large facets along the melt/crystal interface.

Results shown here demonstrate current capabilities of a new approach designed to couple predictions of facet formation with transport phenomena during directional melt growth. Important information gleaned from our calculations can be itemized as follows:

- Predictions of facet size and undercooling profiles are qualitatively consistent with the expected sensitivity to operating parameters. Facets increase in size with increasing crystal-growth rate and decreasing furnace temperature gradient. When melt convection is unimportant and internal radiation is modeled using an enhanced crystalline thermal conductivity, semiquantitative agreement is found between facet sizes predicted here and those calculated using the Brice–Voronkov theory. As explained in (Liu *et al.*, 1999), discrepancies can partially be explained by the small level of undercooling appearing on the off-facet region in some of our calculations. However, in a number of cases (particularly for small G values), discrepancies are probably due to nonuniformity in R ¹² (in the case of $|\theta_0| = \pi/4$) as well as deviations of the thermal field near the facet from that assumed in (Voronkov, 1972).
- Including melt convection in the analysis is shown to be important for the largest crucible considered here ($B^* = 4$ cm). The increase in flow intensity with system size, the direction of the resultant flow (towards the interface at its center), and the overall ‘flattening’ of the melt/crystal interface shape due to flow, are all similar to observations made for a cylindrical geometry (Derby *et al.*, 1994). Following the ideas of Brice (1970) and Voronkov (1972), the increase in R due to convection should promote larger facet sizes, while the increase in the thermal gradient at the interface (also due to convection) should favor smaller facet sizes. Our calculations show that the increase in R as a result of convection dominates and leads to an increase in facet size. Interestingly, facet sizes calculated in this case significantly deviate (for small G values) from values predicted using the Brice–Voronkov approach. This is probably due to an increase in the deviation between thermal fields assumed in Voronkov (1972) and those calculated here.
- An increase in facet size due to melt convection was observed for the standard bottom-seeded configuration and specific singular orientation $|\theta_0| = 0$ studied here. Looking at Figure 3.5 it is evident that for large enough $|\theta_0|$ values (appearing near the crucible walls) R may not change or may even decrease due to convection. A certain decrease in R near the crystal periphery due to melt convection can be observed when looking at previous results for cylindrical crystals (see, e.g. Figure 3.9 in Brandon *et al.*, 1996). A decrease in R due to convection could conceivably lead to reduction in facet sizes

¹² R is assumed uniform in the analysis of Brice (1970) and Voronkov (1972).

near the crucible wall. Finally, considering top-seeded crystal-growth with $|\theta_0| = 0$, demonstrates that the associated inverted flow pattern (i.e. flow away from the interface at its center) acts to increase curvature (decrease R) near the system center, thereby causing a reduction in facet size compared to the situation where flow is not considered. Note that this significant result, which has possible implications for natural-convective-flow-dominated CZ systems, was obtained for a relatively small scale system ($B^* = 2$ cm) in which bottom seeding does not lead to significant flow.

- Taking internal radiation effects into account for the case of optically thin (or transparent) crystalline phases is a nontrivial task. The combination of extremely deep interfaces due to radiation in slabs with numerical difficulties associated with modeling kinetics (see Liu *et al.*, 1999), render calculations quite challenging. We demonstrate a certain capability for calculating partially faceted interfaces in this case. Ongoing work includes implementing new numerical meshing strategies aimed at giving us the capability to accurately and thoroughly study effects associated with transparent crystalline phases of the type studied here.
- Using parameters close to those used by Petrosyan and Bagdasarov (1976) we attempt to reproduce their experimental result concerning positioning of facets (near the crystal periphery). Two singular surfaces coplanar with the growth direction were chosen in this study of a slab-shaped crystal. One of the resultant facets appears near the crucible wall while the other is not as close to the wall as shown in (Petrosyan and Bagdasarov, 1976). This is not very surprising since facet positioning is very sensitive to the distribution of the crystallographic orientation angle along the interface. Effects of melt convection discussed above, variations in optical properties in semi-transparent crystals (Brandon and Derby, 1992a), and the effect of differences in geometry (slab versus cylinder, Virozub and Brandon, 1998) may lead to changes in the distribution of θ causing facets (of a particular surface orientation) to be close to or far from the crucible walls. An accurate quantitative prediction of facet positioning along the interface requires, in the case of (Petrosyan and Bagdasarov, 1976), the analysis of a cylindrical system¹³ with a good knowledge of the degree of transparency of crystals grown.

ACKNOWLEDGMENTS

This Research was supported by The Israel Science Foundation administered by The Israel Academy of Sciences and Humanities. AV acknowledges partial support by the Israel Absorption Ministry.

¹³ Note that the computation of facetting in a cylindrical system with $\theta_0 \neq 0$ requires a three-dimensional analysis.

NOTE ADDED IN PROOF

Since the completion of this manuscript an important contribution to this field has appeared in the literature. In (Lan and Tu, 2001) a slightly different approach is used to extend the ideas discussed here to three-dimensional geometries.

REFERENCES

- Adornato, P. M. and Brown, R. A. (1987) 'Convection and segregation in directional solidification of dilute and non-dilute binary alloys: Effects of ampoule and furnace design' *J. Cryst. Growth*, **80**, 155–190.
- Amon, J., Dumke, F. and Müller, G. (1998) 'Influence of the crucible shape on the formation of facets and twins in the growth of GaAs by the vertical gradient freeze technique' *J. Cryst. Growth*, **187**, 1–8.
- Bauser, E. and Strunk, H. P. (1984) 'Microscopic growth mechanisms of semiconductors: Experiments and models' *J. Cryst. Growth*, **69**, 561–580.
- Brandon, S. (1997) 'Flow fields and interface shapes during horizontal Bridgman growth of fluorides' *Model. Simul. Mater. Sci. Eng.*, **5**, 259–274.
- Brandon, S. and Derby, J. J. 1992a 'Heat transfer in vertical Bridgman growth of oxides: effects of conduction, convection and internal radiation' *J. Cryst. Growth*, **121**, No. 3, 473–494.
- Brandon, S. and Derby, J. J. (1992b) 'A finite element method for conduction, internal radiation and solidification in a finite axisymmetric enclosure' *Int. J. Num. Meth. Heat Fluid Flow*, **2**, 299–333.
- Brandon, S., Gazit, D. and Horowitz, A. (1996) 'Interface shapes and thermal fields during the gradient solidification method growth of sapphire single crystals' *J. Cryst. Growth*, **167**, No. 1–2, 190–207.
- Brice, J. C. (1970) 'Facet formation during crystal pulling' *J. Cryst. Growth*, **6**, 205–206.
- Chang, C. J. and Brown, R. A. (1983) 'Radial segregation induced by natural convection and melt/solid interface shape in Vertical Bridgman growth' *J. Cryst. Growth*, **63**, 343–364.
- Chernov, A. A. (1973) 'Crystallization' *Ann. Rev. Mater. Sci.*, **3**, 397–454.
- Christodoulou, K. N. and Scriven, L. E. (1992) 'Discretization of free surface flows and other moving boundary problems' *J. Comp. Phys.*, **99**, No. 1, 39–55.
- Chung, H., Dudley, M., Larson Jr., D. J., Hurle, D. T. J., Bliss, D. F. and Prasad, V. (1998) 'The mechanism of growth-twin formation in zincblende crystals: new insights from a study of magnetic liquid encapsulated Czochralski-grown InP single crystals' *J. Cryst. Growth*, **187**, 9–17.
- Cockayne, B. (1968) 'Developments in melt-growth oxide crystals' *J. Cryst. Growth*, **3**, 60–70.
- Cockayne, B., Chesswas, M. and Gasson, D. B. (1969) 'Facetting and optical perfection in Czochralski grown garnets and ruby' *J. Mater. Sci.*, **4**, 450–456.
- Cockayne, B. and Roslington, J. M. (1973) 'The dislocation-free growth of gadolinium gallium garnet single crystals' *J. Mater. Sci.*, **8**, 601–605.
- Cockayne, B., Roslington, J. M. and Vere, A. W. (1973) 'Macroscopic strain in faceted regions of garnet crystals' *J. Mater. Sci.*, **8**, 382–384.

- Dahlquist, G. and Björck, Å. A. (1974), *Numerical Methods*, Prentice-Hall, Inc., Englewood Cliffs, N.J.
- Derby, J. J., Brandon, S., Salinger, A. G. and Xiao Q. (1994) 'Large-scale numerical analysis of materials processing systems: High-temperature crystal-growth and molten glass flows' *Comp. Meth. Appl. Mech. Eng.*, **112**, 69–89.
- Dupret, F., Nicodème, P., Ryckmans, Y., Wouters, P. and Crochet, M. J. (1990), 'Global modelling of heat transfer in crystal-growth furnaces' *Int. J. Heat Mass Transfer*, **33**, No. 9, 1849–1871.
- Dupret, F. and van den Bogaert, N. (1994), 'Modelling Bridgman and Czochralski growth'. *Handbook of Crystal Growth Vol. 2b: Bulk Crystal Growth, Growth Mechanisms and Dynamics*, ed. D. T. J. Hurle, North-Holland, Amsterdam, 875–1010.
- Flemings, M. C. (1974), *Solidification Processing*, Mc-Graw Hill, New York.
- Fratello, V. J. and Brandle, C. D. (1993) 'Physical properties of a $Y_3Al_5O_{12}$ melt' *J. Cryst. Growth*, **128**, 1006–1010.
- Hulme, K. F. and Mullin, J. B. (1962) 'Indium-antimonide a review of its preparation, properties and device applications' *Solid State Electron.*, **5**, 211–247.
- Hurle, D. T. J. and Cockayne, B. (1994), 'Czochralski growth'. *Handbook of Crystal Growth Vol. 2a: Bulk Crystal Growth, Basic Techniques*, ed. D. T. J. Hurle, North-Holland, Amsterdam, 99–211.
- Hurle, D. T. J. (1995) 'A mechanism for twin formation during Czochralski and encapsulated vertical Bridgman growth of III-V compound semiconductors' *J. Cryst. Growth*, **147**, No. 3–4, 239–250.
- Kim, D. H. and Brown, R. A. (1991) 'Modelling of the dynamics of HgCdTe growth by the Vertical Bridgman method' *J. Cryst. Growth*, **114**, 411–434.
- Lan, C. W. and Tu, C. Y. (2001) 'Three dimensional simulation of facet formation and the coupled heat flow and segregation in Bridgman growth of oxide crystals' *J. Cryst. Growth*, **233**, 523–536.
- Landau, L. D. and Lifshitz, E. M. (1959), *Fluid Mechanics*, 1st edn. Pergamon Press, Oxford.
- Liu, Y., Virozub, A. and Brandon, S. (1999) 'Facetting during directional growth of oxides from the melt: coupling between thermal fields, kinetics and melt/crystal interface shapes' *J. Cryst. Growth*, **205**, No. 3, 333–353.
- Müller, G. and Ostrogorsky, A. (1994), 'Convection in melt growth'. *Handbook of Crystal Growth Vol. 2b: Bulk Crystal Growth, Growth Mechanisms and Dynamics*, ed. D. T. J. Hurle, North-Holland, Amsterdam, 709–819.
- Petrosyan, A. G. (1994) 'Crystal-growth of laser oxides in the vertical Bridgman configuration' *J. Cryst. Growth*, **139**, 372–392.
- Petrosyan, A. G. (1998) *Personal communication*.
- Petrosyan, A. G. and Bagdasarov, Kh. S. (1976) 'Faceting in Stockbarger grown garnets' *J. Cryst. Growth*, **34**, 110–112.
- Petrosyan, A. G., Shirinyan, G. O., Ovanesyan, K. L. and Avetisyan, A. A. (1978) 'Facet formation in garnet crystals' *Kristall und Technik*, **13**, No. 1, 43–46.
- Tsiveriotis, K. and Brown, R. A. (1992) 'Boundary-conforming mapping applied to computations of highly deformed solidification interfaces' *Int. J. Num. Meth. Fluids*, **14**, No. 8, 981–1003.
- Virozub, A. and Brandon, S. (1998) 'Radiative heat transport during the vertical Bridgman growth of oxide single crystals: slabs versus cylinders' *J. Cryst. Growth*, **193**, 592–596.

- Virozub, A. and Brandon, S. (2002) 'Selecting finite element basis functions for computation of partially faceted melt/crystal interfaces appearing during the directional growth of large-scale single crystals' *Model. Simul. Mater. Sci. Eng.* **10**, 57–72.
- Voronkov, V. V. (1972) 'Supercooling at the face developing on a rounded crystallization front' *Krystallografiya*, **17**, No. 5, 909–917.
- Xiao, Q. and Derby, J. J. (1993) 'The role of internal radiation and melt convection in Czochralski oxide growth: deep interfaces, interface inversion, and spiraling' *J. Cryst. Growth*, **128**, 188–194.
- Yeckel, A., Doty, F. P. and Derby, J. J. (1999) 'Effect of steady crucible rotation on segregation in high-pressure vertical Bridgman growth of cadmium zinc telluride' *J. Cryst. Growth*, **203**, 87–102.
- Yokayama, E. and Kuroda, T. (1990) 'Pattern formation in growth of snow crystals occurring in the surface kinetic process and the diffusion process' *Phys. Rev. A.*, **41**, No. 4, 2038–2049.
- Zydzik, G. (1975) 'Interface transitions in Czochralski growth of garnets' *Mater. Res. Bull.*, **10**, 701–708.

4 Theoretical and Experimental Solutions of the Striation Problem

HANS J. SCHEEL

SCHEEL CONSULTING, Sonnenhof 13, CH-8808 Pfäeffikon, Switzerland

ABSTRACT

Striations are growth-induced inhomogeneities that hamper the applications of solid-solution crystals and of doped crystals in numerous technologies. Thus the optimized performance of solid solutions often can not be exploited. It is commonly assumed that striations are caused by convective instabilities so that reduced convection by microgravity or by damping magnetic fields was and is widely attempted to reduce inhomogeneities.

In this chapter it will be shown that temperature fluctuations at the growth interface cause striations, and that hydrodynamic fluctuations in a quasi-isothermal growth system do not cause striations. The theoretically derived conditions were experimentally established and allowed the growth of striation-free crystals of $\text{KTa}_{1-x}\text{Nb}_x\text{O}_3$ 'KTN' solid solutions for the first time.

Hydrodynamic variations from the accelerated crucible rotation technique (ACRT) did not cause striations as long as the temperature was controlled within 0.03°C at 1200°C growth temperature. Alternative approaches to solve the segregation and striation problems are discussed as well.

4.1 INTRODUCTION

Solid solutions or mixed crystals are special crystals or alloys in which one or more lattice sites of the structure are occupied by two or more types of atoms, ions or molecules. By varying the concentration of the constituents, the physical or chemical properties of solid solutions can be optimized for specific applications, so that solid solutions play an increasing role in research and technology. One example are III-V semiconductors where the bandgap and thus emission and absorption wavelengths can be adjusted, along with the lattice constant to match the available substrates for epitaxial growth, for optical communication systems. Another example are III-V compounds for photovoltaic devices where

the composition can be adjusted to optimize the solar-cell efficiency and to maximize radiation resistance (Loo *et al.* 1980). In certain cases, properties and effects may be obtained in solid solutions that are not observed in the constituents: The phase transition temperature and the related anomaly of a high dielectric constant may be shifted to the application temperature for electro-optic, nonlinear-optic and acousto-optic applications (Chen *et al.* 1966, Scheel and Günter 1985). The hardening effect of solid solutions is often used to improve the mechanical properties (Nabarro 1975).

The statistical distribution of species in a given lattice site normally is at random, but can deviate in the direction of ordering (with the extreme case of a superlattice) or in the direction of clustering (with the extreme case of immiscibility or phase separation) as it was shown by Laves 1944. This site distribution has an impact on the physical properties and can be controlled to some extent in metallic alloys, with their high diffusivities, by preparation or annealing conditions. However, in oxide systems with low diffusivities, the control of the distribution of species on lattice sites during crystal growth experiments has not been reported and will not be considered here.

In this chapter the bulk fluctuations of concentration will be treated with respect to the application-dependent homogeneity requirements, the types of inhomogeneities and their origin, and how inhomogeneities can be reduced or completely suppressed. There is a strong tendency for fluctuations of the growth conditions causing concentration fluctuations along the growth direction known as striations or growth bands. The suppression of striations is an old problem in crystal-growth technology, so that several authors had described striations as an 'intrinsic', 'inherent' or 'unavoidable' phenomenon in crystal growth, see Rytz and Scheel 1982, Scheel and Günter 1985.

Based on the segregation analyses for melt growth by Burton *et al.* (1953) and for growth from diluted solutions by Van Erk 1982, the role of hydrodynamics will be discussed, and the experimental conditions for growth of striation-free crystals derived. This theoretical result will be confirmed by the growth of quasi striation-free crystals of solid solutions. Finally, alternative approaches to reduce or eliminate striations are discussed, also novel approaches that require to be tested.

4.2 ORIGIN AND DEFINITIONS OF STRIATIONS

Nearly all crystals have inhomogeneities and growth bands called striations. Early observations of striations in semiconductor crystals have been reported by Goss *et al.* (1956) and by Bardsley *et al.* (1962) and for CaF_2 by Wilcox and Fullmer (1965). Hurle (1966) has shown for semiconductor crystals and Cockayne and Gates (1967) for Czochralski-grown oxide and fluoride crystals, that striations are caused by temperature fluctuations that may be correlated with thermal unsymmetry or with convective oscillations when a critical Rayleigh number is surpassed.

Many compounds like GaAs and LiNbO₃ are not line compounds, but have an existence range, that is they have a certain degree of solid solubility with one or both of the constituents. This causes a difference of the congruent melting composition from the stoichiometric composition. Therefore the grown crystals show variations of composition, often in the form of striations, depending on the exact growth conditions (melt composition and growth temperature and their fluctuations). This topic is discussed by Miyazawa in this volume for oxides and by Wenzl *et al.* (1993) for GaAs and compound semiconductors.

Also, melt-grown elements like silicon and line compounds like Al₂O₃ show striations due to impurities, in the case of silicon–oxygen striations from partial dissolution of the SiO₂ crucible. Very pronounced striations are often found in doped crystals (semiconductors, lasers) and in crystals of solid solutions.

The homogeneity requirements depend on the material and on the application. Examples of the maximum composition (X) variations $\Delta X/X$ are given in Table 4.1.

Corresponding to these tolerance limits, analytical methods are to be applied or developed in order to assist in the achievement of ‘striation-free’ crystals. In addition to the well-established methods to visualize striations, Donecker *et al.* (1996) developed a colorful optical diffraction method to visualize striations and demonstrated it with oxide, doped InP and Si_{1-x}Ge_x crystals.

It is recommended to use the term ‘striation-free’ in those cases where striations can not be detected or where they are not harmful for the specific application. An absolute striation-free crystal may neither be achieved nor proven, although in faceted growth or in liquid-phase epitaxy in the Frank–Van Der Merwe growth mode quasi striation-free crystals and layers could be expected when step-bunching is prevented.

Various definitions for striations had been suggested. In the following ‘functional terms’ are proposed that relate to the origin of the specific striations (instead of type-I, type-II, etc.). Striations are defined as growth-induced inhomogeneities in the crystal that are aligned along the faceted or non-faceted growth surface, or in the case of faceted growth with step-bunching are related to the traces of macrosteps.

Table 4.1 Homogeneity requirements of material classes

Crystals, substrates, epilayers	$\Delta X/X$
Semiconductors and solid solutions GaAs/GaP, (Ga,In)As, (Ga,In)Sb, (Cd, Hg)Te	10^{-4} to 10^{-5}
Dielectrics Piezo-electrics, pyroelectrics, electro-optic, Nonlinear-optic and laser crystals	10^{-5} to 10^{-7}
Magnetic and magneto-optic crystals and layers	10^{-4} to 10^{-5}
Metals and alloys	10^{-2} to 10^{-3}

These, often periodic, inhomogeneities are caused in the first case by growth rates which fluctuate with time due to temperature fluctuations and are schematically shown in Figure 4.1(a). Therefore they could be named ‘thermal striations’. In Czochralski crystal pulling these striations are frequently linked to crystal rotation rate, since the crystal feels any unsymmetry in the heater-insulation configuration (Camp 1954): these specific thermal striations are called ‘rotational striations’ or in short ‘rotationals’. It was shown by Witt *et al.* (1973) by using time markers and etching of crystal cross sections, that remelting may occur followed by fast growth, so that they defined microscopic (instantaneous) and macroscopic (average) growth rates and thus could explain complex striation patterns. The fluctuating temperatures at the growth interface, leading to growth-rate fluctuations in Czochralski growth, are related to convective instabilities (Hurle 1967), to interactions of several different kinds of flows, which will be discussed further below.

The second class of striations is caused by lateral growth-rate differences as shown in Figure 4.1(b) and are named ‘macrostep-induced striations’ or ‘kinetic striations’. Facetted growth may be observed in growth from melts in small temperature gradients, and it is practically always observed in growth from solutions and from high-temperature solutions. At high densities of growth steps, i.e. at high supersaturation respectively growth rates, the bunching of steps occurs and leads to macrosteps with a large integer of the height of the monostep. For a qualitative explanation of this phenomenon Frank (1958) and Cabrera and Vermilyea (1958) applied the kinematic wave theory that was developed by Lighthill and

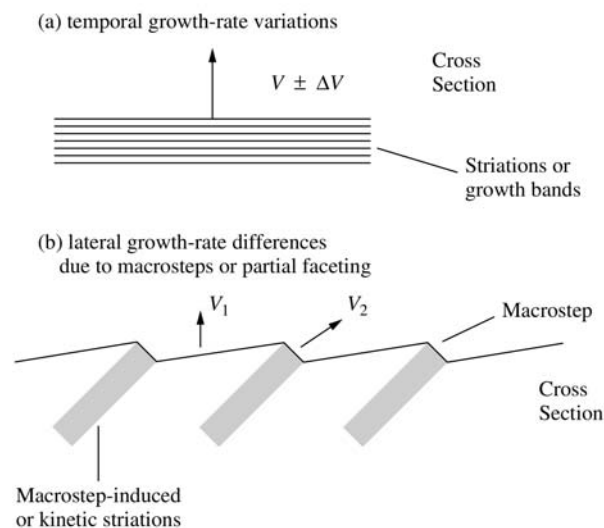


Figure 4.1 Definition of striations (a) caused by temporal growth-rate and temperature fluctuations as ‘thermal striations’, (b) caused by macrosteps and lateral growth-rate differences as ‘macrostep-induced striations’ or as ‘kinetic striations’.

Whitham (1955) for the general traffic-flow problem. As shown in Figure 4.1(b) growth surfaces with macrosteps respectively with a terrace-and-riser structure with different local growth mechanisms and growth rates: The terrace grows due to lateral propagation of single or double steps with the facet growth rate v_1 , whereas the macrostep has the velocity v_2 . These growth-rate differences cause corresponding differences in impurity or dopant incorporation and thus lead to the striations which mark the traces of the macrosteps. These ‘macrostep-induced’ or ‘kinetic striations’ are shown in Figure 4.2 with LPE-grown multilayers, where the correspondence of the kinetic striations (visible in the angle-lapped and etched p-GaAs layers) with the marked macrosteps is clearly recognized (Scheel 1980). In that work the transition of the misoriented macrostep-surface to the facet with a continuous step propagation by the Frank–Van Der Merwe growth mode is described, a transition that of course leads to layers with excellent homogeneity, i.e. without striations. Chernov and Scheel (1995) analyzed the conditions for achieving such atomically flat surfaces and extremely homogeneous layers (and crystals), see also the epitaxy review of Scheel in this volume.

Macrosteps can be regarded as a first step towards growth instability and are formed not only at high supersaturation, but also in the presence of certain impurities, and on misoriented surfaces (Chernov 1992). When the thermodynamic driving force is further increased, then the impurity built up in front of

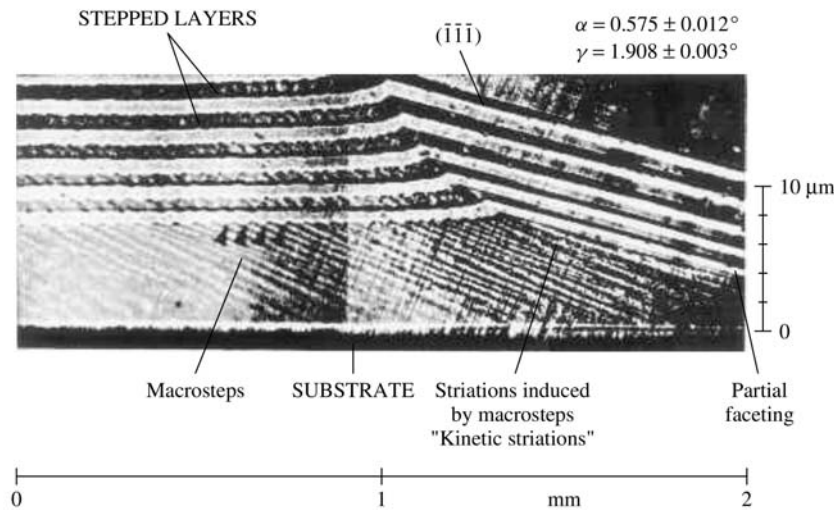


Figure 4.2 Macrostep-induced striations visible in the etched p-GaAs layers of an 11-layer p/n-GaAs structure grown by liquid phase epitaxy (Scheel 1980). On the GaAs substrate of 0.58° misorientation first a thick layer is grown, which on the right side shows the transition to the $\{111\}$ facet, whereas the macrostepped surfaces on the left side cause the striations. Angle-lapped ($\gamma = 1.9^\circ$) and etched, composite differential interference (Nomarski) micrograph.

the growing crystal may reach a critical level and is suddenly incorporated, then crystal growth continues until again the impurity is incorporated, and so on. This oscillation of growth rate and impurity incorporation leading to striations was analyzed theoretically and experimentally by Landau (1958). This kind of inhomogeneity could be named 'instability-induced striations'.

4.3 HOMOGENEOUS CRYSTALS WITH $k_{\text{eff}} \rightarrow 1$

The segregation problem is defined by the distribution coefficient k which gives the concentration ratio of a constituent in the grown crystal to that in the growth melt or solution as will be discussed later. Normally k is not unity so that either more constituent is incorporated ($k > 1$) or less constituent than in the growth fluid is built into the crystal ($k < 1$). In these cases $k = 1$ could be achieved in quasi-diffusionless growth, at very high solidification rates. These cannot be applied in bulk crystal growth, but might be acceptable in certain cases of low-dimensional growth, for instance in one-dimensional whiskers or thin rods, or in two-dimensional structures like thin plates or in lateral growth of thin layers.

Mateika (1984) has shown that in the complex garnet structures with tetrahedral, octahedral and dodecahedral sites and by crystal-chemical considerations, cations could be introduced and combined, so that $k = 1$ was achieved. In order to obtain a garnet substrate crystal with a specific lattice constant, the ionic radii and valency of the cations had to be taken into account. For example, the garnet $\text{Gd}_3\text{Sc}_x\text{Ga}_{5-x}\text{O}_{12}$ with $a = 12.543 \text{ \AA}$ could be grown from melt with $x = 1.6$, when $k(\text{Sc}) = 1$.

A constant effective distribution coefficient of unity could also be achieved in crystal growth from high-temperature solutions. By the use of solutions an additional degree of freedom is obtained, since the distribution coefficient also depends on the properties of the solvent and on solvent-solute interactions. Systematic experiments with the growth of oxide solid solutions have shown that different solvents and solvent mixtures may cause $k_{\text{eff}} > 1$ and $k_{\text{eff}} < 1$ for a given solid solution. By proper mixing of the solvent it is then possible to obtain $k = 1$ and thus eliminate the segregation problem. Two examples are given with the perovskite solid solutions $\text{Gd}_{1-x}\text{Y}_x\text{AlO}_3$ and $\text{Gd}_{1-x}\text{La}_x\text{AlO}_3$ that are grown from solvent mixtures with the major components PbO and PbF_2 and the minor components B_2O_3 and excess Al_2O_3 (Scheel and Swendsen 2001).

In Figure 4.3 the measured effective distribution coefficients of the La and Y dopants in GdAlO_3 are shown as a function of the PbO – PbF_2 solvent composition. For the pure PbO flux, k_{eff} for La is nearly four, whereas for equal concentrations of oxide and fluoride k_{eff} is less than 0.5. At a composition of about 37 mol% PbF_2 , $k_{\text{eff}} = 1$ is obtained. In the case of Y-doped GdAlO_3 , a nearly pure PbO solvent is required to obtain $k_{\text{eff}} = 1$.

An example of garnet solid solutions grown from PbO – PbF_2 solvent mixtures is shown in Figure 4.4 using the data of Krishnan (1972). Here the distribution

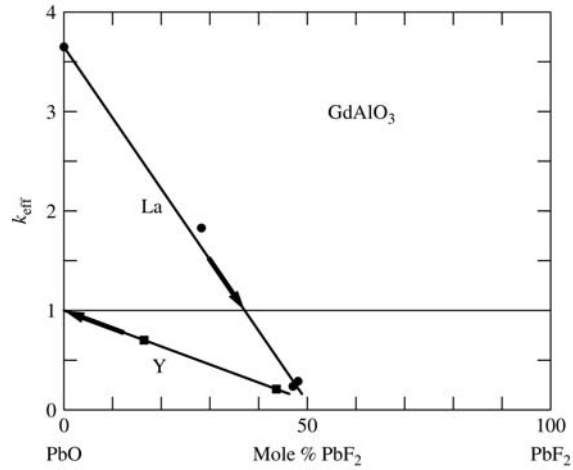


Figure 4.3 The dependence of the effective distribution coefficient on solvent composition in growth of La-doped and Y-doped gadolinium aluminate, after Scheel and Swendsen 2001.

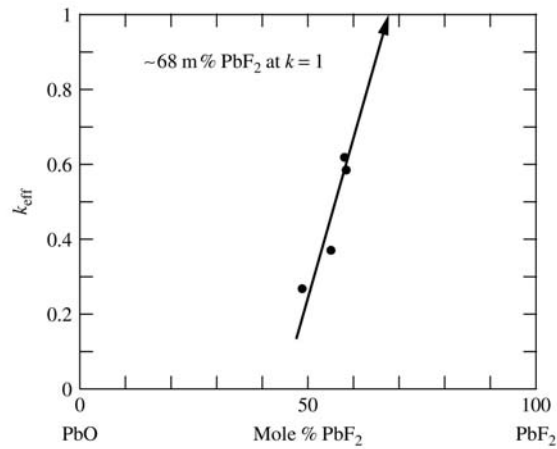


Figure 4.4 The dependence of the effective distribution coefficient on the PbO–PbF₂ solvent ratio in flux growth of Cr-doped yttrium iron garnet, after Scheel and Swendsen 2001.

coefficient for Cr in yttrium-iron garnet increases with increasing PbF₂ concentration, so that by extrapolation a solvent mixture with about 32 mol% PbO should give $k_{\text{eff}} = 1$. Another example of $\text{Ga}_{2-x}\text{Fe}_x\text{O}_3$ solid solutions grown from PbO–B₂O₃ and Bi₂O₃–B₂O₃ solvent mixtures shows that $k_{\text{eff}} = 1$ can be approached with the Bi₂O₃-rich flux (data of Schieber 1966).

A systematic investigation would help to understand these approaches to achieve $k_{\text{eff}} = 1$ and to establish rules for the general applicability.

4.4 SEGREGATION PHENOMENA AND THERMAL STRIATIONS

The concentration of the constituents of a solid solution generally differs from that in the liquid from which the mixed crystal is grown, a phenomenon known as segregation. In equilibrium or at very low growth rates the ratio of the concentration of component A in the solid to that in the liquid is defined as equilibrium segregation (or distribution) coefficient

$$k(A)_0 = C(A)_S / C(A)_L \quad (4.1)$$

k_0 may be derived from the equilibrium phase diagram by the ratio of solidus and liquidus concentrations of A at a given temperature.

In a crystallizing system with a limited melt volume, segregation at the growing interface leads to a continuous change of the fluid: $C(A)_L$ decreases for $k_{\text{eff}} > 1$, and $C(A)_L$ increases for $k_{\text{eff}} < 1$, so that the concentration $C(A)_S$ in the solid continuously changes. This causes an inherent concentration gradient in the crystal of which the concentration at any location of the growth front is given by

$$C(A) = k_{\text{eff}} C_0 (1 - g)^{k_{\text{eff}}^{-1}} \quad (4.2)$$

where g is the fraction of crystallized material and C_0 the initial concentration as derived by Pfann (1952). Here it is assumed that k_{eff} does not vary with concentration or temperature changes. Obviously the inherent concentration gradient can be made zero by keeping the fluid concentration constant. This can be done by growth at constant temperature in combination with transporting feed material from a higher temperature, a growth technique called gradient-transport technique (Elwell and Scheel 1975). However, this approach generally involves large temperature gradients (for acceptable growth rates) and thus leads to temperature fluctuations, so that striations cannot be prevented.

In Figure 4.5 the phase diagram of the system $\text{KTaO}_3\text{--KNbO}_3$ of Reisman *et al.* (1955) is presented where the gradient-transport technique, using the temperature difference T_3 to T_4 , is shown. Numerous groups listed by Rytz and Scheel (1982) using this approach could not grow the required striation-free crystals of KTN ($\text{KTa}_{1-x}\text{Nb}_x\text{O}_3$) solid solutions. For electro-optic and other optical applications the variation of x must be smaller than 0.00003, and this requires temperature fluctuations smaller than 0.01°C as is indicated in Figure 4.5. Also shown is the slow-cooling technique, where a quasiisothermal solution is cooled from T_1 to T_2 . This allows to grow striation-free crystals, and the inherent concentration gradient can be kept within tolerated limits by using a large melt. For the KTN system Rytz and Scheel (1982) have calculated the mass of melt M

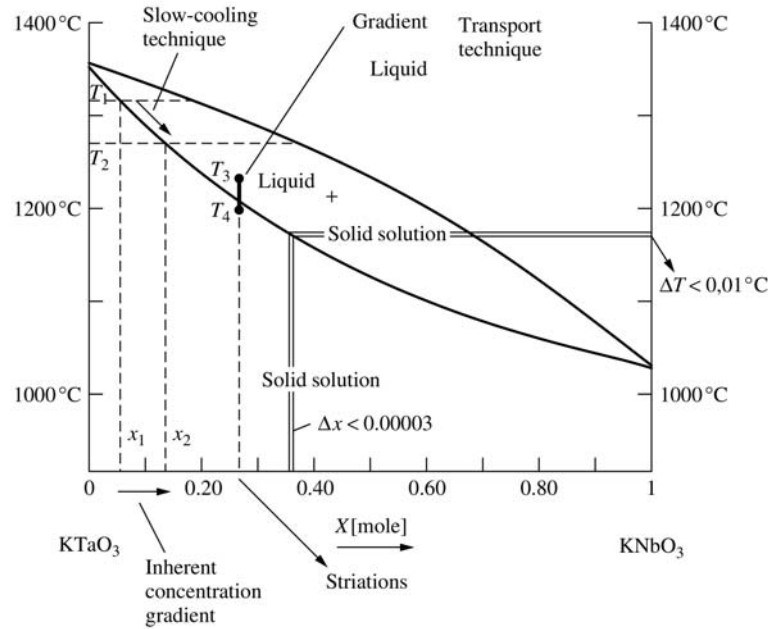


Figure 4.5 The phase diagram $\text{KTaO}_3\text{--KNbO}_3$ of Reisman *et al.* (1955) with indicated growth techniques and resulting inhomogeneities, after Rytz and Scheel 1982.

that is required to grow a crystal of specified volume V with a tolerated inherent concentration difference $x_1 - x_2$. These data and also the temperature cooling range can be read from the nomogram shown in Figure 4.6. For example, a KTN crystal of 1 cm^3 with $\Delta x < 0.02$, requires a melt of 1000 g that is cooled by 12°C . The results of growth experiments will be discussed further below.

In normal crystal growth we have neither the case of very fast growth and $k_{\text{eff}} = 1$ nor are we near equilibrium with very low growth rates and $k_{\text{eff}} = k_0$, as crystals should be grown at the fastest possible rate that still gives high structural perfection. Figure 4.7 shows the situations at the crystal/liquid interface for the three cases of equilibrium (which theoretically could also be achieved by ‘complete’ mixing), for the steady-state normal crystal growth, and for fast diffusionless solidification. Also shown are the concentrations in the solid and in the liquid with the diffusion boundary layers. In the steady-state crystal growth the effective distribution coefficient k_{eff} lies between the equilibrium distribution coefficient k_0 and 1 and is dependent on the diffusion boundary layer δ and the growth rate v as shown in Figure 4.7.

For the case of pulling a rotating crystal from the melt by the Czochralski technique, the flow analysis of Cochran (1934) towards an infinite rotating disc was applied by Burton, Prim and Slichter (BPS, 1953a) in order to derive the effective distribution coefficient. Thereby it was considered that the solute concentration

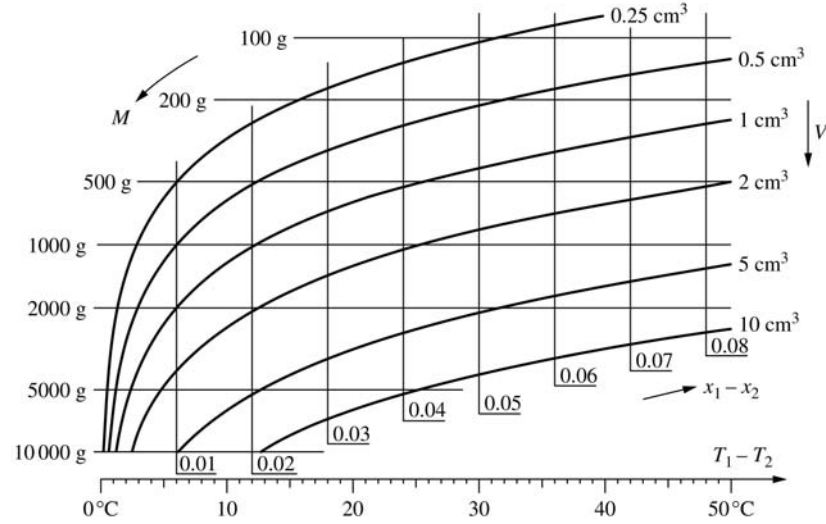


Figure 4.6 Nomogram to read the experimental parameters for growth of KTN solid solution crystals of a specified maximum inhomogeneity $x_1 - x_2$ and volume V . M = mass of the melt, $T_1 - T_2$ is the cooling interval (Rytz and Scheel 1982).

profile is virtually uniform in the radial direction, i.e. the diffusion boundary layer δ can be regarded as having constant thickness across the idealized flat growth interface. Up to a not too large growth rate, δ depends essentially on the crystal rotation rate ω (except for the rim, which is neglected), the kinematic viscosity ν , and a bulk diffusion coefficient D (which includes solute diffusion and solvent counter-diffusion) by

$$\delta = 1.6 D^{1/3} \nu^{1/6} \omega^{1/2}. \quad (4.3)$$

BPS derived for the steady-state case, in which equilibrium prevails at the interface virtually independently of growth rate, the equilibrium distribution coefficient

$$k_{\text{eff}} = k_0 / [k_0 + (1 - k_0) \exp -(v\delta/D)] \quad (4.4)$$

with v the growth rate. In the following, this approximation can be utilized, since the growth-rate dependence of k_0 will be negligible due to the fact that in our attempt to grow striation-free crystals the effective variations of the growth rate are small.

In the accompanying experimental paper Burton *et al.* (1953b) measured the distribution coefficients of several elements in solid/liquid germanium and were able to correlate them with atomic size, respectively, the tetrahedral covalent radii: the larger the element, the smaller the distribution coefficient. They also measured striations by means of incorporated radioactive tracers and photographic

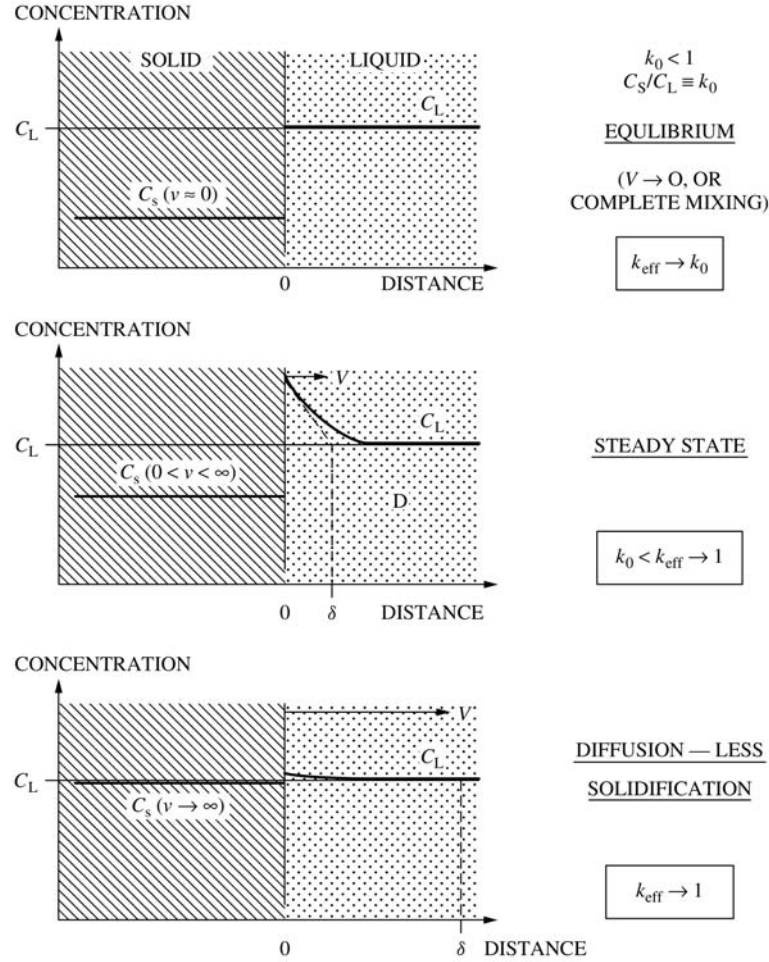


Figure 4.7 The concentration relations at the growth interface and the effective distribution coefficients for three growth situations: near equilibrium k_{eff} approaches k_0 , in very fast solidification k_{eff} approaches unity, and in typical crystal growth k_{eff} is between k_0 and 1. The diffusion boundary layer thickness δ depends on the growth rate v and on the flow rate of melt or solution.

film and pointed out the importance of adequate stirring for the growth of homogeneous crystals.

For growth of mixed crystals from dilute solutions, van Erk (1982) has considered the complex solute–solvent interactions and has derived the effective distribution coefficient for diffusion-limited growth as

$$\ln k_{\text{eff}} = \ln k_0 - (k_{\text{eff}} - 1)(v\delta/D). \quad (4.5)$$

The plotted solutions of Equations (4.4) and (4.5) shown in Figures 4.8 and 4.9, respectively, look similar, but the sensitivity to fluctuations of the growth parameters is different (Scheel and Swendsen 2001).

Growth from solutions is normally limited by volume diffusion, and the relatively fast interface kinetics can be neglected. Based on the diffusion-boundary

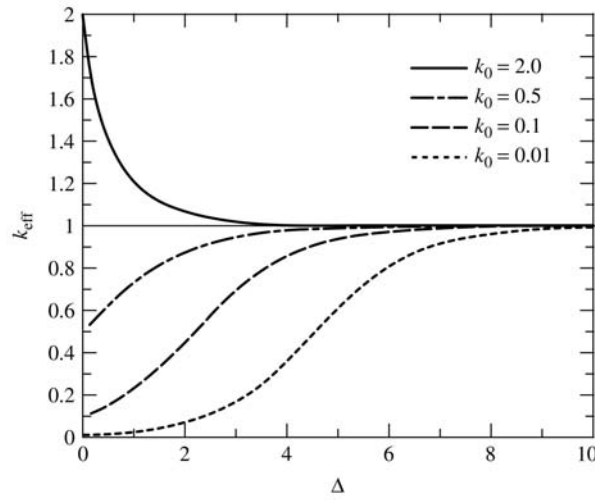


Figure 4.8 The effective distribution coefficient as a function of the exponent $(v\delta/D) = \Delta$ from the Burton-Prim-Slichter Equation (4.4) for four values of k_0 (Scheel and Swendsen 2001).

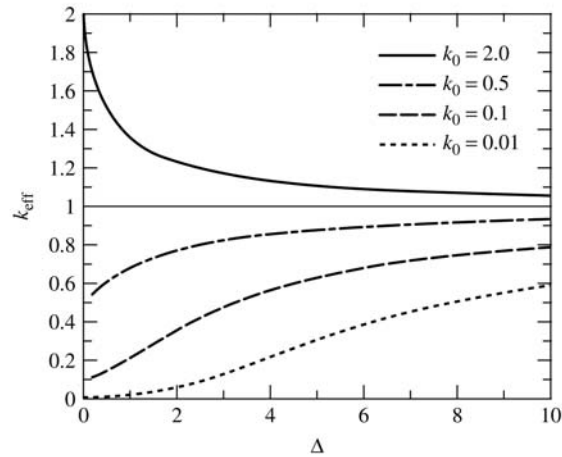


Figure 4.9 The effective distribution coefficient as a function of the exponent Δ from the Van Erk theory and Equation (4.5) for four values of k_0 (Scheel and Swendsen 2001).

layer concept, Nernst (1904) has derived the growth rate as

$$v = D(n_{\infty} - n_e)/\rho_c \delta \quad (4.6)$$

with n_e and n_{∞} the equilibrium and effective bulk concentrations of the solute in the solution, and ρ_c is the solute density. The time constant for the effects of temperature fluctuations (and thus on growth rate v) is on the order of seconds, while that for hydrodynamic fluctuations on δ and v is on the order of minutes. In steady-state growth, within a given range of time and temperature, the diffusion coefficient D and the equilibrium distribution coefficient k_0 in Equations (4.4) and (4.5) can be taken as constants. Therefore the changes in the effective distribution coefficient k_{eff} are essentially determined by the product $(v\delta)$ of the exponent. As a first approximation this product is constant due to the inverse relation between v and δ in the growth-rate Equation (4.6). This means that hydrodynamic changes, which lead to changes of δ , are compensated by growth-rate changes. On the other hand, growth-rate changes caused by temperature fluctuations are not compensated and thus lead to changes of k_{eff} and to thermal striations.

It follows from this discussion that for growth of striation-free crystals the temperature fluctuations should be suppressed to less than about 0.01 °C, and therefore also the temperature gradients should be minimized to less than about 1 °C per cm. On the other hand the crystal has to be cooled to remove the latent heat at practical growth rates, and to control nucleation.

The application of forced convection is recommended for efficient growth. Homogenizing the melts and solutions facilitates the achievement of above temperature conditions, and it reduces the diffusion problems leading to growth instability as discussed in Chapter 6 of Elwell and Scheel (1975). Stirring may be achieved by a continuous flow along the growth interface, by Ekman or Cochran flow towards the rotating growth surface, by periodic flow changes, as in reciprocating stirring in growth from aqueous solutions or by accelerated crucible rotation technique (ACRT) in growth from high-temperature solutions or in growth by the Bridgman–Stockbarger technique, etc.

For many years the favored approach to minimize striations was to reduce convection, to apply microgravity or in the case of semiconductors to apply convection-damping magnetic fields. But the above discussion has shown that, except for special cases requiring large temperature gradients, forced convection has many advantages, not least to achieve economic growth rates approaching the maximum stable growth rates for inclusion-free crystals.

From the above discussion we can also derive the experimental conditions to induce regular striations and superlattice structures, for instance by applying a large temperature gradient in combination with periodic hydrodynamic changes (by ACRT) and applying a constant mean supersaturation, respectively, a constant mean growth rate.

The suppression of striations represents an old problem in crystal-growth technology, and several authors have described striations as an ‘inherent’, ‘intrinsic’

or 'unavoidable' phenomenon in crystal growth, for example Byer (1974), Räuber (1978), and Reiche *et al.* (1980).

In the following, the theoretical considerations discussed above will be applied to an example of growing striation-free crystals of KTN solid solutions which could long not be achieved despite the numerous attempts listed by Rytz and Scheel (1982).

4.5 GROWTH OF STRIATION-FREE KTN CRYSTALS

The solid-solution system $\text{KTa}_{1-x}\text{Nb}_x\text{O}_3$ (KTN) is of interest due to its very large electro-optic coefficient which can be optimized for specific application temperatures by the choice of x (Scheel and Günter 1985). The composition with $x = 0.35$ is used for room-temperature applications, because the ferroelectric transition temperature is then 10°C and the very large dielectric constant and electro-optic coefficient are observed just above the transition. However, for optical applications the inhomogeneity in refractive index should be less than 10^{-6} , requiring that the crystals and layers be striation-free to this level.

As discussed above, this homogeneity can not be achieved by a gradient-transport technique, but only by slow-cooling of nearly isothermal solutions. The latter was applied by Rytz and Scheel (1982) and Scheel and Sommerauer (1983) who, furthermore, combined an ultra-precise temperature control with optimized temperature distribution in the furnace and applied stirring by the accelerated crucible rotation technique (ACRT) (Scheel 1972) and thus could obtain striation-free KTN crystals for the first time. A typical crucible arrangement with bottom cooling to provide a nucleation site is shown in Figure 4.10 along with the applied ACRT cycle. In ACRT the crucible is periodically accelerated and decelerated so that by inertia the liquid is moving relative to the crucible wall and forms a spiral when seen from top. This spiral shear flow (or spiral shearing distortion) was analyzed and simulated by Schulz-DuBois (1972). He also analyzed the Ekman layer flow in which, under optimized conditions, the liquid is always pumped through a thin Ekman layer at the bottom of the crucible when this is accelerated and decelerated. In Chapter 7 of the book of Elwell and Scheel (1975) the derivation of optimized ACRT stirring based on the kinematic viscosity of the liquid and on the crucible dimension is treated.

Temperature control with a precision of 0.03°C at around 1300°C could be achieved by using a thermopile of Pt-6%Rh versus Pt-30%Rh thermocouples (Scheel and West 1973). In Figure 4.11(a) the electromotive forces, i.e. the high-temperature sensitivities of conventional thermocouples and of the 6-fold thermopile are compared whereby the room-temperature sensitivity of the thermopile (Figure 4.11(b)) is practically zero, so that cold-junction compensation is not required. The temperature distribution in the chamber furnace was optimized by arranging heating elements and ceramic insulation according to the reading of numerous thermocouples in the system, and the control thermopile was positioned at the optimum site between heating elements and crucible. KTN crystals

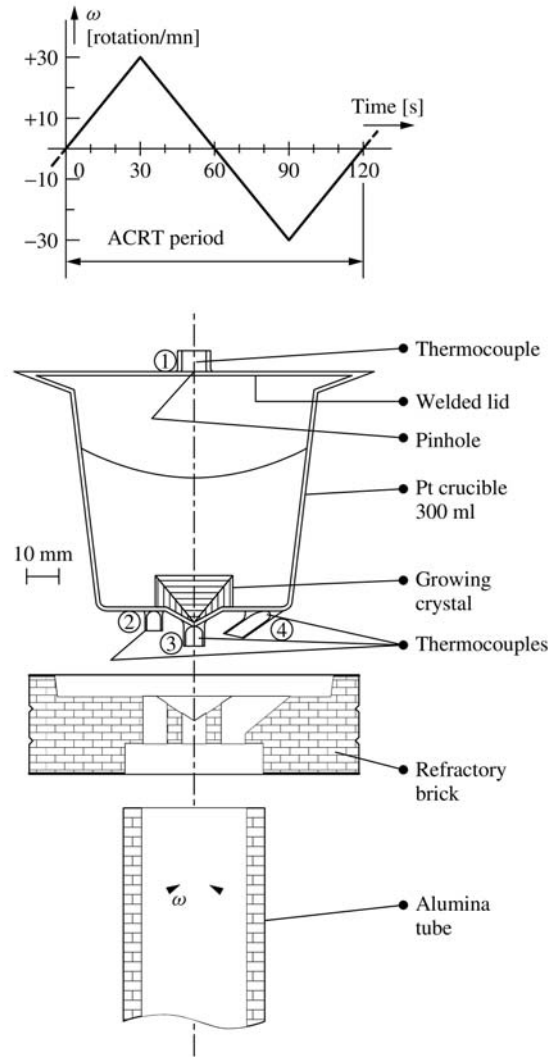


Figure 4.10 Side view of a 300-cm³ platinum crucible, with welded lid and slightly cooled spot at crucible bottom for nucleation control, used in the ACRT experiments for growth of KTN crystals (Rytz and Scheel 1982). A typical ACRT period is also shown.

with $x = 0.01$ and $x = 0.25$ and up to $33 \times 33 \times 15 \text{ mm}^3$ in size were grown, see Table 4.2 for details of the results.

In the best crystals no striations were visible in a polarizing microscope, although very faint striations could be revealed by using extremely sensitive methods (Scheel and Günter 1985).

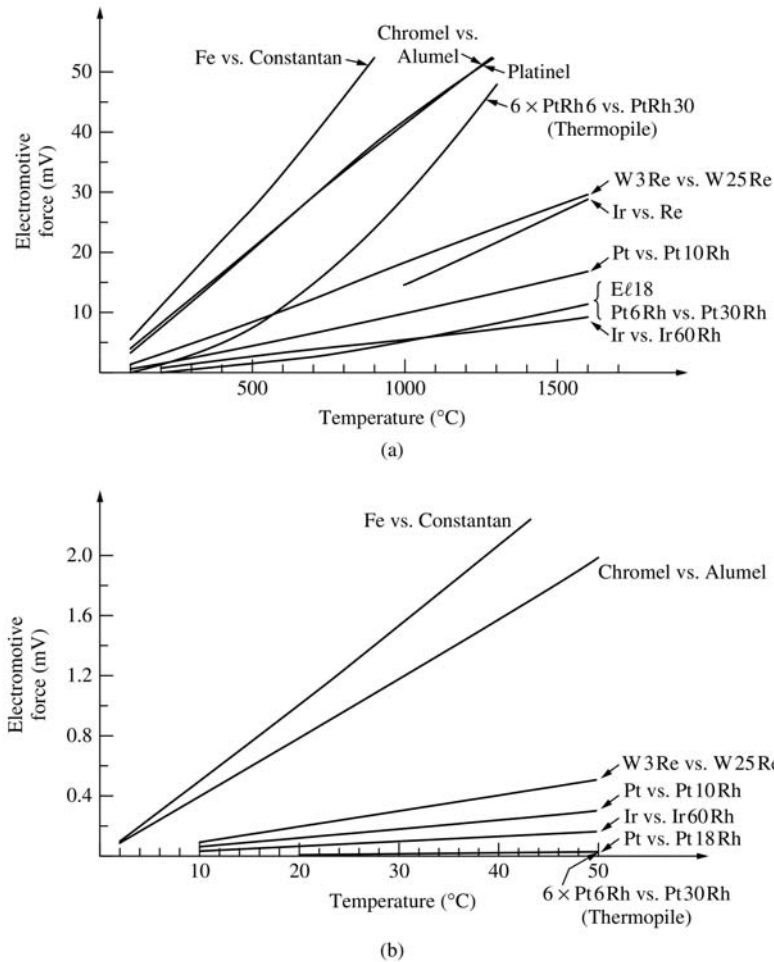


Figure 4.11 The electromotive forces of various common thermocouples (a) for high temperatures, (b) for the temperature range 0 to 50°C. Note that the thermopile of $6 \times \text{PtRh}6\%$ versus $\text{PtRh}30\%$ has a very high sensitivity at high temperatures and practically no sensitivity around room temperature (Scheel and West 1973, from Elwell and Scheel 1975).

4.6 ALTERNATIVE APPROACHES TO REDUCE STRIATIONS

Based on the early studies of striations discussed in Section 4.2, the striations were generally connected with convective oscillations: a clear distinction between the effects of hydrodynamics and of temperature as discussed by Scheel and Swendsen (2001) and in Section 4.4 was not consequently attempted before. This explains the numerous approaches to *reduce* convection in order to solve

Table 4.2 Results of ‘striation-free’ $\text{KTa}_{1-x}\text{Nb}_x\text{O}_3$ crystals

with $x \sim 0.01$ and $T_c \sim 0$ K (Rytz and Scheel 1982) (cooling rate 0.15°C per hour; ACRT) Crystal size up to $3.5 \times 3.0 \times 1.8 \text{ cm}^3$ with ‘perfect’ regions up to $0.8 \times 0.4 \times 0.4 \text{ cm}^3$ $x = 0.0070 \pm 0.00002$ and $\Delta x < 0.0003/\text{cm}$ (detection limit of ARL electron microprobe and of acoustic resonance measurements) Very faint striations by polarizing microscope, not detectable by electron microprobe	
with $x \sim 0.25$ and $T_c \sim 300$ K (Scheel and Sommerauer 1983) (cooling rate 0.13°C per hour; ACRT; growth rate $\sim 500 \text{ \AA/s}$) Crystal size up to $3.6 \times 3.3 \times 1.5 \text{ cm}^3$ with ‘perfect’ regions up to $0.5 \times 0.5 \times 0.25 \text{ cm}^3$ $\Delta T = 0.1^\circ\text{C} \sim \Delta x = 0.0003/\text{cm}$ at $x = 0.25$ No striations detectable in polarizing microscope and by interferometry (no strain birefringence)	
Best literature values for $x \sim 0.25\text{--}0.3$:	always with striations $\Delta x = 0.006/\text{cm}$ Fay 1967 $\Delta x = 0.002/\text{cm}$ Levy and Gashler 1968

the striation problem, whereas it was discussed above that *forced convection* and even *oscillating convection* of quasi-isothermal solutions can solve the striation problem.

In the following, first the attempts to reduce convection will be briefly discussed on the base of the Rayleigh number Ra . At a critical value of Ra one expects the onset of convection in a fluid between a warm bottom plate and a cool top plate (although in reality convection will always occur whenever there is a temperature difference in a real growth system):

$$Ra = \frac{g\alpha L^3 \Delta T}{k\nu} \quad (4.7)$$

where α is the thermal expansion coefficient, L the fluid height, ΔT the temperature difference, k thermal conductivity, ν the kinematic viscosity, and g the gravitation constant. The first approaches have been to reduce L by means of shallow melts or by baffles below the growth interface in Czochralski crystal pulling. Also double crucibles may have a certain effect on striations (Kozhemyakin 2000), but their greatest advantage is the increased axial crystal yield with the same composition, as it was shown by Benson *et al.* 1981 for silicon and later applied to GaAs and LiNbO_3 growth.

Edge-defined film-fed growth EFG allows $k_{\text{eff}} \sim 1$ to be approached as was shown theoretically by Kalejs (1978) and experimentally by Fukuda and Hirano (1976) and Matsumura and Fukuda (1976) for platelet growth of doped LiNbO_3 and LiTaO_3 . Shaped growth by pulling downwards has been studied by Miyazawa (1982) who grew relatively homogeneous Te-doped GaSb platelets by ‘shaped melt lowering’. A capillary-controlled Czochralski process for shaped crystals

of $\text{Sr}_x\text{Ba}_{1-x}\text{Nb}_2\text{O}_6$, which has similarity with Stepanov and EFG, was applied by Ivleva *et al.* (1987, 1995) and has led to nearly striation-free crystals due to the thin melt layer between shaping multicapillary die and the crystal. Nakajima (1991) and Kusunoki *et al.* (1991) tried to grow InGaAs solid-solution crystals by ramp-cooling and by GaAs supply at constant temperature similar to W. Bonner, but it seems that large homogeneous crystals for technological use as substrates has not yet been achieved. Ostrogorsky and Müller (1994) proposed a submerged-heater method for vertical Bridgman growth, where the combined effect of thin melt layer and stabilizing temperature gradient should minimize striations, but the complexity has hampered technological application.

Large-scale application has found the modified Czochralski process for pulling huge halide scintillator crystals (up to 700 mm diameter and 550 kg weight) from small melt volumes with liquid feeding by Gektin and Zaslavsky, see in this volume. In this case, there is a combined effect of small liquid volume and forced convection due to counterrotation of crystal and crucible.

But from the time of Skylab and with the available funding for space experiments, the interest shifted in the direction of microgravity, of reduction of g in Equation (4.5). In practical fabrication of semiconductor crystals it was recognized that microgravity would not be applicable for various reasons, so that here the parameter ν of Equation (4.7) was considered: by application of magnetic fields the viscosity was increased, and convection was damped. Magnetic fields were first introduced in 1980 by SONY to silicon production, followed by Fukuda and Terashima, who in 1983 applied magnetic field to GaAs growth, which in industry is still applied in LEC production of specific GaAs products.

Alternative approaches to apply forced convection have been discussed in the Elwell–Scheel book, for instance ‘sloshing’ of the crucible by moving the center of the container in a horizontal circular path described first by Gunn (1972) as ‘sloshing’ and later as a special vibration technique by Liu *et al.* (1987). Kirgintsev and Avvakumov (1965) compared various stirring techniques including vibrators and found the latter not very effective. Hayakawa and Kumagawa (1985) and more recently Kozhemyakin (1995) and Zharikov *et al.* revived the interest in vibration stirring, although it has not yet found application in real crystal production.

An optimized technology for growth from solutions using a large rotating seed crystal (or a substrate for liquid phase epitaxy) is shown in Figure 4.12. In bulk growth the grown crystal can be cut off and, after etching to remove the surface damage from slicing, the seed crystal can be used again for the next growth cycle, a little like the large-diameter seed crystals recently developed in silicon Czochralski technology. The optimum crystallographic orientation of the seed is important firstly in view of the growth mechanism to remain at a flat growth surface and to prevent macrostep formation, and secondly with respect to the application of the crystal. In this configuration, a sufficiently high seed rotation rate provides Ekman layer flow and thus a quasiconstant diffusion boundary layer along the crystal surface.

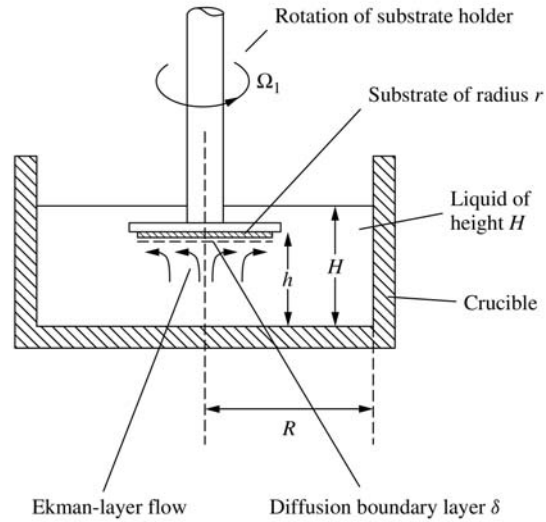


Figure 4.12 An ideal growth system for growth of striation-free large-diameter crystals and of thick and homogeneous LPE layers.

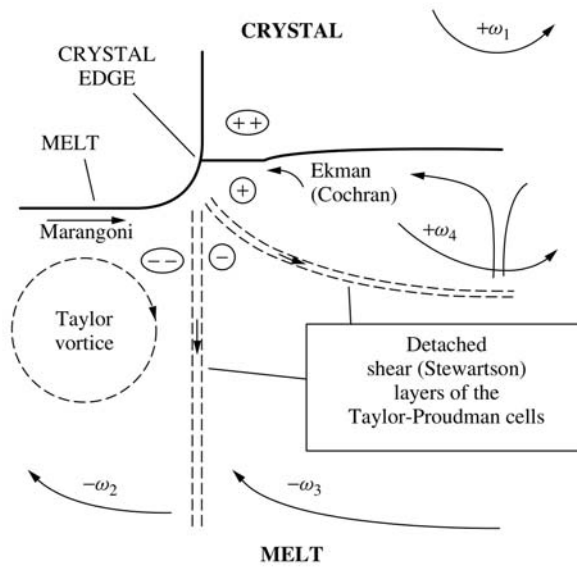


Figure 4.13 More than six types of flow, differing in direction and/or velocity, below the edge of a Czochralski-grown crystal for the case of crystal rotation $+\omega_1$ and crucible counterrotation $-\omega_2$ above the critical Rossby number (Scheel and Sielawa 1985).

For growth from melts by Czochralski crystal pulling there are six or more different kinds of flows below the rim of the crystal as shown in Figure 4.13: flows with different directions and/or different velocities. Double crucibles discussed above will help somewhat to simplify the flow pattern but have practical disadvantages in the growth process. A technologically simpler approach consists of a solid ring coaxial with the crystal rotation axis and rotating with same direction and velocity as the crystal. This ring can be introduced into the melt after complete melting and it can be easily removed at the end of the growth process. In simulation experiments it was shown that at optimized setting of the rotation rate of crystal and ring, and counterrotation of the crucible, the melt fraction inside the ring is nearly stationary and separated from the well-mixed bulk melt, see Figure 4.14. This co-rotating ring Czochralski CRCZ approach of Scheel (1995) has the positive double-crucible effects without the disadvantages of a double crucible: an increased yield of axially homogeneous crystal

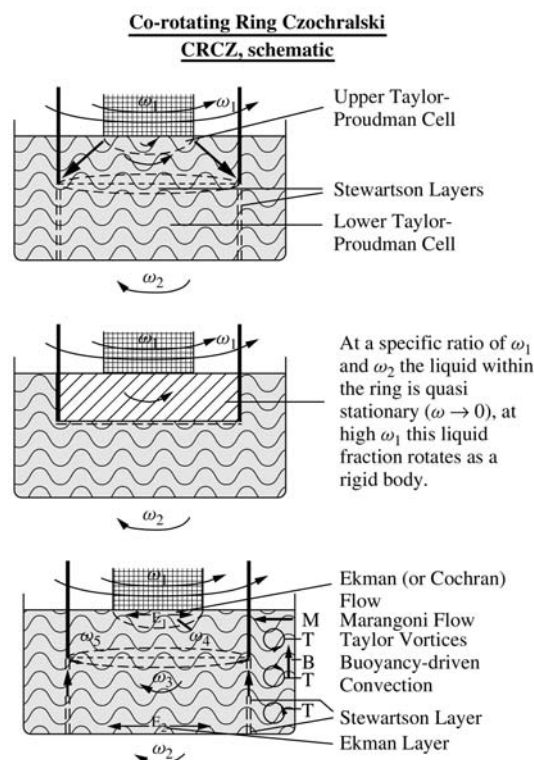


Figure 4.14 Schematic presentation of the Co-rotating ring Czochralski CRCZ concept where the complex flow region of Figure 4.13 is transferred deeper into the melt and where the liquid fraction within the ring can be separated from bulk melt flow under optimized conditions (Scheel 1995).

and reduced striations. Numerical simulations of CRCZ have started (Kakimoto 2002; Zhong Zeng 2001), but the growth technology has yet to be developed.

4.7 DISCUSSION

Several experimental and theoretical solutions were presented to overcome the as intrinsic regarded striation problem:

1. $k_0, D, v, \delta = \text{constant}$: very difficult; chance with rotating seed (Figure 4.12) & with CRCZ (Figure 4.14)
2. $k_0, D, v = \text{constant}$; δ may vary Rytz & Scheel 1982; Scheel and Sommerauer 1983; Scheel and Swendsen 2001
3. $k_{\text{eff}} = 1$ for growth from melt: Mateika 1984
4. $k_{\text{eff}} = 1$ for growth from solution: Scheel and Swendsen 2001
5. Avoid solid solutions by growth of simple stoichiometric compounds with well-defined site distribution from ultra-pure chemicals

Further conditions are

- (a) Continuous flat or smooth growth surface
- (b) Isothermal growth surface with $\Delta T/T < 10^{-5}$
- (c) Homogeneous melt or solution with $\Delta n/n < 10^{-6}$
- (d) Constant growth rate with $\Delta v/v < 10^{-5}$.

These indicated tolerances are typical values and depend on the individual system and on the tolerated inhomogeneity of the crystal. Therefore it is advisable to analyze a new growth system and the phase relations theoretically so that the required technological parameters can be established. With respect to optimized hydrodynamics, simulation experiments with a liquid of similar kinematic viscosity are very useful in the early phase and may be complemented by numerical simulation for process optimization. However, the latter require reliable material (liquid) parameters, which often are not available. In certain cases dimensionless numbers may be helpful to get a feel for the convection regime.

In conclusion, one can say that the striation problem is solvable (on earth) but requires a certain theoretical and technological effort. Hydrodynamic fluctuations are not harmful as long as the fluid is sufficiently isothermal, as long as the transport of fluid of different temperature to the growth interface is suppressed.

REFERENCES

- Bardsley W., Boulton J. S. and Hurle D. T. J. (1962), *Solid State Electron.* **5**, 365.
 Burton J. A., Prim R. C. and Slichter W. P. (1953a), *J. Chem. Phys.* **21**, 1987.

- Burton J. A., Kolb E. D., Slichter W. P., and Struthers J. D. (1953b), *J. Chem. Phys.* **21**, 1991.
- Byer R. L. (1974), *Ann. Rev. Mater. Sci.* **4**, 147.
- Cabrera N. and Vermilyea D. A. (1958) in *Growth and Perfection of Crystals*, editors R. H. Doremus, B. W. Roberts and D. Turnbull, Wiley, New York and Chapman and Hall, London, p. 393.
- Camp P. R. (1954), *J. Appl. Phys.* **25**, 459.
- Chen F. S., Geusic J. E., Kurtz S. K., Skinner J. C. and Wemple S. H. (1966), *J. Appl. Phys.* **37**, 388.
- Chernov A. A. (1992), *J. Cryst. Growth* **118**, 333.
- Chernov A. A. and Scheel H. J. (1995), *J. Cryst. Growth* **149**, 187.
- Cockayne B. and Gates M. P. (1967), *J. Mater. Science* **2**, 118.
- Donecker J., Lux B. and Reiche P. (1996), *J. Cryst. Growth* **166**, 303.
- Elwell D. and Scheel H. J. (1975) *Crystal Growth from High-Temperature Solutions*, Academic Press, London, New York, Chapter 7.
- Frank F. C. (1958) in *Growth and Perfection of Crystals*, editors R. H. Doremus, B. W. Roberts and D. Turnbull, Wiley, New York and Chapman and Hall, London, p. 411.
- Fukuda T. and Hirano H. (1976), *J. Cryst. Growth* **35**, 127.
- Goss A. J., Benson K. E. and Pfann W. G. (1956), *Acta Met.* **4**, 332.
- Gunn J. B. (1972), *IBM Tech. Discl. Bull.* **15**, 1050.
- Hayakawa Y. and Kumagawa M. (1985), *Cryst. Res. Technol.* **20**, 3.
- Hurle D. T. J. (1966), *Philos. Mag.* **13**, 305.
- Hurle D. T. J. (1967), in *Crystal Growth*, editor H. S. Peiser, Pergamon, Oxford, 659–663.
- Ivleva L. I., Yu. S. Kuz'minov V. V. Osiko and Polozkov N. M. (1987), *J. Cryst. Growth* **82**, 168.
- Ivleva L. I., Bogodaev N. V., Polozkov N. M. and Osiko V. V. (1995), *Opt. Mater.* **4**, 168.
- Kakimoto K. (2002), private communication.
- Kalejs J. P. (1978), *J. Cryst. Growth* **44**, 329.
- Kirgintsev A. N. and Avvakumov E. G. (1965), *Sov. Phys.-Cryst.* **10**, 375.
- Kozhemyakin G. N. (1995), *J. Cryst. Growth* **149**, 266.
- Kozhemyakin G. N. (2000), *J. Cryst. Growth* **220**, 39.
- Krishnan R. (1972), *J. Cryst. Growth* **13/14**, 582.
- Kusonoki T., Takenaka C. and Nakajima K. (1991), *J. Cryst. Growth* **115**, 723.
- Landau A. P. (1958), *Fiz. Metal. Metalloved* **6**, 193.
- Laves F. (1944), *Die Chemie* **57**, 30–33; reprinted in *Z. Krist.* **151** (1980) 21.
- Lighthill M. J. and Whitham G. B. (1955), *Proc. Roy. Soc.* **229**, 281.
- Liu W.-S., Wolf M. F., Elwell D. and Feigelson R. S. (1987) *J. Cryst. Growth* **82**, 589.
- Loo R., Kamath G. S. and Knechtli R. C. (1980), *Radiation damage in GaAs solar cells*, 14th IEEE Photovoltaics Specialists Conference.
- Mateika D. (1984) in *Current Topics in Materials Science*, editor E. Kaldis, North-Holland/Elsevier, Chapter 2.
- Matsumura S. and Fukuda T. (1976), *J. Cryst. Growth* **34**, 350.
- Miyazawa S. (1982), *J. Cryst. Growth* **60**, 331.
- Nabarro F. R. N. (1975) in *Solution and Precipitation Hardening. The Physics of Metals, Part 2, Defects*, editor P. B. Hirsh, Cambridge University Press Cambridge, p. 152.
- Nakajima K. (1991), *J. Cryst. Growth* **110**, 781.
- Nernst W. (1904), *Z. Phys. Chem.* **47**, 52.

- Ostrogorsky A. G. and G. Müller (1994), *J. Cryst. Growth* **137**, 66.
- Pfann W. G. (1952), *J. Met.* **4**, 747.
- Räuber A. (1978), in *Current Topics in Materials Science* Vol. 1, editor E. Kaldis, North-Holland, Amsterdam, p. 481.
- Reiche P., Schlage R., Bohm J., and Schultze D. (1980), *Kristall U. Technik* **15**, 23.
- Reisman A., Triebwasser S. and Holtzberg F. (1955), *J. Am. Chem. Soc.* **77**, 4228.
- Rytz D. and Scheel H. J. (1982), *J. Cryst. Growth* **59**, 468.
- Scheel H. J. (1972), *J. Cryst. Growth* **13/14**, **560**.
- Scheel H. J. (1980), *Appl. Phys. Lett.* **37**, 70.
- Scheel H. J. (1995), US Patent 5,471,943.
- Scheel H. J. and Günter P. (1985), Chapter 12 in *Crystal Growth of Electronic Materials*, editor E. Kaldis, Elsevier, 149–157.
- Scheel H. J. and Sielawa J. T. (1985), Proceedings International Symposium on High-Purity Materials, Dresden/GDR May 6–10, 1985, 232–244.
- Scheel H. J. and Sommerauer J. (1983), *J. Cryst. Growth* **62**, 291.
- Scheel H. J. and Swendsen R. H. (2001), *J. Cryst. Growth* **233**, 609.
- Scheel H. J. and West C. H. (1973), *J. Phys E* **6**, 1178; see also Elwell and Scheel (1975) Chapter 7.
- Schieber M. (1966), *J. Appl. Phys.* **37**, 4588.
- Schulz-DuBois E. O. (1972), *J. Cryst. Growth* **12**, 81.
- Van Erk W. (1982), *J. Cryst. Growth* **57**, 71.
- Wenzl H., Oates W. A. and Mika K. (1993), Chapter 3 in *Handbook of Crystal Growth* Vol. 1, editor D. T. J. Hurle, Elsevier, Amsterdam.
- Wilcox W. R. and Fullmer L. D. (1965), *J. Appl. Phys.* **36**, 2201.
- Zhong Zeng (2001), private communication.

5 High-Resolution X-Ray Diffraction Techniques for Structural Characterization of Silicon and other Advanced Materials

KRISHAN LAL

National Physical Laboratory New Delhi-110 012 India

5.1 INTRODUCTION

The increasing density of devices on individual integrated circuits requires an unprecedented level of homogeneity in chemical composition and structural perfection of silicon and other semiconductor crystals (Claeys and Deferm 1996, Bullis and Huff 1993). A strict control of composition and trace impurities as well as on structural quality with particular emphasis on defects like dislocations, point defects and their clusters is needed. Therefore, the demand on material characterization technology is increasing as advances in other sectors of technology are reaching newer levels of sophistication (Laudise 1972, Lal 1991a).

Structural characterization of materials involves phase identification as well as determination of real structure. We shall be concerned with determination of real structure, which requires information about all types of defects and their concentrations in a given material (Lal 1998). The information regarding crystalline perfection may be required from the surface or from the bulk of the crystal. In the case of thin-film single-crystal substrate systems, the interface region is also important.

A wide variety of experimental techniques are available for observation and characterization of defects in bulk single crystals and thin films. These include chemical etching by suitable solvents (Sangwal 1987), decoration, birefringence (for specific materials) (Mathews *et al.* 1973), electron microscopy/diffraction (Heydenreich 1982, Spence 1984) and high-resolution X-ray diffraction techniques (Lang 1958, 1970, Kato 1975, Tanner 1976, Lal 1982, 1991a, 1991b 1998). The recently developed scanning tunneling microscopy (Binnig *et al.* 1982, Hansma and Tersoff 1987) and atomic force microscopy (Binnig *et al.* 1986, Alexander *et al.* 1989) are used to reveal atomic arrangement on solid surfaces. In this chapter, we shall consider

fundamentals of high-resolution X-ray diffraction techniques and their illustrative applications.

5.2 HIGH-RESOLUTION X-RAY DIFFRACTION TECHNIQUES

5.2.1 THEORETICAL BACKGROUND

The kinematical theory (Cullity 1967, James 1950, Guinier 1952, and Barrett and Massalski 1968) and the dynamical theory of X-ray diffraction (Laue 1960, Zachariasen 1945, Batterman and Cole 1964, Kato 1992, Pinsker 1978, Schneider and Bouchard 1992) are used to understand diffraction of X-rays from single crystals. Since, the semiconductor crystals are nearly perfect it is necessary to use the dynamical theory of X-ray diffraction. The kinematical theory can be used only when one is dealing with rather imperfect crystals or their dimensions are small. When a parallel beam of monochromatic X-rays travels through a crystal, electrons of the atoms in its path become scattering centres due to their interaction with the electric vector of the X-ray beam. An atom located in the interior of the crystal will receive not only the incoming radiation whose intensity has decreased due to scattering and absorption by layers above it but also it will receive scattered waves from all the other atoms that are irradiated. This implies that interaction between the scattered and the incoming waves as well as among the scattered waves is to be considered for determining the total wave field and the intensity of the diffracted beam and the shape of the diffraction curves or rocking curves. The diffraction curve is essentially a plot of the diffracted intensity as a function of the glancing angle θ around the exact Bragg angle θ_B . In the following, we give the most essential steps needed for calculation of diffracted intensity in the case of Bragg geometry (reflection) as well as the Laue geometry (transmission).

In the dynamical theory one solves Maxwell's equations for propagation of X-rays inside the crystal that is oriented near a diffraction maximum, so that:

$$\mathbf{K}_H = \mathbf{K}_0 + \mathbf{H} \quad (5.1)$$

Here \mathbf{K}_0 is the wave vector of the incident beam and \mathbf{K}_H is that of the scattered beam from the crystal lattice having periodicity \mathbf{H} ($H = 1/d$, or reciprocal of the lattice spacing of the diffracting planes). The X-rays propagating in the crystal will satisfy Maxwell's equations (e.g. Batterman and Cole 1964):

$$\nabla \times \mathbf{E} = -\partial \mathbf{B} / \partial t = -\mu_0 \partial \mathbf{H} / \partial t \quad (5.2)$$

$$\nabla \times \mathbf{H} = \partial \mathbf{D} / \partial t = \epsilon_0 \partial (\kappa \mathbf{E}) / \partial t \quad (5.3)$$

Here \mathbf{E} , \mathbf{D} , \mathbf{B} and \mathbf{H} are the four vector fields: the electric vector, the displacement vector, the magnetic vector and the magnetic induction vector, respectively. The

conductivity σ of the crystal is taken as zero at X-ray frequencies. Also, the crystal is considered as nonmagnetic and it behaves like empty space so that $\mu = \mu_0$. The structure of the crystal is introduced by the dielectric constant κ , which is related to the electron density ρ through

$$\kappa(\mathbf{r}) = 1 - r_e(\lambda^2/\pi)\rho(\mathbf{r}) \quad (5.4)$$

Here, r_e is the classical radius of electron ($= e^2/4\pi\epsilon_0 mc^2 = 2.818 \times 10^{-13}$ cm) and λ is the wavelength of the X-rays. The electron density $\rho(\mathbf{r})$ at any point \mathbf{r} inside the crystal can be expressed as a Fourier sum over the reciprocal lattice. Hence, we can express Equation (5.4) as:

$$\kappa(\mathbf{r}) = 1 - \Gamma \Sigma_H F_H \exp(-2\pi i \mathbf{H} \cdot \mathbf{r}) \quad (5.5)$$

where F_H is the structure factor and $\Gamma = r_e \lambda^2 / \pi V$. The dielectric constant $\kappa(\mathbf{r})$ is very close to unity, differing from it by a few parts per million or so. A sum of plane waves is assumed as the solution of Maxwell's equations, and can be expressed in the form:

$$\mathbf{A} = \exp(2\pi i \nu l) \Sigma_H \mathbf{A}_H \exp(-2\pi i \mathbf{K}_H \cdot \mathbf{r}) \quad (5.6)$$

Here, \mathbf{A} stands for \mathbf{E} , \mathbf{D} , \mathbf{B} or \mathbf{H} . When only one reciprocal lattice point is near the Ewald sphere, one obtains the following fundamental set of equations for the wave field inside the crystal after some mathematical analysis:

$$[k^2(1 - \Gamma F_0) - (\mathbf{K}_0 \cdot \mathbf{K}_0)]E_0 - k^2 P \Gamma F_H E_H = 0 \quad (5.7a)$$

$$-k^2 P \Gamma F_H E_0 + [k^2(1 - \Gamma F_0) - (\mathbf{K}_H \cdot \mathbf{K}_H)]E_H = 0 \quad (5.7b)$$

Here, the parameter P represents both states of polarization and equals 1 for σ polarization and is $\cos 2\theta$ for the π state. k is the vacuum value of the wave vector. From these basic equations one can, after some analysis, obtain the wave vectors as well as expressions for the wave amplitudes. The relationship between different wave vectors is elegantly represented by using the dispersion-surface concept. It is not possible to cover all aspects here. We shall consider the most essential part, which helps in calculating diffraction curves.

5.2.1.1 Laue Case

For symmetrical Laue geometry we finally get the following expressions for intensities of the diffracted ($I_{H\omega}^e$) and the forward diffracted beams ($I_{0\omega}^e$)

$$\begin{aligned} \frac{I_{0\omega}^e}{I_0} &= \frac{1}{4} \left[1 \mp \frac{\eta'}{|1 + (\eta')^2|^{1/2}} \right]^2 \exp \left[-\frac{\mu_0 t_0}{\gamma_0} 1 \mp \frac{|P|\varepsilon}{|1 + (\eta')^2|^{1/2}} \right] \\ \frac{I_{H\omega}^e}{I_0} &= \frac{1}{4} \frac{1}{1 + (\eta')^2} \exp \left[-\frac{\mu_0 t_0}{\gamma_0} \left\{ 1 \mp \frac{|P|\varepsilon}{|1 + (\eta')^2|^{1/2}} \right\} \right] \end{aligned} \quad (5.8)$$

Here, ω refers to a particular polarization state of either the α or the β branch of the dispersion surface, I_0 is the intensity of the exploring beam and t_0 is the thickness of the crystal. The upper negative sign is for the α branch of the dispersion surface, whereas for β branch positive sign has to be used. Also, it has been assumed that the crystal is centrosymmetric. The orientation of the crystal is defined with respect to the exact diffraction condition by $\Delta\theta$. It is related to a parameter η' by the expression:

$$\eta' = (\Delta\theta \sin 2\theta) / |P|\Gamma|F_H'| \quad (5.9)$$

Theoretical diffraction curves can be obtained from Equations (5.8) and (5.9). The absolute value of integrated intensity can be calculated from the area under the diffraction curve. The half-width can be obtained from Equation (5.8) as the angular spread corresponding to $\Delta\eta' = 2$, i.e.

$$[\Delta\theta]_{\text{HW}} = 2|P|\Gamma|F_H'| / \sin 2\theta \quad (5.10)$$

5.2.1.2 Bragg Case

In the case of Bragg diffraction the diffracted beam emerges from the same surface on which it is incident. It shows interesting features like total reflection for nonabsorbing crystals. For a centrosymmetric crystal, the reflection coefficient defined as $|E_H^e/E_0^i|^2$ is given by the following expression:

$$\frac{|E_H^e|^2}{|E_0^i|^2} = |b||\eta \pm (\eta^2 - 1)^{1/2}|^2 \quad (5.11)$$

For symmetrical Bragg geometry $b = -1$.

All real crystals have finite absorption coefficients for X-rays and therefore the structure factor, the wave vectors, the dielectric and η are complex quantities. For symmetrical Bragg geometry $\eta (= \eta' + i\eta'')$ is defined by:

$$\begin{aligned} \eta' &= (-\Delta\theta \sin 2\theta + \Gamma F_0') / |P|\Gamma F_H' \\ \eta'' &= -(F_H'' / F_H')(\eta' - 1 / |P|\varepsilon) \end{aligned} \quad (5.12)$$

Figure 5.1 shows a diffraction curve of a silicon crystal calculated for 111 reflection and $\text{MoK}\alpha_1$ radiation for symmetrical Bragg geometry. This curve shows very high reflectivity at the peak and its half-width is only ~ 3 arcsec.

5.2.2 HIGH-RESOLUTION X-RAY DIFFRACTION EXPERIMENTS: A FIVE-CRYSTAL X-RAY DIFFRACTOMETER

To obtain diffraction curves of real crystals, one would ideally require an absolutely parallel and monochromatic X-ray beam, which obviously one cannot

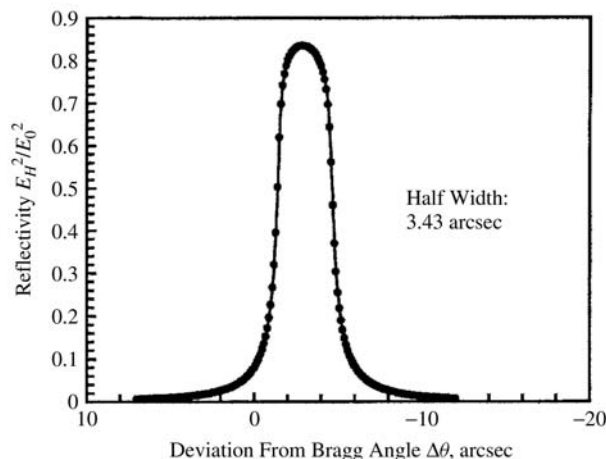


Figure 5.1 A theoretical diffraction curve of a perfect silicon crystal for (111) diffracting planes calculated on the basis of the plane-wave dynamical theory for symmetrical Bragg geometry and $\text{MoK}\alpha_1$ radiation. (Reprinted from Krishan Lal, PINSA **64A**(5) (1998) 609–635, copyright (1998) with permission from PINSA.)

achieve. One has to work with a beam that is nearly parallel and monochromatic. The divergence and the wavelength spread are to be reduced sufficiently so that the broadening produced by these two sources is a small fraction of the theoretical half-width of the diffraction curve of interest. This problem is quite challenging and several approaches are used.

Conventionally, the divergence of X-ray beams can be reduced by using long collimators fitted with fine slits, which is not practical to reduce divergence to the arcsec level. Nearly perfect single crystals are used as monochromators and collimators due to their small angular range of diffraction. By successive diffraction from nearly perfect crystals, it is possible to obtain nearly parallel and monochromatic X-ray beams. The use of channel-cut monolithic monochromators of the Bonse–Hart type (Bonse and Hart 1965) has made it possible to use a single unit for two or even more reflections. It is profitable to combine X-ray sources having low dimensions with long collimators and one or more monochromator crystals to achieve high-quality X-ray beams. Several types of multocrystal X-ray diffractometers have been developed. Some of these are now commercially available. The author and his coworkers have developed different types of multocrystal X-ray diffractometers (Lal and Singh 1977, Lal and Bhagavannarayana 1989, Lal *et al* 1990a, Lal *et al* 1996a and Lal 1993). A five-crystal X-ray diffractometer with state-of-the-art level resolution is briefly described in the following (Lal 1993, 1998).

Figure 5.2 shows a schematic line diagram of the five-crystal X-ray diffractometer designed, developed and fabricated in the author's laboratory. It can be used with a fine-focus sealed X-ray tube or a rotating-anode X-ray generator.

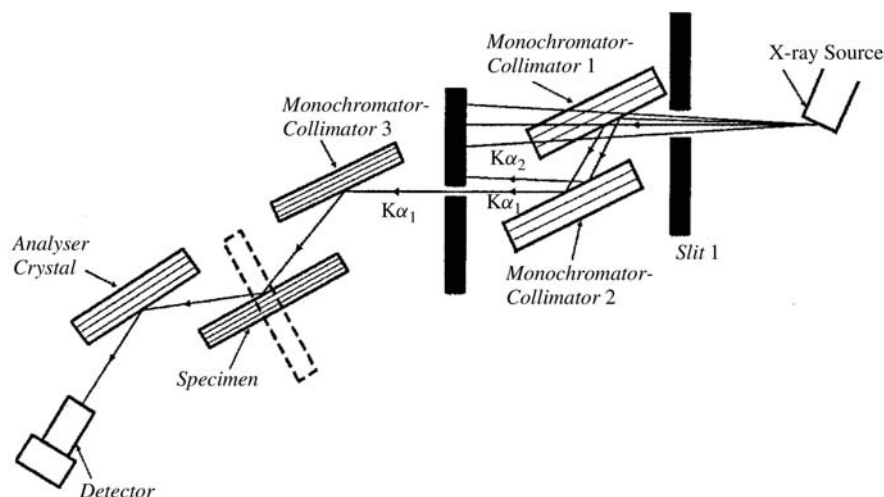


Figure 5.2 A schematic line diagram of the five-crystal X-ray diffractometer designed, developed and fabricated in the author's laboratory. (Reprinted from Krishan Lal, PINSA **64A(5)** (1998) 609–635, copyright (1998) with permission from PINSA.)

A long collimator is combined with a set of two plane silicon monochromator crystals of Bonse–Hart type (Bonse and Hart 1965). The beam diffracted from the monochromator crystals consists of $K\alpha_1$ (for $0.1 \times 0.1 \text{ mm}^2$ source) or well-resolved $K\alpha_1$ as well as $K\alpha_2$ components of the $K\alpha$ doublet (with a focal spot of $0.4 \times 0.4 \text{ mm}^2$). The $K\alpha_1$ beam is isolated with the help of a fine slit and is further diffracted from a third monochromator-collimator crystal as shown in Figure 5.2. The third crystal is oriented for diffraction from (800) planes in (+, −, +) geometry. The small intrinsic angular width of its diffraction curve leads to a substantial reduction in divergence as well as the wavelength spread of the beam (about 1/50th of the intrinsic spread of the $K\alpha_1$ beam). The specimen generally occupies the fourth crystal position and can be oriented in Bragg or Laue geometries. The X-ray beam diffracted from the fourth crystal stage is further diffracted from the fifth crystal, which acts as an analyzer. The analyzer crystal is very effective in determining spatial variations in lattice parameters of the specimen located at the fourth crystal position. It also enables accurate determination of changes in lattice parameters produced by external influences such as high electric fields (Lal and Thoma 1983 and Lal and Goswami 1987). It has been found that in the case of specimens with epitaxial films, there is a finite mismatch between crystallographic orientations of the film and the substrate in addition to the lattice mismatch between the two (Lal *et al.* 1996b and Goswami *et al.* 1999). With the use of the analyzer crystal, the two mismatches can be conveniently isolated and measured with low level of uncertainty.

The diffractometer is generally oriented in (+, −, +, −, +) geometry. There is considerable flexibility in fixing the geometry to meet a given requirement. The

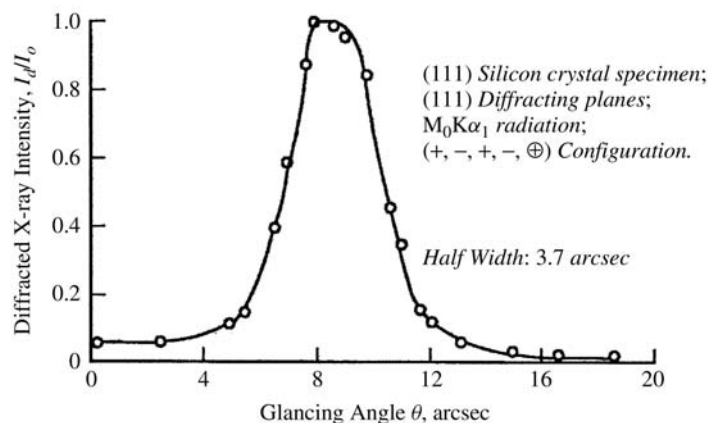


Figure 5.3 A typical high-resolution X-ray diffraction curve of a nearly perfect silicon single crystal recorded with (111) planes on the five-crystal X-ray diffractometer in symmetrical Bragg geometry. $\text{MoK}\alpha_1$ radiation and (+, −, +, −, ⊕) configuration were employed. (Reprinted from Krishan Lal, *PINSA* **64A(5)** (1998) 609–635, copyright (1998) with permission from PINSA.)

specimen crystal can occupy any of the positions, from first to fifth. Figure 5.3 shows a typical diffraction curve of a silicon single crystal located at the fifth crystal position in (+, −, +, −, ⊕) configuration of the diffractometer (Lal 1993). This is an as-recorded curve without any corrections being applied. The intensity at the peak is nearly equal to that of the exploring beam and its half-width is only 3.7 arcsec as compared to 3.3 arcsec of the theoretically calculated curve under ideal experimental conditions (Figure 5.1). Even when one uses relatively higher-order reflections, the dispersion broadening does not significantly affect the shape of experimental diffraction curves. For example, the experimentally recorded diffraction curve of (400) planes is only 1.7 arcsec in half-width (Lal 1998). The theoretical value of half-width for this set of planes is ~ 1.4 arcsec. Due to these features, the diffractometer allows one to make high-resolution X-ray diffraction experiments with low experimental uncertainty.

The diffractometer can be used for making high-resolution X-ray diffraction experiments of a wide variety, including (i) diffractometry; (ii) topography; (iii) determination of absolute value of integrated X-ray intensity; (iv) diffuse X-ray scattering measurements; (v) measurement of curvature of wafers and determination of biaxial stress in thin-film-single-crystal substrate systems; (vi) accurate determination of lattice parameters of crystals; (vii) accurate determination of lattice and orientational mismatches between epitaxial films and their substrates; (viii) accurate determination of orientation of crystal surfaces as well as straight edges on wafers; and (ix) determination of absorption coefficient of single crystals for X-rays.

5.3 EVALUATION OF CRYSTALLINE PERFECTION AND CHARACTERIZATION OF CRYSTAL DEFECTS

Evaluation of crystalline perfection is concerned with identification and characterization of all types of crystal defects and determination of their densities. Since the presence of grain boundaries means that the material is not a single crystal, we will not discuss characterization of grain boundaries in this paper. Low-angle boundaries produce tilts of ≥ 1 arcmin between adjoining subgrains. Recent experimental investigations have shown that some crystals contain very low-angle boundaries with tilt angles of less than 1 arcmin (Murthy *et al.* 1999, Kumar *et al.* 1999). Figure 5.4(a) shows a typical diffraction curve of a very low-angle boundary in a bismuth germanate crystal (Murthy *et al.* 1999). In this case, we observe two well-resolved peaks, labelled as a and b, representing two regions of the crystal that are tilted with respect to each other by an angle of only 33 arcsec. Traverse topographs shown in Figure 5.4(b) were recorded by orienting the crystal on each of the peaks. It is seen that in the topograph on the left, recorded with peak a, the entire illuminated region is diffracting except for a small portion near the top. The other topograph recorded with peak b is essentially the small missing part in the topograph recorded on peak a. The subgrains on

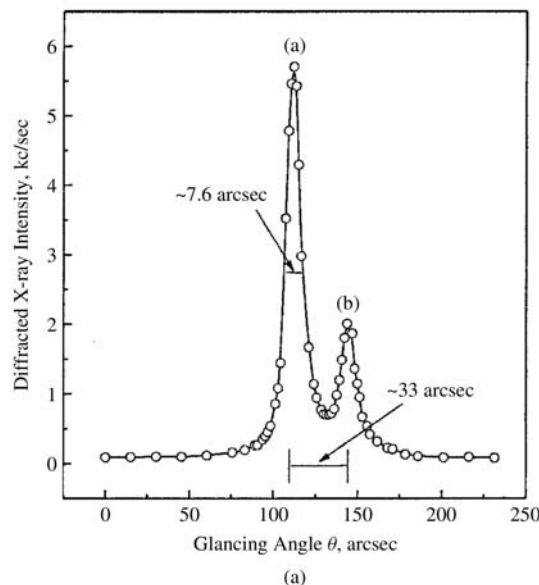


Figure 5.4 (a) A high-resolution X-ray diffraction curve of a bismuth germanate crystal showing a very low-angle boundary. A double-crystal X-ray diffractometer was used in (+, -) geometry with $\text{MoK}\alpha_1$ radiation, (b) A set of two traverse topographs recorded by orienting the bismuth germanate specimen of (a) on the two peaks. (Reprinted from Murthy *et al.*, *J. Cryst. Growth* **197/4** (1999) 865–873, copyright (1999) with permission from Elsevier Science.)

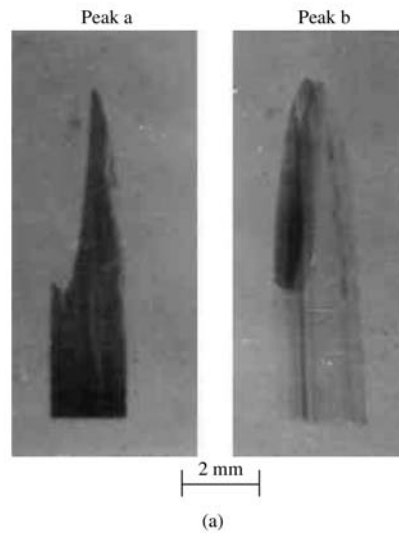
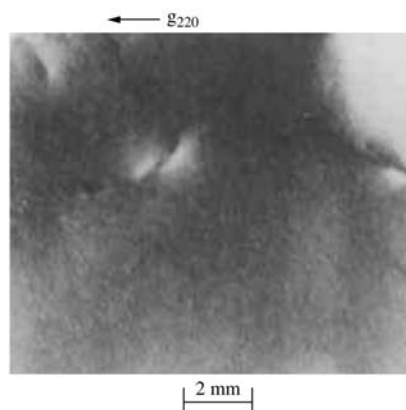
**Figure 5.4** (*continued*)

Figure 5.5 A high-resolution X-ray diffraction traverse topograph of a nearly perfect semi-insulating gallium arsenide crystal recorded in symmetrical Laue geometry and (+, −, +) setting of the diffractometer. Images of only three dislocations are seen. (Reprinted from Krishan Lal *et al.*, *J. Appl. Phys.* **69**(12) (1991) 8092–8095, copyright (1991) with permission from American Institute of Physics.)

the two sides of the very low-angle boundary are directly imaged in this manner. The intensity in these topographs is not uniformly distributed. The changes in contrast are due to deformations present in the subgrains.

We shall now consider an example of direct observation and characterization of dislocations. Figure 5.5 shows a traverse topograph of a nearly perfect gallium

arsenide crystal (Lal *et al.* 1990a). It is seen that the intensity of diffraction is nearly uniform in most parts of the topograph, except near the right-hand top showing a small misoriented region. Images of only three dislocations are prominently seen in an area of about 122 mm². The image of each dislocation is quite large (linear dimension of almost 2 mm). This means that the disturbance produced in regions located about a million atoms away from the dislocation core can be directly photographed. For detailed characterization regarding the nature of defect, traverse topographs are recorded with different diffraction vectors. The strain at the core of dislocations is not isotropic. Therefore, contrast changes with diffraction vector and the defects can be identified from observed variations in contrast (Lang 1958, 1970, Tanner 1976, Lal 1982, 1985). It is possible to determine the magnitude of Burgers vector from the intensity distribution in section topographs (Authier 1977). It may be mentioned that device-quality silicon crystals are expected to be free from dislocations, and in their topographs one observes nearly uniform intensity.

The absolute values of integrated X-ray intensities ρ are also a good measure of gross crystalline perfection. In high-resolution X-ray diffraction experiments, it is possible to make measurements of ρ with a low level of uncertainty. For ideally perfect crystals with moderate values of absorption coefficient μ , ρ is given by (James 1950):

$$\rho = \frac{8}{3\pi} N \lambda^2 |F| \frac{e^2}{mc^2} \frac{1 + |\cos 2\theta|}{2 \sin 2\theta} \quad (5.13)$$

Here N = number of unit cells per unit volume, λ = wavelength of the exploring X-ray beam, F = structure factor of the reflection under consideration, θ = glancing angle and e , m and c are well-known symbols. Integrated intensity expressions for ideally imperfect or mosaic crystals are well known (James 1950). A real crystal is expected to have its integrated intensity in the range lying between that for a perfect and an imperfect crystal. The experimentally measured values of ρ for nearly perfect silicon crystal lie close to that obtained from Equation (5.13) (Lal *et al.* 1990b, Ramanan *et al.* 1995).

Single crystals free from boundaries and dislocations can not be considered as ideally perfect. These may contain varying concentrations of point-defect aggregates and isolated point defects far in excess of those expected on the basis of thermodynamics. Point defects in excess of equilibrium concentrations, caused for instance by thermal treatment are generally clustered and form aggregates. Many of these aggregates are small dislocations loops on slip planes like {111} in silicon crystals.

The strain field produced by the clusters and isolated point defects is very small as compared to that produced by other defects. These can not produce sufficient contrast in X-ray diffraction topographs to be directly observable. However, these induce measurable changes in scattered intensity in the wings of the diffraction curves or produce appreciable scattering from the regions of reciprocal space surrounding a reciprocal lattice point. The intensity of such scattered X-rays is

diffusely distributed without any specular reflection. Therefore, it is known as diffuse X-ray scattering (DXS). Several theoretical formulations are available to compute intensity of scattering due to point defects and their clusters (Krivoglaz 1969, Trinkaus 1972, Dederichs 1973, Larson and Schmatz 1980, Lal 1989). The DXS intensity in reciprocal space in different directions with respect to the reciprocal lattice point under consideration gives important information about point defects and their clusters. It can be determined whether point defects are clustered and if so, one can obtain their size and shape by using model calculations. One particularly useful model that can be used for isolated point defects as well as point defect aggregates is that given by Dederichs (Dederichs 1973). According to this model the DXS intensity is given by:

$$S(\mathbf{R}^* + \mathbf{K}^*) = C_{cl} |F_{pT}|^2 \left| -4\pi \frac{A_{cl}}{V_c} \left[\frac{\mathbf{R}^* \cdot \mathbf{K}^*}{K^{*2}} \right] \left[\frac{\sin(K^* R_{cl})}{K^* R_{cl}} \right] - \frac{4\pi R_{cl}^3}{V_c} \left[\frac{\sin(K^* R_{cl}) - K^* R_{cl} \cos(K^* R_{cl})}{(K^* R_{cl})^3} \right] \right|^2 \quad (5.14)$$

Here, C_{cl} is the cluster density, $F_{p,T}$ is the structure factor corrected for polarization and temperature, V_c is the volume of the unit cell, R_{cl} = cluster radius, $A_{cl} = R_{cl}^2/R^*$, \mathbf{K}^* is a vector that joins the elemental volume of reciprocal space under investigation to the nearest reciprocal lattice point, and \mathbf{R}^* is the reciprocal lattice vector. It may be mentioned that phonons or elastic thermal waves also produce diffuse X-ray scattering. A series of systematic experiments performed in the author's laboratory established clearly that at or near room temperature, the contribution of defects to the observed DXS intensity is predominant (Lal *et al.* 1979, Lal 1989).

In recent times, the volume of reciprocal space being explored has been enhanced, particularly by employing high-brilliance synchrotron sources of X-rays. This technique is referred to as reciprocal lattice mapping. As an illustration, we shall consider here results of a recent study on characterization of point defects and their clusters in silicon crystals grown by Czchoralski (Cz) method and the floatzone (FZ) method. High-purity crystals characterized by high electrical resistivity of about 10 k Ω (Ramanan *et al.* 1995) were used as specimens. Figure 5.6 shows a set of DXS intensity versus K^* plots for the FZ and Cz crystals. It is seen that both curves have nearly the same slope of -2 at low values of K^* . At higher values, the slope increases to -4 in both the cases. It is known that isolated point defects give a slope of -2 in DXS intensity versus K^* plots (Huang scattering). The nature of point defects, whether vacancies or interstitials, is obtained from the observed anisotropy in the distribution of DXS intensity. The anisotropy for any value of K^* is defined as: $\text{anisotropy} = \text{DXS}I_{(\theta > \theta_B)} - \text{DXS}I_{(\theta < \theta_B)}$. A positive value of anisotropy indicates the presence of interstitial defects that extend the surrounding lattice. Vacancies, on the other hand, produce negative anisotropy in the DXS distribution. In the present set of experiments, it was found that the FZ crystals show negative anisotropy, and for the Cz crystals the anisotropy was positive. The presence of a region of slope

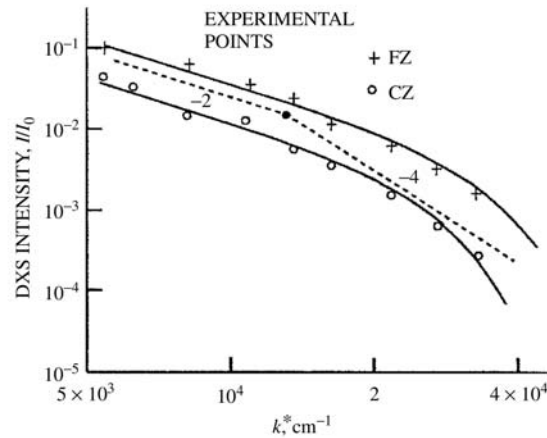


Figure 5.6 A set of log DXS intensity versus Log K^* plots for highly pure silicon crystals grown by the float zone and the Czochralski techniques. (Reprinted from Murthy *et al.*, *J. Cryst. Growth* **197/4** (1999) 865–873, copyright (1999) with permission from Elsevier Science.)

Table 5.1 Values of point defect cluster radius R_{cl} , cluster volume A_{cl} and number of defects per cluster N_{cl}

Specimen	Cluster radius μm	Cluster volume $A_{cl} \text{ cm}^3$	Number of defects per cluster N_{cl}	Nature of defects
Cz	0.8	2.02×10^{-16}	1.26×10^6	Interstitial
FZ	0.6	1.32×10^{-16}	8.3×10^5	Vacancy

–4 at higher values of K^* in Figure 5.6 (Stokes–Wilson) indicates the presence of clustered point defects. To analyze the experimental data, we have used Dederich’s model (Equation. (5.14)). The defect parameters obtained as a result of this analysis are given in Table 5.1. It is seen that sub-micrometer clusters are present in these crystals. The distribution of the DXS intensity is such that the clusters appear to be dislocation loops lying on (111) planes.

In a recent investigation, oxygen has been deliberately introduced in FZ crystals in a controlled manner. It has been observed that when the oxygen concentration approaches values generally observed in Cz crystals interstitial defects provide a dominant contribution to DXS even in FZ (Lal *et al.* 1999).

5.4 ACCURATE DETERMINATION OF CRYSTALLOGRAPHIC ORIENTATION

For all main applications of semiconductor crystals, it is necessary to restrict the orientation of their visible surfaces with respect to the nearest crystallographic

planes to a small fraction of a degree of arc. Also, most wafers have one or two flats or straight edges ground on them. Their orientation is also well specified. The main techniques to determine crystallographic orientations of crystal surfaces and straight edges are (a) optical examination of wafer surfaces after chemical etching (ASTM 1981a); (b) X-ray Laue method (Christiansen *et al.* 1975 and ASTM 1981b); (c) conventional X-ray diffractometry technique (Cullity 1956, ASTM 1981a, Kholodnyi *et al.* 1984); and (d) high-resolution X-ray diffraction techniques (Lal and Goswami 1988, Lal *et al.* 1990c). In this chapter, we shall briefly describe the recently developed high-resolution X-ray diffraction techniques that give unprecedented accuracy and convenience of measurement.

We have utilized very narrow diffraction curves, obtained with nearly perfect crystals on multocrystal X-ray diffractometers, for measurement of crystallographic orientation (Lal *et al.* 1990c). Let us consider a wafer whose surface normal N_s makes an angle α with the normal to the nearest crystallographic set of planes N_p as shown in Figure 5.7. If the crystal is rotated azimuthally around the surface normal N_s , the normal to the lattice planes N_p will rotate on a conical surface as shown in Figure 5.7. If this crystal is oriented for diffraction on a multocrystal X-ray diffractometer, its peak position will depend upon its azimuthal orientation. The glancing angle θ has to be readjusted by say $\Delta\theta$ to bring it back on the peak as the azimuthal orientation is changed. If these rotations for different azimuthal positions are plotted as a function of azimuthal orientation of the specimen one would get a sinusoidal curve, from which one can get the value of α that defines the orientation of the specimen. In practice, this is realized by a device (Lal *et al.* 1990c) that provides azimuthal rotations to the specimen. In general, the axis of rotation of the device and the normal to its flat surface on which the specimen crystal is mounted are not exactly collinear. There is a finite

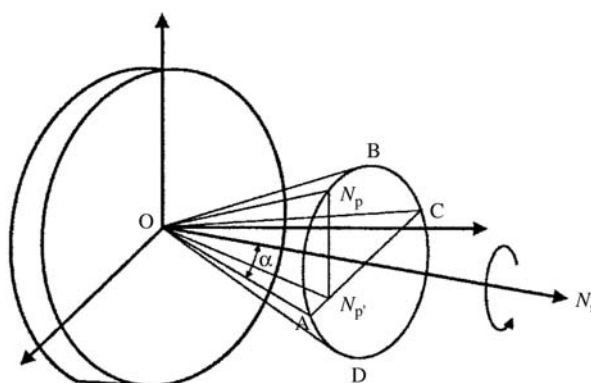


Figure 5.7 A schematic diagram showing movement of normal to the diffracting planes N_p on a conical surface as the crystal is rotated azimuthally around surface normal N_s . (Reprinted from Krishan Lal *et al.*, *Meas. Sci. Technol.* (1990) 793–800, copyright (1990) with permission of Institute of Physics.)

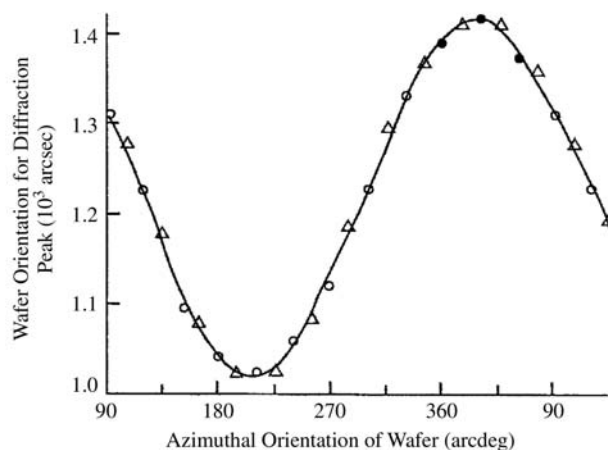


Figure 5.9 A plot of the angle of reorientation of the specimen at the diffraction peak as a function of the azimuthal orientation of a 100-mm diameter (100) silicon wafer. O represents experimental points; experimental points chosen for calculation of A , B , P and Q ; and Δ are the theoretically computed points. (Reprinted from Krishan Lal *et al.*, *Meas. Sci. Technol.* (1990) 793–800, copyright (1990) with permission of Institute of Physics.)

By giving different angular increments ΔP_1 , ΔP_2 , etc., one can get a set of equations whose solution yields values of A , B , P and Q (Lal *et al.* 1990c) and therefore, the orientation is determined.

Figure 5.9 shows a typical plot of the angle of reorientations of a 100 mm diameter silicon single-crystal specimen to bring it at diffraction peak as a function of azimuthal orientations. In this case, the angle between the (100) planes and the surface was determined as 20.26 arcmin. For the device the value of B was found to be 3.36 arcmin. The value of P was zero. Once the values of A , B , P and Q were known values of RN_p were calculated at different azimuthal orientations of the wafer with respect to the device. These are shown as triangles on the curve (Figure 5.9). The fit between the experimental curve and the calculated points is good. The experiments performed on different wafers and on different diffractometers confirmed that the overall uncertainty is less than ± 6 arcsec.

For determination of orientation of flats or straight edges on semiconductor wafers, one can use X-ray Laue techniques (Cullity 1956, ASTM 1987), diffractometric methods (Bond 1976, ASTM 1987) and a recently developed technique based on X-ray diffraction topography (Lal and Goswami 1988). The last technique is very convenient and is a significant improvement over all the other known methods. The specimen crystal is oriented for diffraction on an X-ray diffraction topography set up. Figure 5.10 shows a schematic diagram of the basic principle. A traverse topograph is recorded covering the straight edge at one extreme and a small adjoining region. After the exposure, the specimen, together with the film, is translated by a short distance of about 1 mm or so and a stationary topograph

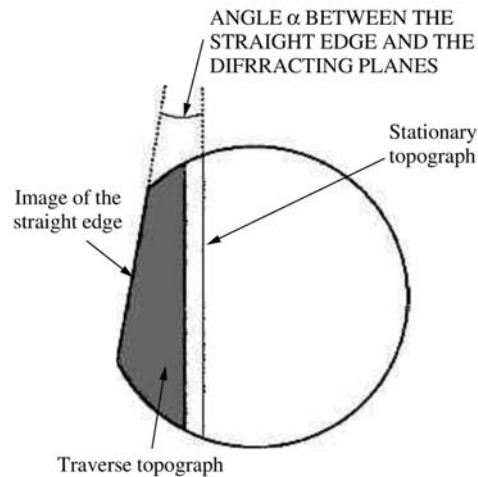


Figure 5.10 A schematic diagram illustrating essential features of the x-ray diffraction topographic method for determining orientations of the straight edges on semiconductor wafers. (Reprinted from Krishan Lal and Niranjana N. Goswami, *J. Rev. Sci. Instrum.* **59**(8) (1998) 1409–1411, copyright (1998) with permission of American Institute of Physics.)

is recorded. The traverse topograph has the image of the straight edge at one extreme. The stationary topograph is the projection of the lattice planes that are nominally parallel to the straight edge. One can conveniently measure the angle between the stationary topograph and the image of the straight edge that determines the orientation. The uncertainty is ± 3 arcmin. It may be mentioned that it is not necessary to use ground, lapped and polished wafers. Raw cut wafers can be used and corrective measures can be taken if necessary.

5.5 MEASUREMENT OF CURVATURE OR BENDING OF SINGLE-CRYSTAL WAFERS

Semiconductor single-crystal wafers used for fabrication of microelectronic devices have to conform to strict specifications in terms of warpage or bending. The bending is restricted to about $30\text{ }\mu\text{m}$ for large size wafers. The site flatness is restricted to $\sim 0.2\text{ }\mu\text{m}$ only for a site area of $26\text{ mm} \times 26\text{ mm}$ (Huff and Goodall 1996). The bending measurements are also required for determining the biaxial stress in thin-film single-crystal substrates systems. Curvature of wafers can be measured optically as well as by using high-resolution X-ray diffraction methods (Segmuller *et al.* 1989, Lal *et al.* 1990a). Figure 5.11 shows a schematic diagram of the bending of a typical semiconductor wafer (with a thin film). If the wafer is not flat, the central region (B) will not touch the flat surface and would

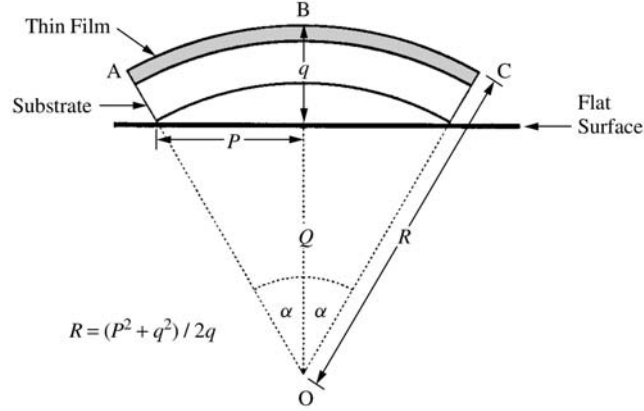


Figure 5.11 A schematic diagram showing measurement of curvature of a wafer by optical techniques.

be above it by a distance q . The radius of curvature R is related to q through:

$$R = (P^2 + q^2)/2q \quad \text{or} \quad R \cong P^2/2q \quad (5.17)$$

As a typical example, a wafer having diameter of 200 mm and with $q = 30 \mu\text{m}$, the value of R will be 166.6 m. A decrease of $3 \mu\text{m}$ in q would mean an increase in R by ~ 20 m. Similarly, for a site flatness of $0.17 \mu\text{m}$ over a site size of $26 \times 26 \text{ mm}^2$ the value of R is ~ 1 km.

In the high-resolution X-ray diffraction technique one utilizes the sharpness of diffraction curves for accurate measurement of bending or radius of curvature. In a bent crystal, the normal to lattice planes that are perpendicular to the crystal surface shows orientational change as one moves from one end of the crystal to the other, as shown in Figure 5.12. Let us suppose that the crystal is oriented for diffraction from one edge, say the right-hand edge on a multocrystal X-ray diffractometer. The specimen is moved across the X-ray beam in a stepwise manner and at each position the orientation of the diffraction vector \mathbf{g} is determined from the rotation needed to bring the specimen back on the diffraction peak. If orientation of \mathbf{g} is plotted as a function of linear position of the specimen across the X-ray beam, one would get a linear plot whose slope gives the value of the radius of curvature. If the crystal is absolutely flat, the slope would be zero and the curve would be a horizontal straight line. For crystals bent in a convex shape, the plot will be a straight line with positive slope whereas for concave-shaped crystals, the slope would be negative. The slope of the line gives the value of the radius of curvature. In this case, even when there is a 2 arcsec deviation in the orientation of diffraction vector \mathbf{g} at the two extremes of the wafer, one can conveniently determine the radius of curvature. This essentially means that a radius of curvature of 20 km for a wafer of diameter of 200 mm can be measured.

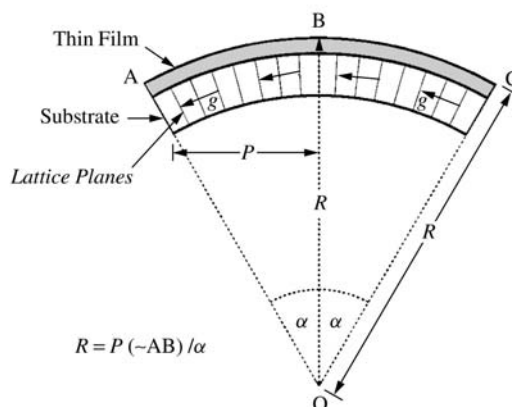


Figure 5.12 A schematic diagram showing measurement of curvature of a wafer by the high-resolution X-ray diffraction method.

Also, the resolution of measurement is high (less than 1 m for $R = 200$ m). For a site flatness of $0.17 \mu\text{m}$ over a site size of $26 \text{ mm} \times 26 \text{ mm}$ the difference in orientation of \mathbf{g} at two extremes will be ~ 5 arcsec, which can be measured conveniently and with a low level of uncertainty. This technique is also being used for determination of biaxial stress in a variety of thin-film single-crystal substrate systems (Segmuller *et al.* 1989, Lal *et al.* 1990a, Goswami *et al.* 1994, Lal *et al.* 1996a).

5.6 CHARACTERIZATION OF PROCESS-INDUCED DEFECTS IN SEMICONDUCTORS: IMPLANTATION-INDUCED DAMAGE

Semiconductor crystals undergo various processing steps such as deposition of thin films of different types of materials under different temperature and pressure conditions, chemical and heat treatments, and introduction of impurities by diffusion or implantation. These processing steps produce changes in the real structure of the crystal. High-resolution X-ray diffraction techniques can be used for characterization of processing-induced defects. Here we shall consider as an example BF_2^+ implantation in silicon single crystals (Lal *et al.* 1991c, 1996c). BF_2^+ implantation is widely used to produce shallow submicrometer $\text{p}^+\text{-n}$ junctions in silicon single crystals. BF_2^+ ion energies were 90 and 135 keV, with the fluence being kept constant at $1 \times 10^{15} \text{ cm}^{-2}$. It was observed that implantation produced a very small broadening of the diffraction curves accompanied by a small but measurable decrease in the peak intensity. However, changes in DXS intensity distribution were significant.

Figure 5.13 shows a set of DXS intensity versus K^* plots for an unimplanted wafer and for specimens implanted with BF_2^+ ions of energy 90 keV and 135 keV.

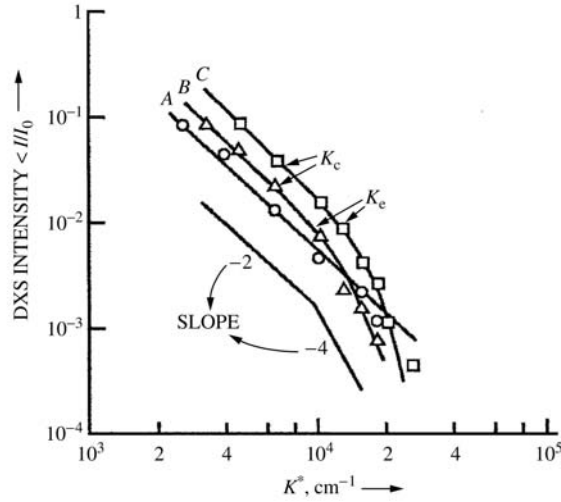


Figure 5.13 A set of DXS intensity versus K^* plots for unimplanted silicon wafer (curve A) and wafers implanted with BF_2^+ ions of energies 90 keV (curve B) and 135 keV (curve C). (Reprinted from Krishan Lal *et al.*, *J. Appl. Phys.* **69**(12) (1991) 8092–8095, copyright (1991) with permission from American Institute of Physics.)

It is seen that the DXS intensity for the unimplanted crystal varies as K^{*-2} at practically all values of K^* except in the highest-value range showing presence of isolated point defects (Huang scattering). Diffuse scattering from clustered point defects exhibits features that are distinct from the scattering by isolated point defects. At large values of K^* the scattered intensity varies as K^{*-4} or even faster than K^{*-4} . It is similar to the approximation given by Stokes and Wilson (1944) for scattering by dislocations. It is customary to refer to it as Stokes–Wilson scattering (see, e.g. Dederichs (1973)). We see from Figure 5.13 that at large values of K^* a Stokes–Wilson region is indicated. Anisotropy for this as well as the other plots (curves B and C) was positive, typical of Czochralski grown crystals (Figure 5.6). Due to implantation the overall DXS intensity increases indicating disordering of the crystal lattice. The Stokes–Wilson region (slope of -4) is quite prominent in implanted crystals showing clustering of point defects. The phenomenological model of Equation (5.14) has been employed to analyze the experimental data and the following values of R_{cl} and A_{cl} were obtained:

$$\begin{array}{llll} \text{BF}_2^+ \text{ energy} & 90 \text{ keV} & R_{\text{cl}} = 1.47 \times 10^{-4} \text{ cm} & A_{\text{cl}} = 2.92 \times 10^{-16} \text{ cm}^3 \\ \text{BF}_2^+ \text{ energy} & 135 \text{ keV} & R_{\text{cl}} = 1.29 \times 10^{-4} \text{ cm} & A_{\text{cl}} = 2.27 \times 10^{-16} \text{ cm}^3 \end{array}$$

The values of N_{cl} (number of defects per cluster) have been determined as 1.46×10^7 (90 keV) and 1.37×10^7 (135 keV). This investigation has shown that all the implanted impurity has not been distributed atomically and a

part of it has been segregated. Agglomeration of point defects had also been observed in BF_2^+ -implanted silicon crystals by cross-sectional transmission electron microscopy (Queirolo *et al.* 1987). There is a good correlation between the two investigations.

We have also employed high-resolution X-ray diffractometry and absolute X-ray integrated intensity measurements to investigate top layers of BF_2^+ -implanted silicon crystals. It is generally considered that at energies of ~ 90 keV and fluence level of $2 \times 10^{-15} \text{ cm}^{-2}$ the top layer becomes amorphous (Wu and Chen 1985, Viridi *et al.* 1992). Precise diffractometry and absolute X-ray integrated intensity measurements have shown that the top layer is not amorphous (Lal *et al.* 1996c). It is disordered but crystalline in nature.

5.7 CONCLUSIONS

In this chapter we have described the basic principles of high-resolution X-ray diffraction and the essential features of a five-crystal X-ray diffractometer developed in the author's laboratory. A number of illustrative examples have been covered: characterization of defects in device-quality crystals; determination of crystallographic orientation; measurement of bending of blank wafers; and characterization of implantation-induced defects in silicon crystals. The range of techniques available is such that these can be suitably combined to meet any challenge concerned with characterization of crystal defects. Of course, there are limitations of spatial resolution in the case of X-rays. Nevertheless, the advantages of nondestructive characterization of large volumes and quantitative information with high sensitivity are remarkable.

5.7.1 ACKNOWLEDGEMENT

The author has benefited by collaborating with a large number of colleagues in his laboratory and other laboratories in India and abroad. Close collaboration with Drs Niranjana Goswami, G. Bhagavannarayana, (late) V. Kumar, S. K. Halder, R. V. A. Murthy, R. R. Ramanan, and A. Chaubey is acknowledged with pleasure. It has been a privilege and pleasure to have long in-depth discussions with Dr. A. R. Verma. Partial support received under an Indo-US project an Indo-Russian ILTP project and an Indo-German project is gratefully acknowledged.

REFERENCES

- Alexander S., Hellemans L., Marti O., Schneir J., Ellings V., Longmire M. and Gurley G. (1989) *J. Appl. Phys.* **65**, 164.
- American Society for Testing and Materials (1981a) *Annual Book of ASTM Standards Part 43 F26-27*, 185.

- American Society for Testing and Materials (1981b) *Annual Book of ASTM Standards Part 11* **E82-63**, 104.
- American Society for Testing and Materials (1987) *Annual Book of ASTM Standards* **F847-87**, 744.
- Authier A. (1977) *Topics in Applied Physics* edited by Queisser H. J. Springer-Verlag, New York, p. 145.
- Barrett C. S. and Massalski T. B. (1968) *The Structure of Metals*, McGraw-Hill, New York, Asian Edition: Eurasia, New Delhi.
- Batterman B. W. and Cole H. (1964) *Rev. Mod. Phys.* **36**, 681.
- Binnig G., Rohrer H., Gerber C. and Weibel E. (1982) *Phys. Rev. Lett.* **49**, 57.
- Binnig G., Quate C. F. and Gerber C. (1986) *Phys. Rev. Lett.* **12**, 930.
- Bond W. L. (1976) *Crystal Technology*, Wiley, New York, p. 304.
- Bonse U. and Hart M. (1965) *Appl. Phys. Lett.* **7**, 238.
- Bullis W. M. and Huff H. R. (1993) *ULSI Science and Technology* edited by G. K. Geller, E. Middleworth and K. Hoh, The Electrochemical Soc, Pennington, USA, p. 103.
- Claeys C. and Deferm, L. (1996) *Solid State Phenom.* **47-48**, 1.
- Christiansen G., Gerward L. and Alstrup I. (1975) *Acta. Cryst.* **A31**, 142.
- Cullity B. D. (1956) *Elements of X-ray Diffraction*, Addison-Wesley, Mass.
- Dederichs P. H. (1973) *J. Phys. F.* **3**, 471.
- Goswami S. N. N., Lal Krishan, Vogt A. and Hartnagel H. L. (1999), to be published.
- Goswami S. N. N., Lal Krishan, Wurfl J. and Hartnagel H. L. (1994) *Physics of Semiconductor Devices*, edited by Lal Krishan, Narosa Publishers, New Delhi, 337.
- Guinier A. (1952) *X-ray Crystallographic Technology*, Hilger and Watts, London.
- Hansma P. K. and Tersoff J. (1987) *J. Appl. Phys.* **61**, R1.
- Heydenreich J. (1982) *Synthesis, Crystal Growth and Characterization* edited by Lal Krishan, North-Holland, Amsterdam, p. 215.
- Huff H. R. and Goodall R. K. (1996) *Solid State Phenom.* **47-48**, 65.
- James R. W. (1950) *The Optical Principles of the Diffraction of X-rays*, G. Bell & Sons, London.
- Kato N. (1975) *Crystal Growth and Characterization* edited by Ueda R. and Mullin J. B., North Holland, Amsterdam p. 279.
- Kato N. (1992) *J. Acta. Cryst.* **A48**, 834.
- Kholodnyi L. P., Terent'ev G. I. and Krol' I. M. (1984) *Meas. Technol.* **27**, 266.
- Krivoglaz M. A. (1969) *Theory of X-ray and Thermal Neutron Scattering by Real Crystals*, Plenum Press New York.
- Kumar V., Lal Krishan, Seetharaman and Gupta S. C. (1999) to be published.
- Lal Krishan and Singh B. P. (1977) *Solid State Commun.* **22**, 71.
- Lal Krishan, Singh B. P. and Verma A. R. (1979) *Acta. Crystallogr.* **A35**, 286.
- Lal Krishan (1982) *Synthesis, Crystal Growth and Characterization* edited by Lal Krishan, North-Holland, Amsterdam p. 215.
- Lal Krishan and Thoma P. (1983) *Phys. Stat. Sol. (a)* **80**, 491.
- Lal Krishan (1985) *Advanced Techniques for Microstructural Characterization* edited by Krishnan R., Anantharaman T. R., Pande C. S. and Arora O. P., Trans Tech Pub., Aedermansdorf, Switzerland, p. 143.
- Lal Krishan and Goswami S. N. N. (1987) *J. Mater. Sci. Eng.* **85**, 147.
- Lal Krishan and Goswami S. N. N. (1988) *Rev. Sci. Instrum.* **59**, 1409.
- Lal Krishan and Bhagavannarayana G. (1989) *J. Appl. Cryst.* **22**, 209.
- Lal Krishan (1989) *Prog. Cryst. Growth Charact.* **18**, 227.

- Lal Krishan, Goswami S. N. N., Wurfl J. and Hartnagel H. L. (1990a) *J. Appl. Phys.* **67**, 4105
- Lal Krishan, Goswami S. N. N. and Verma A. R. (1990b) *Pramana. J. Phys.* **34**, 506.
- Lal Krishan, Bhagavannarayana G., Kumar Vijay and Halder S. K. (1990c) *Meas. Sci. Technol.* **1**, 793.
- Lal Krishan (1991a) *Advances in Crystallography and Crystal Growth* edited by Lal Krishan, Indian National Science Academy, New Delhi p. 125.
- Lal Krishan (1991b) *Crystalline Materials: Growth and Characterization*, edited by Rodriguez-Clemente R. and Paorici C., Trans Tech Pub, Zurich, p. 205.
- Lal Krishan, Bhagavannarayana G and Virdi G. S. (1991c) *J. Appl. Phys.* **69**, 8092.
- Lal Krishan (1993) *Bull. Mater. Sci.* **16**, 617
- Lal Krishan, Mitra Reshmi, Srinivas G. and Vankar V. D. (1996a) *J. Appl. Crystallogr.* **29**, 2.
- Lal Krishan, Goswami S. N. N. and Kuznetsov G. F. (1996b) *Semiconductor Devices* edited by Lal Krishan, Narosa Publishers, New Delhi, p. 113.
- Lal Krishan, Bhagavannarayana G. and Virdi G. S. (1996c) *Solid State Phenom.* **47–48**, 377.
- Lal Krishan (1998), *Proc. Indian National Sci. Acad.* **64**, 609.
- Lal Krishan, Ramanan R. R., Bhagavannarayana G. (2000) *J. Appl. Crystallogr.* **33**, 20.
- Lang A. R. (1958) *J. Appl. Phys.* **29**, 597 and (1970) *Modern Diffraction and Imaging Techniques in Materials Science* edited by Amelinckx S., Gevers R., Remant G. and Landyut L., North-Holland, Amsterdam 407.
- Larson B. L. and Schmatz W. (1980) *Phys. Stat. Sol. (b)* **99**, 267.
- Laudise R. A. (1972) *Analytical Chemistry: Key to Progress in National Problems*, edited by Meinke W. and Taylor J. K. NBS Special Publ 351, NBS, Washington p. 19.
- Laue M. Von (1960) *Roentgenstrahlininterferenzen*, Acad Verlagsgesellschaft, Frankfurt.
- Mathews J. W., Klokholm E., Sadagopan V., Plasket T. S. and Mendel E. (1973) *Acta. Met.* **21**, 203.
- Murthy R. V A., Ravi Kumar M., Choubey A. and Lal Krishan., Kharchanko L., Shleguel , V. and Guerasimov, (1999) *J. Cryst. Growth* **197**, 865 .
- Pinsker Z. G. (1978) *Dynamical Scattering of X-rays in Crystals*, Springer-Verlag, Berlin.
- Queirolo G., Capraara P., Meda L., Guareschi C., Andrele M., Ottaviani G. and Armigliato A. (1987) *J. Electrochem. Soc. Solid State Sci. Technol.* **134**, 2905.
- Ramanan R. R., Bhagavannarayana G. and Lal Krishan (1995) *J. Cryst. Growth* **156**, 377.
- Sangwal K. S. (1987) *Etching of Crystals: Theory, Experiment and Application* (Series editors Amelinckx S. and Nihocal H.), North Holland, Amsterdam.
- Schneider Jochen R. and Bouchard Roland, (1992) *Acta. Crystallogr* **A48**, 804.
- Segmuller A., Noyan I. C. and Speriosu V. S. (1989) *Prog. Cryst. Growth Charact.* **18**, 21.
- Spence J. (1984) *Experimental High Resolution Electron Microscopy* Clarendon Press, Oxford.
- Stokes A. R. and Wilson A. J C. (1944) *Proc. Phys. Soc.* **56**, 174.
- Trinkaus H. (1972) *Phys. Stat. Sol. (b)* **51**, 307.
- Tanner B. K. (1976) *X-ray Diffraction Topography*, Pergamon Press, Oxford.
- Virdi G. S., Rauthan C. M S., Pathak B. C., Khokle W. S., Gupta S. K. and Lal Krishan (1992) *Solid State Electron.* **35**, 535.
- Wu I. W. and Chen (1985) *J. Appl. Phys.* **58**, 3032.
- Zachariasen W. H. (1945) *Theory of X-ray Diffraction in Crystals*, Wiley, New York.

6 Computational Simulations of the Growth of Crystals from Liquids

ANDREW YECKEL and JEFFREY J. DERBY

Department of Chemical Engineering and Materials Science, Army HPC Research Center, and Minnesota Supercomputing Institute, University of Minnesota, Minneapolis, MN 55455-0132, USA

6.1 INTRODUCTION

In this chapter we review the current status and role of computer modeling of hydrodynamics and associated transport processes in bulk crystal growth. Hydrodynamics plays a key role in virtually all bulk crystal-growth systems, having a critical effect on both heat and mass transport. Indeed, hydrodynamics often is inextricably coupled to heat and mass transport, due to thermal and solutal buoyancy effects. Hydrodynamics strongly affects mixing in many systems, thereby affecting growth rates, interface shape, chemical composition of the crystal, and defect formation. Many physico-chemical phenomena, occurring on length scales ranging from atomistic to system scale, are involved in crystal growth. Nevertheless, it is fair to say that the future of crystal-growth modeling depends heavily on progress in hydrodynamics modeling. There already exists a large and rich body of literature on this topic, but much work remains to be done.

The scope of this chapter is limited to continuum representations of heat, mass, and momentum transport in melt and solution growth systems. Atomistic-scale phenomena are not considered, nor is the connection between macroscale phenomena and crystal properties. Nucleation phenomena, and other microscale phenomena, such as morphological instabilities and dendrite formation, also are excluded. All of these are active areas of research in crystal-growth modeling, however, space restrictions do not permit their inclusion. Nor is this chapter meant to serve as a 'how to' manual for hydrodynamic simulation, a subject that would require a lengthy book.

The next section reviews the current capabilities and limitations of mathematical methods used to model hydrodynamics in crystal-growth systems. A brief discussion is given on the subject of commercial software, both general-purpose software for hydrodynamic simulation and software specialized to the needs of crystal-growth researchers. In Section 6.4 we present examples from

our research that illustrate some of the capabilities and limitations of current methods. The first example is a one-dimensional model of multicomponent diffusion during diffusion-limited growth of cadmium zinc telluride (CZT), a ternary II-VI alloy. The model predicts the existence of a retrograde diffusion layer, in which zinc diffuses against its concentration gradient. The results illustrate the need for more research on fundamental model formulation. The second example is an axisymmetric model of the accelerated crucible rotation technique (ACRT), applied to vertical Bridgman growth of CZT. ACRT introduces a hydrodynamic time scale that is much shorter than other transport-related time scales inherent in vertical Bridgman growth, making this a two-dimensional problem that strains even today's largest computers. The last example is a three-dimensional bulk flow model of Czochralski (Cz) growth of bismuth silicon oxide, with crystal rotation. The simulations reveal that two distinct three-dimensional instabilities can occur simultaneously in this system. One instability leads to the formation of baroclinic waves deep within the melt, and the other causes the appearance of rotational spokes at the surface, a consequence of a Rayleigh thermal instability. The results demonstrate that the choice between using a two-dimensional or three-dimensional model can be a difficult one, with enormous consequences.

6.2 TRANSPORT MODELING IN BULK CRYSTAL GROWTH

6.2.1 GOVERNING EQUATIONS

Any attempt to analyze continuum transport phenomena in crystal growth begins with formulating a set of governing equations, which in general is based on well-known principles of conservation of mass, momentum, and energy. Here we provide a brief review of these equations. A general discussion of the equations as applied to crystal-growth systems can be found in Derby *et al.* (1998). A more detailed though somewhat dated discussion of crystal growth modeling is the excellent review article by Brown (1988). For a good general textbook on the subject of continuum transport and conservation principles, applied to physico-chemical systems, we refer the interested reader to Bird *et al.* (1960).

It is important to note that the equations presented here have been derived subject to a number of approximations, not all of which are discussed in the text. Furthermore, in certain special cases not all of these approximations will apply, in which case the equations may take on a somewhat different form. Nevertheless, the equations presented here are applicable to most bulk crystal-growth systems.

Conservation of mass, momentum, and energy, subject to the continuum approximation, are in general described by a set of partial differential equations. Conservation of momentum and continuity are given by the Navier–Stokes

equations for an incompressible, Newtonian fluid:

$$\rho_o \left(\frac{\partial \mathbf{v}}{\partial t} + \mathbf{v} \cdot \nabla \mathbf{v} \right) = -\nabla p + \mu \nabla^2 \mathbf{v} + \rho_o \mathbf{g} [1 - \beta(T - T_o) + \beta_s(c - c_o)] + \mathbf{F}(\mathbf{v}, \mathbf{x}, t) \quad (6.1)$$

$$\nabla \cdot \mathbf{v} = 0 \quad (6.2)$$

where \mathbf{v} is the velocity vector, p is pressure, T is temperature, c is molar concentration, t is time, μ is viscosity, \mathbf{g} is the gravitational vector, and ρ_o is the density at a reference temperature T_o and reference concentration c_o . Density is treated as a constant, except in the gravitational body force term, where the effects of temperature and concentration variations are incorporated, using thermal and species expansivity coefficients β and β_s ; this is the Boussinesq approximation. The term $\mathbf{F}(\mathbf{v}, \mathbf{x}, t)$ accounts for any additional body forces that may act on the fluid volume, e.g. the inductive force due to motion of a conducting liquid in a magnetic field or apparent forces that arise in a noninertial reference frame, such as the Coriolis force.

Conservation of energy is given by

$$\rho_o C_p \left(\frac{\partial T}{\partial t} + \mathbf{v} \cdot \nabla T \right) = \kappa \nabla^2 T \quad (6.3)$$

where C_p is the heat capacity and κ is the thermal conductivity of the material. Whereas Equations (6.1) and (6.2) apply only to liquid or gas phases, Equation (6.3) applies to solid phases as well, within which $\mathbf{v} = \mathbf{V}_T$, the translation velocity relative to the reference frame.

Conservation of mass is given by

$$\frac{\partial c}{\partial t} + \mathbf{v} \cdot \nabla c = \mathcal{D} \nabla^2 c \quad (6.4)$$

where c is the mass density and \mathcal{D} is the diffusion coefficient of the species. As with Equation (6.3), Equation (6.4) applies in all phases, though species transport is often neglected in solid phases in which the diffusivity is very small. For problems in solution growth it is usually convenient to substitute supersaturation, $\sigma \equiv \frac{c - c_s}{c_s}$, for concentration, since supersaturation is the driving force for crystallization (c_s is the saturation concentration). It is important to note that Equation (6.4) implies either that the species is dilute, or that the density of the liquid is nearly constant. In crystal growth from nondilute solutions it is possible for the density to vary considerably over the duration of growth, but the density change with time is typically so slow relative to mass transfer processes that Equation (6.4) remains accurate. Equation (6.4) may also be written for

several species, provided each species is sufficiently dilute that diffusion occurs as a pseudo-binary process (the case of nondilute diffusion in a multicomponent system is discussed in the next section).

Except for the Boussinesq approximation, it has been assumed that all physical properties in Equations (6.1)–(6.4) are constant. It is straightforward to include the effect of temperature and concentration dependent properties, however, provided data are available.

6.2.2 BOUNDARY CONDITIONS

In order to apply Equations (6.1)–(6.4) to real systems, information must be provided about the velocity, temperature, and concentration at all boundaries. Because of the wide variety and complexity of crystal-growth systems, it is not possible to provide a comprehensive list of boundary conditions applicable to these systems, but we briefly mention here some of the most common ones.

Most often, velocity boundary conditions consist of no-slip at solid surfaces:

$$\mathbf{v} = \mathbf{U}_s \quad (6.5)$$

where \mathbf{U}_s is the velocity of the solid surface (which often is zero). At liquid/gas interfaces it is usually assumed that the gas exerts no force on the liquid, in which case a no-stress condition is imposed:

$$\mathbf{n} \cdot (-p\mathbf{I} + \mu(\nabla\mathbf{v} + (\nabla\mathbf{v})^T)) = 0 \quad (6.6)$$

where \mathbf{n} is the unit vector normal to the interface, and \mathbf{I} is the identity tensor. However, Equation (6.6) may be inadequate to describe a system in which temperature or concentration varies along the interface. Such variations result in gradients of surface tension which, in turn, produce a net surface traction and drive fluid motion known as Marangoni flows.

Typically, energy boundary conditions include the specification that the temperature field is continuous, and heat fluxes balance, across all material interfaces. An exception occurs at interfaces at which a phase change occurs, where the energy balance must account for the latent heat of fusion:

$$(-\kappa_l \nabla T|_l + \kappa_s \nabla T|_s) \cdot \mathbf{n}_{sl} = \rho_s \Delta H_f \frac{\partial \mathbf{x}}{\partial t} \cdot \mathbf{n}_{sl} \quad (6.7)$$

where $\partial \mathbf{x} / \partial t$ is the velocity of the solid/liquid interface, ΔH_f is the latent heat of fusion, \mathbf{n}_{sl} is a unit vector normal to the solid/liquid interface, oriented towards the liquid, and the subscripts l and s refer to the liquid and solid sides of the interface.

Perhaps the most difficult area to generalize regarding boundary conditions is the specification of thermal conditions connecting the domain of interest to the

environment. For melt-growth models, these conditions are meant to represent the influence of the furnace, which can strongly affect the temperature field in the liquid and crystal. One approach is to account for furnace heating using simple approximations for convective and radiative transport in terms of a specified furnace temperature profile T_f :

$$-\kappa \mathbf{n}_b \cdot \nabla T = h(T - T_f) + \sigma \epsilon (T^4 - T_f^4) \quad (6.8)$$

where h is a heat transfer coefficient, ϵ is the emissivity, and σ is the Stefan–Boltzmann constant. There are several potential pitfalls to this approach, however. The heat transfer coefficient must account for all convective effects external to the domain, which may require reducing a gas flow through a furnace to a single empirical parameter. Likewise, Equation (6.8) implies that the radiation view factor equals unity everywhere, an unrealistic approximation in many high-temperature growth systems (Siegel and Howell, 1993; Kuppurao and Derby, 1993). Furthermore, transport of energy via internal radiation may be important in high-temperature crystal-growth systems that possess some transparency to infrared radiation (O’Hara *et al.*, 1968; Brandon and Derby 1992), further complicating the situation. Lastly, information is needed regarding T_f , which may require costly experiments or exhaustive furnace heat transfer modeling effort. Nevertheless, the simple form of Equation (6.8) has proved adequate to elucidate key transport phenomena in many systems.

Concentration boundary conditions require that mass fluxes balance across all material interfaces, but unlike temperature, concentration need not be continuous across interfaces. Instead, equilibrium partitioning occurs, according to

$$c_s = k c_l \quad (6.9)$$

where k is the partition coefficient. The solute balance at the interface is given by

$$(-\mathcal{D}_l \nabla c|_l + \mathcal{D}_s \nabla c|_s) \cdot \mathbf{n}_{sl} = -(k - 1) c_l \frac{\partial \mathbf{x}}{\partial t} \cdot \mathbf{n}_{sl} \quad (6.10)$$

These conditions, coupled with diffusion and convection near the interface, have a profound effect on solute segregation in crystal-growth systems.

To complete the specification of governing equations requires a constraint that determines the location of the liquid/crystal interface. Here we distinguish between melt and solution growth systems. In melt-growth systems, the position of the interface is located at the melting-point isotherm:

$$T(r, z, t) = T_m \quad (6.11)$$

This condition neglects the effect of curvature on the free energy of the interface, which is negligible except when interface curvature occurs over sufficiently small scales, such as occurs during dendritic growth. This condition implies that

the kinetics of crystallization are infinitely fast. In solution-growth systems, the location of the interface is controlled by kinetic factors and can be determined only from the initial condition and knowledge of the local interface velocity during growth. In the simplest case, growth from a single solute, the local interface velocity is related to the flux of solute to the interface:

$$\rho_s \frac{\partial \mathbf{x}}{\partial t} = -\mathcal{D}_1 \mathbf{n} \cdot \nabla c|_I = \mathcal{R}(c_1, T) \quad (6.12)$$

where ρ_s is the crystal density and $\mathcal{R}(c_1, T)$ represents surface growth kinetics.

Before we close this section, we note that theoreticians often rescale governing equations prior to analysis, yielding a set of nondimensional equations. In the course of rescaling, various dimensionless groups are introduced that incorporate the effects of geometric and physical parameters. There are several benefits to this rescaling. First, the introduction of dimensionless groups aids the theoretician to assess the magnitude, and therefore importance, of various driving forces that cause flow and transport to occur. Secondly, rescaling often eliminates or minimizes numerical problems that arise when using finite-precision computers to solve the governing equations. Thirdly, introduction of a proper set of dimensionless groups reduces the number of parameters to the minimum that characterize a problem, thereby simplifying parametric analysis of system behavior.

Some common dimensionless groups used in analysis of crystal growth include the Grashof and Prandtl numbers, defined by

$$\text{Gr} \equiv \frac{\rho^2 g \beta \Delta T L^3}{\mu^2} \quad (6.13)$$

$$\text{Pr} \equiv \frac{\mu C_p}{\kappa} \quad (6.14)$$

where L is the characteristic system length and ΔT is a characteristic temperature difference. The Grashof number represents the ratio of buoyancy force to viscous force and is characteristic of the intensity of buoyancy-driven convection. The Prandtl number, a physical property of the material, is the ratio of momentum diffusivity to thermal diffusivity. A low value of Pr , typical of liquid metals and most semiconductor melts, indicates that the thermal field is weakly affected by small changes in the velocity field. A high value of Pr , typical of many oxide melts, indicates the converse, namely that small changes in the velocity field strongly affect the temperature field. As a consequence, low Pr materials behave very differently from high- Pr materials in crystal-growth systems.

For a more detailed discussion of scaling analysis and dimensionless groups, in the context of crystal-growth modeling, the interested reader is referred to Derby *et al.* (1998) and Brown (1988).

6.3 COMPUTATIONAL ISSUES

6.3.1 NUMERICAL METHODS

The equations presented in Section 6.2 rarely can be solved using traditional methods of mathematical analysis, except under extremely restrictive simplifications. Numerical methods have become indispensable, therefore, to the analysis of crystal-growth systems. Here we comment briefly on these methods, including a discussion of commercial software for hydrodynamic analysis.

There exist several well-developed methods widely used to solve equations of continuum transport phenomena. These include finite-difference, finite-element, finite-volume, and spectral methods. Each has its enthusiasts who will hotly debate the superiority of their method of choice, but, in reality, the methods share several common features. Each method reduces the governing equations to a set of differential-algebraic equations (DAEs), which can be integrated in time using one of several standard methods. The result is a set of nonlinear algebraic equations, which must be solved iteratively at each time step. In all cases, the preponderance of computational effort is expended in obtaining a solution to this set of algebraic equations. In our work we have used both the Galerkin finite-element method and the Galerkin/least-squares method to discretize the governing equations (Hughes, 1987). Generally we use a second-order trapezoid rule to time integrate the DAEs (Gresho *et al.* 1980), and Newton's method is our method of choice to solve the set of nonlinear algebraic equations at each time step.

Within each Newton iteration it is necessary to solve a linearized set of algebraic equations, by far the most costly computational step. There are two general approaches to this step. The first approach is to use a direct method, i.e. some form of Gaussian elimination. The alternative is to use an indirect, or iterative method, of which there are many choices, the most popular being some sort of subspace projection method, e.g. the generalized minimal residual method of Saad and Schultz (GMRES) (1986). Direct methods are far more robust and are the method of choice for one- and two-dimensional problems, but are usually too costly for three-dimensional problems, even using the most powerful computers available today. Typically, the numerical analyst is forced to employ less robust iterative methods when tackling three-dimensional problems.

Many computing platforms are available to the numerical analyst, generally belonging to one of three broad classes: fast scalar computers, vector supercomputers, and parallel supercomputers. Vector supercomputers, once the workhorse of hydrodynamic simulation, have in recent years mostly been replaced by fast scalar machines. Indeed, desktop computers that exceed the computing power of a Cray C90 supercomputer, a state-of-the-art multimillion dollar machine 10 years ago, can be purchased today for about \$1000. Such machines are adequate for nearly all two-dimensional hydrodynamic analyses in crystal growth (an exception will be presented in Section 6.4). Fully three-dimensional hydrodynamic calculations continue to be extremely costly and difficult to perform, however.

For many hydrodynamic problems, such calculations remain beyond the reach of fast scalar computers or vector supercomputers. In fact, many existing three-dimensional calculations that have been done using these types of computers have employed very coarse meshes. Accurate hydrodynamic simulation in crystal-growth systems often requires fine spatial discretizations in order to resolve thin boundary layers typical of these systems.

Recent advances in massively parallel supercomputers have dramatically affected the prospect of studying three-dimensional macroscopic transport effects in many systems. In Section 6.4, an example is presented that illustrates the application of massively parallel computing to analyze a complicated, three-dimensional flow in a crystal-growth system. We emphasize that such calculations are by no means routine, however. Parallel computers require special programming methods to exploit the architecture of these machines, and no commercial hydrodynamics codes known to us are yet available that take advantage of massive parallelism.

6.3.2 SOFTWARE: COMMERCIAL VERSUS RESEARCH, GENERAL VERSUS SPECIALTY

For the industrialist interested in modeling bulk crystal growth, but lacking in modeling experience, the question of how best to proceed is critical. Unfortunately there are no easy answers to this question. The choices are many. Some of the possibilities include: using a general-purpose commercial code; using a general-purpose commercial code that has been customized (either by the vendor or the user); using a specialized commercial code that has been tailored to the needs of the crystal-growth industry; contracting the work to a specialist; or developing software in-house.

There are numerous general-purpose codes on the market today that model fluid dynamics and transport phenomena, several of which have found use in the crystal-growth community. Each code has its strengths and weaknesses, and, as a result, each code is usually marketed more actively in some industries than others. We make no attempt to analyze these strengths and weaknesses nor to make any specific recommendations. Indeed, our experience in using such codes is limited; we have rather chosen to develop our own research codes, which are specialized to our needs. We do offer one opinion, however: we believe it is impossible for the commercial code developer to anticipate all possible physical problems, all possible boundary conditions, and so on. Since production crystal-growth systems usually are quite complex, and their behavior is affected by many physical phenomena, creating a general-purpose code that can accurately model such systems presents a special challenge to code developers. Indeed, for some problems there is no suitable choice among the general-purpose commercial codes.

An alternative is to use specialized software. General-purpose code vendors usually sell additional services, including custom code modification for specialized problems, and contract simulation on the request of the customer. There

also have appeared in recent years several vendors of software products that are tailored to meet typical needs of the crystal-growth modeler. But even these specialized products are not suitable in every situation that might arise in crystal growth. So, like the general-purpose code developers, these vendors also usually offer customized products and contract simulation.

The last alternative we mention is developing and using software in-house. This could range from hiring a single specialist at smaller companies, to supporting a modeling department at larger companies. In-house code development in most cases is the most time- and capital-intensive approach, so it appears to be relatively rare at companies specializing in crystal growth. At this point it is worth mentioning that licensing or purchasing one or more commercial codes might require devoting one or more staff members to master the codes, which, due to the considerable art sometimes required of successful modeling, is by no means foolproof or trivial. Also, in all cases, whether using a commercial code, or software developed in-house, at least some knowledge of transport phenomena is required to both define the problem to be modeled and to interpret the output from the software.

Our principal advice is to re-emphasize that there is no single clear-cut approach that will be optimal in all situations. Furthermore, the industrialist who solicits opinions from commercial vendors and other experts in modeling is likely to hear several different opinions. In our view, the best approach is to first strive to carefully define the particular problems that are to be modeled, then to solicit opinions both from vendors that provide products and services and from other users of those products and services.

6.4 EXAMPLES OF ONE-, TWO-, AND THREE-DIMENSIONAL MODELS

6.4.1 CAN WE STILL LEARN FROM A 1D MODEL?

Prior to the widespread availability of digital computers, crystal-growth models were simple out of necessity, which usually meant they were restricted to describe one-dimensional behavior. Such models can be quite powerful when appropriately applied. An early example is the well-known Scheil equation (Scheil 1942), derived from a model of segregation during freezing from a completely mixed melt. Another example is the diffusion-only limit, studied by Tiller and coworkers (1953; 1955). A more general result was obtained by Burton *et al.* (BPS) (1953), based on the notion of a completely mixed bulk melt, separated from the crystal by a thin stagnant film in which transport occurs by diffusion only. The BPS model has been successfully fitted to experimental data obtained from many crystal-growth systems. Unfortunately, the model has little predictive capability, largely because the stagnant-film assumption is not a realistic representation of convection in the melt. Other variations on these one-dimensional models include

effects of rotating the crystal and imposing an axial magnetic field; references and discussion can be found in Brown (1988).

Using modern computers, various researchers have compared these and other one-dimensional models to more rigorous two- and three-dimensional models, highlighting various shortcomings of simpler models. Since researchers no longer are confined to such simple models, it is relevant to ask whether anything new can be learned from them. We present an example here that suggests that one-dimensional models are still relevant to understanding crystal-growth systems, namely ternary segregation during diffusion-controlled growth of the II-VI alloy cadmium zinc telluride ($\text{Cd}_{1-x}\text{Zn}_x\text{Te}$, hereafter referred to as CZT).

CZT is employed in room-temperature gamma-ray and X-ray detectors, typically using material with 10% nominal zinc concentration ($x = 0.1$). Compositional inhomogeneity resulting from zinc and cadmium segregation (James *et al.*, 1995) is an important issue in CZT-based detectors. An unresolved issue in modeling CZT growth, however, is whether pseudobinary diffusion (i.e. Equation (6.4)) is adequate to describe multicomponent mass transport and segregation phenomena in this system.

The pseudobinary diffusion model is based on the assumption that the flux of each species in a multicomponent system is simply proportional to the gradient of that species alone; this model is known as Fick's first law of diffusion (Bird *et al.*, 1960). In true multicomponent diffusion, however, the flux of each species is represented by a more complicated, implicit relationship between gradients and fluxes of all species, known as the Stefan–Maxwell equations (Hirschfelder *et al.*, 1954; Lightfoot *et al.*, 1962). To better understand multicomponent mass transfer and segregation during diffusion-controlled growth of CZT, Ponde *et al.* have developed a one-dimensional model based on the Stefan–Maxwell equations (Ponde, 1999; Derby *et al.*, 2000).

Figure 6.1 shows initial results obtained using this multicomponent diffusion model. Concentrations of zinc and cadmium are shown as a function of distance from the solid/liquid interface, under steady-state growth conditions. Zinc

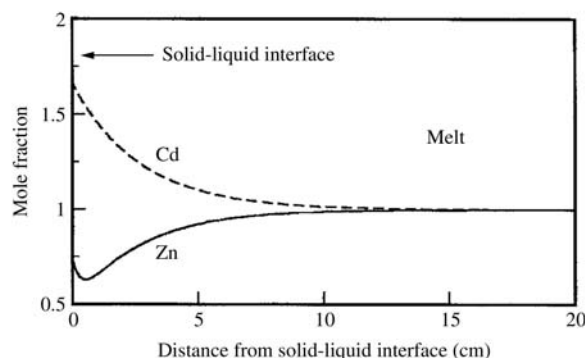


Figure 6.1 Compositional profiles in the melt ahead of the melt-crystal interface are shown for diffusion-controlled solidification of $\text{Cd}_{0.9}\text{Zn}_{0.1}\text{Te}$.

is preferentially incorporated into the growing crystal, causing its depletion at the interface. Conversely, cadmium is rejected at the interface, causing it to accumulate there. At steady-state conditions, zinc must diffuse towards the interface to balance its depletion there, whereas cadmium must diffuse away from the interface, to counter its accumulation. The figure shows that cadmium concentration falls monotonically with distance from the interface. Hence cadmium diffuses along its gradient everywhere, the same as predicted by the pseudobinary diffusion model. Zinc concentration, on the other hand, first decreases, then increases, with distance from the interface. Thus the multicomponent diffusion model predicts that zinc diffuses against its concentration gradient near the interface, a consequence of diffusion coupling between components. Ponde *et al.* described this feature as a retrograde diffusion layer during solidification. Such behavior may have significant consequences in setting compositional variations that occur during growth of II–VI ternary compounds.

6.4.2 IS 2D MODELING ROUTINE AND ACCURATE?

Two-dimensional modeling of crystal-growth systems is now widely regarded as routine and accurate, provided that realistic thermophysical properties are available. We generally agree with this conclusion, with a few caveats. One of these caveats is that multicomponent diffusion effects may have a significant effect on segregation in ternary systems, as discussed in Section 6.4.1. Incorporating the Stefan–Maxwell equations in any model of crystal growth adds considerable complexity to segregation calculations, however, and poses numerical difficulties not encountered when using pseudobinary transport equations. Another caveat is that two-dimensional systems, in which there are multiple, widely disparate, time scales, may require an onerous amount of computing time. One such system, the subject of this section, is vertical Bridgman growth of CZT, using the accelerated crucible rotation technique (ACRT). A final caveat is that two-dimensional models cannot account for three-dimensional behavior, the topic of the next section.

The purpose of ACRT is to promote mixing within the melt. Here, we assess the effectiveness of ACRT for that purpose and discuss the challenges associated with modeling this system. A schematic of a high-pressure vertical Bridgman system is shown in Figure 6.2 along with a sample finite element mesh. Previously we have reported simulations for this system using steady rotation; a detailed description of the model can be found in Yeckel *et al.* (1999). An in-depth analysis of the system using ACRT appeared elsewhere (Yeckel and Derby, 2000). Except for the use of accelerated rotation, values of all physical properties and operating parameters are the same as used in Yeckel *et al.* (1999). The effect of accelerated rotation is accounted for through the no-slip boundary condition at the ampoule walls and solid/liquid interface, given by

$$\mathbf{v} = \Omega(t)r\mathbf{e}_\theta \quad (6.15)$$

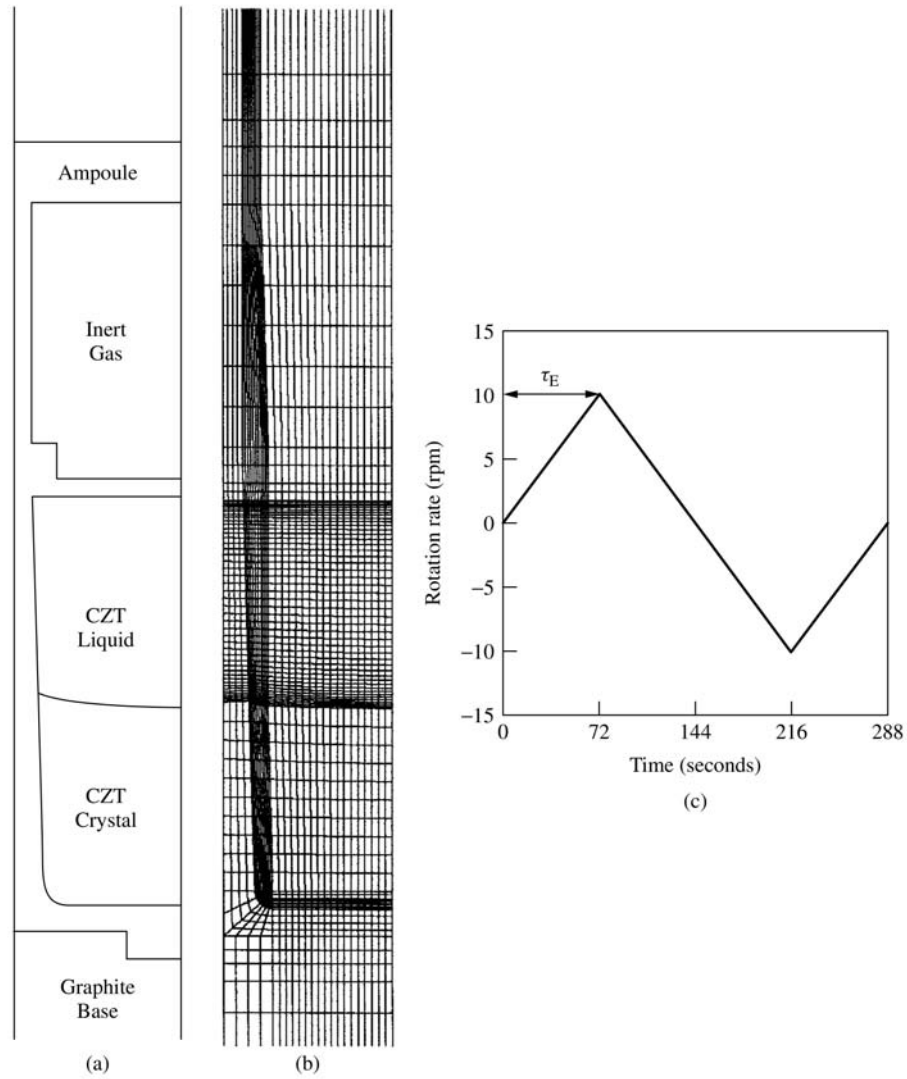


Figure 6.2 (a) Schematic of high-pressure vertical Bridgman system; (b) finite-element discretization; (c) rotation cycle used in this study.

where Ω is the crucible rotation rate, and \mathbf{e}_θ is a unit vector in the azimuthal direction. The periodic rotation cycle, Ω versus time, is shown in Figure 6.2.

Computing a complete segregation curve for this system presents a major computational challenge. The difficulty is brought on by the short time scale introduced when ACRT is used. Whereas a complete growth run typically lasts

100–150 h, the optimum rotation cycle is set by the Ekman time scale (Schulz-Dubois, 1972),

$$\tau_E = \left(\frac{R_o^2}{\Omega \nu} \right)^{1/2} \quad (6.16)$$

equal to 72 s for the conditions studied here. The optimum rotation cycle is a few Ekman time units in length (Yeckel and Derby, 2000). Over the duration of the growth run, therefore, more than one thousand ACRT cycles are needed, each requiring hundreds of time steps for accurate time integration. Hence to compute a single segregation curve requires on the order of one million time steps, a task that would take several months using a modern engineering workstation or a traditional vector supercomputer. Such long computation times make it impractical to simulate a complete growth run for this system. Using a parallel supercomputer for this task holds more promise and is the subject of our ongoing work.

It is possible to learn much about this system without simulating a complete growth run, however. To do so, we proceed as follows. We begin by simulating approximately one-half of a growth run, without rotation. The simulation is then restarted subject to the application of ACRT, and continued for two more hours of growth (approximately 25 ACRT cycles). Figure 6.3 shows the evolution of zinc distribution that follows upon application of ACRT; the number of full

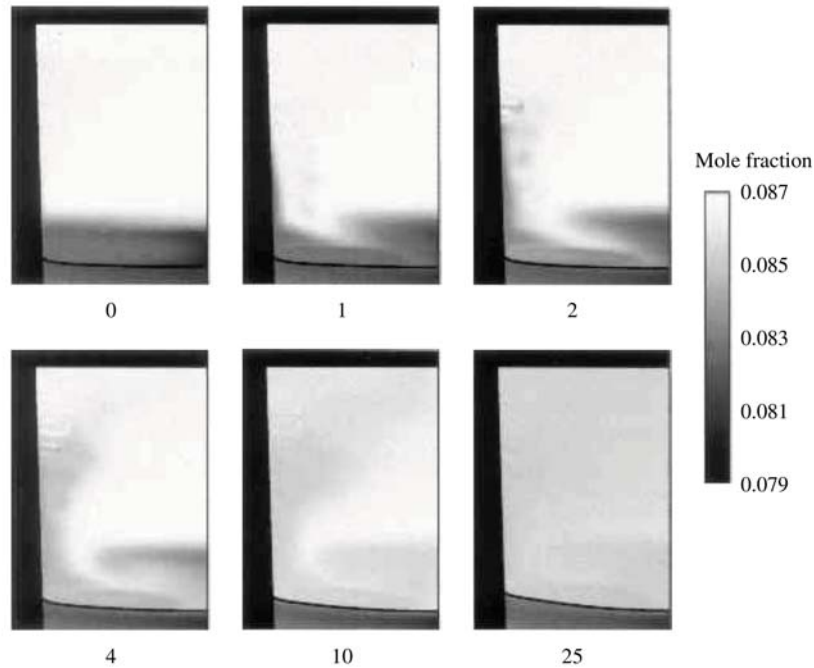


Figure 6.3 Mole fraction zinc versus ACRT cycle.

ACRT cycles undergone is shown below each visualization. At the start of ACRT (i.e. after zero cycles in Figure 6.3), the melt exhibits two distinct zones: a well-mixed bulk zone above, and a depletion layer below, separated by a diffusion layer characterized by a steep concentration gradient. These features, typical of CZT growth without rotation, are explained in Kuppurao *et al.* (1995).

After one ACRT cycle, a plume of zinc-poor liquid has been drawn from the depletion layer into the bulk, along the crucible wall. Likewise, some zinc-rich bulk fluid has been swept into the depletion layer. After two ACRT cycles, the interchange between the two regions continues. Mixing within the depletion zone has markedly increased; the region is much more uniform in concentration, particularly along the solid/liquid interface. Also, concentration variations begin to appear along the sidewall; these are the result of a Taylor–Görtler flow instability, as discussed in Yeckel and Derby (2000). After four ACRT cycles, there is substantial intermixing of the bulk and depletion regions, and, after ten ACRT cycles, substantial intermixing has occurred. The liquid concentration of zinc is nearly uniform throughout the melt after 25 ACRT cycles. The two-hour time span of ACRT growth is too short to meaningfully comment on the details of zinc segregation in the newly grown solid, but the results clearly illustrate the efficacy of ACRT at homogenizing the melt.

Whereas Figure 6.3 illustrates the pattern of mixing in the melt, Figure 6.4 shows a quantitative measure of mixing, the RMS mole fraction variation in the melt, defined by:

$$\Delta c_{\text{rms}} = \frac{1}{\bar{c}V} \int_V (c - \bar{c})^2 dV \quad (6.17)$$

where \bar{c} is the mean zinc mole fraction and V is the melt volume. Figure 6.4 shows that Δc_{rms} decreases steadily with ACRT cycle number for approximately 24 cycles, indicating an increasing degree of compositional homogeneity. After 24 cycles Δc_{rms} begins to slowly increase again. Note that Δc_{rms} cannot reach zero, a state of complete mixing, because zinc segregation ensures the existence

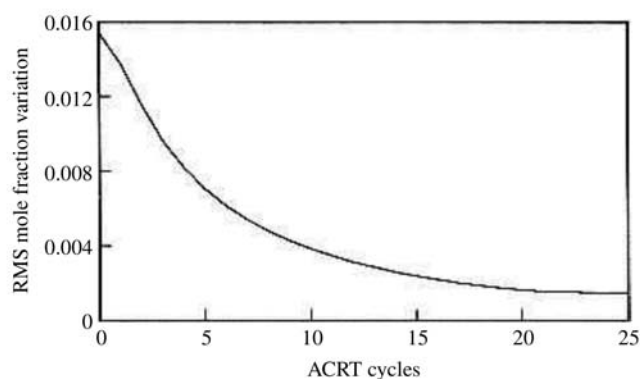


Figure 6.4 RMS mole fraction variation Equation (6.17) versus ACRT cycle.

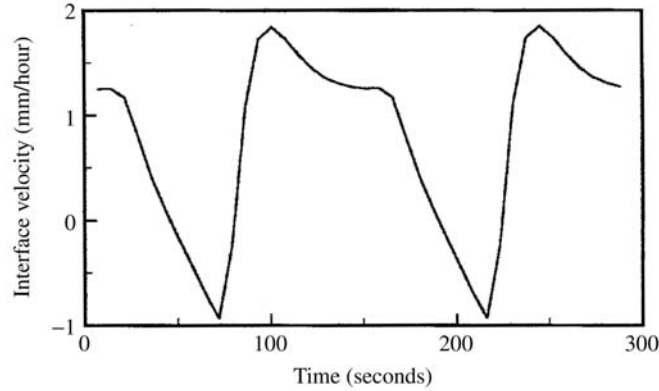


Figure 6.5 Average interface velocity (i.e. instantaneous growth rate) versus time.

of a nonvanishing concentration boundary layer at the solid/liquid interface, even though the bulk may be well mixed. The effect of this boundary layer on Δc_{rms} increases as the melt volume diminishes, causing the slight increase in Δc_{rms} after 24 cycles.

Figure 6.5 shows the average interface velocity (i.e. the instantaneous growth rate) as a function of time during the 25th ACRT cycle. Notably, the growth rate falls below zero during some parts of the cycle, which indicates that a portion of the crystal is melted during this phase, to be recrystallized later in the cycle. The rate of meltback is substantial, nearly reaching 1 mm/h at point D in the cycle. The large variation in growth rate, and the occurrence of meltback, raise the possibility that solute striations will occur. Kim *et al.* (1972) have linked striations with velocity and temperature field oscillations in Bridgman growth caused by an unstable, time-dependent flow. ACRT-induced striations were not observed in the Bridgman experiments of Capper *et al.* (1984; 1986); however, the striation spacing expected from the conditions of their experiments is an order of magnitude smaller than observed in Kim *et al.* (1972), making striations both more difficult to observe experimentally and faster to disappear by solid-state diffusion. On the other hand, the striation spacing expected under the conditions of our simulation, on the order of $2 - 4 \times 10^{-3}$ cm, is comparable to that observed in Kim *et al.* (1972), which indicates that stable striations in the grown solid may occur in the system modeled here. Due to the extreme computational challenges of accurately resolving these fine-scale striations, we do not further address these features here, but defer their analysis to ensuing work.

6.4.3 WHEN ARE 3D MODELS NECESSARY?

At first glance, many crystal-growth systems appear amenable to one- and two-dimensional modeling, and considerable knowledge has been gained over the

years using such models. The assumption of axisymmetry for cylindrical geometries has been particularly useful and would seem to apply to vertical Bridgman, Float-Zone, Czochralski, and other melt-growth systems that produce unfaceted crystals. Furthermore, considerable effort is expended to ensure that these systems display two-dimensional, axisymmetric behavior. This can often be accomplished through careful design or through operation, for example by rotating the heater or crystal, to ensure that the crystal experiences an azimuthally uniform furnace environment, in a time-averaged sense.

Solution-growth systems are another story, since the faceted crystals grown in these systems usually are not well described as two-dimensional objects. Furthermore, solution-growth systems sometimes rely on a crystal support structure that cannot realistically be treated as two-dimensional, e.g. the platform used in rapid growth of KDP crystals (Zaitseva *et al.*, 1995), or the angled support rods used in KTP growth (Bordui and Motakef, 1989). Indeed, our simulations of these systems reveal flows that are strongly three-dimensional in character (Zhou and Derby, 1997; Yeckel *et al.*, 1998; Vartak *et al.*, 2000).

Though it may seem obvious whether a given system is predominantly two-dimensional or three-dimensional in character, several examples from our recent work demonstrate that many crystal-growth systems with axisymmetric, or nearly axisymmetric, geometries can produce strongly three-dimensional flow structures. For example, Xiao *et al.* (1996) demonstrated that flow in a slightly tilted vertical Bridgman system – with its axis tilted as little as one degree from vertical – exhibits a remarkable departure from axisymmetry. Even more confounding is that perfectly axisymmetric geometries sometimes exhibit three-dimensional flow instabilities; an example is the appearance of baroclinic waves in systems that have both rotation and buoyancy as driving forces (Xiao *et al.*, 1995; Xiao and Derby, 1995). Thus the choice between using a two-dimensional or three-dimensional model, of great importance given the drastic difference in computational cost, remains a difficult one. Two-dimensional geometries certainly do not guarantee two-dimensional behavior.

In this section, we present transient, three-dimensional simulations of an axisymmetric Czochralski growth system that simultaneously exhibits two different types of three-dimensional instabilities. The manifestation of these instabilities takes the form of annular wave patterns that appear both on the surface and within oxide melts during Cz growth. Both types of instabilities arise because of the nonlinear interaction of intense rotational and buoyant flows, to which the temperature field is strongly coupled in high Prandtl number oxide melts. But the instabilities are caused by fundamentally different mechanisms, meaning that each instability occurs independently of the other.

Figure 6.6 shows a schematic of the bulk flow model used to compute time-dependent flows during Cz growth. The bulk flow model is based on assumptions of fixed and flat crystal/melt interface and melt free surface; an extensive description of this model can be found elsewhere. Idealized temperature boundary conditions consist of constant temperature T_h at the wall and bottom of the

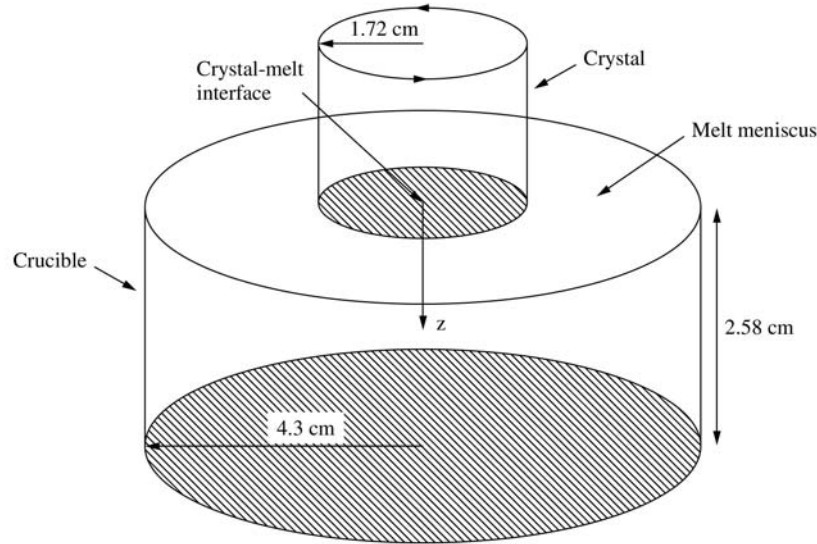


Figure 6.6 Schematic of Czocharalski bulk flow model.

crucible, an insulated melt free surface, and a crystal/melt interface at the melting point T_m . Physical properties used are those of bismuth silicon oxide (BSO), which has a Prandtl number of $Pr = 26$. Operating conditions correspond to $Gr = 1.3 \times 10^5$, equivalent to a system with a crucible radius of 4.3 cm, a crucible depth of 2.58 cm, a crystal radius of 1.72, and a temperature difference across the melt of 23 K. Four crystal rotation rates were used: 13.5, 15.2, 23.0, and 30.4 rpm. Here we briefly summarize the results of the simulations; more detailed analyses are found in Rojo and Derby (1999) and Derby *et al.* (1999).

Figure 6.7 shows the temperature distribution on the melt surface at various rotation rates. The surface distribution exhibits a low-temperature annulus centered around the crystal. This inner region is separated by a sharp transition from a high-temperature outer region, which is nearly isothermal and very near the wall temperature. The size of the hot outer region decreases as rotation rate increases, until, at the highest rotation rate considered, the outer region is confined to a thin annular region next to the outer wall. What is most interesting, however, are the azimuthal temperature variations that appear near the crystal in the cooler region. These azimuthal variations, which we call rotational spokes, are convected by the azimuthal flow driven by the counter-clockwise rotation of the crystal. The radial extent of the spokes, between 12 and 16 in number, increases as the rotation rate is increased.

The rotational spokes in Figure 6.7 bear a strong resemblance to those observed in the experiments of Whiffin *et al.* (1976), who studied the effect of a rotating platinum disk in contact with molten BSO, under the same conditions modeled here. At issue is the mechanism by which rotational spokes occur; these

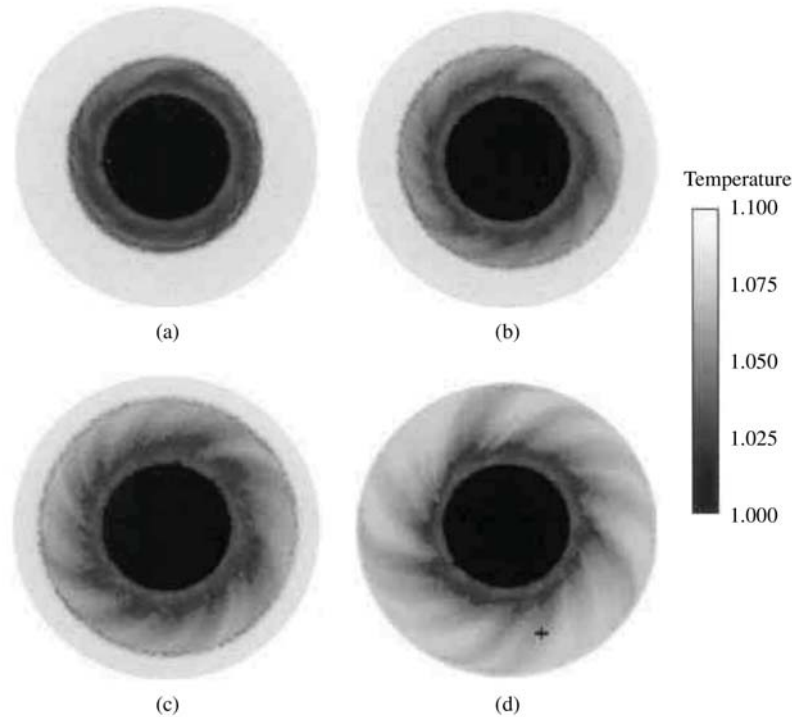


Figure 6.7 Temperature distribution on the melt surface at various rotation rates: (a) 13.5 rpm; (b) 15.2 rpm; (c) 23.0 rpm; (d) 30.4 rpm. Temperature is scaled by melting temperature of BSO.

have alternately been attributed to the baroclinic instability that arises in rotating stratified fluids (Whiffin *et al.*, 1976; Brandle, 1982), the Couette instability characteristic of centrifugal flows (Brice and Whiffin, 1977) or the Rayleigh instability caused by a destabilizing temperature gradient near the melt surface (Jones, 1983; Jones, 1985). The Rayleigh-instability mechanism was used by Jones to explain the appearance of radial spokes, observed in several oxide melts under conditions of no crystal rotation; results of our simulations indicate that a similar mechanism applies to rotational spokes, too.

The key to the Rayleigh instability is the presence of warmer, lighter fluid underlying cooler, denser fluid, which triggers the formation of roll cells. In the case of no crystal rotation studied by Jones, the cause of the destabilizing temperature gradient was assumed to be radiant cooling at the melt surface. A destabilizing temperature gradient also occurs in our simulations, as a consequence of centrifugal pumping of colder fluid, thrown outward along the melt surface by the rotating crystal. By performing a linear stability analysis applicable to high Prandtl number fluids, Jones (1985) calculated a critical value of the Rayleigh number, $Ra_c = 255$, above which the onset of roll cells would

occur, where

$$\text{Ra} = \text{GrPr} \equiv \frac{\rho^2 g \beta C_p \Delta T L^3}{\mu \kappa} \quad (6.18)$$

In Jones' stability analysis, values of L and ΔT correspond to the depth and temperature difference across the thermal boundary layer at the melt surface. Figure 6.8 shows the vertical temperature profile beneath a location centered on one of the spokes in Figure 6.7(d). Using this temperature profile to measure values of L and ΔT yields a computed Rayleigh number of $\text{Ra} = 278$, which compares favorably to the critical value predicted by Jones.

The simulations also reveal that azimuthal wave patterns occur deep within the melt, as shown in Figure 6.9 for the results obtained at 30.4 rpm. These patterns exhibit six- or seven-fold symmetry and occur far below the thermal boundary layer responsible for roll-cell formation near the melt surface. Similar patterns, with two- and four-fold symmetry, were also computed by Xiao and Derby (1995), for a different oxide melt. We attribute these wave patterns to the baroclinic instability (Greenspan, 1968), caused by the interaction of Coriolis and buoyancy forces. We recast our results in terms of dimensionless Rossby and Taylor numbers, to locate our result on the baroclinic stability diagram of Hide and Mason (1975) for a high Prandtl number fluid ($\text{Pr} = 63$), as shown in Figure 6.10. The parameters of our case fall near the regular annular wave regime and are consistent with the six- or seven-fold wave structure that is expected.

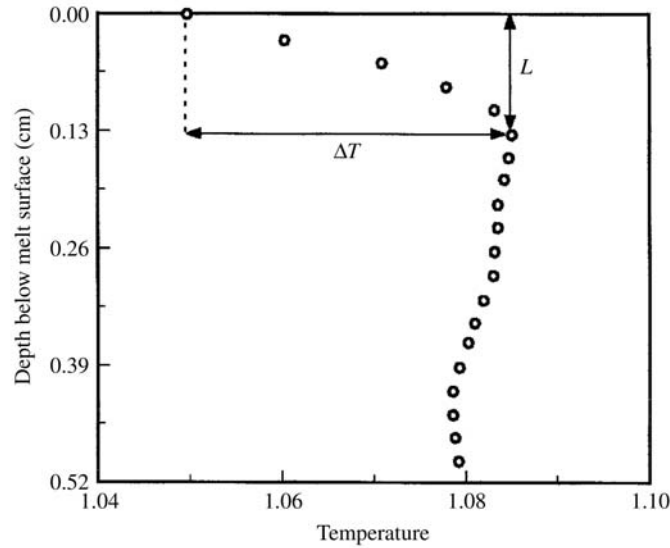


Figure 6.8 Axial temperature profile below the melt free surface at the point indicated in Figure 6.7b. Temperature is scaled by melting temperature of BSO.

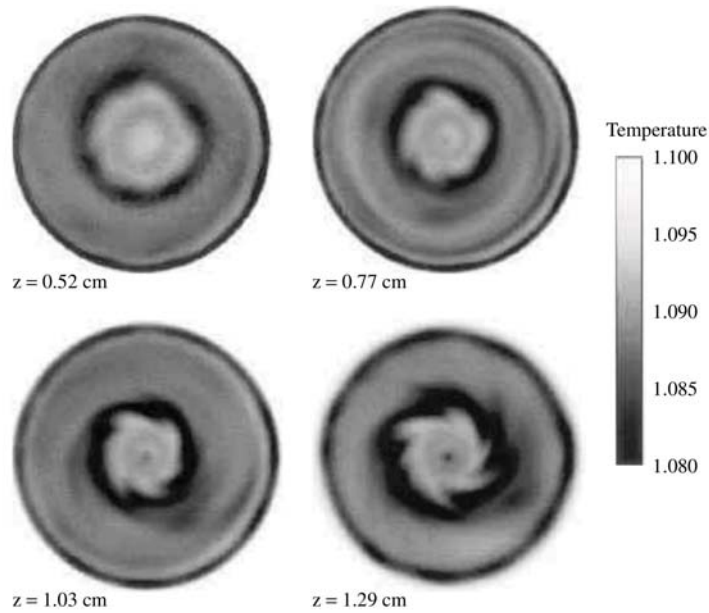


Figure 6.9 Temperature distribution on various horizontal planes within the melt; numbers refer to depth below the melt surface. Temperature is scaled by melting temperature of BSO.

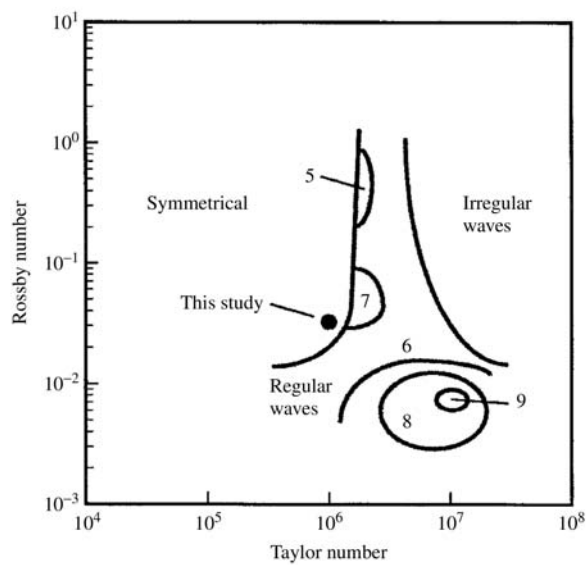


Figure 6.10 Stability diagram of Hide and Mason (1975) for flows in a rotating, differentially heated annulus filled with a high Prandtl number liquid. Asterisk shows parameter location corresponding to BSO calculations presented in Figure 6.9.

6.5 SUMMARY AND OUTLOOK

The examples presented in this chapter were chosen to demonstrate the power of simulation at elucidating answers to important questions in the study of crystal growth and to illustrate the current limitations of hydrodynamics modeling. The first example, the one-dimensional model of multicomponent diffusion in a ternary alloy, raises the question of how well we really understand basic model formulation in some crystal-growth systems. The second example, ACRT applied to vertical Bridgman growth, shows that not all two-dimensional problems are entirely routine, even with today's powerful computers. The third example highlights the risk of relying on a two-dimensional model, even when the geometry and boundary conditions would seem to indicate two-dimensional system behavior. Despite these caveats, however, hydrodynamic simulation has made enormous advances in the past decade, making two-dimensional analysis available at a low cost to a large number of researchers and making realistic three-dimensional analysis feasible at all.

The potential benefits of computer modeling in the analysis and design of bulk crystal-growth systems have been the subject of much discussion in the past decade. The realization of computer modeling as a comprehensive design tool still appears some way off, however. Rather, modeling at present often best serves to complement experimental studies, to provide a basic understanding of phenomena important to crystal-growth processing, and to identify qualitative, and in some cases quantitative, trends in system behavior, with respect to parametric variation. Such information, although failing to provide a complete picture of system behavior, often suggests beneficial modifications to both operation and design, and on occasion suggests entirely new designs. Nevertheless, modeling alone often is of limited use in the absence of good experimental data, human experience, and intuition, especially at the design stage. Furthermore, there yet remain some phenomena, and some physical systems, which are beyond our ability to model, except in the most rudimentary fashion.

The maturation of computational modeling of crystal-growth systems will rely on the increased availability of accurate thermophysical properties, the development of more capable supercomputer hardware and software, the advancement of experimental diagnostics in crystal-growth systems, and increased communication between crystal-growth experimentalists and theoreticians. Great advances in understanding and practice are to be expected in the coming years.

ACKNOWLEDGMENTS

The authors' research programs in crystal-growth modeling have been supported in part by Johnson Matthey Electronics (IRMP, Defense Advanced Research Projects Agency), Lawrence Livermore National Laboratory, the National Aeronautics and Space Administration (Microgravity Materials Science), the National

Science Foundation, Sandia National Laboratories, the University of Minnesota Supercomputer Institute, and the Army High Performance Computing Research Center under the auspices of the Department of the Army, Army Research Laboratory cooperative agreement DAAH04-95-2-0003/contract DAAH04-95-C-0008, the content of which does not necessarily reflect the position or policy of the government, and no official endorsement should be inferred. The authors also gratefully acknowledge significant input from J. C. Rojo and N. Ponde.

REFERENCES

- Bird, R. B., Stewart, W. E., and Lightfoot, E. N. (1960) *Transport Phenomena*. John Wiley; New York.
- Bordui, P. F., and Motakef, S. (1989) *J. Cryst. Growth*, **96**, 405.
- Brandle, C. D. (1982) *J. Cryst. Growth*, **57**, 65.
- Brandon, S., and Derby, J. J. (1992) *Int. J. Num. Meth. Heat Fluid Flow*, **2**, 299.
- Brice, J. C., and Whiffin, P. A. C. (1977) *J. Cryst. Growth*, **38**, 245.
- Brown, R. A. (1988) *AIChE J.*, **34**, 881.
- Burton, J. A., Prim, R. C., and Schlichter, W. P. (1953) *J. Chem. Phys.*, **21**, 1987.
- Capper, P., Gosney, J. J. G., and Jones, C. L. (1984) *J. Cryst. Growth*, **70**, 356.
- Capper, P., Gosney, J. J. G., Jones, C. L., and Kenworthy, I. (1986) *J. Electron. Mater.*, **15**, 371.
- Derby, J. J., Edwards, K., Kwon, Y.-I., Rojo, J. C., Vartak, B., and Yeckel, A. (1998) Large-scale numerical modeling of continuum phenomena in melt and solution crystal growth processes. *p. 119 of*: Fornari, R., and Paorici, C. (eds), *Theoretical and Technological Aspects of Crystal Growth*, vol. 276, Trans Tech Publications, Switzerland.
- Derby, J. J., Kwon, Y.-I., Rojo, J. C., Vartak, B., and Yeckel, A. (1999) *Int. J. Comput. Fluid Dyn.*, **12**, 225.
- Derby, J. J., Ponde, N., De Almeida, V. F., and Yeckel, A. (2000) *p. 93 of*: Roósz, A., Rettenmayr, M., and Watring, D. (eds), *Solidification and Gravity 2000*, vol. 329–330. Switzerland: Trans Tech Publ. Ltd.
- Greenspan, H. P. (1968) *The Theory of Rotating Fluids*. Cambridge University Press, London.
- Gresho, P. M., Lee, R. L., and Sani, R. L. (1980) *p. 27 of*: Taylor, C., and Morgan, K. (eds), *Recent Advances in Numerical Methods in Fluids, Vol. 1*, Pineridge, Swansea.
- Hide, R., and Mason, P. J. (1975) *Adv. Phys.*, **24**, 47.
- Hirschfelder, D. G., Curtiss, C. F., and Bird, R. B. (1954) *Molecular Theory of Gases and Liquids*. John Wiley, New York.
- Hughes, T. J. R. (1987) *The Finite Element Method*. Prentice Hall, Englewood Cliffs, NJ.
- James, R. B., Schlesinger, T. E., Lund, J., and Schieber, M. (1995) *p. 335 of*: Schlesinger, T. E., and James, R. B. (eds), *Semiconductors for Room Temperature Nuclear Detector Applications*, vol. 43. Academic Press, San Diego.
- Jones, A. D. W. (1983) *J. Cryst. Growth*, **61**, 235.
- Jones, A. D. W. (1985) *Phys. Fluids*, **28**, 31.
- Kim, K. M., Witt, A. F., and Gatos, H. C. (1972) *J. Electrochem. Soc.*, **119**, 1218.
- Kuppurao, S., and Derby, J. J. (1993) *Numer. Heat Transfer, Part B: Fundamentals*, **24**, 431.

- Kuppurao, S., Brandon, S., and Derby, J. J. (1995) *J. Cryst. Growth*, **155**, 103.
- Lightfoot, E. N., Cussler, E. L., and Rettig, R. L. (1962) *AIChE J.*, **8**, 708.
- O'Hara, S., Tarshis, L. A., and Viskanta, R. (1968) *J. Cryst. Growth*, **3/4**, 583.
- Ponde, N. (1999) M.S. thesis, University of Minnesota.
- Rojo, J. C., and Derby, J. J. (1999) *J. Cryst. Growth*, **198**, 154.
- Saad, Y., and Schultz, M. H. (1986) GMRES: A generalized minimal algorithm for solving nonsymmetric linear systems. *SIAM J. Sci. Stat. Comp.*, **7**, 856–869.
- Scheil, E. (1942) *Z. Met. kd*, **34**, 70.
- Schulz-Dubois, E. O. (1972) *J. Cryst. Growth*, **12**, 81.
- Siegel, R., and Howell, J. R. (1993) *Thermal Radiation Heat Transfer, Third Edition*. McGraw-Hill, New York.
- Smith, V. G., Tiller, W. A., and Rutter, J. W. (1955) *Can. J. Phys.*, **33**, 723.
- Tiller, W. A., Jackson, K. A. Rutter, J. W., and Chalmers, B. (1953) *Acta Met.*, **1**, 428.
- Vartak, B., Kwon, Y.-I., Yeckel, A., and Derby, J. J. (2000) *J. Cryst. Growth*, **210**, 704.
- Whiffin, P. A. C., Bruton, M., and Brice, J. C. (1976) *J. Cryst. Growth*, **32**, 205.
- Xiao, Q., and Derby, J. J. (1995) *J. Cryst. Growth*, **152**, 169.
- Xiao, Q., Salinger, A. G., Zhou, Y., and Derby, J. J. (1995) *Int. J. Numer. Methods Fluids*, **21**, 1007.
- Xiao, Q., Kuppurao, S., Yeckel, A., and Derby, J. J. (1996) *J. Cryst. Growth*, **167**, 292.
- Yeckel, A., and Derby, J. J. (2000) *J. Cryst. Growth*, **209**, 734.
- Yeckel, A., Zhou, Y. Dennis, M., and Derby, J. J. (1998) *J. Cryst. Growth*, **191**, 206.
- Yeckel, A., Doty, F. P., and Derby, J. J. (1999) *J. Cryst. Growth*, **203**, 87.
- Zaitseva, N. P., Rashkovich, L. N., and Bogatyreva, S. V. (1995) *J. Cryst. Growth*, **148**, 276.
- Zhou, Y., and Derby, J. J. (1997) *J. Cryst. Growth*, **180**, 497.

7 Heat and Mass Transfer under Magnetic Fields

KOICHI KAKIMOTO

*Institute of Advanced Material Study, Kyushu University, Kasuga
816-8580 JAPAN*

ABSTRACT

The heat and mass transfer in the melts during Czochralski crystal growth of semiconductors significantly affect the quality of the single crystals. This chapter reviews the present understanding of heat and mass transfer under several kinds of magnetic fields from the results of flow visualization, and gives details of numerical calculation needed for quantitative modeling of melt convection under the magnetic fields. The characteristics of flow instabilities of melt convection under magnetic fields are also reviewed.

7.1 INTRODUCTION

The Czochralski (CZ) crystal-growth technique is widely accepted for fabricating high-quality substrates for silicon (Si) VLSIs, gallium arsenide (GaAs) monolithic and integrated devices, and indium phosphide (InP) optoelectronic devices.

The breakdown voltage of an oxide layer grown on Si substrates is well known to depend on the conditions under which the Si crystals were grown [1], such as the crystal pulling speed and/or the temperature distribution in the crystals. The origin of the degradation is the formation of voids in the substrate [2], which are formed during single-crystal growth. To avoid the excessive void formation is one of the key points to control characteristics of electronic silicon devices. This can be achieved by controlling the temperature distribution in the growing crystals. Simultaneously, the solid/liquid interface shape should also be controlled to obtain an appropriate temperature distribution near the solid/liquid interface in silicon.

For GaAs, the temperature distribution near the solid/liquid interface modifies the distribution of dislocations, which affects the threshold voltage of source-drain current in metal-semiconductor (MES) transistors [3]. Controlling heat and mass transfer in the melt during crystal growth can reduce this inhomogeneity.

Although the melt convection should, therefore, be controlled, the actual flow in semiconductor melt has been difficult to monitor because these melts are opaque.

The distribution of impurities and point defects in crystals, which affects the degradation of the breakdown voltage for silicon crystals, is thought to depend on the amplitude of temperature fluctuation at a solid/liquid interface [4]. This is mainly caused by the instability of a flow containing laminar and/or turbulent components. Furthermore, temperature fluctuations in the melt cause local alternations between crystallization and remelting. This alternation produces a relatively high microdefect density in the crystals.

The origin of flow instability should therefore be clarified, so that this instability can be controlled and high-quality crystals obtained. Consequently, suppressing flow instabilities during crystal growth is important for fabricating crystals with homogeneous impurity distribution. Despite intensive research [5–8], there are still open questions such as flow structure and impurity transfer under magnetic fields [6, 7].

Application of stationary magnetic fields such as vertical, cusp-shaped and transverse magnetic fields is opening up a new field to controlling heat and mass transfer in electrically conducting melts such as silicon or GaAs. Witt *et al.* [5] first applied magnetic fields in crystal growth of semiconductors from the melt. Subsequently, Hoshi *et al.* [8] reported homogeneous oxygen distribution in silicon crystals by using transverse magnetic fields.

Three types of static-magnetic field such as vertical-magnetic-fields (VMF), cusp-shaped magnetic fields (CMF), and transverse magnetic fields (TMF) have been proposed. Suzuki *et al.* [9] applied TMF to silicon crystal growth, however, the thermal symmetry became asymmetric. Therefore, periodic rotational striations were observed [10].

To overcome the rotational striations, Hirata and Hoshikawa [11, 12] proposed VMF in which axially symmetric magnetic fields were applied perpendicularly to the growth interface. They reported that temperature fluctuations in molten silicon were reduced at a VMF larger than 0.1 T. Moreover, no striations were observed for a magnetic field of more than 0.05 T. However, oxygen concentration distributed inhomogeneously in the radial direction of the grown crystals. Hereafter, Hirata and Hoshikawa [12] developed a new type of magnetic field, which is named cusp-shaped magnetic field (CMF). They obtained crystals with homogeneously distributed oxygen and without rotational striations.

This chapter aims to introduce how silicon melt and oxygen are transferred by convection under the three types of magnetic fields.

7.2 MAGNETIC FIELDS APPLIED TO CZOCHRALSKI GROWTH

Figure 7.1 schematically shows a cross section of a VMF apparatus [13] that allows direct observation of molten silicon flow in the magnetic fields by X-ray radiography. This apparatus consists of four major parts: a set of magnets,

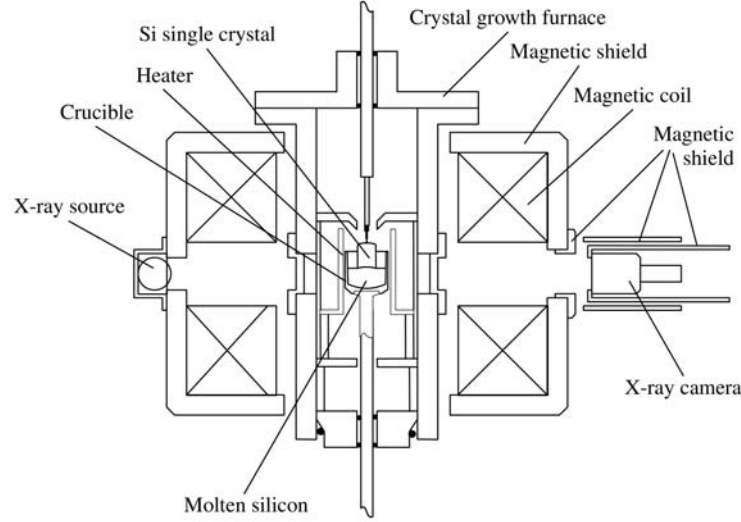


Figure 7.1 Schematic diagram of the magnetic field applied CZ crystal-growth furnace with X-ray radiography system.

an X-ray radiography system, a magnetic shield, and a crystal-growth furnace. Moreover, the system has two cylindrical-solenoid-coils to apply magnetic fields of VMF. Furthermore, CMF can be obtained by changing current direction of one of the two coils.

The X-ray radiography system consists of two sets of X-ray sources and cameras. X-ray sources and cameras are very sensitive to magnetic fields; therefore, shielding is required to observe melt flow under magnetic fields.

7.3 NUMERICAL MODELING

The control-volume method was used for discretizing the governing equations such as continuity, Navier–Stokes, energy, and impurity transfer equations in the present calculation [13]. The alternating directional implicit (ADI) method was used as a matrix solver to carry out a time-dependent calculation with three-dimensional geometry.

The governing equations of continuity, Navier–Stokes, energy, and impurity transfers are expressed in Equations (7.1)–(7.3).

$$\frac{\partial \rho}{\partial t} + \nabla \cdot (\rho u) = 0 \quad (7.1)$$

$$\frac{\partial \Phi}{\partial t} + u \cdot (\rho \nabla \Phi) = \nabla \cdot (\Gamma \nabla \Phi) + S_\phi(\Phi = u, T, c) \quad (7.2)$$

$$S = -\nabla p + F(= \rho g) + f \quad (7.3)$$

where ρ , T , and Γ are density, temperature, and diffusivity for the variables such as velocity, temperature, and impurity concentration. p , f , and g are the pressure, external forces such as Lorentz and viscous forces, and gravitational acceleration, respectively. u , T , and c are velocity, temperature, and impurity concentration, respectively. S is a source term of each variable of velocity, temperature, and impurity concentration.

When the effect of magnetic fields was taken into account, the Lorentz force (f) expressed by Equation (7.4) was included in Equation (7.3) as an external force,

$$f = J \times B \quad (7.4)$$

$$J = \sigma(-\nabla\Psi + u \times B) \quad (7.5)$$

where J , Ψ , σ , and B are the electric current, electric scalar potential, electric conductivity, and magnetic field, respectively.

When the effects of cusp-shaped magnetic fields (CMF) were calculated, the following equation based on Biot and Savart's law was used by taking into account the electric current, which was distributed in the solenoids with a finite volume,

$$dH = \frac{1}{4\pi\mu_0} \left(\frac{I dl \times r}{r^3} \right) dV \quad (7.6)$$

where H , μ_0 , and I are the magnetic field strength, permeability, and current in solenoids, respectively. Here r and V are the distance between some specific point and a part of solenoids, and volume. Equation (7.6) was numerically integrated to obtain the magnetic field at specific points.

When oxygen transfer in the silicon melt was taken into account in the calculation, the following assumptions of equilibrium concentration at an interface between the melt and a crucible, and flux at the boundary melt-gas were imposed as expressed by Equations (7.7) [14] and Equation (7.8) [15],

$$O = 3.99 \times 10^{23} \exp(-2.9 \times 10^4/T) \text{ atoms/cm}^3 \quad (7.7)$$

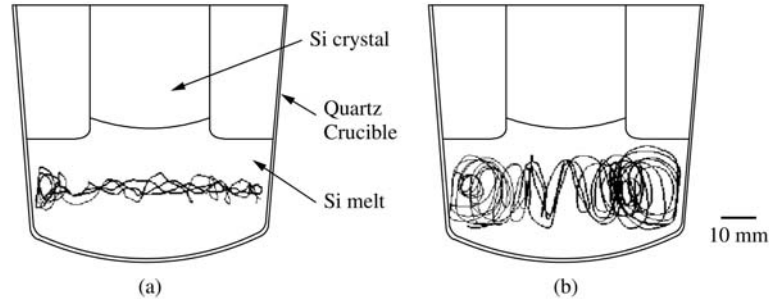
$$q = h(O(\text{melt}) - O(\text{gas})) \quad (7.8)$$

where h and O are the mass transfer coefficient at the interface between the melt and ambient gas, and the oxygen concentration in the melt, respectively. h and $O(\text{gas})$ are fixed as 2 and 0 atoms/cm³, respectively [14]. Equation (7.7) was obtained from thermodynamical calculation under the equilibrium conditions [15]. Thermophysical properties used in the calculation are listed in Table 7.1.

A three-dimensional numerical simulation with a grid size of $50 \times 50 \times 50$ in the r , θ , and z directions was carried out. The geometry of the present calculation was based on the experimental one with 3-inch diameter crucible and

Table 7.1 Thermophysical properties for numerical simulation

Density (kg/m^3)	2520
Heat capacity ($\text{J/m}^3 \text{ K}$)	2.39×10^6
Dynamic viscosity (kg/ms)	7×10^4
Thermal expansion coefficient (K^{-1})	1.4×10^{-4}
Melting temperature (K)	1685
Thermal conductivity (W/m K)	45
Emissivity	0.3
Electrical conductivity (S/m)	1.29×10^6
Crucible radius (m)	3.75×10^{-3}
Melt height (m)	3.40×10^{-3}

**Figure 7.2** Particle paths of one specific tracer in silicon melt (a) with VMF and (b) without magnetic fields.

1.5-inch diameter crystal as shown in Figure 7.2 [16]. The temperature boundary conditions of the melt, which strongly affect the flow mode, were set to be axisymmetric to identify the origin of the nonaxisymmetric temperature, velocity, and oxygen concentration profiles in the melt.

7.4 VERTICAL MAGNETIC FIELD (VMF)

Figures 7.2(a) and (b) show particle paths observed from one direction in molten silicon under VMF with 0.035 T (a) and without magnetic field (b), respectively. The particle path in the figure shows an axisymmetric pattern originated by a buoyancy force induced by the temperature gradient in the melt. Since the flow pattern is axisymmetric, the particle path gave a torus-like pattern due to crucible rotation.

The velocity of molten silicon flow was obtained from tracking a specific tracer. The projected image of the tracer was observed from one direction in the experiment, therefore, the projected velocity of one specific tracer was obtained in the experiment. Hereafter, the projected velocity (V) of one specific tracer

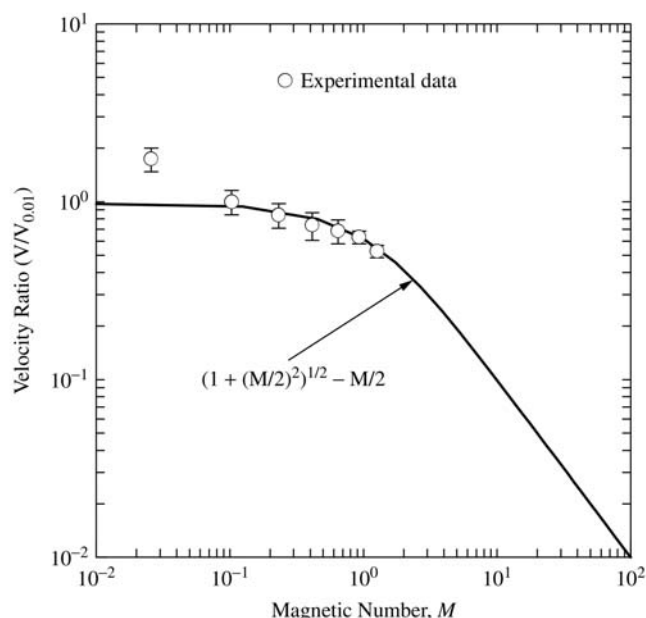


Figure 7.3 Measured and calculated velocity of one specific tracer as a function of magnetic number under VMF.

particle was defined as, $V = \sqrt{(\Delta x/\Delta t)^2 + (\Delta y/\Delta t)^2}$, where Δx and Δy are the horizontal and vertical displacements of the tracer image on a display, and Δt is the time interval between each frame of VTR film. Figure 7.3 shows the normalized velocity as a function of magnetic field strength [17]. Moreover, calculated results are also shown in the figure.

The velocity without VMF of 16.5 mm/s decreased to 5.6 mm/s when 0.035 T of VMF was applied to the melt. This clarifies that the flow velocity of molten silicon in the meridional plane was suppressed by VMF, which can be expressed by numerical simulation except in the case of nonmagnetic fields. The pattern of particle paths was axisymmetric even under VMF, which was kept during observation in the VMF range from 0 to 0.035 T. We estimated a general relationship between the flow velocity and VMF strength in order to speculate on the flow velocity in the range of magnetic field larger than 0.035 T, since it is difficult to observe a moving tracer under large magnetic field.

We proposed a nondimensional number based on Hartman number Ha and Reynold's number Re from analytical and numerical calculations as magnetic number M ($M = \sigma B_0^2 h / \rho v_0 = Ha^2 / Re$) which was able to predict the numerical results [17], where σ is the electrical conductivity, B_0 is the applied field, h is the melt height, ρ is the density and v_0 is the velocity of molten silicon without the magnetic field. Details of the derivation of this equation are shown in an

original paper reported elsewhere [17]. A solid-line ($V/V_0 = \sqrt{1 + (M/2)^2} - M/2$) represents a result obtained from calculation of magnetic number (M).

The above results show that the flow velocity decreased monotonically in the range above $M^{-2} = 1$. Moreover, the result indicates that flow velocity in the VMF with 0.1 T in the present configuration is about 0.1 times the flow velocity without the VMF.

The temperature boundary condition on the crucible wall determines the melt flow and the oxygen distribution in the melt under VMF. The temperature at the bottom of a crucible was set to two different values: 1412 °C (melting point), which is identical to type A in Figure 7.4(a), and 1430 °C, which is identical to type B in Figure 7.4(b), respectively. This study was carried out to clarify how Benard convection occurs under the two different temperature boundary conditions of types A and B [15].

An axisymmetric flow pattern resulted from the numerical simulation with the type-A heating system within the magnetic field from 0 to 0.3 T. However, a nonaxisymmetric flow pattern was observed in the simulation with the type-B heating system as shown in Figure 7.5(a) and (b), which indicate profiles of the velocity and temperature distribution at the top of the melt under a magnetic field of 0.1 T. With a magnetic field larger than 0.1 T, the flow velocity is reduced so that the temperature profile becomes almost axisymmetric. This means that the temperature distribution is mainly determined by heat conduction in view of the small velocity.

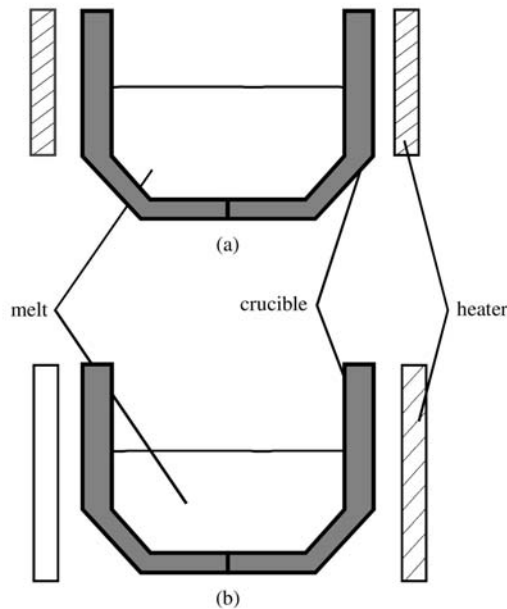


Figure 7.4 Schematic diagrams of two kinds of heating system. (a) type A, (b) type B.

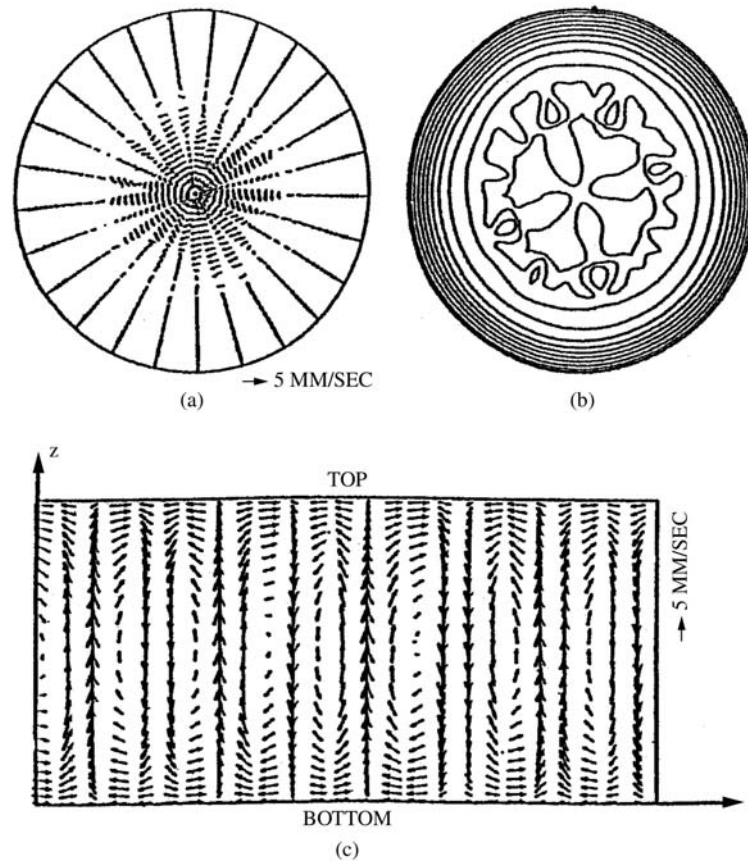


Figure 7.5 (a) Calculated velocity vectors, (b) temperature distribution and (c) velocity vectors in a z - r plane.

To understand the nonaxisymmetric structure, the velocity profile in the z - θ plane is shown in Figure 7.5(c) at a position of 1 cm radius. A cell structure similar to Benard cells can be recognized in the z - θ plane [15]. This kind of cell structure can be observed only in the type-B heating system, while it was not observed in the type-A system. This suggests that the origin of the cell structure was Benard instability.

When vertical magnetic fields were applied to the melt, the radial flow was suppressed due to the Lorentz force [15]. Consequently, the temperature gradient in the radial and vertical directions in the melt increases; so that the system becomes hydrodynamically unstable. Since the formation of the Benard cells relaxes the unstable temperature distribution, the system becomes more stable.

Calculated oxygen concentrations as a function of applied magnetic fields in the center of the crystal grown under a condition of type B are indicated

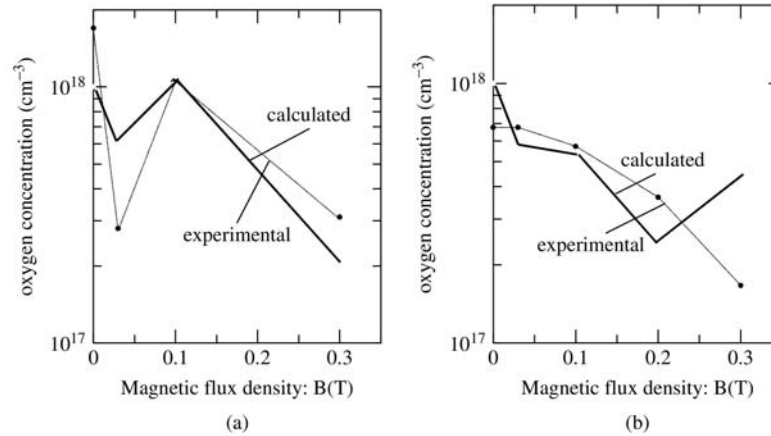


Figure 7.6 Calculated oxygen concentration as a function of magnetic fields for (a) type B and (b) type A.

in Figure 7.6(a) by the solid line. The broken line indicates the experimental results.

The absolute values of numerical results are slightly different from those of the experimental results. This discrepancy may be attributed to unreliable parameters such as the segregation coefficient, the evaporation rate at the free surface, and the dissolution rate at the melt/crucible interface used in the present numerical simulation. An anomaly in the oxygen concentration for both the experimental and numerical results was observed at 0.1 T in a case of type B, while the anomaly was not observed for the type-A heating system shown in Figure 7.6(b). The anomaly can be attributed to the formation of Benard cells, since the strength of the magnetic field in which the anomaly was observed was identical to that in the formation of Benard cells.

High oxygen concentration in crystals could be observed at the condition of the anomaly, since melt with high oxygen concentration transferred from the bottom to the crystal/liquid interface.

7.5 CUSP-SHAPED MAGNETIC FIELDS (CMF)

Two coils with a constant power (1120 A, 200 V) can produce three different types of CMF as follows. (1) The center of CMF was positioned 20 mm above the melt free surface, which was termed uppermost, (2) the distance was set to 10 mm, which was termed upper, (3) the center of CMF was positioned at the melt free surface (symmetric), (4) the center of CMF was positioned 10 mm below the surface (lower), (5) the distance was set to 20 mm below the surface, which was termed lowermost. Some of the configurations; uppermost, symmetric and lowermost are shown in Figure 7.7.

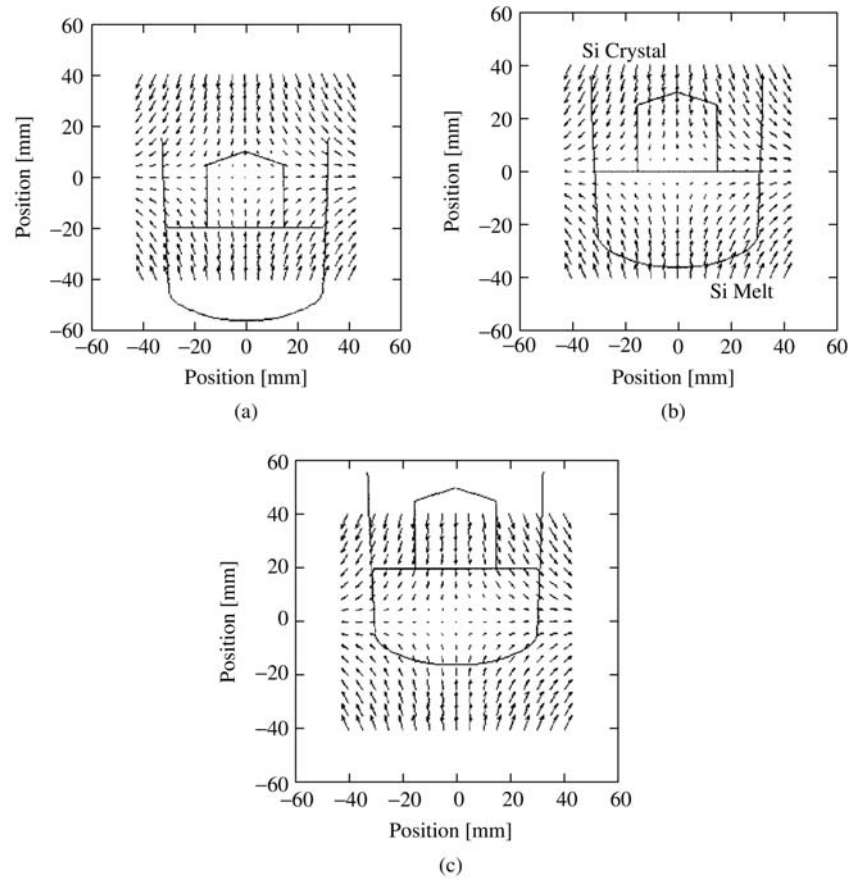


Figure 7.7 The configuration of CMF: (a) the center of CMF positioned 20 mm above the melt free surface (uppermost), (b) the center of CMF positioned at the melt free surface (symmetric) and (c) the center of CMF positioned 20 mm below the melt free surface (lowermost).

Figure 7.8 shows calculated profiles of velocity vectors in the r - z plane for cases of lowermost (a), symmetric (b) and uppermost (c) [18]. The strength of the vertical magnetic fields at the center of the crucible bottom was 0.06 T for a symmetric case (a). The velocity profile characteristics for the surface are as follows: the velocity vectors near the free surface are almost parallel to the magnetic field with a cusp-shaped magnetic field since a flow parallel to a magnetic field does not induce a Lorentz force.

Figure 7.9 [19] shows calculated results of oxygen radial distributions at the top of the melt for cases of lowermost (a), lower (b), symmetric (c), upper (d) and uppermost (e). The crucible rotation rate was set to -3 rpm. The full and broken lines represent experimental and calculated results, respectively. The calculated

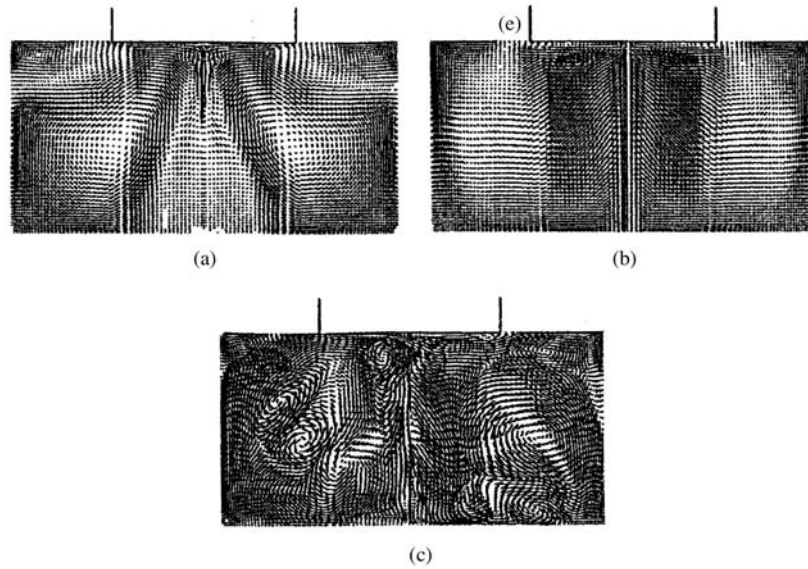


Figure 7.8 Velocity vectors under magnetic fields of the three types. (a), (b), and (c) correspond to cases symmetric and upper, and without magnetic fields, respectively.

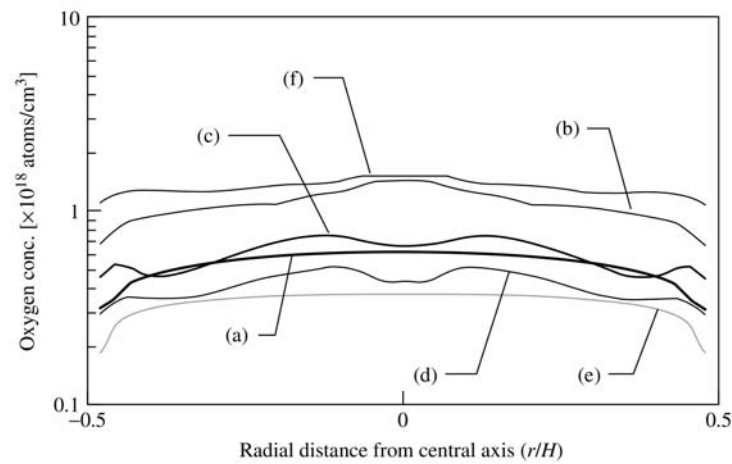


Figure 7.9 Oxygen concentration distribution at the interface along radial direction for cases of (a) lowermost, (b) lower, (c) symmetric, (d) upper and (e) uppermost.

results show that a homogeneous distribution with low oxygen concentration in the crystals can be achieved for upper, uppermost, and lowermost cases, while an inhomogeneous distribution and relatively high oxygen concentration was obtained in cases of lowermost and without the magnetic fields.

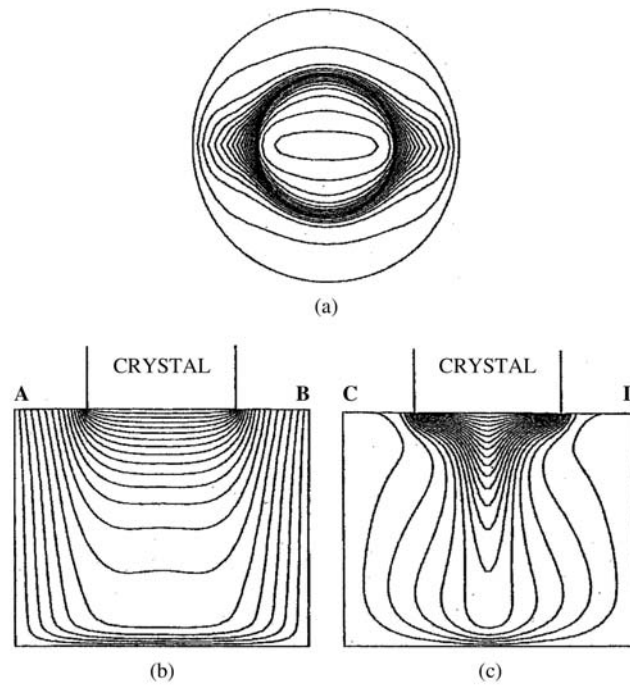


Figure 7.10 Temperature profiles in (a) planes horizontal, (b) planes parallel and (c) perpendicular to the magnetic fields.

7.6 TRANSVERSE MAGNETIC FIELDS (TMF)

Figures 7.10(a)–(c) [20] show temperature profiles of a horizontal plane, and of planes parallel and perpendicular to the magnetic fields in the melt under transverse magnetic fields, respectively. Figures 7.11(a)–(c), respectively, show velocity profiles in the melt in the same planes. Although crystal and crucible rotation rates were set to zero in this case, nonaxisymmetric temperature distribution can be recognized due to unidirectional magnetic fields, which induce nonaxisymmetric flow.

Therefore, the electric potential distribution in the melt becomes nonaxisymmetric as shown in Figure 7.12. These asymmetric temperature and velocity profiles might modify the oxygen concentration in the melt; therefore small oxygen concentration in the melt and crystal might be achieved. Further study should be carried out to clarify the mechanism of oxygen transfer in the melt.

7.7 SUMMARY

Molten silicon flow under magnetic fields of VMF, CMF, and TMF applied CZ crystal growth was discussed. Data obtained using an X-ray radiography

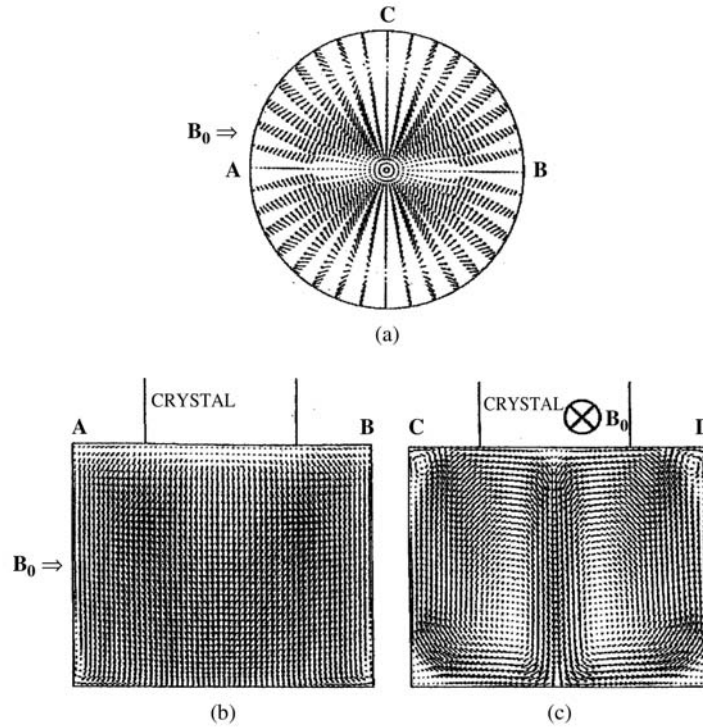


Figure 7.11 Velocity profiles in the melt in planes (a) horizontal, (b) parallel and (c) perpendicular to the magnetic fields.

technique were compared with the results of numerical simulation. In the VMF case, the flow velocity of axisymmetric flow decreased monotonically with increase of magnetic field strength in the range from 0 to 0.035 T. The analysis of flow-velocity reduction under VMF using a magnetic number M describes the reduction of flow velocity by the VMF.

For the case of CMF, molten silicon flow was discussed for three types of configuration between the center of CMF and the melt surface. The flow behavior in the CMF depended on the relative position between magnetic field and the melt.

Three-dimensional flow resulted in the case of TMF, since the distribution of the Lorentz force was nonaxisymmetric.

ACKNOWLEDGMENT

A part of this work was conducted as JSPS Research for the Future Program in the Area of Atomic-Scale Surface and Interface Dynamics.

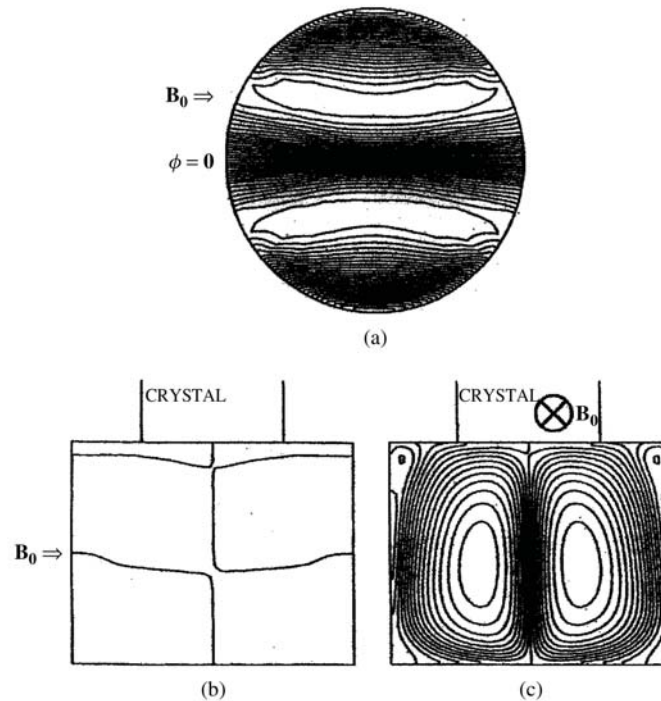


Figure 7.12 Electric potential distribution in the melt in the planes (a) at the top of the melt, (b) parallel and (c) perpendicular to the magnetic fields.

REFERENCES

- [1] H. Oya, Y. Horioka, Y. Furukawa and T. Shingyoji, *Extended Abstracts (The 37th Spring Meeting, 1990)*; The Japan Society of Applied Physics and Related Society.
- [2] M. Itsumi, H. Akiya and T. Ueki, *J. Appl. Phys.* **78** (1995) 5984.
- [3] S. Miyazawa, *Semi-Insulating III-V Materials* (1986) 3.
- [4] H. Yamagishi, I. Fusegawa, K. Takano, E. Iino, N. Fujimaki, T. Ohta and M. Sakurada, *Semiconductor Silicon* (1994) 124.
- [5] A. F. Witt, C. J. Herman and H. C. Gatos, *J. Mater. Sci.* **5** (1970) 882.
- [6] G. Meuller and R. Rupp, *Crystal Properties and Preparation*, Vol. 35 (Trans Tech. Switzerland, 1991) 138.
- [7] D. T. J. Hurle, *J. Cryst. Growth* **65** (1983) 124.
- [8] K. Hoshi, T. Suzuki, Y. Okubo and N. Isawa, *Extended Abstracts of E.C.S. Spring Meeting*, (The Electrochemical Soc., Pennington, 1980) 811.
- [9] T. Suzuki, N. Isawa, Y. Okubo and K. Hoshi, *Semiconductor Silicon 1981*, eds. H. R. Huff, R. J. Kriegler and Y. Takeishi (The Electrochem. Soc., Pennington, 1981) 90.
- [10] H. Hirata and N. Inoue, *Jpn. J. Appl. Phys.* **23** (1984) L527.
- [11] H. Hirata and K. Hoshikawa, *J. Cryst. Growth* **96** (1989) 747.
- [12] H. Hirata and K. Hoshikawa, *J. Cryst. Growth* **113** (1991) 164.

- [13] M. Watanabe, K. Kakimoto, M. Eguchi and T. Hibiya, *The American Society of Mechanical Engineerings, FED* (1991) 255.
- [14] K. Kakimoto, *Prog. Cryst. Growth Charact.* **30** (1995) 191.
- [15] K. Kakimoto, Y. W. Yi and M. Eguchi, *J. Cryst. Growth* **163** (1996) 238.
- [16] M. Watanabe, M. Eguchi, K. Kakimoto and T. Hibiya, *J. Cryst. Growth* **128** (1993) 288.
- [17] K. W. Yi, M. Watanabe, M. Eguchi, K. Kakimoto and T. Hibiya, *Jpn. J. Appl. Phys.* **33** (1994) L487.
- [18] K. Kakimoto, K. Eguchi and H. Ozoe, *J. Cryst. Growth* **180** (1997) 442.
- [19] M. Watanabe, M. Eguchi, K. Kakimoto and T. Hibiya, *J. Cryst. Growth* **193** (1998) 402.
- [20] Masato Akamatsu, Koichi Kakimoto and Hiroyuki Ozoe, *J. Mater. Process. Manuf. Sci.*, **5**, No. 4 (1997) 329.

8 Modeling of Technologically Important Hydrodynamics and Heat/Mass Transfer Processes during Crystal Growth

V. I. POLEZHAEV

*Institute for Problems in Mechanics, Russian Academy of Sciences 117526
Moscow, Prospect Vernadskogo 101*

8.1 INTRODUCTION

Development of the mathematical and physical modeling of crystal growth in recent years gives a precise and adequate description of the fluid flow for the given type of crystal growth models. Czochralski growth as a main industrial method (see overview and references in Hurle, 1993) receives the most effort hour after early studies of flow visualization (Carruthers, 1977) and direct numerical simulation of the fluid flow on the basis of Navier–Stokes equations using idealized Czochralski method for axisymmetrical case (Kobayashi and Arizumi 1980, Langlois, 1977, see references Langlois, 1985).

Over 30 years a number of overviews were published by Carruthers, 1977, Pimputkar and Ostrach, 1981, Polezhaev, 1981, Scheel and Sielawa, 1985, Muller, 1988, Brown, 1988, Polezhaev, 1994, Dupret and Van Den Bogaert, 1994, Muller and Ostrogorsky, 1994 and many others. However, due to the nonlinear and multiparametrical nature of the problem of fluid flow in crucibles is not solved as yet. Development of direct numerical modeling on the basis of unsteady three-dimensional Navier–Stokes equations opens up new possibilities for analysis of most technologically important features of fluid flow and transport. However, a new problem of analysis of the complex fluid flows appears as well as development of special methodology – how to use most efficiently this ‘store of knowledge’ for improvement of technology and quality of crystals.

During the last decade analysis of axisymmetrical models was continued by Bottaro and Zebib 1988, Fontaine, *et al.* 1989, Sacudean, *et al.* 1989, Buckle and Schafer 1993, Kobayashi 1995, Mukherjee *et al.*, 1996, Polezhaev *et al.*, 1997 and many other studies. A new attack on this problem was attempted

in the last decade using direct 3D modeling (Bottaro and Zebib, 1989, Leister and Perec, 1992, Seidi *et al.*, 1994, Xiao and Derby, 1995). In more recent years a number of runs were done for parameters close to the instability (Yi *et al.*, 1995b, Nikitin and Polezhaev, 1999). Recently, direct simulation using 3D unsteady Navier–Stokes equations for the chaotic regime was done by Wagner and Friedrich, 1997. Nikitin and Polezhaev, 1999a, b presented results of transient and chaotic regimes for a benchmark configuration (Wheeler, 1991). Qualitative analysis using available knowledge of different types of instabilities (Carruthers, 1977, Polezhaev, 1984, Ristorcelli and Lumely, 1992) shows a comprehensive picture of the possible mechanisms of instabilities in Czochralski method. However, quantitative results of the values of critical governing parameters such as Grashof and Reynolds numbers for Czochralski model are very restricted.

Critical Grashof numbers for the onset of convective instability and temperature oscillations in an idealized Czochralski model for the 3D case were found by Polezhaev *et al.* 1997, Nikitin and Polezhaev, 1999a and b. Knowledge of the instabilities are not detailed in comparison with classical problems in fluid mechanics such as spherical Couette flow (Beliaev, 1997) or isothermal fluid flow in enclosures with lid rotation (Gelfgat *et al.*, 1996), however, progress is rapid in this direction. Because of the multiparametrical nature, multiscale, unsteady, spatial structure of the fluid flow as well as nonlinearity, instability in the real range of parameters and special technology demands control of the crystal quality and yields methods of the technological hydrodynamics as a separate discipline for quantitative analysis should be focused on the idealized Czochralski model.

Physical modeling using visualization techniques plays an important role in this concept. In the last decade a number of studies were carried out (Jones, 1984, Berdnikov *et al.*, 1990, and recently by Verezub *et al.*, 1995, Kosushkin, 1997, Krzyminski and Ostrogorsky, 1997). High Pr number transparent liquids are used in most cases and low Pr number melt in recent work for molten hot solution. For the lowest Pr number for semiconductor melts (real silicon melts) an X-ray technique was developed (Kakimoto *et al.*, 1989). For GaAs melt a special system was developed with a ceramic imitation crystal (Kosushkin, 1997). Control of the boundary conditions is one of the problems for quantitative comparison simulation and experimental data (Kakimoto *et al.*, 1989, 1993, Mukherjee *et al.*, 1996, Polezhaev, 1998). This problem needs special efforts and is not discussed here.

This chapter, following the strategy and methods of our previous works, presents a summary of the recent activity of the mathematical modeling by author and his colleagues (Polezhaev *et al.* 1997 and 1998, related to the benchmark problem (Wheeler, 1991) and extension of the benchmark problem to three-dimensional regimes using direct numerical modeling and linear-stability analysis. The hierarchy of the models is discussed and new results of multiparametrical research using parameters of the idealized industrial LEC GaAs configuration, and specialized computer video techniques are presented.

8.2 TECHNOLOGICALLY IMPORTANT HYDRODYNAMICS PROCESSES DURING CRYSTAL GROWTH

One of the well-known characteristics of the grown crystal is macroinhomogeneity, induced by impact of gravity-driven convection on the bulk segregation. It was found first for enclosures (cylinder, sphere, square, Polezhaev, 1974) and for the 2D Bridgman configuration: horizontal (Polezhaev *et al.* 1981 (see references Polezhaev, 1984), for 3D in a horizontal layer by Polezhaev *et al.* 1998c and axisymmetric vertical (Brown, 1988, Motakef, 1990). Spreading of the maximum of temperature/concentration macroinhomogeneity, induced by thermal gravity-driven convection in the cases of forced, buoyancy, and surface-tension driven convection under gravity/magnetic fields in uniform and conjugated cases are realized (see references in Polezhaev, 1992). The value of this maximum strongly depends on the crystallization rate and is of interest in low gravity (Alexander, 1990).

For the ground-based environment the problem of the 'optimal mixing' (how to provide transport of the species to the front and avoid striations due to instability) is of particular interest. The accelerated crystal/crucible rotation technique (ACRT) was proposed by Scheel, 1972 and efficiently used for high-temperature solution growth (see references in Scheel and Sielawa, 1985). However, as was discussed in the cited paper, the problem for semiconductor melts is more complicated. One of the possible domains on the amplitude-frequency diagram was found for real material and configurations in the cited paper. Note that for modern crystal growth applications the famous qualitative picture of the complex fluid flow in a crucible (Scheel and Sielawa, 1985) which includes forced types of flows like elementary Cochran, Taylor–Proudman-type, thermal convection including Rayleigh–Bernard and Marangoni flows should be realized in quantitative form, using realistic boundary conditions and taking into account nonlinear coupling phenomena, spatial effects, etc.

There are a number of new promising methods of control, using dynamical/thermal actions on the melt. Vibration of the seed is one of the possible control features (Verezub *et al.*, 1995). Acoustic control action (Kozkemiakin *et al.* 1992) is one of the so-called 'low energetic' possibilities for control of the transport phenomena during crystal growth. Temporal oscillations of the power heater (Zakharov *et al.*, 1998) is also one of them. The key problem of how to find 'optimal parameters' consists in using quantitative analysis of the fluid flow/transport fields in the general case of industrial regimes with coupling convection and rotation in the Czochralski model. This will be discussed below in Section 8.6.

Because of the trend to large-scale bulk-crystal production, inhomogeneities in transition and turbulence regimes as well as in the limiting case of the statistically average temperature on inhomogeneities in the Czochralski model as well as convective instabilities induced by the forced flows instabilities and nonlinear interaction of the forced and natural convection are of special interest

now. Three-dimensional effects and asymmetry of the transport processes were studied by Polezhaev *et al.* 1998c. Order structure and spoke patterns in 3D convection were studied both experimentally and theoretically by Yi *et al.* 1995b). Characteristics of fluid flow in transient and turbulent regimes for the Czochralski model are one of the problems. There are only a few papers in this area (Berdnikov *et al.*, 1990, using physical experiments, Wagner and Friedrich, 1997 using mathematical modeling – with surface-tension driven effects on the melt surface and Nikitin and Polezhaev, 1999 – with gravity-driven convection). The above-mentioned problems correspond to the ‘optimal mixing’ as one of the key problem. For multiparametrical computer optimization adequate and operative computer tools are needed. Common and specialized models as well as techniques of multiparametrical analysis transition and turbulent fluid flows and, specifically, evaluation of 3D effects and comparison with axisymmetrical 2D one should be developed also for clear understanding of fluid-flow phenomena in a crucible.

We will focus below on new results concerning elementary critical values of the onset of the oscillations, induced by thermal gravity-driven convection as the leading mechanism, coupling with forced convection due to crystal/crucible rotation, including effects of 3D instability on the basis of the unsteady two- and three-dimensional models in the industrial technological range of parameters, which are unknown as yet.

8.3 BENCHMARK PROBLEM

The problem formulation and a range of problem parameters are described in the axisymmetrical case as suggested by Wheeler, 1991 and will be used below. The geometry of the problem is a vertical cylindrical crucible radius R_c , which is filled by the melt to the height H (Figure 8.1). The crucible can be rotated with constant angular velocity Ω_c and it is in a constant gravitational field with acceleration g . In the center of the upper free surface of the melt is placed the crystal of radius R_s . The crystal can be rotated with constant angular velocity Ω_s . It is supposed that the temperature T_s of the crystal surface is constant, the temperature of crucible side wall is T_c and the crucible bottom is adiabatic. The melt surface between crystal and crucible wall is free and plane and its temperature is a linear function of radius. It is supposed that the melt is a Boussinesque fluid and the flow is axisymmetrical.

Unsteady Navier–Stokes equations in velocity and pressure variables and the temperature equation using a cylindrical coordinate system (r, z) and nondimensional variables can be written in the following form:

$$(1/r)\partial(ru)/\partial r + \partial w/\partial z = 0 \quad (8.1)$$

$$\partial u/\partial t + u\partial u/\partial r + w\partial u/\partial z - v^2/r = -\partial p/\partial r + \nabla^2 u - u/r^2 \quad (8.2)$$

$$\partial v/\partial t + u\partial v/\partial r + w\partial v/\partial z + uv/r = \nabla^2 v - v/r^2 \quad (8.3)$$

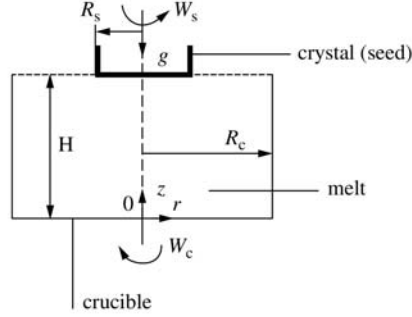


Figure 8.1 Scheme of the mathematical model of idealized Czochralski growth.

$$\partial w / \partial t + u \partial w / \partial r + w \partial w / \partial z = -\partial p / \partial z + \nabla^2 w + \text{Gr}T \quad (8.4)$$

$$\partial T / \partial t + u \partial T / \partial r + w \partial T / \partial z = (1/\text{Pr}) \nabla^2 T \quad (8.5)$$

Boundary conditions:

$$\begin{aligned} u = w = \partial T / \partial z = 0, \quad v = r \text{Re}_c & \quad \text{for } 0 \leq r \leq 1, \quad z = 0 \\ u = w = 0, \quad v = \text{Re}_c, \quad T = 1 & \quad \text{for } r = 1, \quad 0 \leq z \leq \alpha \\ \partial u / \partial z = \partial v / \partial z = w = 0, \quad T = (r - \gamma) / (1 - \gamma) & \quad \text{for } \gamma \leq r \leq 1, \quad z = \alpha \\ u = w = T = 0, \quad v = r \text{Re}_s & \quad \text{for } 0 \leq r \leq \gamma, \quad z = \alpha \\ u = v = \partial w / \partial r = \partial T / \partial r = 0 & \quad \text{for } r = 0, \quad 0 \leq z \leq \alpha \end{aligned} \quad (8.6)$$

Here t -time, u, v, w -radial, azimuthal and axial components of velocity vector, p -pressure, T -temperature,

$$\nabla^2 = (1/r)(\partial / \partial r(r \partial / \partial r)) + \partial^2 / \partial z^2$$

Nondimensional variables are introduced in the following way (dash over symbol denotes dimensional value)

$$\begin{aligned} (r', z') &= R_c(r, z) \\ (u', v', w') &= (v/R_c)(u, v, w) \\ p' &= (\rho v^2 / R_c^2) p - \rho R_c g z \\ t' &= (R_c^2 / \nu) t \\ T' &= T_s + (T_c - T_s) T \end{aligned}$$

There are the following nondimensional parameters in the equations and in the boundary conditions:

Two nondimensional geometrical parameters

$$\alpha = H/R_c, \quad \gamma = R_s/R_c$$

$Pr = \nu/\kappa$ – the Prandtl number

$Re_s = \Omega_s R_c^2/\nu$ – the crystal Reynolds number

$Re_c = \Omega_c R_c^2/\nu$ – the crucible Reynolds number

$Gr = g\beta(T_c - T_s)R_c^3/\nu^2$ – the Grashof number.

Here ν –kinematical viscosity, β –thermal expansion coefficient, ρ –melt density, κ –temperature conductivity.

For the benchmark configuration Wheeler, 1991 supposed for all test variants $H/R_c = 1.0$, $R_s/R_c = 0.4$, and $Pr = 0.05$. The values of other parameters are given in (Wheeler, 1991, Buckle and Schafer, 1993). Benchmark cases are as follows: A1, A2, A3 – $Re_s = 10^2, 10^3, 10^4$ and C1, C2, C3 – $Gr = 10^5, 10^6, 10^7$. One can see other benchmark cases in Table 8.1.

The typical characteristic (for instance, amplitude of the temperature oscillations or value of macroinhomogeneity, etc.) of the fluid flow/transport in the melt

Table 8.1 Numerical results for benchmark configuration (axisymmetrical case)

Regime	Gr	Re_s	Re_c	Buckle and				
				Bessonov	Schafer	S. Nikitin	Ermakov	N. Nikitin
A1	0	1.E2	0	−0.2198	−0.2345	−0.2198	−0.2172	
A2	0	1.E3	0	−5.0587	−5.3642	−4.9254	−5.0344	
A3	0	1.E4	0	−43.119	−40.443	−51.805	−43.206	−42.778
B1	0	1.E2	−2.5E1	−0.0454	−0.0502	−0.0475	−0.0452	
				0.1183	0.1180	0.1167	0.1186	
B2	0	1.E3	−2.5E2	−1.5061	−1.6835	−1.5301	−1.5097	
				1.1812	1.2414	1.1430	1.1832	
B3	0	1.E4	−2.5E3	−8.3106	−8.5415	−9.1298	−8.6607	−8.0881
				5.4813	5.2708	4.7729	5.5192	5.4294
D3	1.E5	1.E3	0	25.106	24.829	24.871	25.121	
C1	1.E5	0	0	28.440	28.437	28.404	28.420	
C2	1.E6	0	0	92.930	92.100	92.518	92.690	

Characteristics of the formulations and numerical schemes are shown below

	Bessonov	Buckle & Schafer	S. Nikitin	Ermakov	N. Nikitin
Mesh r, z	80×64	64×64	80×80	80×80	64×64
Numerical scheme	FV	FDM	FDM	CVM	FDM/S
Formulation	Velocity	Velocity	Vorticity	Velocity	Vorticity
	Pressure	Pressure	Stream f.	Pressure	Velocity

for the Czochralski model may be written as follows:

$$A = f(\text{Re}_c, \text{Re}_s, H/R_c, R_s/R_c, \text{Gr}, \text{Pr}, b\gamma, b\gamma_0) \quad (8.7)$$

Here $b\gamma$, – type of boundary conditions and $b\gamma_0$ – type of initial values.

Motivation of the benchmark problem (besides being a problem of experimental study and difficulty for computer resolution of the fine boundary layer, secondary structures, etc.), presented by Wheeler, 1991 and confirmed now, is that the characteristic function A of the fluid flow in the melt is multiparametrical even for the simplified (idealized) model of Czochralski growth for unicomponent melt flow without Marangoni convection, radiation, etc. Two geometrical parameters, H/R_c , R_s/R_c , two dynamical parameters for forced fluid flow – Re_c , Re_s and one – Gr number – for gravity-driven natural convection, and Pr number as the parameter of physical properties, $b\gamma$ – type of boundary conditions, $b\gamma_0$ – type of initial values are very important for convection and heat transfer. It should be taken into account that during crystal growth some of parameters, for instance, H/R_c , as well as Gr and $b\gamma$ are time-dependent functions. Therefore the problem of fluid flow in the Czochralski model initiates the development of analysis of gravity-driven and rotational low Prandtl melt flow – nonlinear interaction, temperature oscillations, transition to chaos as a fundamental fluid dynamics problem in such a complicated situation.

It should be noted that in the early statement of the problem (Langlois, 1985) it was other additional factors such as radiation, Marangoni effect, magnetic fields, which are important for technological needs, but this makes the problem more complicated for analysis and control. This is why the so important thermal control parameter as temperature boundary conditions ($b\gamma$) was not discussed enough on the early stage of research. Because of the multiparametrical nature of the problem the parameters of crystal growth are different for most of the published works. A number of other peculiarities exist for real crystal technologies of the above-mentioned crystals: silicon (Kakimoto *et al.*, 1993, bottom cooling, $\text{Pr} = 0.01$), GaAs (Zakharov *et al.* 1998, bottom heating, adiabatic melt surface, $\text{Pr} = 0.07$) with counterrotation for semiconductors and rotation of the crystal for oxides (Xiao and Derby, 1995, adiabatic bottom, $\text{Pr} = 8$). There are different configurations when using special liquids for modeling: Berdnikov *et al.*, 1990 (water, $\text{Pr} = 7$, alcohol, $\text{Pr} = 15$), Mukherjee *et al.*, 1996 (silicone oil, $\text{Pr} = 890$), Krzysinski and Ostrogorsky, 1997 (NaCl-CaCl_2 melt, $\text{Pr} = 0.5$). Kobayashi, 1995 reported results of a multiparametrical analysis, using $H/R_s = 2.0$, $R_c/R_s = 2.5$, $\text{Pr} = 1$, with the Marangoni effect and pulling velocity, however, without information related to the calculations, type of boundary conditions and initial values and different scales for nondimensional parameters. This situation does not help the analysis of a general picture of the fluid flow. Therefore the basic configuration for benchmark calculation and multiparametrical research is useful.

Certainly, the above-mentioned statement does not cover all important problems. In Polezhaev *et al.* 1998, and Nikitin and Polezhaev 1999b this benchmark

problem was extended to the case of 3D Navier–Stokes equations. The general 3D case will be taken into account below (Section 8.4.6). Bottom heating for a GaAs crucible (Zakharov *et al.*, 1998) with an adiabatic melt surface and counter-rotation is another typical configuration that we propose for systematically research (Section 8.6).

8.4 HIERARCHY OF THE MODELS AND CODES AND SUMMARY OF BENCHMARK EXERCISES

Unsteady Navier–Stokes equations for the 3D case is a very delicate model and it is rational to develop a hierarchy of the models and codes on the basis of this system. New tools for modeling that were developed by the author and his colleagues during recent years in the IPM RAS are briefly described below with comments and a summary of the benchmarking results (references are made mainly to original methods and software). The sequence of these tools is as follows:

(1) Elementary two-dimensional nonlinear convective processes in enclosures for cartesian and cylindrical coordinates

A common PC-based system COMGA (computer laboratory) which includes a user-friendly interface and video visualization is an efficient tool for research and elucidation of unsteady convective processes on the basis of Navier–Stokes equations, specifically for the initial stage (Ermakov *et al.* 1992, Ermakov *et al.* 1997). This system includes most of the technologically important hydrodynamics, heat/mass transfer processes during crystal growth as mechanical (forced) convection (rotation, vibration and coupling) gravity-driven and surface-tension-driven. For nonuniform media each of these groups also consists of several elementary processes dependent on the direction of the heat/mass flux. For instance, the gravitational-type convection in a binary (double-diffusion) system consists of ten cases for different mutual directions of heat and mass flux and gravity vector. A similar situation exists for surface-tension-driven convection in a binary system with different mutual directions of heat and mass flux and free surface vector and the same for other groups of driven forces. Well-known international benchmark problems (De Vahl Davis and Jones, 1983, B. Roux, 1990) and different classical problems such as Rayleigh–Bernard, Marangoni, dynamical control actions with different angles of inclination, vibration, rotations have been analyzed during recent years (see classification and extended references Ermakov *et al.*, 1997). The computer laboratory also includes possibilities for analysis transient and chaotic fluid flow for all of the above-mentioned elementary processes.

(2) Axisymmetrical idealized Czochralski model.

The statement of this problem corresponds to Equations (8.1)–(8.7). Special versions of the above-mentioned system for the axisymmetric idealized Czochralski model, named ‘Intex’ (Ermakov *et al.*, 1997) and video techniques for visualization and saving of information, television and video recorder, as well as software for presentation are developed for this goal. A film for 200 s

of a calculation run was presented by 2000 files that took up 37.7 Mb. Graphic information with 3400 Mb can be saved on a three-hour videocassette, which is efficient for multiparametrical computer modeling. Examples of the videofilm pictures are shown in Figures 8.2–8.4. The central difference approximation was used for the benchmark problem. Calculations were made on the uniform grids 21×21 , 41×41 , 81×81 for each variant to investigate the convergence of solutions. The results are given in Polezhaev *et al.* (1998d). Coincidence of results obtained with the data of the work of Buckle and Schafer, 1993 for variants C1 and C2 (thermal convection only) can be considered as good, but such coincidence is absent for variants A1–A3 (rotation of crystal). The discrepancy, for example, in the case of the slow flow regime A1 ($Re_s = 100$) is large for such fine grids. The calculations also show that the accuracy of results becomes worse

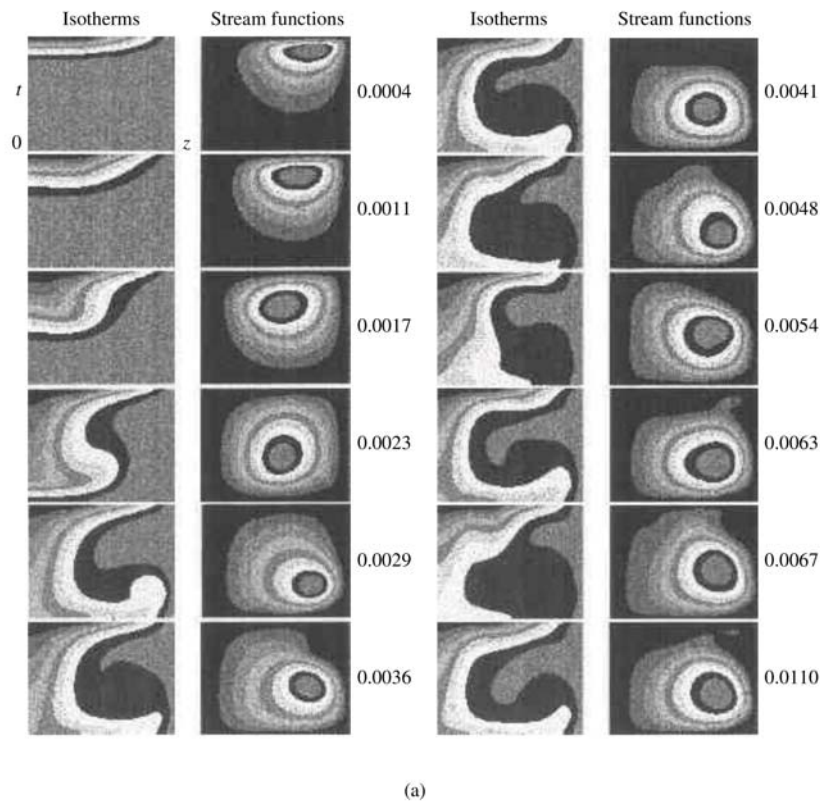


Figure 8.2 Temporal behavior of the temperature/isolines of stream function for benchmark problem ($Gr = 6 \times 10^6$, $W_s = W_c = 0$). Values on the right show nondimensional time: (a) linear temperature profile on the melt surface, (b) adiabatic boundary conditions on the melt surface.

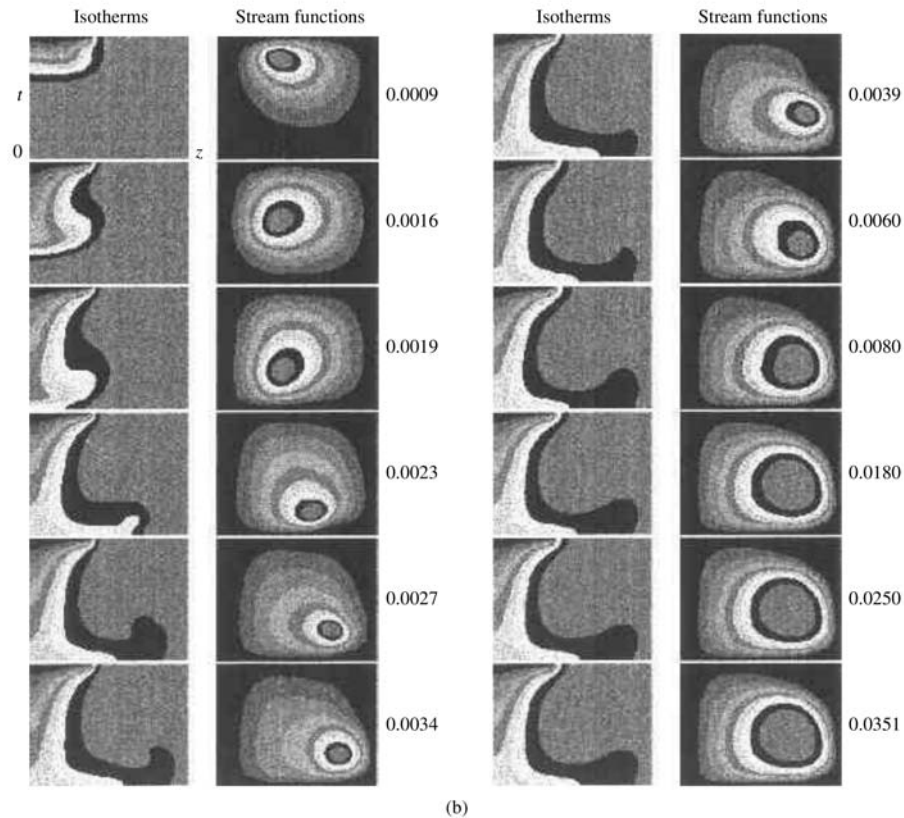


Figure 8.2 (continued).

when there is a counteraction of different mechanisms of flow (thermal convection, rotation of crystal and crucible). For variant C3 ($Gr = 10^7$) the oscillation regime of flow was obtained. A number of calculations were made to find the critical Grashof number that takes place for Grashof numbers between 2×10^6 and 3×10^6 .

Besides this common type of system two other methods (control volume schemes for primitive – velocity-pressure formulation and spectral-difference) were employed. The first one is based on an implicit variant of the splitting method on a staggered mesh. Second-order derivatives (central differences for convective terms) are used. Calculations were made on the uniform meshes up to 160×160 . For variant C3 ($Gr = 10^7$) in comparison with the same results in work Polezhaev *et al.*, 1998d. Coincidence nonperiodic oscillations were obtained instead of periodic ones in the mark of Buckle and Schafer, 1993. For the second method, based on the spectral-difference scheme (Nikitin, 1994) there is the best correlation for the ψ_{\max} related to the C2 problem: asymptotic value

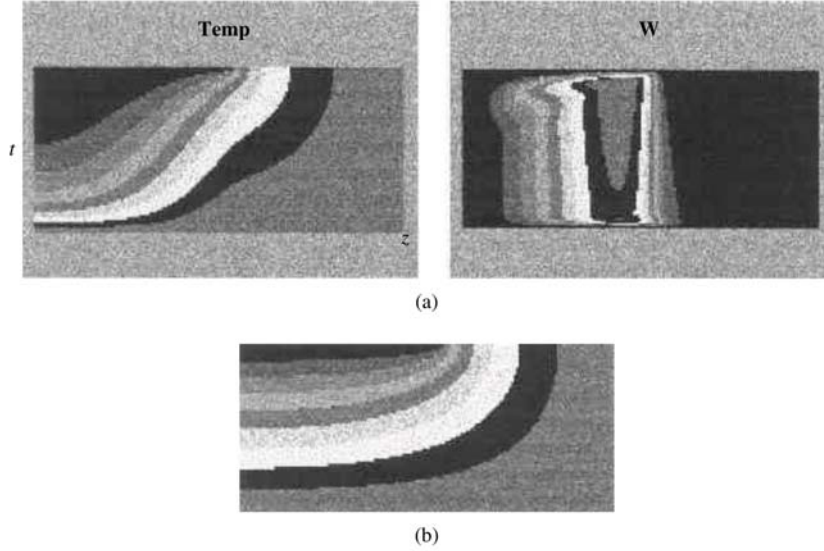
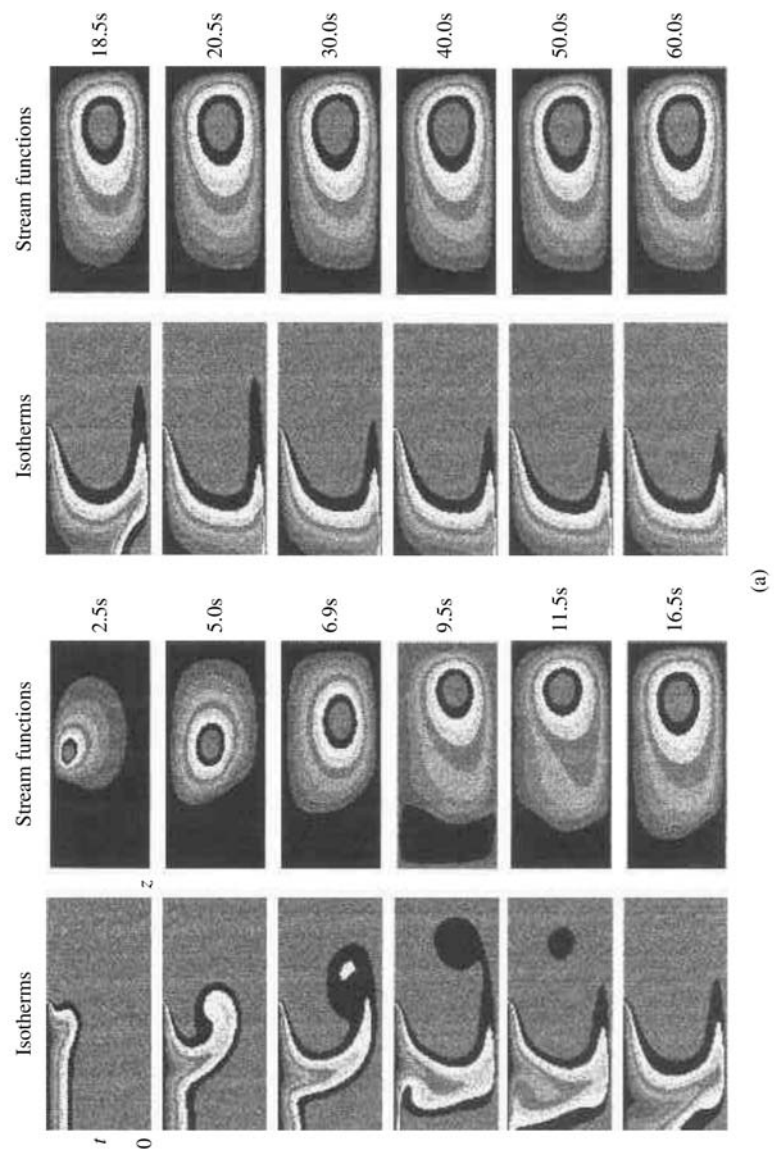


Figure 8.3 Temperature/flow fields (forced convection and temperature fields without convection, steady-state regime) for the model of Czochralski growth of GaAs (axisymmetrical case). (a) isotherms left/stream and functions (right) without thermal convection. Steady-state regime. ($Gr = 0$ $W_s = -6$ rpm, $W_c = 16$ rpm); (b) isotherms without convection and rotation. Steady-state regime. ($Gr = W_s = W_c = 0$).

$\psi_{\max} = 93.179$ (1.2 % difference from the results of the work of (Buckle and Schafer, 1993) (64×64) and 0.7 % for the same result by FDM (81×81). However, for B3 the asymptotic value $\psi_{\max} = 55.833$, which is 5.6 % different from the work of Buckle and Schafer, 1993 and 14.5 % from the same result of FDM. Nonperiodic behaviour of the temperature oscillations was also achieved by this method for the problem C3. Using this method, the critical value onset of oscillations was calculated. The most exact critical Grashof value for the onset of temperature oscillations for $Re_s = Re_c = 0$ using the axisymmetrical approach was found as $Gr_c = 2.5 \times 10^6$, which is well correlated with the same result with the use of FDM.

Table 8.1 presents comparisons of results in the work (Polezhaev *et al.*, 1998a) for different regimes of the benchmark ($H/R_c = 1$, $R_s/R_c = 0.4$, $Pr = 0.05$, linear temperature profile on the surface melt), with the uniform meshes used – from 64×64 to 80×80 . Values of the minimum (regimes A1, A2, A3, B1, B2, B3) and maximum (regimes B1, B2, B3, D3, C1, C2) of stream functions are shown. One can see that correlations of the results is adequate for steady-state regimes using such a uniform mesh. However, it is not so simple to provide accurate calculation results of the temperature oscillation even for the axisymmetrical model (Nikitin and Polezhaev, 1999a). Therefore stability analysis is a very important tool in this case.



(a)

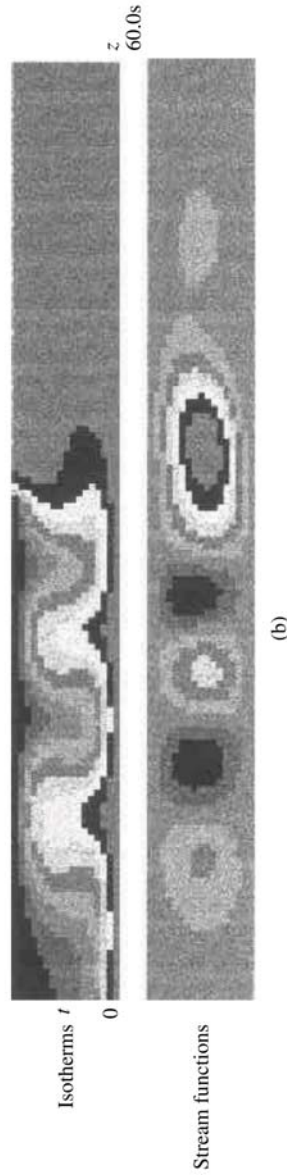
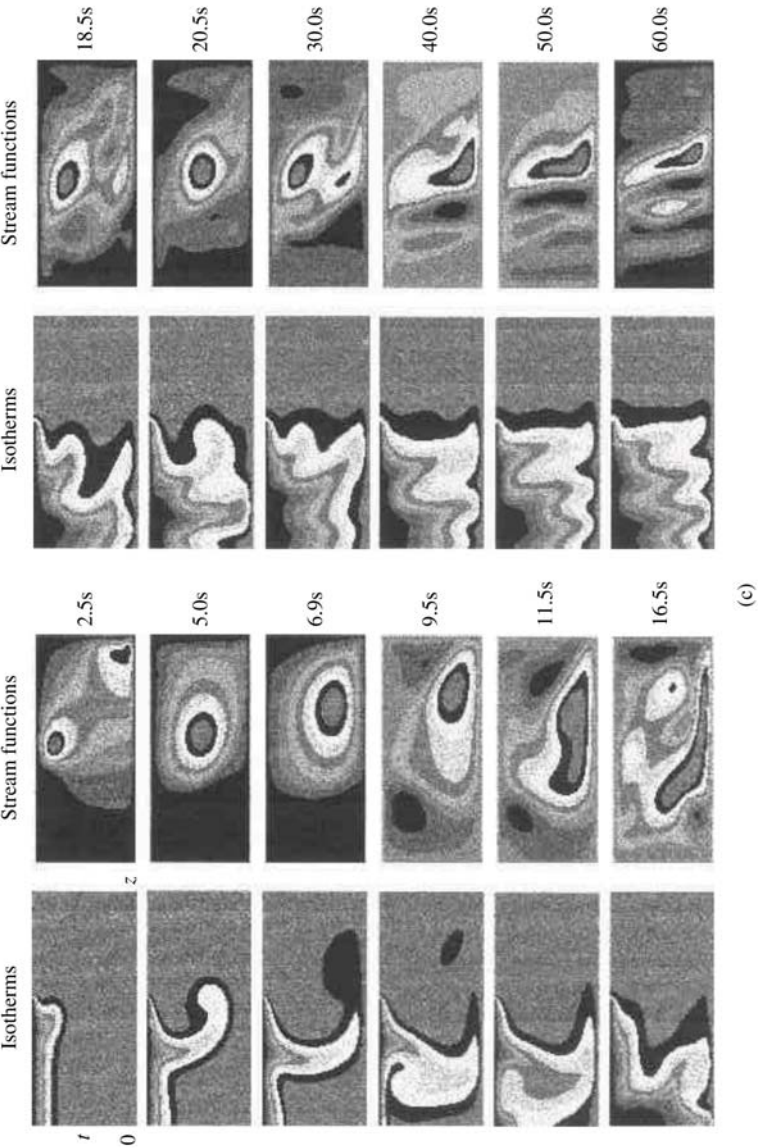
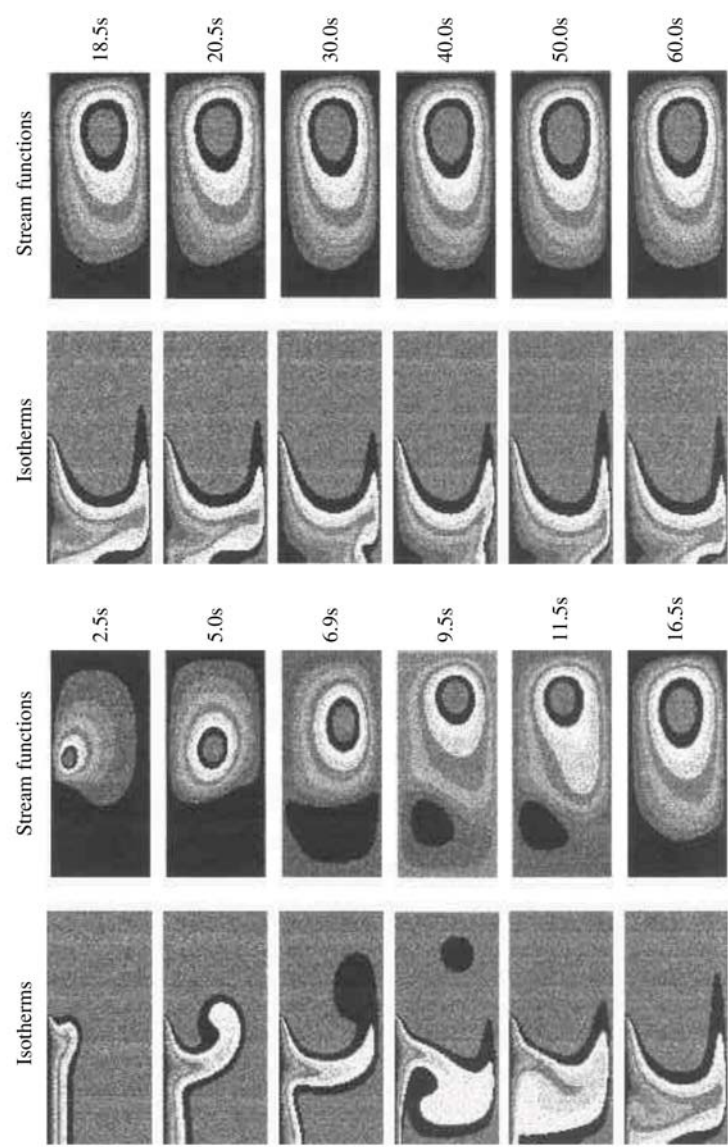


Figure 8.4 Interaction of gravity-driven and forced convection and instabilities for the model of Czochralski LEC growth of GaAs (axisymmetrical case) values on the right show dimensional time in seconds: (a) evolution of the thermal convection without rotation ($Gr_c = 7.8 \times 10^7$, $W_s = W_c = 0$); (b) convective cells of the Rayleigh–Bernard type of thermal convection for the case of reduced melt level ($H = 1$ cm); (c) evolution of the thermal convection and counter-rotation of crystal/crucible ($Gr = 7.8 \times 10^7$, $W_s = -6$ rpm, $W_c = 16$ rpm); (d) evolution of the thermal convection and crystal rotation ($Gr = 7.8 \times 10^7$, $W_s = -6$ rpm, $W_c = 0$); (e) evolution of the thermal convection and crucible rotation ($Gr = 7.8 \times 10^7$, $W_s = 0$, $W_c = 16$ rpm).





(d)
Figure 8.4 (continued)

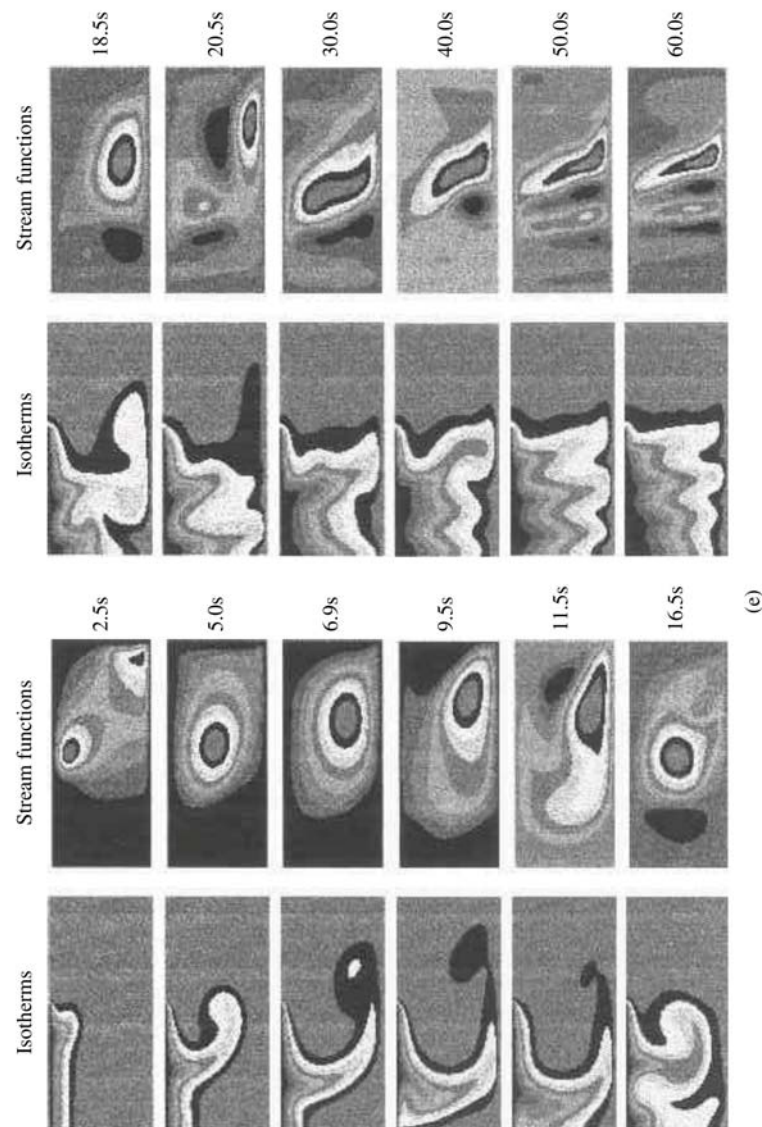


Figure 8.4 (*continued*)

(3) Direct numerical simulation of three-dimensional equations for the Czochralski model.

Using the spectral-difference method 2D and 3D problems as well as linear analysis were carried out (Nikitin and Polezhaev, 1999a, Polezhaev *et al.*, 1998b). The governing system of equations for the spectral-difference method is written for velocity-vorticity variables in the next vector form:

$$\begin{aligned}\partial V / \partial t &= V \times \omega - \nabla \pi - \nabla \times \omega + GrTk_z \\ \nabla V &= 0 \\ \omega &= \nabla \times V \\ \partial T / \partial t + \nabla(VT) &= (1/Pr)\nabla^2 T\end{aligned}$$

Here $V(t, r, \theta, z)$ – velocity, $\omega(t, r, \theta, z)$ – vorticity, $\pi = P/\rho + V^2/2$, $P(t, r, \theta, z)$ – pressure, ρ – density, k_z – unit vector along z -axis. Definitions of the nondimensional Gr and Pr numbers are the same as above, as well as boundary and initial values, α , γ , Re_s and Re_c . For direct numerical simulation, spectral (Fourier) representations in the azimuthal direction and finite-difference approximations with staggered grids in radial and axial directions were used (Nikitin, 1994). The time advancement is performed by a semi-implicit Runge–Kutta scheme. Using direct simulation all the above-mentioned benchmark problems were carried out (Nikitin and Polezhaev, 1999a).

(4) Three-dimensional linear stability analysis code for Czochralski model.

For stability analysis small three-dimensional perturbations are superimposed on the steady axisymmetric solution and their behaviour is considered within linearized Navier–Stokes equations. The linear stability analysis code for Czochralski model developed by Nikitin (Nikitin and Polezhaev, 1999b) includes procedures for calculation of the axisymmetrical flow and temperature fields, input of the 3D disturbances and calculation of the disturbances evolution. It is possible, using this technique, to analyze types of instabilities (monotonic, oscillatory). Using stability analysis the critical Grashof (Reynolds) number for onset of flow/temperature oscillations in the three-dimensional case may be defined following the evaluation of the temperature disturbances T' in the fixed point and estimate the function $A^n(t)$ were

$$(A^n(t))^2 = (1/2\pi) \sum_0^{2\pi} (T'^n(t, r_o, z_o, \theta))^2 d\theta$$

One can find examples of the growth of function $A(t)$ for different modes in paper Nikitin and Polezhaev, 1999a (see also Section 8.6.2a). Using the above-mentioned parameters of the benchmark configuration, the critical Grashof number for gravity-driven convection (oscillatory for linear temperature distribution on the surface melt and monotonic for adiabatic melt) were found for

the 3D case (Nikitin and Polezhaev, 1999a). Validation of the stability analysis was checked, using direct numerical calculations of the 3D Navier–Stokes equations (Nikitin and Polezhaev, 1999, Polezhaev *et al.*, 1998, see additional information and examples in Section 8.5 and in Section 8.6.2(a) and (b).

(5) Global thermal approach and thermostresses simulation for axisymmetrical Czochralski model.

This approach is widely used now (see Dupret and Van Den Bogaert, 1994, Muller, Ostrogorsky, 1994). The model developed by (Griaznov *et al.*, 1992) includes the crystallization front, heat transfer in crystal, radiation and the field of thermostress. However, this approach is not used at this stage of research to make precise analysis of the fine structure of the fluid flow for analysis of the hydrodynamical reasons of the crystal quality and is very restricted in multiparametrical control possibility analysis. Baumgartl *et al.* (1993) carried out global simulation of heat transport including melt convection in a Czochralski crystal-growth process.

8.5 GRAVITY-DRIVEN CONVECTION INSTABILITY AND OSCILLATIONS IN BENCHMARK CONFIGURATION

Using the linear stability technique the critical Grashof number for onset of temperature oscillations in the three-dimensional case was defined following the evaluation of the temperature disturbances, as described above (Nikitin and Polezhaev, 1999a). The critical Grashof number for onset of temperature oscillations due to convective instability in the benchmark example (linear temperature profile on the melt surface and adiabatic crucible bottom) is found to be 5.5×10^5 for the 3D case (2.5×10^6 in the axisymmetrical case). For $Gr_c > 6 \times 10^6$ nonregular oscillations are developed in the 2D case. Thermal isolation of the melt surface eliminates the temperature oscillations in the melt and the critical Grashof number is higher: $Gr_c = 1.2 \times 10^6$ for the 3D case ($Gr_c > 10^7$ for the axisymmetrical case).

Within these benchmark parameters special attention is paid to the structure of the temperature field during temperature oscillations and the possibility of damping using the temperature regime on the surface melt. Figure 8.2(a) shows isotherms and isolines of stream functions for $Gr = 6 \times 10^6$ without crystal/crucible rotation (benchmark case C2). Initial values were zero velocity and uniform temperature fields inside the melt with instantaneous cooling of the crystal (disc). There are three stages on this figure. First, development of the convective flow and temperature front propagation (until $t = 0.023$, when this front reaches the bottom and a boundary layer is developed on the heated side wall of the crucible. Second, penetration of the heated portion of the melt to the core of the melt (until $t = 0.048$), cooling and dissipating. After that (third stage) a new portion of the heated fluid is coming from the side wall to the top and so on. Videofilm shows this mechanism very clearly. Figure 8.2(b) shows the same run

with only one change – an adiabatic melt surface. For this case stable stratification suppresses the above-mentioned mechanism of the periodic penetration and cooling of the heated layer from the side wall. This is why the critical Grashof number for onset of oscillations in this case for the axisymmetrical approach is more than 10^7 .

Verification of these critical values in the 3D case was done by direct numerical calculation of full nonlinear equations. Direct numerical calculation on the basis of 3D equations (Polezhaev *et al.*, 1998a) showed that there is no difference between the 2D and 3D results in stream function and isotherms fields for the cases $Gr = 5.5 \times 10^5$ (linear temperature profile on the melt) and for $Gr = 10^6$ (adiabatic boundary condition). However, three-dimensional effects (oscillations) exist for $Gr = 10^6$ in the case of a linear profile on the surface melt, as was predicted by linear stability calculations. It is well correlated between the RMS of the oscillations, calculated by two different 3D codes – on the basis of finite difference and spectral-difference methods. In new calculations (Nikitin and Polezhaev, 1999) direct modeling of 3D the regime was done for the benchmark configuration (linear profile of the temperature on the melt surface) for $Gr = 6 \times 10^6$ and 6×10^7 . Nonregular oscillatory regimes with continuous spectra (turbulent) were shown for both cases.

Therefore, in the benchmark configuration two types of the onset of the oscillations are shown. The first one, by reason of the lost symmetry, with lower Grashof number. The second one, by reason of boundary layer-type convective flow instability, with higher Grashof number. Quantitative values are welcome to compare for other researchers. Both instability mechanisms are strongly dependent on the thermal boundary condition on the melt surface. Therefore it may be used for thermal control of the temperature oscillations.

8.6 CONVECTIVE INTERACTION AND INSTABILITIES IN CONFIGURATION OF INDUSTRIAL GaAs CZOCHRALSKI GROWTH

We will show in this section how hierarchy of the models/codes works for analysis of the actual industrial process. One of the possible configurations of the industrial regime for LEC semi-insulating GaAs growth is characterized (Kosushkin 1997, Zakharov *et al.*, 1998) by the following values: $H = 4.0$ cm, $R_s = 4.0$ cm and $R_c = 7.0$ cm, therefore $H/R_c = R_s/R_c = 0.578$. The dynamical regime is counter-rotation with $W_s = 6$ rpm, $W_c = -16$ rpm. Using physical properties for GaAs melt from the above-cited paper and the temperature difference between crystal and crucible as 30°C , one can find nondimensional parameters $Pr = 0.07$, $Gr = 7.8 \times 10^7$, $Re_s = 6 \times 10^3$, $Re_c = -1.6 \times 10^4$. Dimensional rotation speed and time will be used below for easier analysis. There are some changes in thermal boundary conditions in comparison with the above-mentioned benchmark configuration: the bottom is not adiabatic – there is a bottom heat supply so that

the temperature on the bottom is the same as on the side wall: $T_c = T_b$. Adiabatic melt surface is assumed to be as typical for the LEC configuration (Kakimoto *et al.*, 1989).

The goal of this section is to analyze the nature of the oscillations in the melt for semi-insulating GaAs crystal growth with counterrotation and the damping possibilities. The oscillation mechanism for the case of zero rotation and for the coupling of nonlinear flows will be done in axisymmetrical and three-dimensional approaches. Different types of elementary (forced and gravity-driven) convective instabilities (due to cooling above the disc or bottom heating and side heating of crucible) as well as coupling will be discussed. For this part of the chapter related to the parametrical analysis of industrial ground-based regime a monotonic 'upwind' FDM scheme and nonuniform mesh (81×81 grids) for calculations on the basis of the 'Intex' system (Section 8.4) were used.

8.6.1 AXISYMMETRICAL APPROACH: NONLINEAR COUPLING FLUID FLOW AND CONTROL POSSIBILITIES

(a) Forced convection and diffusion.

For the analysis below it is important to clearly understand the impact on temperature field of the forced convection due to rotation. Figure 8.3(a) shows steady-state temperature and flow fields due to forced convection only, which corresponds to zero gravity ($W_s = 6$ rpm, $W_c = -16$ rpm, $Gr = 0$). Classical Taylor–Prandtl flow may be recognized from this picture. The impact of the flow on the temperature field may be recognized by comparison with isotherms for the diffusion regime only with zero velocity (Figure 8.3(b)). The weak oscillations and relatively small impact on temperature field in comparison with gravity-driven convection below (Figure 8.4(a–e)) should be mentioned. Note, that for the 3D case this forced flow is definitely unstable due to a supercritical crucible rotation speed (see Section 8.6.2a).

(b) Thermal gravity-driven convection.

Using parametrical calculation on the basis of the axisymmetrical model with a change of Grashof number (similar to the benchmark configuration in Section 8.5), the critical Gr number for onset of the oscillations was found as $Gr = 1.5 \times 10^8$. Therefore the convective regime without any rotation in the axisymmetrical case should be steady state (note, however, that this critical value corresponds to the melt level $H = 4$ cm only). Ground-based convection without rotation ($Gr = 7.8 \times 10^7$, $W_s = W_c = 0$) was calculated, using for initial values of zero velocity field and uniform temperature in the melt, which is heated until the side wall temperature reaches T_c and the instantaneous cooling disc surface reaches T_s .

Figure 8.4(a) shows the temporal evolution of the thermal convection. One can recognize two kinds of thermal-convection mechanisms in the crucible: (a) local thermals due to the instantaneous crystal cooling from above and

(b) global circulation due to the side heating. However, the local mechanism in the form of thermals dominates in this case only on the initial stage (for about 10–15 s). Thermals were observed on the suddenly heated bottom in water by Sparrow *et al.* 1970 (see also realization of thermals by the computer system COMGA by Ermakov *et al.*, 1997). A similar structure of thermals penetrated from above the cooling water surface was reported by Bune *et al.*, 1985. After long time the distance global type of convection from the side heating dominates (Figure 8.4(a)). Note that this situation exists for low Pr number melts. For high Pr experiments Berdnikov *et al.*, 1990 reported regular oscillations induced by thermals near the above cooled front, which corresponds to recent calculations by Polezhaev *et al.*, 1998b). The long-term regime (Figure 8.4(a)) is steady state (in accordance with estimation of the critical Gr number for axisymmetrical case). It is similar to the benchmark configuration (Figure 8.2(b)) and helps to understand the stabilization.

However, it should be taken into account that the leading long-term convective mechanism is strongly dependent on the melt level. Figure 8.4(b) shows the calculation of convection for small height of the melt level $H = 1$ cm, where bottom heating (Rayleigh–Bernard mechanism) in the form of convective cells dominates. For this case the impact of dynamical control actions may be quite different. These comments show the importance of Pr number and the geometrical configuration for the flow field in the crucible and restricts the parametrical analysis here for the level of 4 cm in low Pr number melt.

(c) Coupling of the thermal convection and crystal/crucible rotation.

The initial stage of this industrial regime is similar to the previous one (Figure 8.4(a)). However the special oscillatory mechanism, which may be recognized as a W-type isotherm structure is realized for long-term duration as shown in Figure 8.4(c). An important feature of the flow field in this case in comparison with the long-term convection structure in Figure 8.4(a) is the strong disturbances due to interaction with the forced type of convection.

More detailed parametrical analysis was done to show the cause of this type of instability. Figure 8.4(d) shows the interaction of the thermal convection and crystal rotation only. One can see that convection is dominant again for a crystal rotation speed of 6 rpm ($Re_s = 6 \times 10^3$), because of the high value of the governing parameter $Gr/Re^2 > 5$. Only weak instability exists in the bottom region near the axis in this case in accordance with stability analysis (Nikitin, Polezhaev, 1999a). Therefore this type of interaction is not the reason for the flow-field structure in Figure 8.4(c). The next run with crucible rotation and zero velocity of the crystal rotation (Figure 8.4(e)) definitely shows that the reason for the strong instability in Figure 8.4(c) is coupling of thermal convection and crucible rotation because of the high crucible rotation speed (it is the small value of the governing parameter $Gr/Re^2 = 0.3$). There are a number of qualitative reasons for this type of instability, for instance, Kurpers and Lortz, 1956 (see Ristorcelli and Lumely 1992) reported a similar mechanism by reason of convection and rotation of the container. However, quantitative analysis is very

important here because of the strong dependency of parameters. We will return to a discussion of this phenomena on the basis of the 3D model using stability analysis (Section 8.6.2(a)).

(d) Analysis of control possibility using axisymmetrical model.

There are two primitive possibilities for control of the above mentioned type of instability: (a) to reduce crucible speed rotation, (b) to reduce the gravity level. Using analysis on the basis of axisymmetrical model it was shown by Polezhaev *et al.* 1997, that for the last case temperature oscillations in GaAs melt may be avoided for $g/g_0 = 0.01$. Temporal behaviour of this case in comparison with Figures 8.39(a) and 8.4(c) shows that W-type isotherms are completely eliminated. A similar effect of the elimination of the temperature oscillations may be achieved using reduction of crucible rotation speed, to 1.5 rpm. However, the impact of thermal convection on the temperature field in this case is quite different. Another more complicated possibility (time-dependent temperature on the side wall due to variation of the heater capacity) is discussed by Zakharov *et al.*, 1998. These control possibilities, termed 'low energetic possibilities alternative to microgravity', were studied in the framework of the project NASA-RSA (Polezhaev *et al.*, 1998b). However, the analysis on the basis of the axisymmetrical model shows a possibility to avoid only some (but probably the strongest) of mechanisms of oscillations and must be checked on the basis of 3D models.

8.6.2 THREE-DIMENSIONAL ANALYSIS

(a) Stability analysis of the elementary fluid flows.

Results of the linear stability analysis using the technique of Nikitin and Polezhaev, 1999a for this configuration (Figures 8.5–8.7) show structures of three-dimensional disturbances in two different (r , z and azimuthal, $z = \text{const}$) cross sections and temporal behavior of 3D disturbances for elementary processes: thermal convection without any rotation Figure 8.5, crystal (disc) rotation without convection (Figure 8.6) and the same for only crucible rotation (Figure 8.7). The critical Grashof number for convection in the configuration discussed here was found to be 2.5×10^6 which is not far from $Gr_c = 1.2 \times 10^6$ for the benchmark configuration in the above-mentioned Section 8.5.2 and significantly smaller than 1.5×10^8 for the axisymmetrical case. Therefore it must be the oscillatory regime in the 3D case instead of steady state in Figure 8.4(a). There is a global structure of temperature disturbances in the r – z plane (Figure 8.5(a)) and a periodically azimuthal temperature structure (Figure 8.5(b)) with half the period in the 3D benchmark configuration (Nikitin and Polezhaev, 1999a).

The critical rotation speed of the crystal under 3D disturbances was found to be $(W_s)_c = 7.7 \text{ rpm}$. It corresponds to a critical $Re_s = 7.7 \times 10^3$, which is smaller than for the Cochran flow because of disturbances in the enclosure, as shown in the r – z plane in Figure 8.6a. Azimuthal disturbances are nonsymmetrical in this case (Figure 8.6(b)). Anyway, the critical W_s value is higher

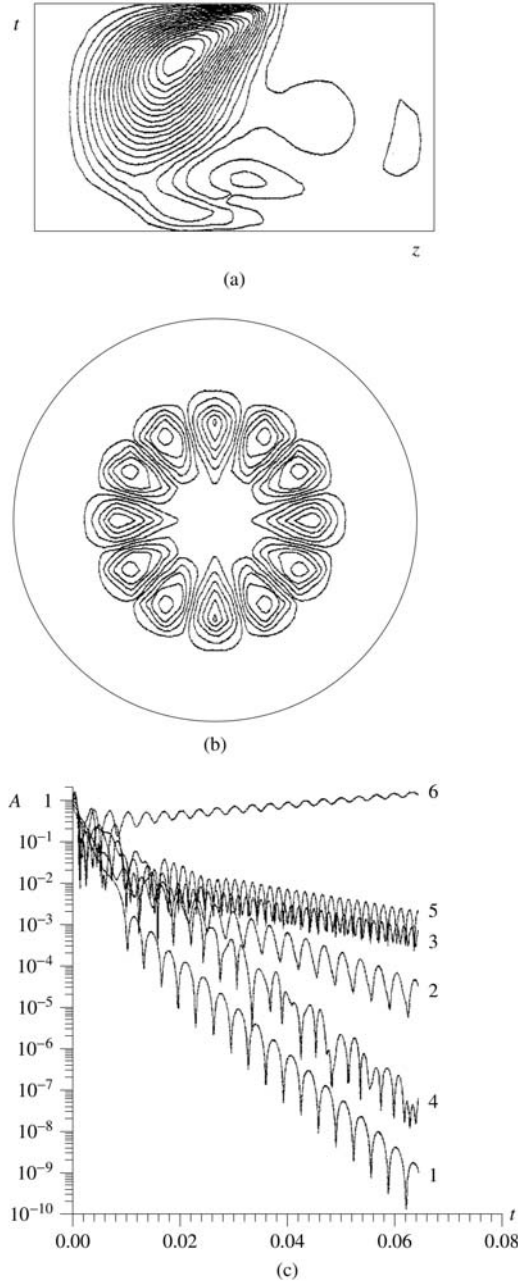


Figure 8.5 Three-dimensional instability for Czochralski LEC growth of GaAs configuration for thermal convection without rotation $Gr_{ec} = 2.5 \times 10^6$; (a) structure of the isotherms disturbances in $r-z$ plane; (b) structure of the isotherms disturbances in the azimuthal plane; (c) temporal behavior of the different temperature modes.

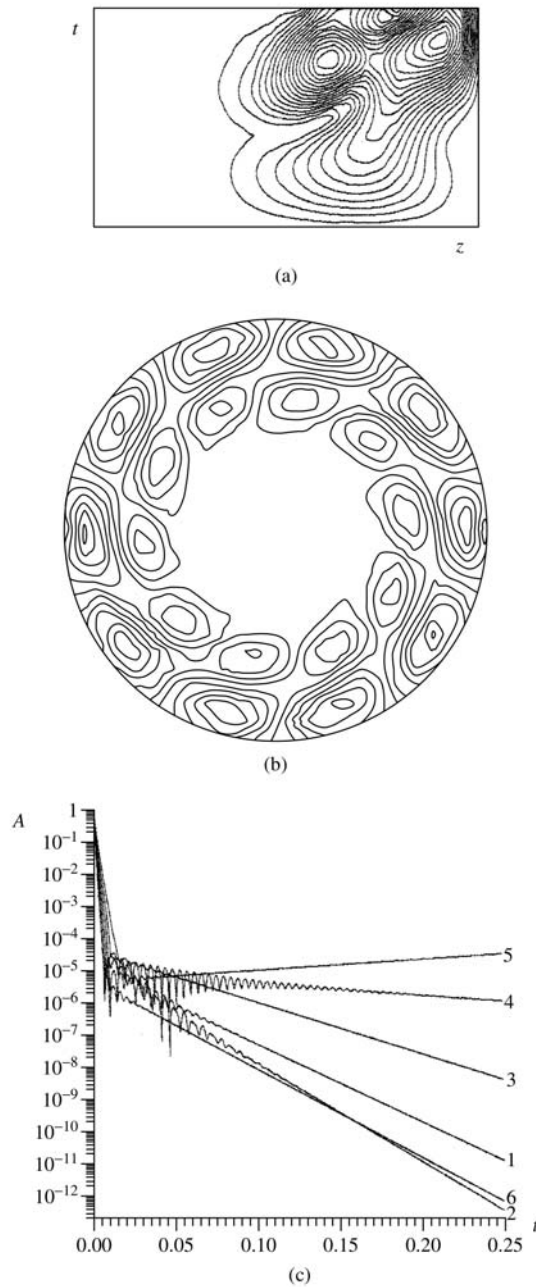


Figure 8.6 Three-dimensional instability for Czochralski LEC growth of GaAs configuration for disc rotation only $(W_s)_c = 7.7$ rpm: (a) structure of the isotherm disturbances in the r - z plane; (b) structure of the isotherm disturbances in azimuthal plane; (c) temporal behavior of temperature modes.

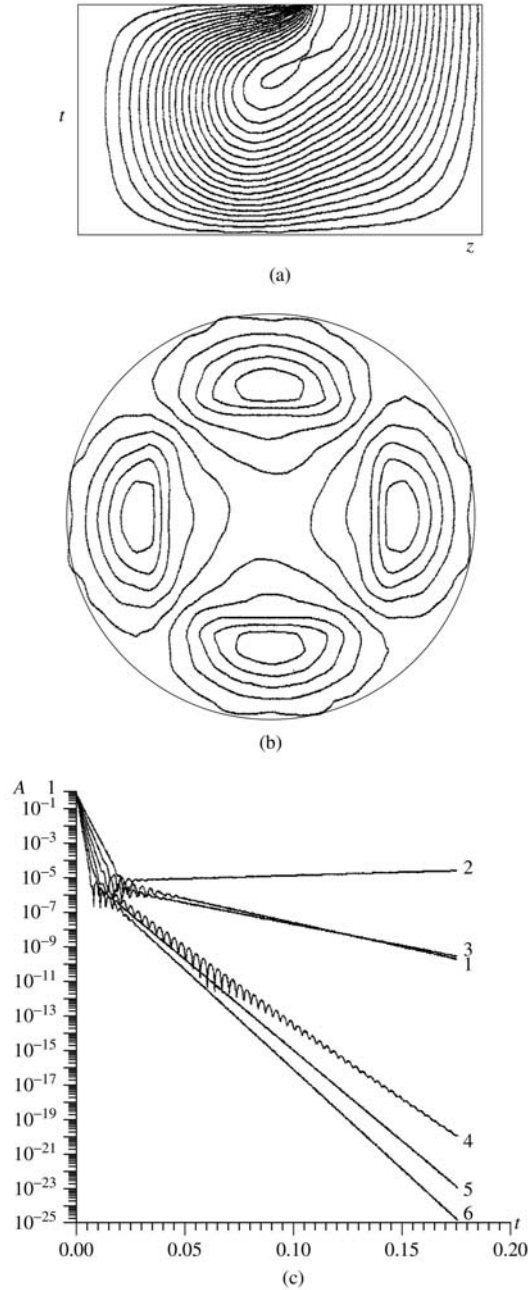


Figure 8.7 Three-dimensional instability for Czochralski LEC growth of GaAs configuration for crucible rotation only ($W_{cc} = -1.2$ rpm); (a) structure of the isotherm disturbances in the r - z plane; (b) structure of the isotherm disturbances in azimuthal plane; (c) temporal behavior of temperature modes.

than the industrial value 6.0 rpm. Therefore, it confirms, as was noted above (Section 8.6.1) that crystal rotation is not the reason for instability even in the 3D case. However, critical crucible rotation speed $(W_c)_c$, which was found to be about 1.2 rpm ($Re_c = 1.2 \times 10^3$), is more than 10 times lower than the industrial one 16 rpm. Azimuthal disturbances are symmetrical in this case (Figure 8.7(b)). Therefore temperature oscillations in this case will be present even in zero gravity. A monotonic instability in both cases of the elementary forced convection may be noted (Figures 8.6(c) and 8.7(c)). Therefore analysis of stability of the elementary mechanisms helps to recognize the possible impact of the elementary processes on the final structure of flow/temperature fields.

(b) Direct numerical simulation of the coupling regimes on the basis of unsteady 3D model.

Simulation of the three-dimensional industrial case ($Gr = 7.8 \times 10^7$, $Re_s = 6 \times 10^3$, $Re_c = -1.6 \times 10^4$), which was done using the spectral-finite difference technique (Nikitin and Polezhaev, 1999b and Polezhaev *et al.*, (1998b)) shows chaotic temporal behaviour of the flow/temperature fields. The results of the calculations are mainly qualitative, because a relatively coarse uniform mesh was used. There is not enough space for discussion of the computation technique and results, but in the cited paper the method of analysis chaotic (turbulent) regime

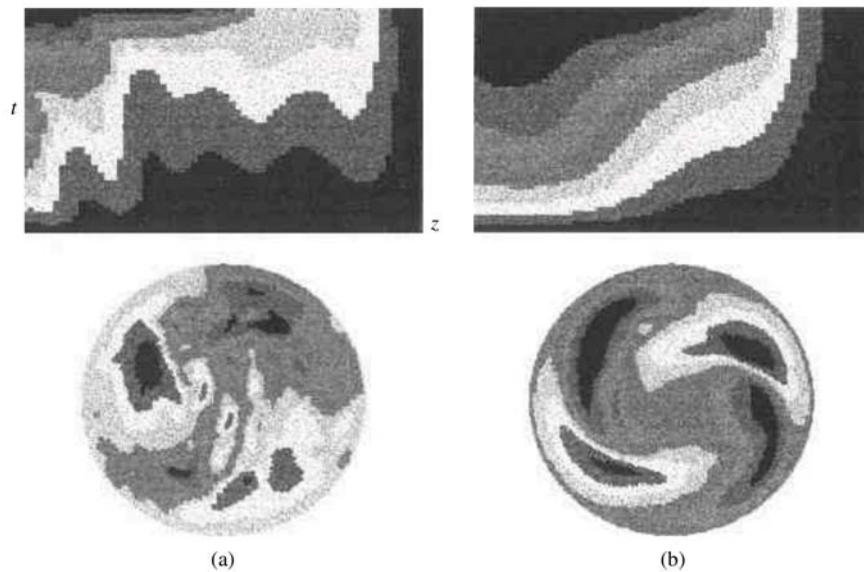


Figure 8.8 Direct simulation of thermal convection and counter-rotation in GaAs ‘Czochralski method. Fragment of instantaneous isotherms of unsteady 3D modeling. Up: r - z plane, down: azimuthal plane, $z = 0.95$: (a) ground-based industrial regime ($Gr = 7.8 \times 10^7$, $W_s = 6$ rpm, $W_c = -16$ rpm); (b) industrial regime under reduced gravity ($Gr = 7.8 \times 10^5$, $W_s = 6$ rpm, $W_c = -16$ rpm): laminar flow.

for the benchmark configuration was discussed in detail. Three-dimensional runs here show a typical turbulent temperature field for the industrial regime in the azimuthal plane (Figure 8.8(a)), but in the $r-z$ plane (Figure 8.8(b)) qualitatively similar to the axisymmetrical ones (Figure 8.4(c)). A special run was carried out with low gravity $Gr_c = 7.8 \times 10^5$ ($g/g_o = 0.01$). A fragment of the instantaneous isotherms structure is shown in Figure 8.8(b) (Polezhaev *et al.*, 1998b). In this case isotherms in the $r-z$ plane (Figure 8.8(b)) are similar to axisymmetrical ones for zero gravity (Figure 8.3(a)). Therefore conclusions related to the possibility to eliminate oscillations using thermal and dynamical control as alternatives to microgravity in industrial regimes of GaAs LEC, which was found using the axisymmetrical model, are confirmed qualitatively in the 3D case. The difference is that regular temperature oscillations exist in the 3D case for the industrial regime even in the low-gravity environment.

8.7 CONCLUSIONS

Instabilities induced by nonlinear interaction of the thermal convection and crystal/crucible rotation for the idealized Czochralski model for the industrial LEC GaAs crystal-growth regime, which characterize nondimensional parameters $H/R_c = 0.578$, $R_s/R_c = 0.578$, $Gr = 7.7 \times 10^8$, $Pr = 0.07$, $Re_s = 6.6 \times 10^3$, $Re_c = -1.6 \times 10^4$ (this corresponds to a GaAs melt $H = R_s = 4$ cm, $R_c = 7$ cm, $W_s = 6$ rpm, $W_c = -16$ rpm) are analyzed using an axisymmetrical approach, 3D stability and direct numerical simulation.

As a result of modeling of gravity-driven convection in a crucible in the Czochralski method that three different possible mechanisms of gravity-driven convection in the crucible are shown: side heating, above cooling near the crystal front and bottom heating. The critical Grashof number for onset of temperature oscillations due to convective instability in this configuration is found to be 1.5×10^8 in the axisymmetrical case and 2.5×10^6 for the 3D case.

The critical Reynolds number for disc rotation is found in the 3D case $(Re_s)_c = 7.7 \times 10^3$ and for crucible rotation $(Re_c)_c = 1.2 \times 10^3$ (this corresponds to the critical rotation speed of the crystal of 7.7 rpm and 1.2 rpm for crucible rotation). High stability of the elementary flows, induced by thermal convection, crystal/crucible rotation is found in the axisymmetrical case. Coupling of convection and crucible rotation is the main reason for instability, which is realized even in the 2D case. The results of the modeling encourage research into the possibility of symmetrization of the temperature and flow fields during Czochralski growth as an important control action.

Possibilities to reduce temperature oscillations in GaAs melt (thermal, dynamical, geometrical, etc., control actions including possibilities to reduce gravity) may be analyzed in quantitative form using an actual technological environment. However- it seems that industrial control actions are far from optimal. One of the possible reasons high crucible rotation speed (more than ten times higher than

critical). It should be concluded also that for a given industrial ground-based technological process the microgravity level $g/g_0 = 10^{-3}$ may be enough for damping the largest oscillations in LEC GaAs melt in the crucible for the growth of semi-insulating GaAs.

Tools for modeling using hierarchy of the models/codes for analysis of technologically important fluid dynamics, heat/mass transfer processes are developed and results using benchmark configurations for axisymmetrical and three-dimensional cases are summarized. For the benchmark configuration $Gr_c = 2.5 \times 10^6$ in the axisymmetrical case and 5.5×10^5 for the 3D case and $G_c = 3.5 \times 10^5$ for $Re_s = 10^3$, $Re_c = 0$ are presented for this benchmark as well as steady-state results for the axisymmetrical case. A strong impact of the boundary temperature conditions on the melt's surface (adiabatic: $Gr_c > 10^7$ in the axisymmetrical and $Gr_c = 1.2 \times 10^6$ for the 3D case) is shown. It is also shown that the two-dimensional axisymmetrical model is efficient for prediction of a number of technologically important fluid flows and heat/mass transfer in the r - z plane and may be a powerful tool for parametrical research together with 3D stability and direct simulation.

ACKNOWLEDGMENTS

The author would like to make acknowledgment to V. A. Kosushkin for technological consulting, S. A. Nikitin, N. V. Nikitin and O. A. Bessonov for help in the developments of the concept and results, M. N. Myakshina for the help in calculations and graphics and O. A. Rudenko for the preparation of the manuscript.

This work was partly supported by the NASA-RSA program (TM-11 project).

REFERENCES

- Alexander J. I. D. (1990), Low gravity experiment sensitivity of residual acceleration. A review. *Microgravity Sci. and Technol.*, **3**, 52.
- Baumgartl J., Bune A., Koai K., *et al.* (1993) Global simulation of heat transport, including melt convection in a Czochralski crystal growth process – combined finite element/finite volume approach, *Mater. Sci. Eng. A* **173**, 9.
- Beliaev Yu. N. (1997), Hydrodynamical instability and turbulence in spherical Couette flow, *Moscow State Univ.*, 348 (in Russian).
- Berdnikov V. S., Borisov V. L., Markov V. A. and Panchenko V. I. (1990), Laboratory modeling of the macroscopic transport processes in the melt during crystal growth by the method of pulling In: Avduevsky V. S., Polezhaev V. I. (eds.) *Hydrodynamics, heat and mass transfer during material processing*, 68, Nauka, Moscow (in Russian).
- Bottaro, A. and Zebib A., (1988) Bifurcation in axisymmetric Czochralski natural convection, *Phys. Fluids* **31**, 495.
- Bottaro, A. and Zebib A., (1989) Three dimensional thermal convection in Czochralski melt, *J. Cryst. Growth* **97**, 50.

- Brown R. A., (1988) Theory of transport processes in single crystal growth from the melt, *AIChE J.*, **34**, 881.
- Buckle, U. and Schafer, M. (1993), Benchmark results for the numerical simulation of flow in Czochralski crystal growth, *J. Cryst. Growth* **126**, 682.
- Bune A. V., Ginzburg A. T., Polezhaev V. I., and Fedorov K. N. (1985), Numerical and laboratory modeling of the development of convection in a water layer cooled from the surface *Izvestiya, Atmos. Oceanic Phys.* **21** (9), 736.
- Carruthers J. R. (1977), Thermal convection instability relevant to crystal growth from liquids, In: *Preparation and Properties of Solid State Materials* (eds. W. R. Wilcox, R. A. Lefever), Vol. 3, 1, Marcel Dekker, Inc. New York and Basel.
- De Vahl Davis G., Jones I. P. (1983) Natural convection in a square cavity: a comparison exercise, *Int. J. Numer. Methods fluids*, (1983) **3**, 227–248.
- Dupret F., Van Den Bogaert N. (1994), Modelling Bridgman and Czochralski Growth, In: *Handbook of Crystal Growth*, ed. D. T. J. Hurle, Vol. 2, 875.
- Ermakov, M. K. Griaznov V. L., Nikitin S. A., Pavlosky D. S., Polezhaev V. I. (1992), A PC-based System for Modelling of Convection in Enclosures on the basis of Navier-Stokes Equations, *Int. J. Numer. Methods Fluid*, **15**, 975–984.
- Ermakov M. K., Nikitin S. A. and Polezhaev V. I., (1997), A System and computer laboratory for modelling of the convective heat – and mass transfer processes, *Fluid Dynamics* **32** (3), 338.
- Fontaine J.-P., Randriamampianina A., Extremet G. P., and Bontoux P. (1989), Simulation of steady and time-dependent rotation-driven regimes in a liquid-encapsulated Czochralski configuration, *J. Cryst.-Growth* **97**, 116.
- Gelfgat Yu. M., Bar-Yoseph P. Z., and Solan A. (1996), Stability of confined swirling flow with and without vortex breakdown, *J. Fluid Mech.* **311**, 1.
- Griaznov V. L., Ermakov M. K., Zakharov B. G. *et al.* (1992), Czochralski growth of gallium arsenide: technological experiments and numerical simulation. In *Fluid flow phenomena in crystal growth. Euromech colloquium* N. 284, Aussois, France, October 13–16, 1992, 15.
- Hurle D. T. J. (1993) Crystal Pulling from the Melt, Springer, *J. Cryst. Growth*, **156**, 383.
- Jones A. D. W. (1984), The temperature field of a model Czochralski Melt, *J. Cryst. Growth* **69**, 165.
- Kakimoto K., Egushi M., Watanabe M. *et al.* (1989), Direct observation by X-ray radiography of convection of boric oxide in the GaAs liquid encapsulated Czochralski growth. *J. Cryst. Growth* **94**, 405.
- Kakimoto K. Watanabe M., Egushi M., *et al.* (1993), Order structure in non-axisymmetric flow of silicon melt convection, *J. Cryst. Growth* **126**, 435.
- Kirdyashkin A. G. (1979), Structure of the thermal gravitational flows, In: *Models in mechanics of continuous media*, Proceedings of the Vth all-Union School on the models in mechanics of continuous media, 69, Novosibirsk 1979.
- Kobayashi N. and Arizumi T. (1980), Computational studies on the convection caused by crystal rotation in a crucible, *J. Cryst. Growth* **47**, 419.
- Kobayashi N. (1995), Steady state flow in a Czochralski crucible. *J. Cryst. Growth* **147**, 382.
- Kosushkin V. G. (1997), Investigation of low frequency oscillation and crucible and crystal rotation control in GaAs crystal pulling technique. Proceedings of the Joint Xth

- European and VIth Russian Symposium on Physical Sciences in Microgravity, St. Petersburg, Russia, June 15–21, 1997, 122.
- Kozkemiakin G. N., Kosushkin V. G., Kurockin S.Yu. (1992), Growth of GaAs crystal pulled under the presence of ultrasonic vibrations, *J. Cryst. Growth* **121**, 240.
- Krzyminski U., Ostrogorsky A. G. (1997), Visualization of convection in Czochralski melts using salts under realistic thermal boundary conditions, *J. Cryst. Growth* **174**, 19.
- Langlois W. E. (1985), Buoyancy-driven flows in crystal-growth melts *Ann. Rev. Fluid Mech.* **17**, 191.
- Leister H.-J., Peric', M. (1992), Numerical simulation of a 3D Czochralski melt flow by a finite volume multigrid algorithm *J. Cryst. Growth* **123**, 567.
- Mihelcic' M. and Wingerath K. (1984), Three dimensional simulations of the Czochralski bulk flow, *J. Cryst. Growth* **69**, 473.
- Motakef S. (1990) Magnetic field elimination of convective interference with segregations during vertical-Bridgman growth of doped semiconductors *J. Cryst. Growth* **104**, 833.
- Mukherjee D. K., Prasad V., Dutta P., Yuan T., (1996), Liquid crystal visualization of the effects of crucible and crystal rotation on Cz melt flows, *J. Cryst. Growth* **169**, 136.
- Muller E. (1988) Convection and Inhomogeneities in Crystal Growth from the Melt Crystal, Vol. 12 (Springer, Berlin; (1988).
- Muller, G. and Ostrogorsky A. (1994), Convection in melt growth, In: *Handbook of Crystal Growth* **2**, 711.
- Nikitin N. V. (1994), A spectral finite-difference method of calculating turbulent flows of an incompressible fluid in pipes and channels, *Comput. Meth. Math. Phys.* **34**(6), 765.
- Nikitin N. V., Polezhaev V. I. (1999a), Three dimensional convective instability and temperature oscillations in Czochralski model *Izv. RAS, MZG*, **6**, 26, (translated: *Fluid Dynamics* **26**, 3).
- Nikitin N. V., Polezhaev V. I., Three dimensional features of transitional and turbulent convective flows in Czochralski model *Izv. RAS, MZG*, (accepted 1999b, translated: *Fluid Dynamics* **34**, 6).
- Pimputkar M., Ostrach S. (1981), Convective effects in crystal growth from melt. *J. Cryst. Growth* **55**, 614.
- Polezhaev V. I. (1974), Effect of the maximum temperature stratification and its application *Rep. Acad. Sci. USSR, ser. Hydrodynamics*, **218**, 783–786 (in Russian).
- Polezhaev V. I. (1981), Hydrodynamics, heat and mass transfer processes during crystal growth In: *Crystals: Growth, Properties and Applications* **10**, 87.
- Polezhaev V. I. (1992), Convective Processes in Microgravity. Proceedings of the First International Symposium on Hydrodynamics and Heat/Mass Transfer in Microgravity, **15**, Gordon and Breach
- Polezhaev V. I., (1994), Modelling of hydrodynamics, heat and mass transfer processes on the basis of unsteady Navier-Stokes equations. Applications to the material sciences at earth and under microgravity, *Comput. Methods Appl. Mech. Eng.* **115**, 79.
- Polezhaev V. I. (1998), Simulation aspects of technologically important hydrodynamics, heat/mass transfer processes during crystal growth, International School on Crystal Growth Technology, Beatenberg, Switzerland, 5–16 Sept. 1998, Book of lecture notes, (ed.) H. J. Scheel, 188.

- Polezhaev V. I., Nikitin S. A., Nikitin N. V. (1997), Gravity-driven and rotational low Prandtl melt flow in enclosure: nonlinear interaction, temperature oscillations and gravitational sensitivity. Proceedings of the Joint Xth European and VIth Russian Symposium on Physical Sciences in Microgravity, St. Petersburg, Russia, June 15–21, 1997, 28.
- Polezhaev V. I., Bessonov O. A., Nikitin N. V. and Nikitin S. A. (1998a), Three dimensional stability and direct simulation analysis of the thermal convection in low Prandtl melt of Czochralski model, The Twelfth International Conference on Crystal Growth, July 26–31, 1998, Jerusalem, Israel, Abstracts, 1998, 178.
- Polezhaev V. I., Bessonov O. A., Nikitin N. V., Nikitin S. A., Kosushkin V. G., *et al.* (1998b), Low energetic possibility for control of crystal growth, The Inst. for Problems in Mech. RAS, Report on the Project TM-11.
- Polezhaev V. I., Bessonov O. A., Nikitin S. A. (1998c), Dopant inhomogeneities due to convection in microgravity: spatial effects, *Adv. Space Res.* **22** (8), 1217.
- Polezhaev V. I., Ermakov M. K., Nikitin N. V. and Nikitin S. A. (1998d), Nonlinear interactions and temperature oscillations in low Prandtl melt of Czochralski model: validation of computational solutions for gravity-driven and rotatory flows. Intern. Symp. on Advances in Computational Heat Transfer, 26–30 May, Cesme, Turkey, 1997. In: Advances in Computational Heat Transfer, 492, Begell House.
- Rappl H. O., Matteo Ferraz L. F., Scheel H. J., *et al.* (1984), *J. Cryst. Growth* **70**, 49.
- Ristorcelli J. R. and Lumely J. L. (1992), Instabilities, transition and turbulence in the Czochralski crystal melt, *J. Cryst. Growth* **116**, 447.
- Roux B., (ed.), (1990), Numerical simulation of oscillatory convection in low-Pr fluids. *Notes on Numerical Fluid Mechanics*, **27**, Vieweg.
- Sacudean M. E., Sabhapathy P. and Weinberg F. (1989), Numerical study of free and forced convection in the LEC growth of GaAs, *J. of Crystal Growth* **94**, 522.
- Scheel H. J., (1972) *J. Cryst. Growth* **13/14**, 560.
- Scheel H. J., Sielawa J. S. (1985), Optimum convection conditions for Czochralski growth of semiconductors, 6th Internat. Symp. 'High Purity Materials in Science and Technology', Dresden, GDR, May 6–10, 1985, Proc. I. Plenary Paper, Akad. der Wiss. der DDR, 1985, 232.
- Seidi A., McCord G., Muller G., Leister H.-J. (1994), Experimental observation and numerical simulation of wave patterns in a Czochralski silicon melt: *J. Cryst. Growth* **137**, 326.
- Sparrow E. M., Husar R. B., Goldstein R. J. (1970), Observations and other characteristics of thermals, *J. Fluid Mech.*, **41**, 793.
- Verezub N. A., Zharikov E. V., Mialdun A. Z. *et al.* (1995), Physical modeling of the low frequency vibration crystal actions on the flow and heat transfer in Czochralski method, The Inst. Probl. Mech. RAS, preprint N 543, 66, Moscow.
- Wagner C., Friedrich R. (1997), Turbulent flow in idealized Czochralski crystal growth configuration, In: *New Results in Numerical and Experimental Fluid Mechanics*: Braunschweig, Germany, 367, ed. by Horst Korner and Reingard Hilbig.-Braunschweig: Vieweg.
- Wheeler A. A. (1991), Four test problems for numerical simulation of flow in Czochralski crystal growth. *J. Cryst. Growth* **102**, 691.
- Xiao Q., Derby J. J. (1995), Three-dimensional melt flow in Czochralski oxide growth: high-resolution, massively parallel, finite element computations: *J. Cryst. Growth* **152**, 169.

- Yi K.-W., Booker V. B., Egushi M., Shyo T., Kakimoto K. (1995a), Structure of temperature and velocity fields in the Si melt of a Czochralski crystal growth system, *J. Cryst. Growth* **156**, 383.
- Yi K.-W., Booker V. B., Kakimoto K. Egushi M., *et al.* (1995b), Spoke patterns on molten silicon in Czochralski system, *J. Cryst. Growth* **144**, 20.
- Zakharov B. G. Kosushkin V. G., Nikitin N. V., Polezhaev V. I. (1998), Technological experiments and mathematical modeling of the fluid dynamics and heat transfer in Gallium Arsenide single-crystal growth processes *Fluid Dynamics* **33** (1), 110.

Part 2

Silicon

9 Influence of Boron Addition on Oxygen Behavior in Silicon Melts

KAZUTAKA TERASHIMA

*Silicon Melt Advanced Project, Shonan Institute of Technology Fujisawa,
Kanagawa 251, Japan*

ABSTRACT

The oxygen concentration in silicon crystals is markedly changed by adding impurities. The solubility of oxygen atoms in boron-doped silicon melt increases with increasing boron concentration. The dissolution rate of fused quartz also increases with increasing boron concentration. It has been found that the fraction of cristobalite area grown on a fused quartz rod surface changes the fused quartz dissolution rate. The evaporation rate of silicon monoxide has a tendency to increase with increasing boron concentration. The importance of understanding silicon melt will be discussed. The strategy to grow well-controlled silicon crystals and recent results are described.

9.1 INTRODUCTION

Large-diameter silicon crystals are of extreme importance for electronics. The diameter of silicon has increased with time and many silicon suppliers now have the capability to grow 12-inch diameter crystals. The formation of grown-in defects, detrimental to large-scale integrated circuits, changes with increase in crystal diameter. The origin of these defects is not fully understood because of the lack of data and of the understanding of the growing interface. In our opinion, the origin of defects is partly or mainly related to the melt conditions. Our strategy for research is shown in Figure 9.1. First, the dependence of melt properties on temperature and impurity concentration should be studied. The density of silicon melts is bound to vary significantly by impurity addition [1] resulting in changes in melt convection [2, 3], but the reason for the density change is not well understood. Secondly, we will study the evaporation of SiO and incorporation of ambient gases. Thirdly, the physics of silicon crystals at

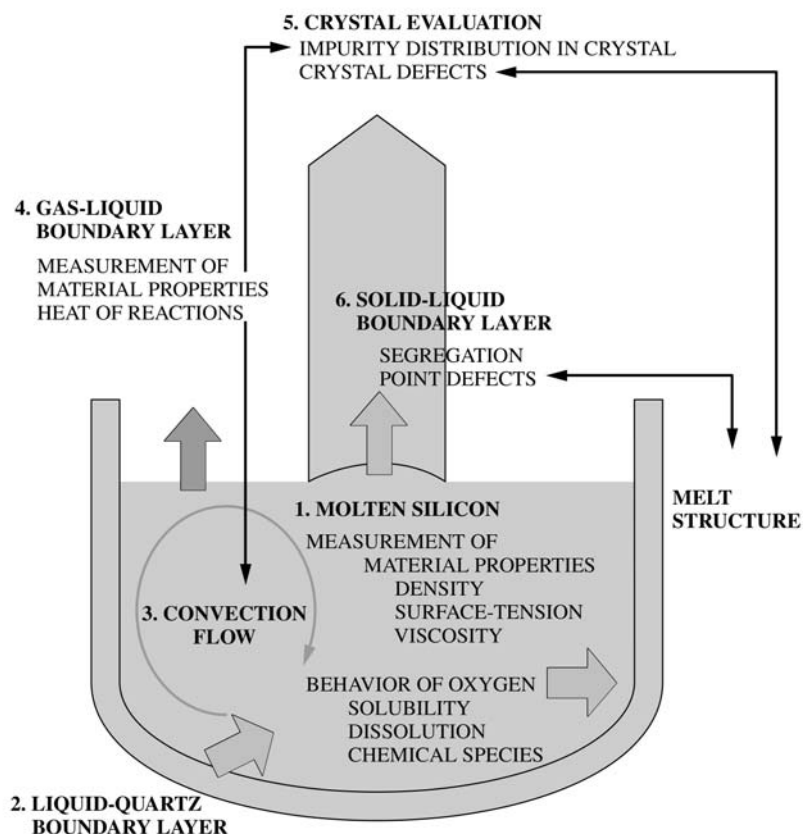


Figure 9.1 Strategy for the research of Si crystal growth.

high temperatures is important. Finally, the most important research area is the growing interface.

The melt properties should be studied more precisely, especially the variation with impurity species of fundamental physical properties such as density, surface tension and viscosity. The structure of the melt, its dependence on chemical bonding, and the dependence of the crystal/melt interface and induced defects on the melt structure are of essential interest. The oxygen concentration in Si crystals has been reported to change strongly with high boron doping [4, 5]. We report here the variation in oxygen solubility, fused quartz dissolution rate, and SiO evaporation from the melt surface with boron addition to silicon melts.

9.2 OXYGEN BEHAVIOR IN BORON-DOPED SILICON MELTS

Oxygen dissolves into silicon melts from the fused quartz crucible wall up to the solubility limit. The oxygen solubility changes with impurity addition and

prediction of oxygen incorporation into the growing crystal requires data on oxygen dissolution rate, solubility and SiO evaporation rate from the free surface of the melt. Highly boron-doped silicon of large diameter has attracted much attention for p-type epitaxial wafers due to its iron-gettering ability. In this section, oxygen solubility, fused quartz dissolution rate and evaporation from the melt surface are reported as a function of boron concentration in the melt.

9.2.1 OXYGEN SOLUBILITY IN SILICON MELT

9.2.1.1 Experimental

Our experimental method is basically the same as Huang [6]. A silicon rod 13 mm in diameter and 33 mm in length was fixed in a 13-mm inner-diameter quartz ampoule with a flat bottom. The upper space in the ampoule was sealed with a quartz rod with a slightly smaller diameter and it was welded completely to the inside wall of the ampoule after evacuation to about 10^{-5} Torr. The quartz ampoule with a pure silicon rod or silicon rod with boron powder inside was covered with a graphite holder and heated to various temperatures in the range of 1430–1470 °C for 120 min in an Ar atmosphere. The furnace used in this experiment was a horizontal three-zone type. The sample was quickly drawn from the furnace for quenching, after equilibration has presumably been attained in 120 min. The size of the specimen was $3 \times 3 \times 2.5 \text{ mm}^3$. The samples were mirror polished. The oxygen and boron concentrations were measured using a secondary ion mass spectrometer (SIMS) (CAMECA, IMS-3f/4) instrument. The relative error of the SIMS measurements was less than 5 %.

9.2.1.2 Results and discussion

Oxygen concentration increases with increasing boron concentration as shown in Figure 9.2. When the boron concentration is $5 \times 10^{20} \text{ atoms/cm}^3$, the oxygen concentration is $4 \times 10^{18} \text{ atoms/cm}^3$. This oxygen concentration is about twice the value for undoped silicon. The results of undoped silicon in our laboratory showed good agreement with the reported value by Carlberg [7]. The dependence of the oxygen concentration on the silicon-melt temperature in boron-doped silicon melts is given in Figure 9.3. According to our experimental data, oxygen concentration increases with increasing boron concentration independent of the silicon melt temperature. The cause of this phenomenon is discussed below.

To discuss the relation between boron atoms and oxygen atoms in a silicon melt, first we assume the generation of boron oxide species. If X atoms of boron react with one oxygen atom, the following chemical reaction occurs:



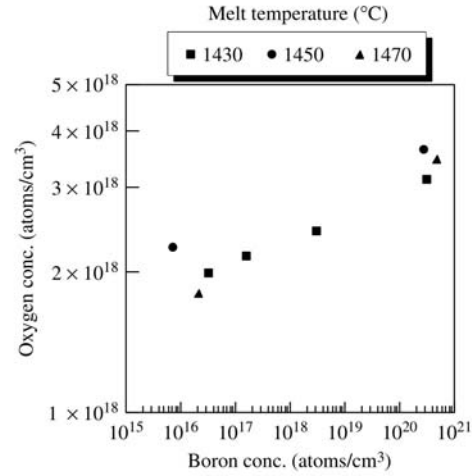


Figure 9.2 Dependence of the oxygen concentration on the boron concentration in a boron-doped silicon melt.

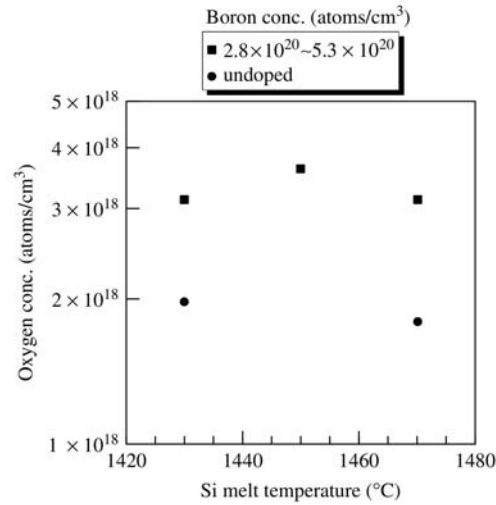


Figure 9.3 Dependence of the oxygen concentration on the Si melt temperature in a boron-doped silicon melt.

The equilibrium constant K is given by the following expression:

$$K = \frac{[B_xO]}{[B]^x[O]} \quad (9.2)$$

where $[O]$, $[B]$ and $[B_xO]$ are the total oxygen concentration, the boron concentration, and B_xO concentration in the boron-doped silicon melt, respectively.

It is assumed that there are two kinds of oxygen in a boron-doped silicon melt: one is uncombined or isolated oxygen atoms, the other is combined with boron atoms in the form of B_xO . Then the following calculation can be carried out:

$$[O] = [O]_{Si} + [B_xO] = [O]_{Si} + K[B]^X [O] \quad (9.3)$$

$$\Delta[O]/[O] = K[B]^X \quad (9.4)$$

$\Delta[O] = [O] - [O]_{Si}$ is the increased oxygen concentration due to boron addition in the silicon melt. Equation (9.4) can be rewritten as follows:

$$\ln\{\Delta[O]/[O]\} = \ln K + X \ln\{[B]\} \quad (9.5)$$

The values of X and K are calculated by using our results. X and K values are obtained from the following process. The relationship between the increase of oxygen concentration and boron concentration in silicon melt is plotted in Figure 9.4. The gradient corresponds to X . In Figure 9.4, $\ln[B]$ being equal to 0, the value of $\ln(\Delta[O]/[O])$ gives K . Table 9.1 shows X and K . According to

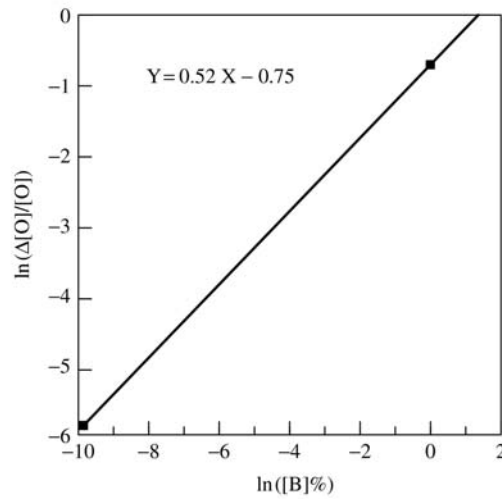


Figure 9.4 Relationship between the increase of oxygen concentration and boron concentration in a silicon melt: Silicon melt temperature = 1470 °C.

Table 9.1 Calculated X and the equilibrium constant K

Si melt temperature (°C)	X	Equilibrium constant: K
1430	0.16	0.51
1450	0.089	0.54
1470	0.52	0.47

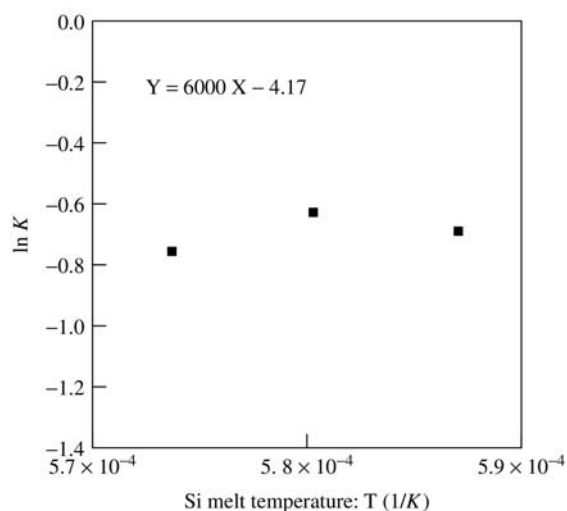


Figure 9.5 Relationship between equilibrium constant and Si melt temperature in a boron-doped silicon melt.

Table 9.1, the ratio of boron to oxygen varies with temperature. The dependence of K on the silicon melt temperature in boron-doped silicon melt is given in Figure 9.5. The value of K is smaller than unity and the dependence on the silicon-melt temperature has no definite tendency. The activation energy of the boron-oxygen reaction ΔE is given by the following expression:

$$\ln K = \frac{-\Delta E}{RT} + N \quad (9.6)$$

where R is the gas constant and N is a constant unrelated to the silicon-melt temperature. According to Equation (9.6) and Figure 9.4, ΔE is almost zero. So there is no activation energy in this reaction. This means the stable chemical species of B_xO is not generated by boron addition in the silicon melt, even though boron seems to attract oxygen. The analysis indicates that about 52 % of all oxygen in a silicon melt relate to added boron. These results indicate that the influence of boron doping involves a shift in oxygen solubility above the values for an undoped melt.

Next, the diameter of boron and silicon ions should be considered as a measure to discuss the solubility variation. At room temperature the silicon ion diameter is 0.39 Å and the boron ion diameter is 0.2 Å. If boron ions substitute the silicon ion sites in the melt, the distance between boron ions and silicon ions as nearest neighbours should shrink. This tendency may attract oxygen ions. Oxygen ions relax the shrinkage of the melt structure. The structural variation of silicon melt with and without boron and oxygen atoms is now under investigation. We next consider equilibrium of silicon melt with silicon oxides. Carlberg [8] calculated

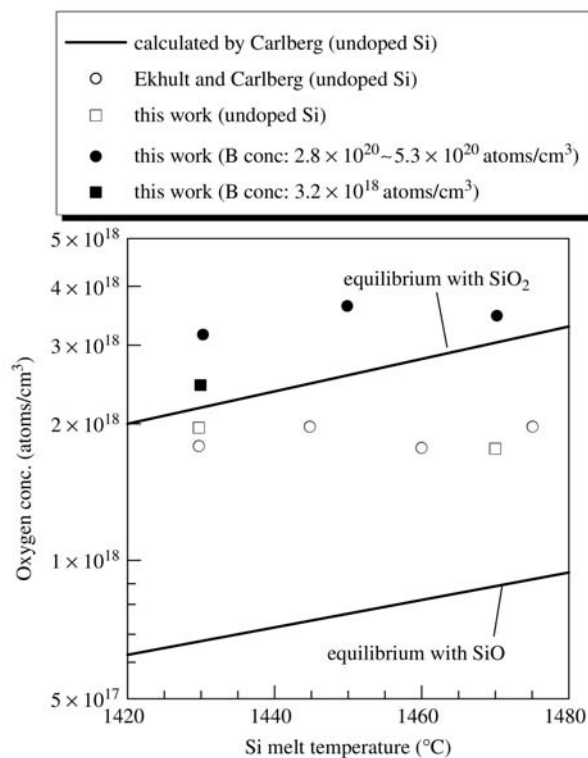


Figure 9.6 Relationship between oxygen concentration and temperature (This work: closed circles, closed squares and open squares).

oxygen solubilities in silicon melt in equilibrium with SiO₂ and SiO from thermodynamics. Our results are plotted in Figure 9.6 with the calculated equilibrium values given by solid lines. Our oxygen solubilities in boron-doped silicon melt are denoted by closed circles and a square, and those of undoped melt denoted by open circles and open squares, which all lie between the equilibrium values with SiO₂ and SiO.

For a boron-doped silicon melt the oxygen concentrations approach the equilibrium values with SiO₂. When the boron concentration is higher than about 1×10^{18} atoms/cm³, oxygen concentrations increase above the values of equilibrium with SiO₂. In other words, the oxygen solubility shifts above the values for the undoped case. Also, in the case where the boron concentration is 1×10^{20} atoms/cm³ the oxygen concentration values approach the equilibrium values that SiO₂ with increasing silicon melt temperature. When boron is doped in a silicon melt, then with increasing silicon melt temperature the oxygen concentration approaches a value that is consistent with an equilibrium with SiO₂.

A thin brown film was observed with increasing silicon melt temperature, but is not observed at 1430 °C. This brown-coloured layer was reported as an

SiO_{2-δ} layer by Carlberg [7]. The fraction of thin brown film area around the interface of the quenched silicon sample and the quartz varies depending on the boron concentration and temperature. The interface change strongly affects the oxygen solubility, because the equilibrium with the interface determines the oxygen concentration in the silicon melt. We believe the interface variation between Si melts and fused quartz is the most important phenomenon affecting oxygen solubilities. The holding-time dependence and the variation of chemical reaction rate by adding boron are now under investigation.

9.2.2 FUSED QUARTZ DISSOLUTION RATE IN SILICON MELTS

9.2.2.1 Introduction

Fused quartz is the material most commonly used as crucible material to hold the melt in silicon crystal-growth by the Czochralski method. During crystal-growth, the fused quartz crucible gradually dissolves in molten silicon, so that the grown crystal contains a high concentration of oxygen, on the order of 10¹⁷ to 10¹⁸ atoms/cm³, which causes crystalline defects during the following heat treatments. As device dimensions shrink, the effective control of oxygen in silicon becomes increasingly important. Therefore it is desirable to control the dissolution of fused quartz in the molten silicon. But there is no data on the dependence of the fused-quartz dissolution rate on the boron concentration in silicon melts. It has been found that the dissolution rate in a silicon melt markedly varies in the presence of boron in silicon melt and due to its impact on oxygen concentration.

9.2.2.2 Experimental

Fused quartz rods 10 mm in diameter and 100 mm in length were prepared for this experiment. Silicon melts were contained in either a fused-quartz crucible (quartz crucible, hereafter) or a carbon crucible coated with SiC by chemical vapour deposition (SiC-coated crucible, hereafter). The size of the crucible was 50 mm in diameter and 84 mm in depth. The depth of the silicon melt in the crucible was about 50 mm. The starting material was polycrystalline silicon. The boron was put onto the crucible bottom, then polycrystalline silicon was put into the crucible. The rod was immersed to 20 mm in depth in the melts for 5 h and then withdrawn. The weight losses of the fused-quartz rods by dissolution were measured.

9.2.2.3 Results

By using SiC-coated crucibles there is initially no oxygen in the silicon melts. The fused-quartz dissolution rate increases with increasing boron concentration

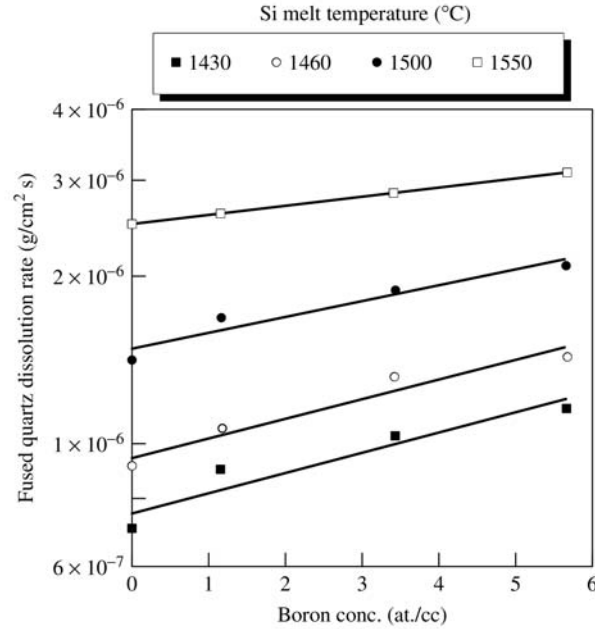


Figure 9.7 Dependence of the fused quartz-dissolution rate on the boron concentration in a boron-doped silicon melt by using a SiC-coated crucible.

as shown in Figure 9.7, and with increasing silicon melt temperature as shown in Figure 9.8. Also, the dependence of the dissolution rate on the boron concentration is small at 1550 °C. On the other hand, at the silicon melt temperature of 1430 °C the dissolution rate is strongly affected by boron as shown in Figure 9.8. Rods immersed in undoped silicon melts show an opaque surface that is brown at a 1430 °C melt temperature and white at 1550 °C. Rods immersed in boron-doped silicon melt ($>5.65 \times 10^{20}$ atoms/cm³) at 1430 °C show white opaque parts on the surface. By observing the fused-quartz rod cross sections, there are no opaque parts at the rod centre, opaque parts are observed only on the rod surface. Rods immersed in boron-doped silicon melts ($>5.65 \times 10^{20}$ atoms/cm³) at 1550 °C are markedly transparent. For the fused quartz samples immersed in undoped silicon melts at 1430 °C and 1550 °C and those immersed in boron-doped melts at 1430 °C the opaque surface fraction is crystallized and by X-ray diffraction shows the cristobalite pattern, whereas the transparent rods show the broad diffraction of amorphous silica.

9.2.2.4 Discussion

Our results show that the oxygen and boron concentrations in silicon melts affect the fused-quartz dissolution rate. The activation energy of the fused-quartz

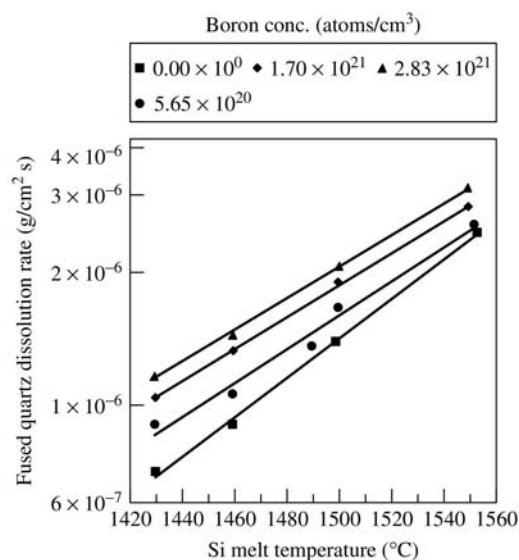


Figure 9.8 Dependence of the fused-quartz dissolution rate on the Si melt temperature in a boron-doped silicon melt by using a SiC-coated crucible.

dissolution is influenced by boron and by oxygen in silicon melts and is given by the following expression:

$$\text{Dissolution rate} = A_0 \exp(-\Delta E/RT) \quad (9.7)$$

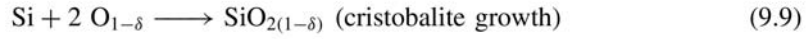
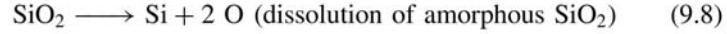
where R is the gas constant and A is a pre-exponential factor. ΔE and A_0 are calculated according to Figures 9.7 and 9.8 and are shown in Table 9.2. A_0 expresses the frequencies and modes of molecular collisions. A_0 values are influenced by the boron concentration in silicon melts. The A_0 decreases with increasing boron

Table 9.2 Calculated activation energy: ΔE and pre-exponential factor: A_0

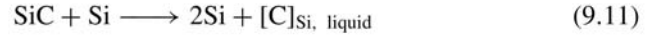
Boron conc. (atoms/cm ³)	Crucible	ΔE (kcal/mol)	A_0
0	SiC-coated carbon	151	172
6×10^{20}	SiC-coated carbon	128	11.6
2×10^{21}	SiC-coated carbon	121	5.54
3×10^{21}	SiC-coated carbon	119	4.73
0	fused quartz	122	2.82
6×10^{20}	fused quartz	145	46.4
3×10^{21}	fused quartz	157	180

concentration in the case of a SiC-coated crucible, and increases with increasing boron concentration when quartz crucibles are used. These phenomena are related to variations of the silicon melt structure. The structure of boron-doped silicon melt is now under investigation by using energy-dispersive X-ray diffractometry. If SiO_2 dissociates into silicon and oxygen, the combination energy is 145–153 kcal/mol [9]. This value is practically the same as our calculated ΔE . This result indicates that fused-quartz dissolution occurs with breaking of Si–O bonds.

Next we consider the chemical reactions on the fused-quartz rod surface. The following chemical reactions occur:



And by using SiC-coated crucibles the following reaction occurs:



There is some carbon contamination in silicon melts when SiC-coated crucibles were used. Table 9.2 shows that the activation energy of the fused-quartz dissolution rates is not markedly affected by crucible materials. The carbon solubility in silicon melt is less than 0.1 at.% [10]. In this experiment, the boron concentration in silicon melts is ten times the carbon concentration. Whereas carbon slightly affects the fused-quartz dissolution rate, reaction (9.11) seems not to be dominant. Because oxygen evaporates as SiO from the silicon melt surface, the lack of oxygen is indicated as $\text{O}_{1-\delta}$ in reactions (9.9) and (9.10). The fused-quartz dissolution rate ΔV is expressed by

$$\Delta V = |V_i - V_{ii} + V_{iii}| \quad (9.12)$$

where V_i , V_{ii} and V_{iii} are for Equations (9.8), (9.9) and (9.10), respectively. If oxygen transfer from the fused-quartz rod surface to silicon melt increases, reaction (9.8) is enhanced. So reaction (9.9) is retarded and $\text{SiO}_{2(1-\delta)}$ does not grow on the fused-quartz rod surface because this experiment is an open system. Because of $\text{SiO}_{2(1-\delta)}$ scarceness, reaction rate (9.10) is low. On the other hand, if reaction (9.9) is enhanced, $\text{SiO}_{2(1-\delta)}$ is apt to grow on a fused-quartz rod surface. The oxygen diffusion layer is related to reactions (9.8), (9.9) and (9.10). When the oxygen diffusion layer is formed, reactions (9.9)/(9.10) start and eventually all reactions (9.8), (9.9) and (9.10) reach steady state. The oxygen diffusion layer formation is affected by the oxygen diffusion rate in silicon melt. In the near future, we will publish the effect of boron concentration on oxygen diffusion. In the present work we assumed that oxygen diffusion in silicon melts was not affected by boron addition.

In the case of SiC-coated crucibles, there is initially no oxygen in silicon melts. Oxygen solubility in boron-doped silicon melts is about twice the value for undoped silicon melts [11]. Therefore the oxygen concentration on the fused-quartz rod surface in boron-doped silicon melt is about twice the value for undoped silicon melt. Because of SiO evaporation from the melt surface, oxygen concentrations are almost the same in undoped and boron-doped silicon melts. And these values are very low. So it is possible that the oxygen concentration gradient in the oxygen diffusion layer on the fused-quartz rod surface in boron-doped silicon melts is larger than the value for undoped silicon melt due to the higher oxygen solubility. Therefore when boron is doped in silicon melts, reaction rate (9.8) is enhanced. And because of oxygen scarceness in the bulk silicon melt, reaction (9.9) may be suppressed. So $\text{SiO}_{2(1-\delta)}$ is not apt to grow on the fused-quartz rod.

In the case of quartz crucibles there is much oxygen in silicon melts because of crucible dissolution. Oxygen concentration on the fused-quartz rod surface in boron-doped silicon melt is about twice as high as the value for undoped silicon melt in the case of SiC-coated crucibles. Just after withdrawing the fused-quartz rod from silicon melt we quenched the silicon melt in the quartz crucible and measured the oxygen concentration in this bulk silicon by SIMS. When the boron concentration is $5.65 \times 10^{20} \text{ atom/cm}^3$, the oxygen concentration is $3.5 \times 10^{18} \text{ atoms/cm}^3$. In the case of undoped melt the oxygen concentration is $8 \times 10^{17} \text{ atoms/cm}^3$. So in the crucible used in our experiment, the oxygen concentration gradient in the oxygen diffusion layer on the fused-quartz rod surface in boron-doped silicon melts is smaller than the value of undoped silicon melts. In this case the dissolution rate of the quartz rod is decreased by doping boron in silicon melts.

9.2.3 EVAPORATION FROM FREE SURFACE OF BORON-DOPED SILICON MELTS IN FUSED-QUARTZ CRUCIBLE

9.2.3.1 Introduction

The influence of the addition of boron on the weight variation due to evaporation and the chemical species evaporated from boron-doped silicon melt were investigated. It was found that boron assisted the evaporation from the silicon melt and the dominant evaporated substance was found to be silicon monoxide.

9.2.3.2 Experimental

The influence of the addition of boron on the evaporation loss of the silicon melt was investigated by the analysis of its deposits. A thermogravimetric method, which is basically the same as that reported by Huang *et al.* [12–14], was used

to measure the weight changes of the silicon melt due to evaporation. Quartz crucibles 20 mm in diameter and 60 mm deep, containing 20.00 g Si (purity 11N) and 0.15 g boron (purity 5N) which corresponded to 10^{21} atoms/cm³, were hung on an electric balance with 0.1 mg sensitivity (METTLER AT200). The samples were heated to 1450 °C or 1550 °C and maintained within 3 °C of the set-point value for 12 h. A schematic of the experimental apparatus for collecting deposits is shown in Figure 9.9.

The power of the heater was controlled so that there were no temperature variations during the deposit sampling. The quartz crucible was supported by a high-purity carbon susceptor at the centre in the chamber. The crucible was covered by a special funnel-shaped deposit collector made of quartz (Figure 9.9). The evaporated species from the boron-doped silicon melt were deposited on the inner wall of the deposit collector. The temperature of the deposit regions was also measured by a B-type thermocouple set on the deposit collector side. The entire system was enclosed in a water-cooled stainless-steel chamber into which argon gas with purity 6N flowed at a rate of 2.0 l/min to protect the hot zone

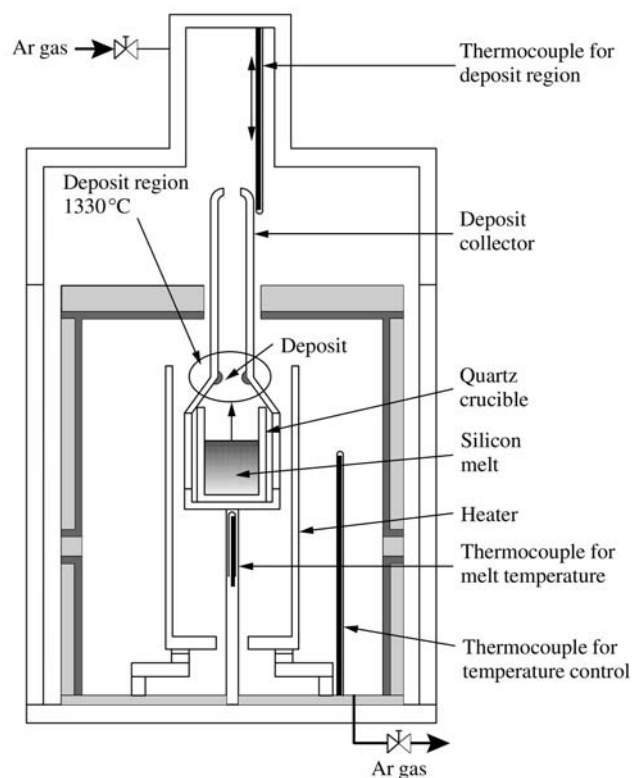


Figure 9.9 Schematic of experimental apparatus for collection of deposits evaporated from the boron-doped Si melt.

against oxidation. The quartz crucible had an internal diameter of 50 mm, a height of 84 mm and a thickness of 4 mm. The crucible contained 200.00 g of Si (purity 11N) and 0.15 g of boron (purity 5N) which corresponded to 10^{20} atoms/cm³ in the silicon melt. The chamber was heated to 1550 °C at a heating rate of 750 °C/h to realize complete melting. The reference temperature of the silicon melt was measured using a B-type thermocouple fixed under the crucible. Then, the heater power was adjusted so that the reference temperature of the silicon melt was 1550 °C and was maintained within 3 °C for a period of 13 h.

The deposits on the inner wall of the collector were analysed using an electron-probe microanalyser (EPMA: JXA-8621MX) to identify the evaporated species. The EPMA was used with an acceleration voltage of 15 kV, a current of 50 mA and a beam diameter of 20 µm.

9.2.3.3 Results and Discussion

The weight variations due to the evaporation of the boron-doped silicon melt with different boron concentrations (undoped, 10^{21} atoms/cm³ boron-doping) and at different temperatures (1450 °C, 1550 °C) under atmospheric pressure (770 Torr) in the chamber are shown in Figure 9.10. The vertical axis denotes the weight variations, while the horizontal axis denotes the holding time for the measurements. The weight variations were regulated by dividing the weight change ΔW by the initial weight W . The data denoted by dashed lines show the results of

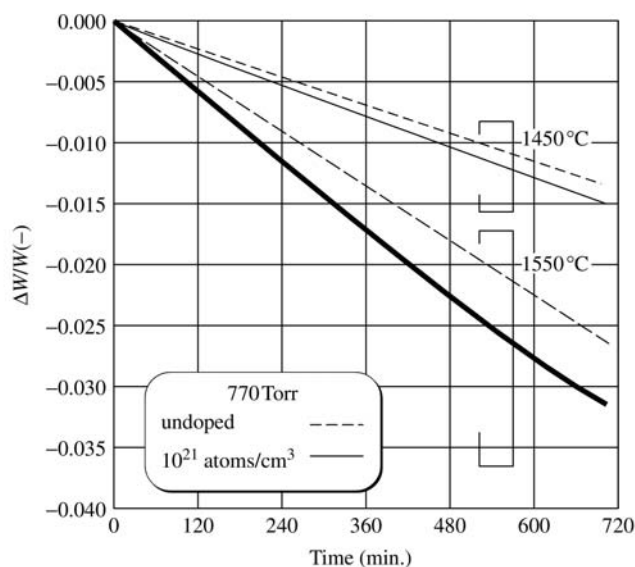


Figure 9.10 Weight variations of the boron-doped silicon melt caused by evaporation.

undoped silicon melt, while solid lines show those of 10^{21} atoms/cm³ boron-doped silicon melt with respect to each temperature condition.

It is obvious that the weight variation of the boron-doped silicon melt is larger than that of the undoped one at 1450 °C. The increase of evaporation loss due to boron addition, however, is comparatively small at 1450 °C. The weight variations of both the boron-doped silicon melt and of the undoped one almost doubled with elevating the temperature by 100 °C from 1450 °C to 1550 °C. In particular, the influence of boron addition on the weight variation of the silicon melt is enhanced at 1550 °C compared to the result at 1450 °C. Boron assisted the evaporation of the silicon melt remarkably when the temperature of the silicon melt was high. Here it is interesting to note which chemical species is evaporating from the boron-doped silicon melt under such active evaporation conditions.

Silicon and oxygen atoms were clearly detected, while no boron was measured by EPMA. The evaporation species from the boron-doped silicon melt is thought to be silicon monoxide from these analyses. It can be concluded that boron in silicon melt enhances the evaporation of silicon monoxide. Details are given in [15].

9.3 CONCLUSION

The main results of this study are:

1. Oxygen concentration increases with increasing boron concentration in silicon melts.
2. Fused-quartz dissolution rate increases with increasing boron concentration.
3. Evaporation of silicon monoxide is enhanced with boron addition into silicon melts.

As mentioned above, the oxygen incorporation is associated with impurity doping. The impurity atoms will slightly change the structure of the oxygen-containing silicon melt. Our recent study of oxygen distribution on a wafer cut from a highly boron-doped crystal suggests that the oxygen transport is strongly affected by the presence of boron. The study of fundamental physical constants such as diffusion coefficients is now of interest. These parameters are believed to be very important to control the uniformity of large-diameter silicon crystals grown by the Cz method.

ACKNOWLEDGMENTS

The author deeply thanks Dr S. Kimura of the National Institute for Research of Inorganic Materials for his fruitful suggestion. The author is much indebted to Mitsubishi Materials Silicon Co. Ltd., Komatsu Electronic Metals Co. Ltd.,

and to Toshiba Ceramics Co. Ltd. for their positive support of this fundamental research of silicon melts. This work was conducted as JSPS Research for the Future Program in the Area of Atomic-Scale Surface and Interface Dynamics.

REFERENCES

1. J. Kawanishi, K. Sasaki, K. Terashima and S. Kimura: *Jpn. J. Appl. Phys.* **34** (1995) L1509.
2. S. Togawa, S. Chung, S. Kawasaki, K. Izunome, K. Terashima and S. Kimura: *J. Cryst. Growth* **160** (1996) 41.
3. S. Togawa, S. Chung, S. Kawasaki, K. Izunome, K. Terashima and S. Kimura: *J. Cryst. Growth* **160** (1996) 49.
4. K. Choe: *J. Cryst. Growth* **147** (1995) 55.
5. K. G. Barraclough, R. W. Series, D. S. Kemp and G. J. Rae: VII Int. Conf. Crystal Growth, Stuttgart, Germany. ICCG-7, Sept. (1983) SY4/3.
6. X. Huang, K. Terashima, H. Sasaki, E. Tokizaki and S. Kimura: *Jpn. J. Appl. Phys.* **32** (1993) 3671.
7. T. Carlberg: *J. Electrochem. Soc.* **133** (1986) 1940.
8. T. Carlberg: *J. Electrochem. Soc.* **136** (1989) 551.
9. M. W. Chase, J. L. Curnutt, R. A. McDonald and A. N. Syverud: JANAF Thermochemical Tables, 1978 supplement, *J. Phys. Chem. Ref. Data*, **7**, 793 (1978).
10. A. R. Bean and R. C. Newman: *J. Phys. Chem. Solids* **32** (1971) 1211.
11. K. Abe, T. Matsumoto, S. Maeda, H. Nakanishi, K. Hoshikawa and K. Terashima: *J. Cryst. Growth* **181** (1997) 41.
12. X. Huang, K. Terashima, H. Sasaki, E. Tokizaki, Y. Anzai and S. Kimura: *Jpn. J. Appl. Phys.* **33** (1994) 1717.
13. X. Huang, K. Terashima, H. Sasaki, E. Tokizaki, S. Kimura and E. Whitby: *Jpn. J. Appl. Phys.* **33** (1994) 3808.
14. X. Huang, K. Terashima, K. Izunome and S. Kimura: *Jpn. J. Appl. Phys.* **33** (1994) 902.
15. S. Maeda, M. Kato, K. Abe, H. Nakanishi, K. Hoshikawa and K. Terashima: *Jpn. J. Appl. Phys.* **36** (1997) L971.

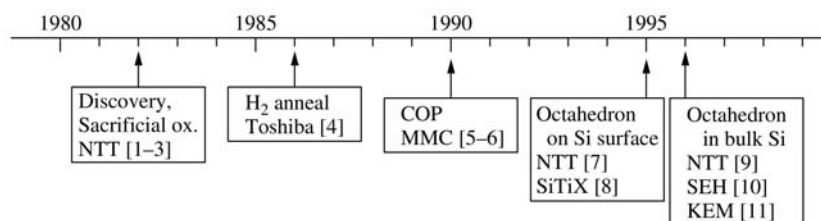
10 Octahedral Void Defects in Czochralski Silicon

MANABU ITSUMI

*NTT Lifestyle and Environmental Technology Laboratories 3-1, Morinosato
Wakamiya, Atsugi-Shi, Kanagawa, 243-0198 Japan*

10.1 BACKGROUND

During the past 20 years there have been several breakthroughs in the research on grown-in defects in Czochralski silicon (CZ-Si) for commercial use (Figure 10.1). The presence of oxide defects originating in CZ-Si (Figure 10.2) was reported from 1979 to 1982 (Nakajima *et al.* 1979, Itsumi *et al.* 1980, Itsumi and Kiyosumi 1982), and it was soon proposed that they could be eliminated by sacrificial oxidation (Itsumi and Kiyosumi 1982), nitrogen annealing (Kiyosumi *et al.* 1983), and hydrogen annealing (Matsushita *et al.* 1986). In those days, the origin of the defects was not clear. From 1990 onwards, when crystal-originated particles (COPs) were reported (Ryuta *et al.* 1990, Ryuta *et al.* 1992), the problem was studied in-depth (Yamagishi *et al.* 1992, Sadamitsu *et al.* 1993, Park *et al.* 1994, Itsumi 1994). Despite systematic examination of crystal-growth conditions and wafer-annealing conditions, the origin of the defects remained unclear until in 1995 octahedral void defects were found just under oxide defects (Itsumi *et al.* 1995, Miyazaki *et al.* 1995) (Figure 10.3) and in 1996 were also found in bulk CZ-Si (Ueki *et al.* 1996, Kato *et al.* 1996, Nishimura *et al.* 1996, Ueki *et al.* 1997) (Figure 10.4). Various observation methods for COP detection using particle counters (Ryuta *et al.* 1990, Ryuta *et al.* 1992), copper decoration (Itsumi and Kiyosumi 1982, Itsumi 1994, Itsumi *et al.* 1995), laser-scattering tomography (LST) (Ueki *et al.* 1996, Kato *et al.* 1996, Nishimura *et al.* 1996), sample thinning with a focused ion beam (FIB), observation with transmission electron microscopy (TEM), and other related techniques were refined and applied to many samples. It was then recognized that the octahedral void defects are a cause of oxide defects, of flow-pattern defects (FPDs), and of COPs (Yanase *et al.* 1996, Mera *et al.* 1996, Itsumi 1996, Tamatsuka *et al.* 1997, Inoue 1997a and b, Rozgonyi *et al.* 1997, Vanhellemont *et al.* 1997, Graf *et al.* 1998). These defects were then looked for in the megabit-level dynamic random access memories (RAMs) (Gonzalez *et al.* 1996, Furumura 1996, Yamamoto and Koyama



- [1] O. Nakajima, M. Itsumi, N. Shiono, and Y. Yoriume, Extended Abstract (The 26th Spring Meeting, Mar. 1979), Japan Society of Applied Physics 30p-R-1, 512 (1979) (in Japanese).
- [2] M. Itsumi, Y. Yoriume, O. Nakajima, and N. Shiono, Extended Abstract (The 27th Spring Meeting, Mar. 1980), Japan Society of Applied Physics Phys. 3p-E-1, 553 (1980) (in Japanese).
- [3] M. Itsumi and F. Kiyosumi, *Appl. Phys. Lett.* **40** (6), 496 (1982).
- [4] Y. Matsushita, M. Watatsuki, and Y. Saito, Extended Abstract, 18th Conf. Solid State Devices and Materials Tokyo, 529 (1986).
- [5] J. Ryuta, E. Morita, T. Tanaka, and Y. Shimanuki, *Jpn. J. Appl. Phys.* **29**, No. 11, L1947 (1990).
- [6] J. Ryuta, E. Morita, T. Tanaka, and Y. Shimanuki, *Jpn. J. Appl. Phys.* **31**, Part 2, No. 3B, L293 (1992).
- [7] M. Itsumi, H. Akiya, T. Ueki, M. Tomita, and M. Yamawaki, *J. Appl. Phys.* **78**(10), 5984 (1995).
- [8] M. Miyazaki, S. Miyazaki, Y. Yanase, T. Ochiai, and T. Shigematsu, *Jpn. J. Appl. Phys.* **34**, 6303 (1995).
- [9] T. Ueki, M. Itsumi, and T. Takeda, (1996) Int. Conf. on Solid State Devices and Materials, Yokohama, LA-1, 862 (1996).
- [10] M. Kato, T. Yoshida, Y. Ikeda, and Y. Kitagawara, *Jpn. J. Appl. Phys.* **35**, 5597 (1996).
- [11] M. Nishimura, S. Yoshino, H. Motoura, S. Shimura, T. Mchedlidze, and T. Hikone, *J. Electrochem. Soc.* **143**, 243 (1996).

Figure 10.1 Representative research of grown-in defects in CZ-Si.

1996, Muranaka *et al.* 1997, Makabe *et al.* 1998). The octahedral void defects have since become of significant scientific interest.

10.2 OBSERVATION METHODS

The locations (2-dimensional coordinates) of COPs on a Si wafer treated with SC1 ($\text{NH}_4\text{OH}:\text{H}_2\text{O}_2:\text{H}_2\text{O} = 1:1:5$, $75\text{--}85^\circ\text{C}$) were detected as localized light scatterers by using a particle counter (or a surface-scanning inspection system). Atomic-force microscopy (AFM) was used to observe the shape of the COPs (Ryuta *et al.* 1990, Ryuta *et al.* 1992). Single pits or dual pits were observed. Viewed from the top, the etch pits on a (001) Si surface were square or rectangular and those on a (111) Si surface were triangular or hexagonal.

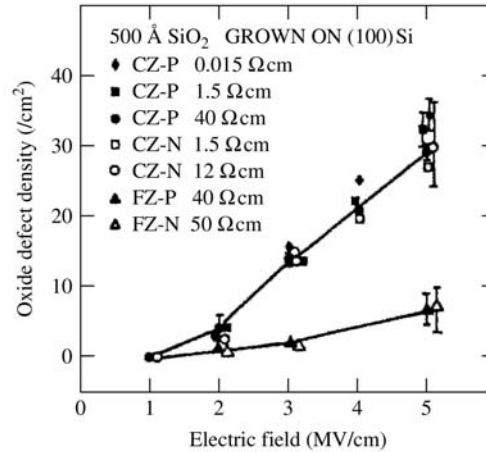


Figure 10.2 The dependence of oxide defect density on oxide electric field.

FPDs formed by vertical immersion of Si wafers in unstirred Secco etch solution can be easily observed using low-power optical microscopy (Yamagishi *et al.* 1992). We can observe a small etch-pit at the apex of a V-shaped etch feature, which is due to the vertical flow of etchant initiated by gas bubbles nucleating at the etch pit.

The locations of the oxide defects (weak spots) in thermal oxide grown on Si wafers were determined by using electrical copper decoration. The samples were then thinned to several hundred nanometers by using a FIB so that they could be observed by cross-sectional TEM (Itsumi *et al.* 1995). Copper decoration does not obliterate the shape of the oxide defects because it requires only a small electronic current if the decoration condition is optimized. The Si wafer with oxide film on its front side was immersed in methanol and the rear side of the wafer was brought downward into direct contact with a gold-coated cathode. A copper mesh anode was immersed in the liquid above the wafer and the required test voltage was applied. The voltage at the oxide surface was measured with a surface-voltage probe, and the oxide electric field strength was calculated as the applied voltage divided by the oxide thickness. Localized copper decorations at defect sites in the oxide were observed with a low-power optical microscope.

The locations (3-dimensional coordinates) of the grown-in defects in bulk Si were determined by laser-scattering tomography (LST) (Moriya *et al.* 1989, Ogawa *et al.* 1997) and then the thickness of the samples was reduced to several hundred nanometers by using FIB so that they could be observed by cross-sectional TEM (Ueki *et al.* 1996, Kato *et al.* 1996, Nishimura *et al.* 1996, Ueki *et al.* 1997). The sample-preparation procedure (Figure 10.5) is as follows: The wafers were cleaved to form specimens with the size of several millimeters by several centimeters. The locations (3-dimensional coordinates) of the grown-in defects were determined by LST. Then, four dots were made on one side

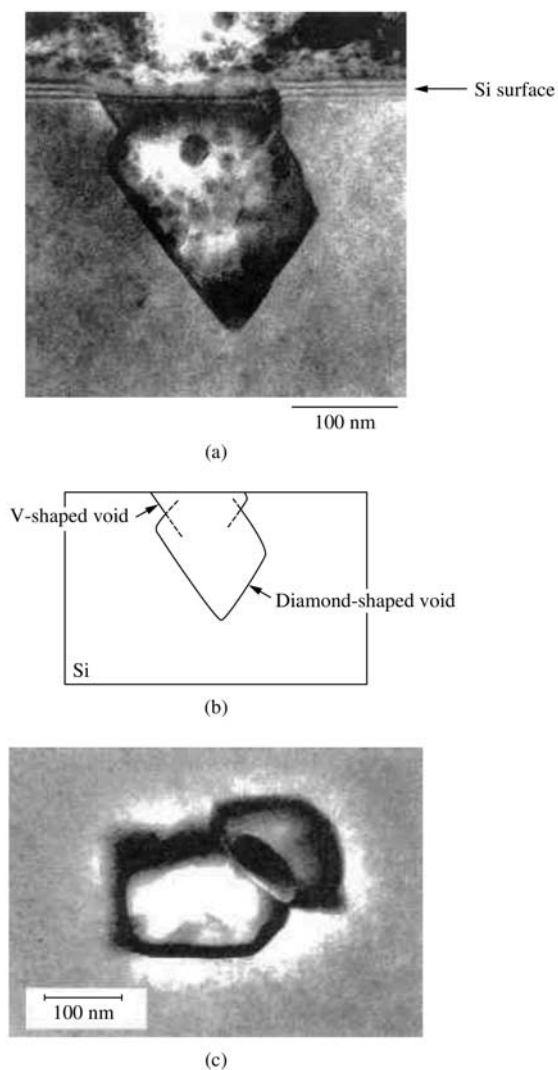


Figure 10.3 Octahedral-structured defects found on the surface of (001)-oriented CZ-Si: (a) cross-sectional view; (b) schematic illustration of (a); (c) plan view. (Part(a) – Reprinted from M. Itsumi *et al.*, *J. Appl. Phys.* **78/10** (1995) 5984–5988, copyright (1995) with permission from the American Institute of Physics.)

surface area surrounding the defect by using FIB (first marking). The arrangement of the four dots was then reconfirmed using LST, and a new set of four dots closer to the defect was made on the same surface (second marking). After that, the specimens were cut out using a diamond saw. Finally, the FIB thinning and TEM observations were repeated a few times so that the defects might be

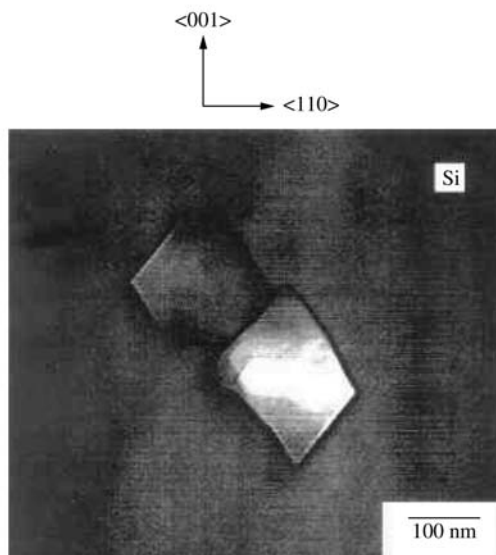


Figure 10.4 A dual-type octahedral void defect found in bulk CZ-Si. Cross-sectional view. (001)-oriented Si.

included in the specimens. The specimens were thinned by FIB to about 300 nm for TEM observation. The samples were also analyzed using energy-dispersive X-ray spectroscopy (EDS or EDX). Analysis by Auger electron spectroscopy (AES) with a more precise detection limit was also done using Ar sputtering.

It is not easy to make the specimen thin enough for TEM observation and at the same time be certain that it contains the defect. This is because the defect cannot be monitored in situ during the FIB specimen-thinning process. A stereo method was therefore developed to determine the precise location of the defects in specimens. First, FIB is used to form two dot markers on one side of the specimen and two dash markers on another side. Then the specimen is tilted by -15° , 0° , $+15^\circ$, and the defect and the two kinds of markers are observed by TEM at each of the tilt angles. The location of the defect can be calculated from the observed distances between the defect and the markers. This method enables us to obtain TEM specimens less than 200 nm thick.

10.3 CHARACTERIZATION

As shown in Figure 10.6, octahedral void defects are basically determined by eight (111) subplanes. But defects observed were often either an incomplete octahedral structure that is partially truncated by a (001) subplane (Figure 10.7), or two incomplete octahedral defects convoluting each other (dual-type void defects). This author observed twenty defects by TEM and found all of them to be

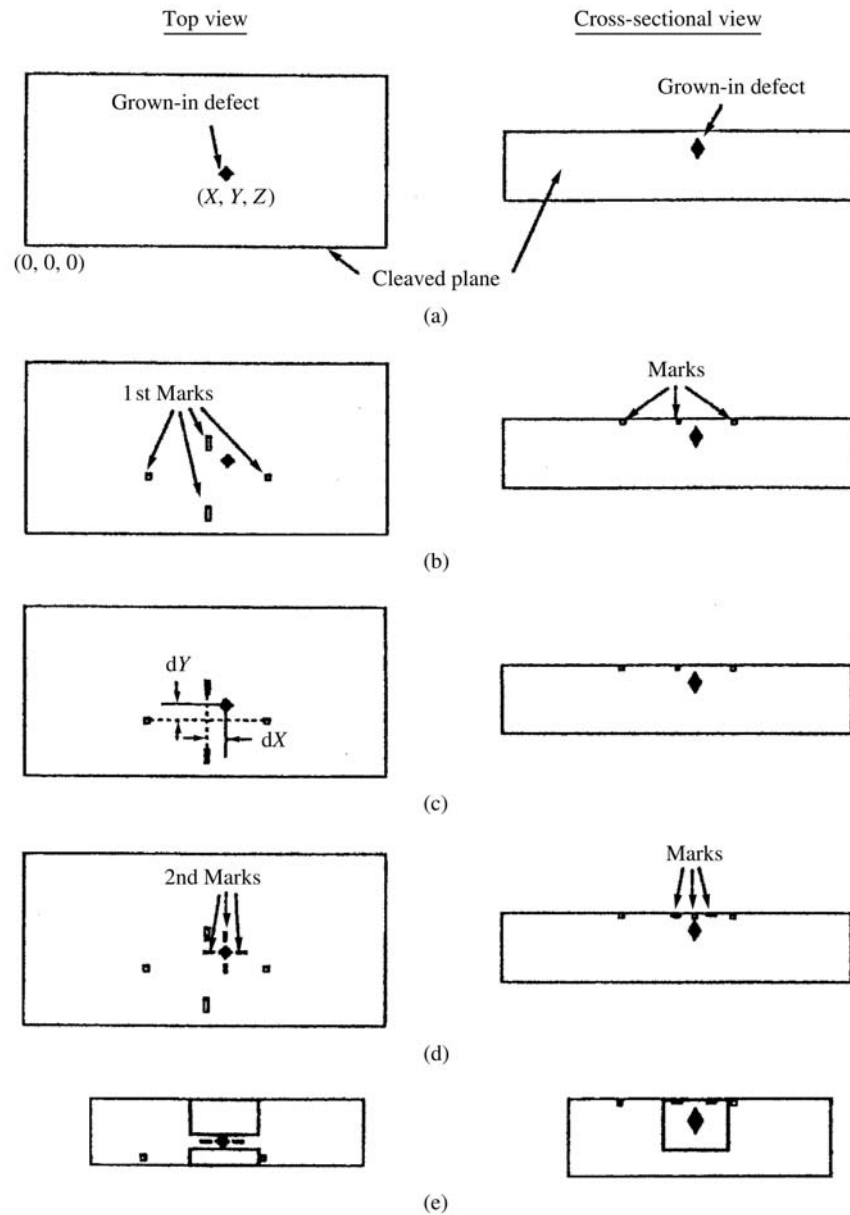


Figure 10.5 Sample-preparation procedure. (a) the first coordinate measurement with infrared tomography; (b) the first marking with a FIB; (c) the second coordinate measurement; (d) the second marking; (e) sample thinning with a FIB. (Reprinted from M. Itsumi *et al.*, *Jpn. J. Appl. Phys.* **37**(1) (1998) 1228–1235, copyright (1998) with permission from the Institute of Pure and Applied Physics.)

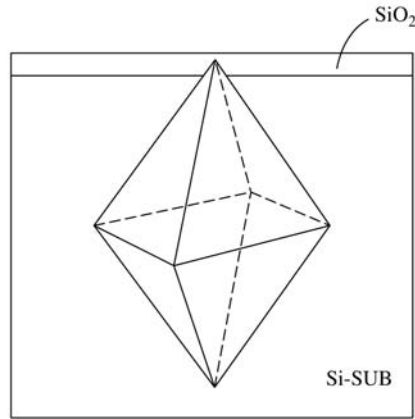


Figure 10.6 Schematic illustration of the octahedral structure.

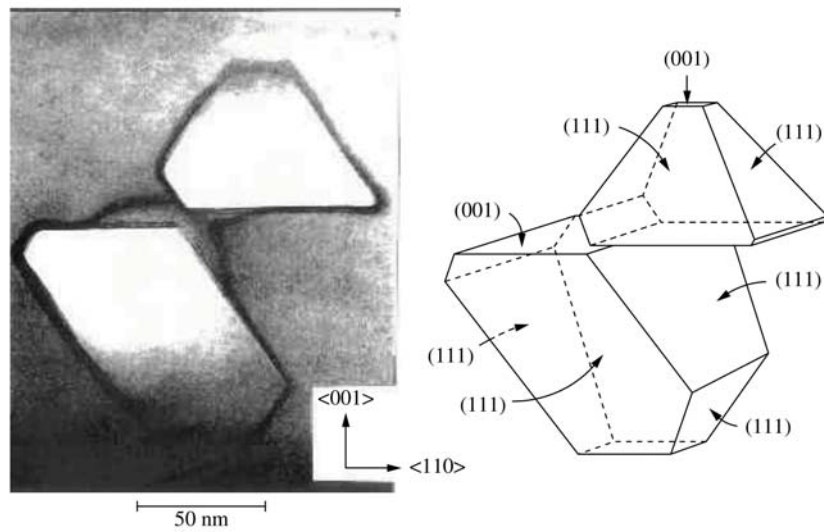


Figure 10.7 An incomplete dual-type octahedral void defect found in bulk CZ-Si.

dual-type void defects. The defects were about $0.1\ \mu\text{m}$ across, the defect density per unit volume was $10^5\text{--}10^6\ \text{cm}^{-3}$, and the defect density per unit area was $1\text{--}10\ \text{cm}^{-2}$. The void defects were randomly distributed throughout the Si wafer. The defects are basically void defects, and the inner walls of the void defects are covered with oxide 2–4 nm thick. A top view of a defect – for example, Figure 10.3(c) – indicates that the shape of the defect is square-like and the sides are oriented along the $[110]$ axes. A superimposed dual-type square structure is observed in many cases. These features are common to the crystal obtained

from most prominent Si vendors because most of the vendors use similar growth conditions (for example, the growth rate for Si wafers 6–8 inches in diameter is about 1 mm/min).

The spatial relation of the two voids of the dual-type defect was examined and two types of configuration were found. In one type the two voids overlap each other (Figure 10.8) and in the other type the two voids are close to each other (Figure 10.9) (Ueki *et al.* 1998a). In the overlapping type, a hole is formed

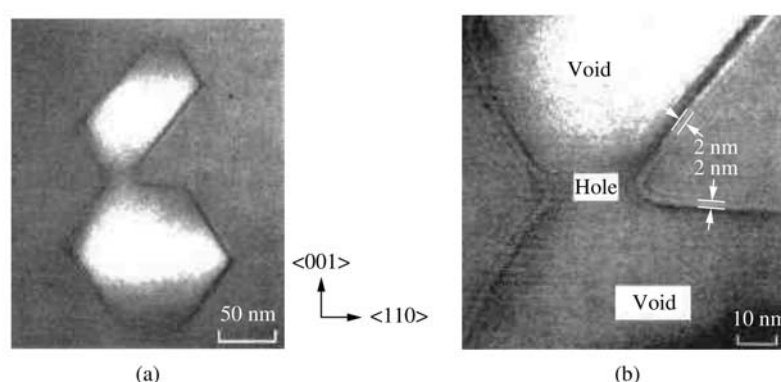


Figure 10.8 TEM micrographs of two overlapping voids: (a) cross-sectional view; (b) enlargement of the connection region.

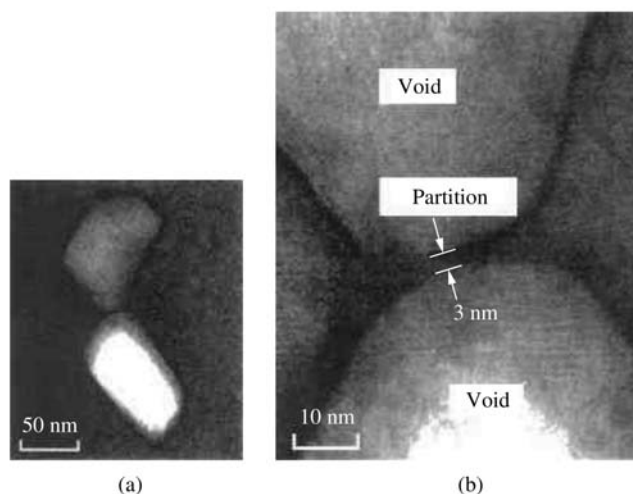


Figure 10.9 TEM micrographs of two adjacent voids: (a) cross-sectional view; (b) enlargement of the connection region. (Reprinted from M. Itsumi and T. Takeda, *Jpn. J. Appl. Phys.* **37**(1) (1998) 1667–1670, copyright (1998) with permission from the Institute of Pure and Applied Physics.)

in the connection part. It is also observed that the thickness (2–3 nm) of oxide on the side walls of one void is similar to that of oxide on the side walls of the other void. In the adjacent type, a partition layer of oxide 2–3 nm thick is located between the two voids. In this type, too, the side walls of both voids are covered with oxide 2–3 nm thick. How the two voids are generated is not clear and several models have been proposed (Kato *et al.* 1996, Tanahashi *et al.* 1997, Voronkov 1999).

Several researchers (Gonzalez *et al.* 1996, Furumura 1996, Yamamoto and Koyama 1996, Muranaka *et al.* 1997, Makabe *et al.* 1998) have found 0.1- μm dual-type or single-type square defects over the locally oxidized silicon (LOCOS) area in the memory cells of MOS RAMs. They reported that these defects cause excessive leakage current between neighboring cells and they asserted that this leakage current is more serious than that due to gate-oxide defects because the area of the LOCOS is much larger than that of the gate oxide. In any case, 0.1- μm defects will seriously affect the production yield and reliability of the next-generation Si LSIs with design rules of about 0.1 μm .

10.4 GENERATION MECHANISM

The formation of the octahedral void defects is closely related to the agglomeration of vacancies during the growth process. Two kinds of point defects in Si crystal are vacancies and self-interstitials, and their relative prevalence is determined by the growth conditions. It is widely believed that voids are vacancy-related defects, or that the agglomeration of (supersaturated) vacancies results in the formation of voids. It is also believed that the dislocation clusters are self-interstitial-related defects or the agglomeration of (supersaturated) self-interstitials results in the formation of dislocation clusters. The oxidation-induced stacking fault (OSF) ring is an important parameter: void defects as the vacancy-related defect are observed inside the OSF ring and dislocations as self-interstitials-related defects are observed outside the OSF ring. The radius of the OSF ring depends on the growth rate versus and the temperature gradient G at the solid/liquid interface of the growing crystal. When the growth rate decreases or the temperature gradient becomes larger (i.e., when v/G decreases), the radius of the OSF ring becomes small and finally the OSF ring shrinks closer to the center of Si crystal. When v/G further decreases sufficiently, the OSF ring reaches the center of the crystal and disappears there. In this case, a self-interstitial-rich region is formed throughout the wafer. When the growth rate increases or the temperature gradient becomes smaller (i.e., when v/G increases), on the other hand, the radius of the OSF ring becomes large and the OSF ring approaches the outer surface of the crystal. When v/G is sufficiently high, the OSF ring reaches the outer surface and disappears there. In this case, a vacancy-rich region is formed and void defects are observed throughout the wafer. Several researchers (deKock and Wijgert 1980, Voronkov 1982, Roksnoer 1984, Habu *et al.* 1994,

Brown *et al.* 1994, Dornberger and Ammon 1996, Nakamura *et al.* 1998, Abe 1999) have shown that there is a critical value of v/G (about $0.15 \text{ mm}^2/^\circ\text{C min}$ in the growth-rate region from 0.3 to 5 mm/min) that separates the vacancy-rich region from the self-interstitial-rich region.

The formation process is shown schematically in Figure 10.10. First, vacancies and oxygen atoms are incorporated from the liquid phase into the solid Si crystal. As the crystal grows and cools, vacancy supersaturation is followed by vacancy agglomeration at some nucleation sites and voids begin to form when the temperature is about 1100°C . From about 1100°C to about 1070°C , the size of the voids increases owing to vacancy agglomeration. Oxygen agglomeration is followed by the growth of oxide on the inner walls of the voids. As a result, $0.1\text{-}\mu\text{m}$ octahedral void defects are generated. The concentration and the diffusion coefficient of vacancies in the growing Si crystal are important factors in generating void defects.

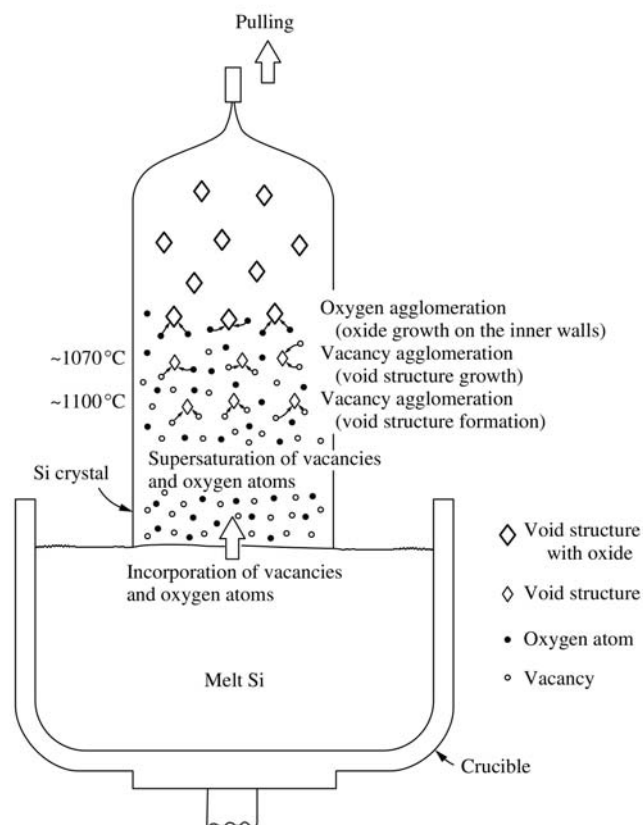


Figure 10.10 Schematic illustration of the formation of octahedral void defects during Si crystal growth.

The density and the size of the octahedral void defects strongly depend on the growth rate (i.e., cooling rate). When the cooling rate increases from 0.3 °C/min to 30 °C/min, their density increases and their size decreases (Saishoji *et al.* 1998).

10.5 ELIMINATION

Decreasing the Si growth rate was effective in decreasing the density of the octahedral void defects (Tachimori *et al.* 1990) but it increased their volume. Measures suggested to eliminate the void defects situated at the surface of Si wafers include sacrificial oxidation (Itsumi and Kiyosumi 1982), nitrogen annealing (Kiyosumi *et al.* 1983), hydrogen annealing (Matsushita *et al.* 1986), and epitaxial-layer growth. Measures suggested to eliminate void-related oxide defects after oxide growth include HCl-added oxidation (Itsumi and Kiyosumi 1982, Itsumi 1994, Itsumi *et al.* 1996), ion implantation through oxides (Itsumi 1994), and wafer rotation with deionized water (Itsumi 1994).

To examine the shrinkage process of the dual-type void defects, Ueki *et al.* prepared CZ-Si samples about 3 μm thick and annealed them in vacuum at about 1100 °C (Ueki *et al.* 1998b). They used ultrahigh-voltage electron microscopy (3 MeV) to observe these thick specimens and found that two voids did not shrink at the same time but that the smaller one shrunk first while the larger one remained unchanged until the smaller one had vanished (Figure 10.11). Then it too began to shrink. This selective extinction of the smaller void solely is very surprising. In addition, a detailed observation revealed that the smaller void begins to shrink from the adjacent region between the two voids. These phenomena suggest a selective emission of vacancies from the adjacent region of the smaller void into the Si bulk (or a selective injection of interstitial Si from the Si bulk into the adjacent region of the smaller void). This experimental finding might possibly imply the presence of the nucleus of the void defect. Before annealing, the thickness of the inner wall was about 2 nm for both the larger void and the smaller void. This thin wall was oxide. As the smaller void shrank, the thickness of its wall was zero while the thickness of the wall of the larger void was the same as the as-grown thickness (about 2 nm). These results suggest that the void shrinks after the side-wall oxide film disappears. The force driving void shrinkage may be related to minimizing the surface energy of the void walls during annealing. It is assumed that minimizing the surface energy first takes place selectively in the smaller void and, after the extinction of the smaller void, minimizing the surface energy takes place in the larger one. The mechanism of the preferential extinction of the adjacent region between two voids is not clear at present.

It was reported that the introduction of impurities (such as oxygen, nitrogen, or boron) into the CZ-Si significantly influences the generation of void defects (Graf *et al.* 1998, Ohashi *et al.* 1999, Kato *et al.* 1999). The size and density of the void defects tend to increase with increasing oxygen concentration. The generation of void defects was strongly suppressed by a boron concentration above a critical level (about 5×10^{18} atoms/cm³). A small amount of nitrogen

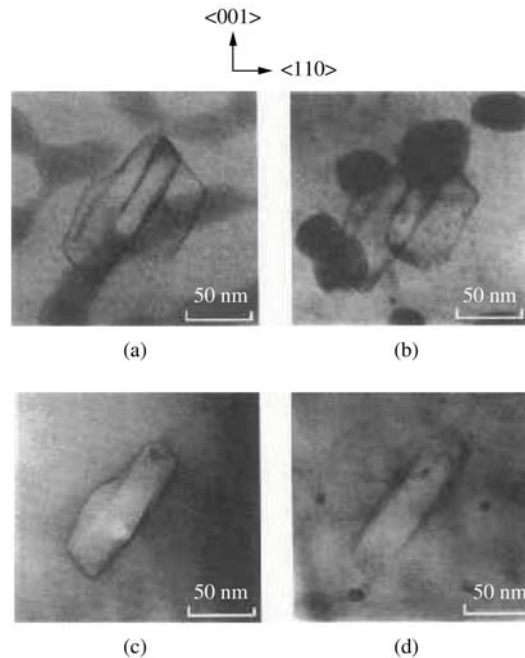


Figure 10.11 TEM micrographs of a void defect shrinking during annealing. (a) before annealing; (b) after annealing at 1080 °C for 30 min; (c) after annealing at 1090 °C for 30 min; (d) after annealing at 1110 °C for 30 min. (Reprinted from T. Ueki *et al.*, *Jpn. J. Appl. Phys.* **37**(2) (1998) L771–L773, copyright (1998) with permission from the Institute of Pure and Applied Physics.)

(about 1×10^{15} atoms/cm³) results in the generation of smaller void defects and in the easier elimination of void defects during additional annealing. This nitrogen-doping method does not increase production cost and might deserve further study.

10.6 OXIDE DEFECT GENERATION

When octahedral void defects are situated on the Si surface (Figure 10.12), thermal oxidation is followed by the generation of oxide defects. The oxide defect density measured by using electrical copper decoration agrees well with that measured by using metal-oxide-silicon capacitor dielectric breakdown tests. The sensitivity of oxide defect detection depends strongly on the oxide thickness (Figure 10.13): oxide defects are more easily detected when the oxide thickness is from 20 to 100 nm. This strange oxide-thickness dependence, which was also reported by other researchers (Yamabe *et al.* 1983), can be explained in terms of the curvature radius of the corners of the octahedral voids and the size of the void defects themselves (Itsumi *et al.* 1998a).

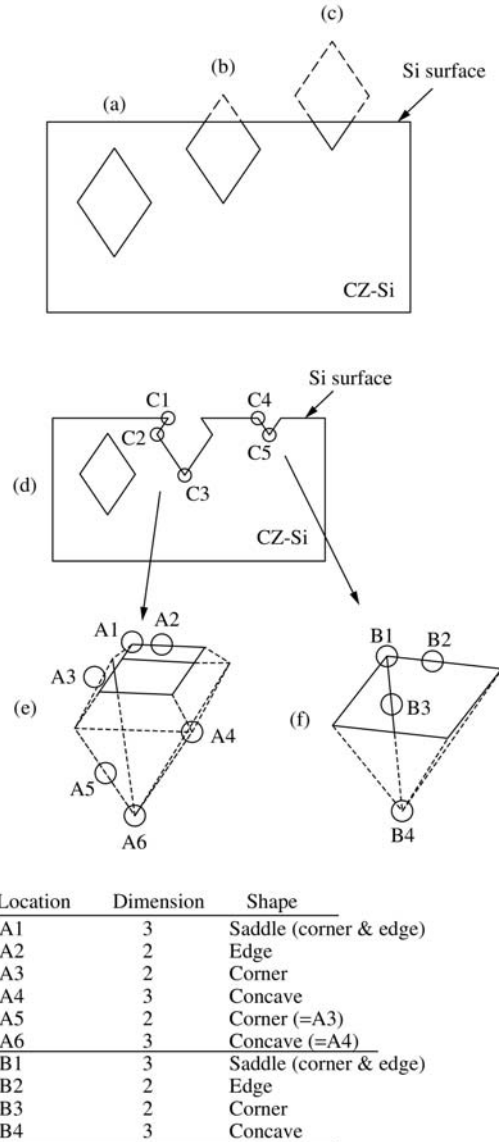


Figure 10.12 A Schematic illustration of an octahedral void defect and a Si surface. (a) when the void defect is in the bulk CZ-Si; (b) when the upper part of the void defect is truncated by the Si surface and a diamond-shaped structure appears; (c) when the bottom part of the void defect is truncated by the Si surface and a V-shaped structure appears; (d) cross section showing edges (C1 and C4) and corners (C2, C3, and C5); (e) bird's-eye view of diamond-shaped structure; (f) bird's-eye view of V-shaped structure. C1 corresponds to A1 or A2. C2 corresponds to A3 or A4. A1 is a corner and an edge. B1 is also a corner and an edge.

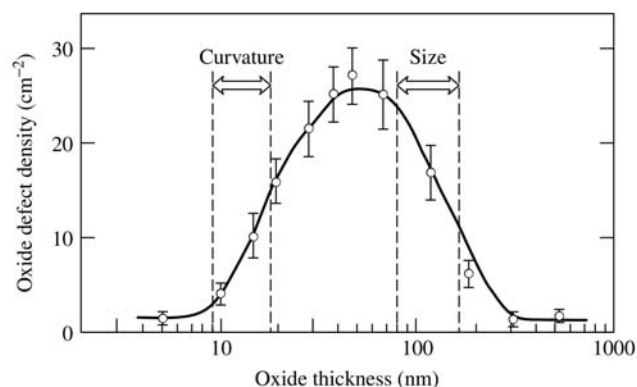


Figure 10.13 The dependence of oxide defect density on oxide thickness. Oxide electric field was 5×10^6 V/cm. This curve represents, in a sense, the detection sensitivity curve of oxide defect generation related to void defects. (Reprinted from M. Itsumi *et al.*, *J. Appl. Phys.* **84**(3) (1998) 1241–1245, copyright (1998) with permission from the American Institute of Physics.)

The curvature radius of the corners of the octahedral voids in bulk Si was about 5 nm (Figure 10.14(a)). When the octahedral voids were situated at the Si surface, the curvature radius of the corners of the octahedral voids was 10–15 nm (Figure 10.14(b)). When oxide with a thickness of less than 10 nm was grown, the effect of the corner curvature of the voids was really small. When oxide with a thickness of more than 10 nm was grown, the effect of the corner curvature of the voids became strong, inducing oxide thinning (defective spot) at the corners (Marcus and Sheng 1982, Hsueh and Evans 1983, Sunami *et al.* 1985). On the other hand, when the oxide thickness exceeded the size of the void defects (100–150 nm) (Figure 10.15), voids were filled with the oxide, eliminating the thin-oxide region (defective spot) (Figure 10.16).

In addition to the oxide thinning with the corner effect, contamination, which may be in the voids, may be related to the oxide-defect generation. HCl-added oxidation was effective in decreasing oxide defects related to octahedral void defects. This effect of HCl-added oxidation can be explained in terms of contamination gettering (or passivation) with HCl (Itsumi *et al.* 1996).

When a thick oxide was thermally grown on Si substrate, an oxide-surface pit was observed on the void defect (Itsumi *et al.* 1998, Itsumi *et al.* 1999b) (Figure 10.17). The diameter of the pit was 1 μm or less and this pit might affect the geometrical shape and electrical reliability of the aluminum interconnects on it. The number of pits (and also octahedral defects and COPs) detected by the particle counter increased with increasing oxide thickness. This shows that a thicker oxide leads to the enlargement of COPs, resulting in the number of COPs being larger than the detection limit of the particle counter. This experimental result resembles the famous findings that the number of COPs increases with

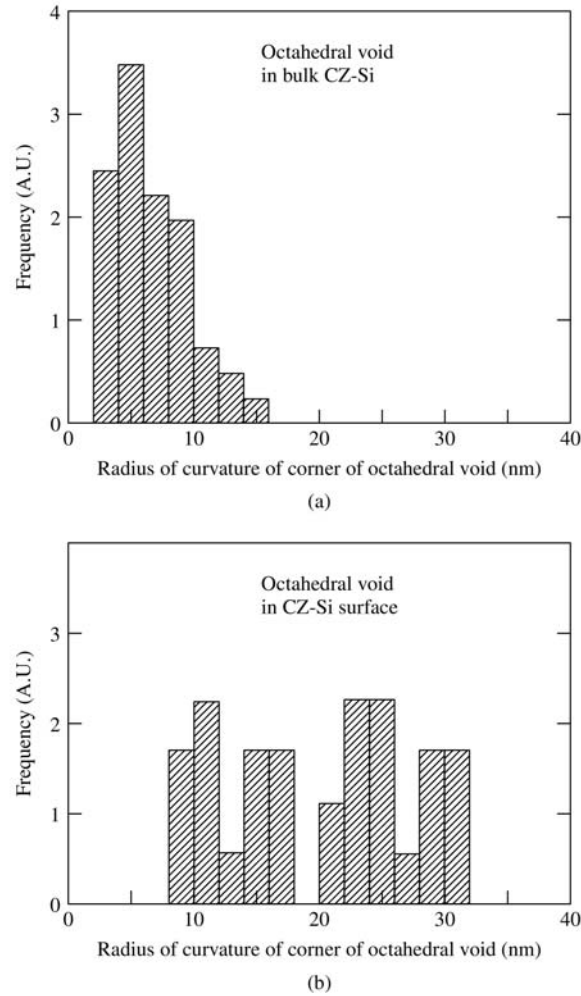


Figure 10.14 Histograms of the curvature radii of the corners of the octahedral void defects (a) in bulk CZ-Si; (b) on the surface of CZ-Si.

increasing SC1 cleaning cycles. In addition, the introduction of an epitaxial layer was effective for eliminating the oxide-surface pits with octahedral defects, which also resembles the result of SC1 cleaning.

10.7 CONCLUDING REMARKS

This review of the structural and chemical characteristics of octahedral void defects in CZ-Si outlined the mechanism of their generation, the way they

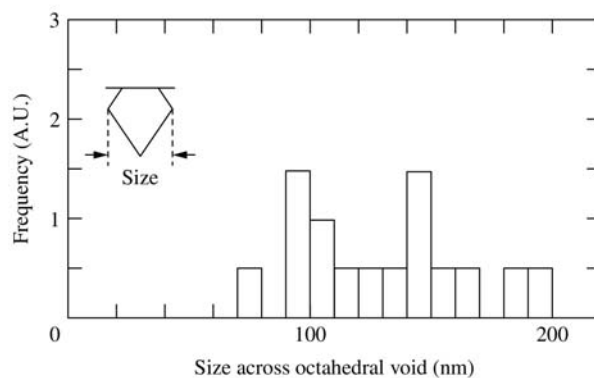


Figure 10.15 Histograms of the size of the octahedral void defects on the surface of CZ-Si.

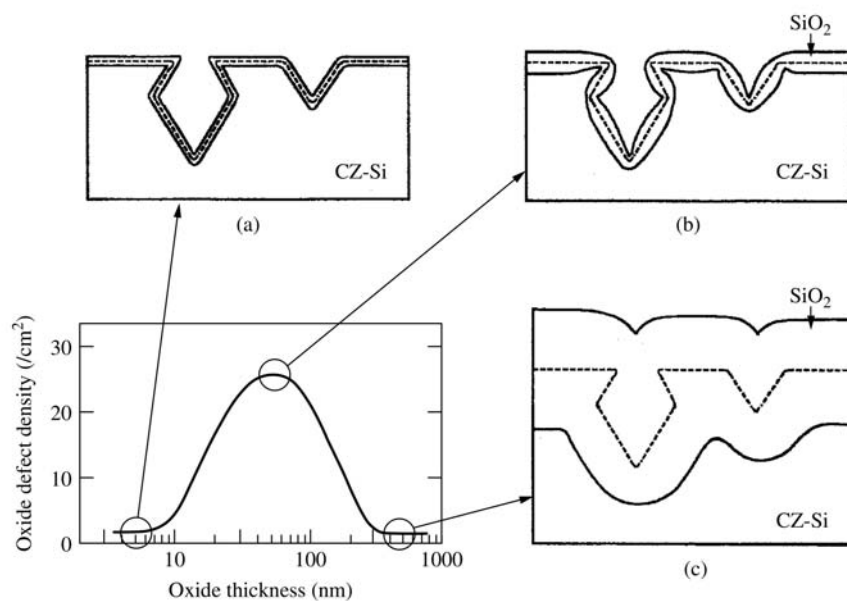


Figure 10.16 A Schematic illustration showing the dependence of oxide defect density on oxide thickness. The dotted lines represent the original Si surface before thermal oxidation. (a) when oxide thickness is less than 10 nm; (b) when oxide thickness is about 50 nm; (c) when oxide thickness is greater than 200 nm.

shrink, and how they can be eliminated. It also described a semiquantitative model explaining the noteworthy dependence of oxide defect density on oxide thickness. Many questions, however, remain. The most important concerns the dual voids. What is the mechanism of their formation? Do the two voids grow

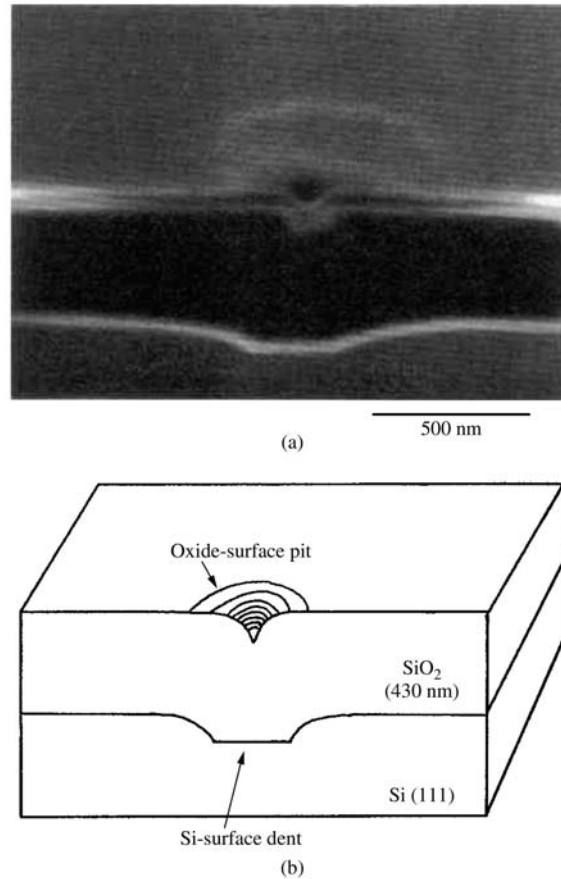


Figure 10.17 An oxide-surface pit and an underlying Si-surface dent: (a) SIM image; (b) schematic illustration [Itsumi 1999] (Reprinted from M. Itsumi *et al.*, *J. Appl. Phys.* **86**(3) (1999) 1322–1325, copyright (1999) with permission from the American Institute of Physics.)

simultaneously (from the same nucleus) or sequentially? If sequentially, what triggers the generation of the second void? Another important problem is the effect of impurities (oxygen, nitrogen, and carbon) on the generation of void defects, but we do not yet have enough information about this problem. It is necessary to examine the effect of these impurities more systematically and in more detail. This should lead to the development of a practical and economical way to grow Si with few void defects, partly because the introduction of small amounts of impurities during CZ-Si growth will not increase production cost much. And this scientific and practical study will lead to the production of the higher-quality and lower-priced large-diameter Si wafers needed for the rapidly expanding multimedia technologies.

REFERENCES

- Abe T. (1999), The European Material Conference (E-MRS) Spring Meeting (Strasbourg, June), E-I.1, E-2.
- Brown R. A., D. Maroudas, and T. Sinno (1994), *J. Cryst. Growth* **137**, 12.
- Dornberger E. and W. von Ammon (1996), *J. Electrochem. Soc.* **143**, 1648.
- Furumura Y. (1996), Proceedings of The 2nd International Symposium on Advanced Science and Technology of Silicon Materials (Nov. (1996), Hawaii), 418.
- Gonzalez F., G. A. Rozgonyi, B. Gilgen, and R. Barbour (1996), *High Purity Silicon IV (ECS)*, C. L. Claeys, P. Rai-Choudhury, P. Stallhofer, J. E. Maurits, (eds), (The Electrochemical Society, Pennington, N.J., USA) 357.
- Graf D., M. Suhren, U. Lambert, R. Schmolke, A. Ehlert, W. von Ammon, and P. Wagner (1998), *J. Electrochem. Soc.* **145**, No. 1, 275.
- Habu R., T. Iwasaki, H. Harada, and A. Tomiura (1994), *Jpn. J. Appl. Phys.* **33**, 1234.
- Hsueh C. H. and A. G. Evans (1983), *J. Appl. Phys.* **54**(11), 6672.
- Inoue N. (1997a), *Oyo-Buturi* (A Monthly Publication of The Japan Society of Applied Physics) **66**, No. 7, (ISSN 0369-8009), 715 (in Japanese).
- Inoue N. (1997b), Proceedings of The Kazusa Akademia Park Forum on The Science and Technology of Silicon Materials Nov. 12-14, Chiba, edited by K. Sumino, 135.
- Itsumi M., Y. Yoriume, O. Nakajima, and N. Shiono (1980), Extended Abstract (The 27th Spring Meeting, Mar. 1980), Japan Society of Applied Physics 3p-E-1, 553 (in Japanese).
- Itsumi M. and F. Kiyosumi (1982), *Appl. Phys. Lett.* **40**(6), 496.
- Itsumi M. (1994), *J. Electrochem. Soc.* **141**, No. 9, 2460.
- Itsumi M., H. Akiya, T. Ueki, M. Tomita, and M. Yamawaki (1995), *J. Appl. Phys.* **78**(10), 5984.
- Itsumi M. (1996), *Symposium Proceedings of Material Research Society* Volume 442, 'Defects in Electronic Materials II' (edited by J. Michel, Dec. 1996, Boston) 95.
- Itsumi M., H. Akiya, T. Ueki, M. Tomita, and M. Yamawaki (1996), *J. Appl. Phys.* **80**, No. 12, 6661.
- Itsumi M., M. Maeda, and T. Ueki (1998a), *J. Appl. Phys.* **84**, No. 3, 1241.
- Itsumi M., Y. Okazaki, M. Watanabe, T. Ueki, and N. Yabumoto (1998b), *J. Electrochem. Soc.* **145**, No. 6, 2143.
- Itsumi M., M. Maeda, T. Ueki, and S. Tazawa (1999), *J. Appl. Phys.* **86**, No. 3, 1322.
- Kato M., T. Yoshida, Y. Ikeda, and Y. Kitagawara (1996), *Jpn. J. Appl. Phys.* **35**, 5597.
- Kato M., M. Tamatsuka, M. Iida, H. Takeno, T. Otogawa, and T. Masui (1999), Extended Abstracts (The 46th Spring Meeting, March, 1999); The Japan Society of Applied Physics and Related Societies 29a-ZB-7, 470. (in Japanese)
- Kiyosumi F., H. Abe, H. Sato, M. Ino, and K. Uchida (1983), Denshi-Tsushin Gakkai, Technical Report SSD 83-66, 1 (1983).
- Kock A. J. R. de and W. M. van de Wijgert (1980), *J. Cryst. Growth* **49**, 718.
- Makabe K., M. Miura, M. Kawamura, M. Muranaka, H. Kato, and S. Ide (1998), Extended Abstracts (The 45th Spring Meeting, 1998); The Japan Society of Applied Physics and Related Societies 30p-YA-5, 413 (in Japanese).
- Marcus R. B. and T. T. Sheng (1982), *J. Electrochem. Soc.* **129**, No. 9, 1278.
- Matsushita Y., M. Watatsuki, and Y. Saito (1986), Extended Abstract, 18th Conf. Solid State Devices and Materials, Tokyo, 529.

- Mera T., J. Jablonski, M. Danbata, K. Nagai, and M. Watanabe (1996), Symposium proceedings of Material Research Society Volume 442, 'Defects in Electronic Materials II' (edited by J. Michel, Dec. 1996, Boston) 107.
- Miyazaki M., S. Miyazaki, Y. Yanase, T. Ochiai, and T. Shigematsu (1995), *Jpn. J. Appl. Phys.* **34**, 6303.
- Moriya K., K. Hirai, K. Kashima, and S. Takasu (1989), *J. Appl. Phys.* **66**, 5267.
- Muranaka M., M. Miura, H. Iwai, M. Kawamura, Y. Tadaki, and T. Kaeriyama (1997), Extended Abstracts of the 1997 International Conference on Solid State Devices and Materials, Hamamatsu, 396.
- Nakajima O., M. Itsumi, N. Shiono, and Y. Yoriome (1979), Extended Abstract (The 26th Spring Meeting, Mar. 1979), Japan Society of Applied Physics 30p-R-1, 512 (in Japanese).
- Nakamura K., T. Saishoji, and J. Tomioka (1998), *Electrochem. Soc. Proc.* **98-13**, 41.
- Nishimura M., S. Yoshino, H. Motoura, S. Shimura, T. Mchedlidze, and T. Hikone (1996), *J. Electrochem. Soc.* **143**, 243.
- Ogawa T., G. Kissinger, and N. Nango (1997), *Electrochem. Soc. Proc.* **97-12**, 132.
- Ohashi W., A. Ikari, Y. Ohta, A. Tachikawa, H. Deai, H. Yokota, and T. Hoshino (1999), Extended Abstracts (The 46th Spring Meeting, March, 1999); The Japan Society of Applied Physics and Related Societies 29a-ZB-1, 468 (in Japanese).
- Park J. G., H. Kirk, K.-C. Cho, H.-K. Lee, C.-S. Lee, and G. A. Rozgonyi (1994), Semiconductor Silicon, edited by H. R. Huff, W. Bergholz, and K. Sumino (Electrochem. Soc., Pennington, 1994) p. 370.
- Rozgonyi G., M. Tamatsuka, Ki-Man Bae, and F. Gonzalez (1997), Proceedings of The Kazusa Akademia Park Forum on The Science and Technology of Silicon Materials Nov. 12-14, Chiba, edited by K. Sumino, 215.
- Roksnoer P. J. (1984), *J. Cryst. Growth* **68**, 596.
- Ryuta J., E. Morita, T. Tanaka, and Y. Shimanuki (1990), *Jpn. J. Appl. Phys.* **29**, No. **11**, L1947.
- Ryuta J., E. Morita, T. Tanaka, and Y. Shimanuki (1992), *Jpn. J. Appl. Phys.* **31**, Part **2**, No. **3B**, L293.
- Sadamitsu S., S. Umeno, Y. Koike, M. Hourai, S. Sumita, and T. Shigematsu (1993), *Jpn. J. Appl. Phys.* **32**, 3675.
- Saishoji T., K. Nakamura, H. Nakajima, T. Yokoyama, F. Ishikawa, and J. Tomioka (1998), *Electrochem. Soc. Proc.* **98-13**, 28.
- Sunami H., T. Kure, K. Yagi, Y. Wada, and K. Yamaguchi (1985), *IEEE J. Solid-State Circuits* **SC-2**, No. **1**, 220.
- Tachimori M., T. Sakon, and T. Kaneko (1990), The Japan Society of Applied Physics and Related Societies, The 7th Kessho Kougaku (Crystal Engineering) Symposium, 27. (in Japanese)
- Tamatsuka M., Z. Radzinski, G. A. Rozgonyi, S. Oka, M. Kato, and Y. Kitagawara (1997), Extended Abstracts of the 1997 International Conference on Solid State Devices and Materials, Hamamatsu, 392.
- Tanahashi K., N. Inoue, and Y. Mizokawa (1997), *Mater. Res. Soc. Symp. Proc.* **442**, 131.
- Ueki T., M. Itsumi, and T. Takeda (1996), Int. Conf. on Solid State Devices and Materials, Yokohama, LA-1, 862.
- Ueki T., M. Itsumi, and T. Takeda (1997), *Jpn. J. Appl. Phys.* **36**, Part **1**, No. **3B**, 1781.
- Ueki T., M. Itsumi, and T. Takeda (1998a), *Jpn. J. Appl. Phys.* **37**, Part **1**, No. **4A**, 1667.

- Ueki T., M. Itsumi, K. Yoshida, A. Takaoka, T. Takeda, and S. Nakajima (1998b), *Jpn. J. Appl. Phys.* **37**, Part 2, No. 7A, L771.
- Vanhellemont J., E. Dornberger, D. Graf, J. Esfandyari, U. Lambert, R. Schmolke, W. von Ammon, and P. Wagner (1997), Proceedings of The Kazusa Akademia Park Forum on The Science and Technology of Silicon Materials Nov. 12–14, Chiba, edited by K. Sumino, 173.
- Voronkov V. V. (1982), *J. Cryst. Growth* **59**, 625.
- Voronkov V. V. (1999), The European Material Conference (E-MRS) Spring Meeting, (Strasbourg, June) E-IV.1, E-6.
- Yamabe K., K. Taniguchi, and Y. Matsushita (1983), in Proceedings of the International Reliability in Physics Symposium, 184.
- Yamagishi H., I. Fusegawa, N. Fujimaki, and M. Katayama (1992), *Semicond. Sci. Technol.* **7**, A135.
- Yamamoto H. and H. Koyama (1996), Proceedings of the 2nd International Symposium on Advanced Science and Technology of Silicon Materials (Nov. 1996, Hawaii), 425.
- Yanase Y., T. Kitamura, H. Horie, M. Miyazaki, and T. Ochiai (1996), Extended Abstracts (The 43rd Spring Meeting, 1996); The Japan Society of Applied Physics and Related Societies 26p-X-5, 184.

11 The Control and Engineering of Intrinsic Point Defects in Silicon Wafers and Crystals

R. FALSTER¹, V. V. VORONKOV² and P. MUTTI²

¹ MEMC Electronic Materials SpA, Viale Gherzi 31, 28100 Novara, Italy

² MEMC Electronic Materials SpA, via Nazionale 59, 39012 Merano, Italy

ABSTRACT

The control of intrinsic point defects in the growth of silicon crystals and the processing of silicon wafers is an increasingly important aspect of the manufacture of silicon materials for the microelectronic industry. This chapter summarizes many aspects of the problem of the incorporation of excess intrinsic point defects and reactions that produce harmful agglomerated defects and the enhanced precipitation of oxygen under certain conditions. Recent advances have led to the production of microdefect-free large-diameter silicon crystals. Point-defect engineering in thin silicon wafers has also led to an important advance in the control of oxygen precipitation for IC applications. Proper control of vacancy-concentration profiles installed during rapid thermal processing of silicon wafers effectively programs silicon wafers to produce robust oxygen-precipitate distributions ideal for internal gettering applications. The intrinsic point defect processes that underlie defect engineering in both crystal growth and wafer processing are the same and results from experiments in both can be joined to give useful information toward a coherent, unified picture of the intrinsic point-defect parameters and reactions.

11.1 INTRODUCTION

Increasing levels of integration and linewidth shrinking in integrated circuit design along with reduced thermal budgets IC processing are placing increasing demands on the silicon substrates used in their manufacture. If the polished Czochralski-grown silicon wafer – as opposed to epitaxial substrates – is to survive as a suitable electronic material for new generations of advanced IC devices, then it appears that new, cost-effective, approaches to the engineering of defects in CZ-grown silicon must be implemented. The problem is two-fold: (1) two

classes of defects *intrinsic* to melt-grown silicon, vacancy- and interstitial-type agglomerated defects and (2), the control of the precipitation of oxygen. Intrinsic point-defect-related agglomerates or *microdefects* are formed during the crystal growth process. The precipitation of oxygen occurs during processing of silicon wafers into ICs, but with a strong connection and coupling to details of crystal-growth processes and wafer heat treatments preceding device processing. These defect types are not new to silicon technology but the demands on their control have increased dramatically in recent years. Furthermore, as the silicon industry matures, there is a need to simplify material-selection processes. Uncertainty of performance must be eliminated and with it the need to highly *tailor* silicon products to specific applications. The complications that arise out of the complex interactions of defects from initial solidification of the silicon crystal ingot through device processing add undesirable costs and rigidity to the use of silicon as an electronic material. Native point defects play the key role in these problems. Control and engineering of these during both crystal-growth and wafer processing can produce solutions that offer significant simplifications in the use of CZ silicon polished wafers in advanced IC applications.

11.1.1 VACANCY-TYPE DEFECTS

The first challenge lies with a defect unique to silicon grown from the melt, an agglomeration of excess vacancies into a rather low-density (typically approximately 10^6 cm^{-3} for the case of CZ silicon) void-type microdefect (Ueki *et al.* 1997). If present, this type of defect can result in the failure of gate oxides and they are of increasing importance in device geometries on the order of the void sizes (on the order of 100–150 nm), isolation failures and other topological faults (Park *et al.* 1999). Depending on the mode of detection, void-type defects are also referred to as D-defects, COPs, flow pattern defects, light-scattering tomography defects and GOI-defects.

11.1.2 SILICON SELF-INTERSTITIAL-TYPE DEFECTS

There exists another and, if anything, even more harmful defect type unique to silicon grown from a melt: agglomerates of excess silicon self-interstitials into large dislocation loops. These defects are sometimes referred as A-defects or large etch pit defects. Their density is generally far lower than that of the void microdefects but their size is usually orders of magnitude larger – hence their importance.

11.1.3 THE PRECIPITATION OF OXYGEN

The control of the behaviour of oxygen in silicon is undeniably one of the most important challenges in semiconductor materials engineering. In the 20 or so

years since the discovery of the internal gettering effect in silicon wafers, many scientists and engineers have struggled with the problem of precisely and reliably controlling the precipitation of oxygen in silicon that occurs during the processing of wafers into integrated circuits (ICs). This has been met with only partial success in the sense that the ‘defect engineering’ of conventional silicon wafers is still, by and large an *empirical* exercise. It consists largely of careful, empirical *tailoring* of wafer type (oxygen concentration, crystal-growth method, and details of any additional pre-heat treatments, for example) to match the *specific* process details of the application to which they are submitted in order to achieve a good *and* reliable internal gettering (IG) performance. Reliable and efficient IG requires the robust formation of oxygen-precipitate-free surface regions (denuded zones) and a bulk defective layer consisting of a minimum density (at least about 10^8 cm^{-3} (Falster *et al.* 1991)) oxygen precipitates during the processing of the silicon wafer. Uncontrolled precipitation of oxygen in the near surface region of the wafer represents a risk to device yield.

11.2 THE CONTROL OF THE AGGLOMERATION OF INTRINSIC POINT DEFECTS DURING CRYSTAL GROWTH

11.2.1 THE v/G RULE FOR THE TYPE OF GROWN-IN MICRODEFECTS

Early studies of grown-in microdefects in float-zoned silicon (de Kock 1973) showed that swirl-microdefects (A- and B-defects) disappear if the growth rate v exceeds some threshold value. Crystals grown at larger v were found to contain a different kind of grown-in microdefect, D-defects (Veselovskaya *et al.* 1977, Roksnoer and van den Boom 1981). The threshold (or critical) growth rate for the change-over from A/B defects to D-defects was found to be proportional to the near-interface axial temperature gradient G (Voronkov 1982, Voronkov *et al.* 1984). In other words, the type of grown-in microdefects is controlled simply by the ratio v/G . Swirl (interstitial type) defects are formed if v/G is below some universal critical ratio ξ_t and D-defects are formed otherwise. This simple ‘ v/G rule’ holds both for float-zoned and Czochralski-grown crystals (Voronkov and Falster 1998), in spite of a great difference in the oxygen content. The physical meaning of this rule is very simple (Voronkov 1982): the type of intrinsic point defects incorporated into a growing crystal is controlled by the parameter v/G , according to the defect transport equations for diffusion, convection and annihilation of point defects in the vicinity of the interface.

Growing a crystal at $v/G > \xi_t$ results in incorporation of vacancies, while the interstitial concentration is undersaturated and decays fast due to recombination with vacancies. The vacancies agglomerate into voids (D-defects) on further cooling – if the vacancy concentration is not too low (Voronkov and Falster 1998). The identification of D-defects with voids was recently demonstrated (Ueki *et al.* 1997, Nishimura *et al.* 1998). At low vacancy concentration (for instance, at v/G

only slightly larger than the critical ratio ξ_i) the dominant agglomeration path is production of oxide particles instead of voids (Voronkov and Falster 1998). Accordingly the main vacancy region of a crystal (that containing voids) is surrounded with a narrow band of oxide particles (P-band). The presence of P-band is manifested by the formation of ring-distributed stacking faults during high-temperature oxidation of wafers. Beside this OSF ring (P-band) there is a well-pronounced band of still lower vacancy concentration (the L-band) where vacancy agglomeration is suppressed, and appreciable vacancy concentration is frozen-in to enhance oxygen precipitation (Falster *et al.* 1998b).

Growing a crystal at $v/G < \xi_i$ results in incorporation of self-interstitials, while the vacancy concentration is undersaturated and decays rapidly. The self-interstitials agglomerate into A/B-swirl-defects. The A-defects were found to be extrinsic dislocation loops (Foell and Kolbesen 1975) while B-defects seem to be small globular clusters of interstitials (Petroff and de Kock 1975) (most likely, including carbon interstitials). Particularly, at low interstitial concentration only B-defects are formed. At still lower concentrations, no defects are formed. Accordingly, the main interstitial region of a crystal (that containing A-defects) is surrounded with a band of B-defects. This marginal B-band of interstitial region is analogous to the P-band of vacancy region.

Some crystals, due to axial and/or radial variation in v/G , consist of well-separated vacancy and interstitial regions. The boundary between these regions is approximately marked by the position of the OSF ring, and still better marked by the position of the L-band. An example of this defect-banding phenomenon is shown in Figure 11.1.

11.2.2 ALTERNATIVE VIEWS TO THE v/G RULE

There is an opinion (Abe 1999) that the type of microdefects, either A/B-defects or D-defects (that is, the type of incorporated point defects, either interstitial

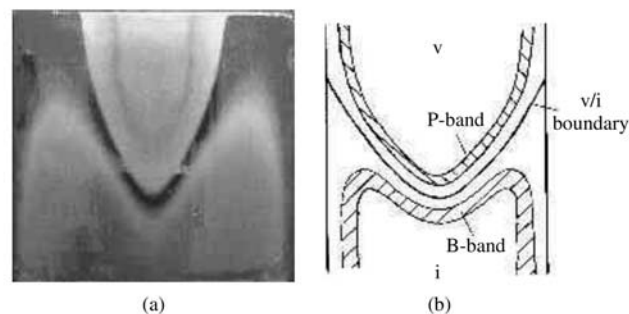


Figure 11.1 (a) An axial cross section of an etched cu-decorated CZ crystal section at the transition from vacancy-type defect growth conditions (the upper 'U-shaped' section) and interstitial-type defect conditions (the lower 'M-shaped' structure); (b) A schematic diagram of the structure.

or vacancy) is controlled simply by the value of the near-interface temperature gradient G : vacancies at lower G , interstitials at higher G . This notion is based on the fact that increasing the growth rate v is accompanied by some decrease in G . It was then thought (Abe 1999) that the actual reason for the change-over from interstitial to vacancy is not an increase in v (in v/G) but a decrease in G . This notion is certainly not true since the change-over in early float-zoned crystals occurs at very high values of $G(v)$, about 300 K/cm (de Kock 1973). A similar change-over in modern Czochralski crystals occurs at much smaller gradient, about 30 K/cm (Falster *et al.* 1998b). In both cases the change-over occurs at about the same v/G ratio (around 0.15 mm²/min K).

It should also be remarked that the measured (decreasing) dependence of G on v was considered (Abe 1999) as contradicting the heat balance equation at the interface ($Qv = \chi G - \chi' G'$ where Q is the heat of fusion per a unit volume of crystal and χ is the heat conductivity of crystal; χ' and G' refer to the melt). Actually there is no contradiction at all. The temperature field in the crystal, including the value of G , is completely decoupled from the above heat balance – if the interface shape is specified. This is so because the interface temperature is fixed: it is the melting temperature of 1412 °C. This boundary condition, together with the heat loss boundary condition at the crystal surface, defines the temperature field of the crystal. Increasing v means that

- (a) The convection heat flux from the interface into the crystal is increased, and all the crystal bulk becomes a little hotter; accordingly G is somewhat decreased. The computed function $G(v)$ for float-zoned crystals (Voronkov *et al.* 1984) decreases on v only slightly, by less than 30 % within the relevant range of v . The measured gradient showed no resolvable dependence on v (Voronkov *et al.* 1984).
- (b) The melt temperature gradient G' should be remarkably diminished, by a proper increment of the heater power, to keep the heat balance at the interface. The required decrease in $G' = (\chi G - Qv)/\chi'$ is caused both by an increase in v and a decrease in $G(v)$.

It is therefore clear that the decreasing dependence of G on v is a ‘normal’ (though not very significant) effect that casts no doubt on the v/G rule for the interstitial to vacancy change-over.

11.2.3 VOID REACTION CONTROL

One approach to an engineering improvement of the microdefect problem is to grow crystals in the vacancy mode but to engineer the reactions that produce voids. It is found that the resultant density of voids is proportional to the factor $q^{3/2} C_v^{-1/2}$ (Voronkov and Falster 1998), where q is the cooling rate at the

temperature at which the reaction occurs and C_v the local concentration of vacancies. The v/G model (Voronkov 1982), although only a one-dimensional model, usually gives C_v accurately at distances greater than about a centimeter or so from the crystal surface. For a more complete and detailed picture, numerical simulation must be performed. The void reaction occurs over a very narrow temperature range (about 5 K) at a temperature that depends on C_v (Voronkov and Falster 1998). The range of typical reaction temperatures lies between about 1000 and 1100 °C (Falster *et al.* 1998b, Puzanov and Eidenzon 1992, Saishoji *et al.* 1998). The problem of reducing void defect density is thus a coupled engineering problem. A growing silicon ingot is a rigid object. One must engineer simultaneously the coupled problems of the incorporation of vacancies near the growth interface (v and G at about the melt temperature) and the cooling rate at the reaction temperature (v and G at a temperature that depends on C_v). This can be done, but for largely practical reasons, only about a factor of 10 reduction in void density is possible. For some applications, this is not enough improvement to insure device yields that are not limited by the starting substrate defectivity.

11.2.4 PERFECT SILICON

A more robust solution to the microdefect problem and one that circumvents the question and resultant complications of whether or not the material is sufficiently improved to meet the needs of an arbitrary IC process is not to control the microdefect reaction, but to suppress it. As described above, there exist two marginal bands straddling the transition from vacancy- to interstitial-type silicon in which the reactions that produce microdefects do not occur. In these regions, the concentrations of either vacancies or self-interstitials are too low to drive the reactions during the cooling of the crystal. They differ in character due to the differing effects of unreacted vacancies or interstitials on the subsequent nucleation of oxygen clusters at lower temperatures. Excess vacancies enhance the clustering, while excess interstitials suppress it. In terms of process control, the width in v/G space around the critical value that produces sufficiently low concentrations of both vacancies or interstitials is on the order of 10%. Growth processes that can control v/G to within 10% around the critical value both axially and radially are capable of producing microdefect-free silicon. This is not an easy task. Methods exist that result in the partial relaxation of this requirement such that the production of such 'perfect silicon' is practically possible along nearly the entire crystal length. In general, three types of perfect silicon are possible: (1) entirely vacancy-type, exhibiting a generally enhanced oxygen precipitation, (2) entirely interstitial-type perfect material in which oxygen precipitation is suppressed and (3) a mixed type. Figure 11.2 illustrates the difference between sections of vacancy defective, interstitial defective and interstitial-perfect silicon when decorated by copper.

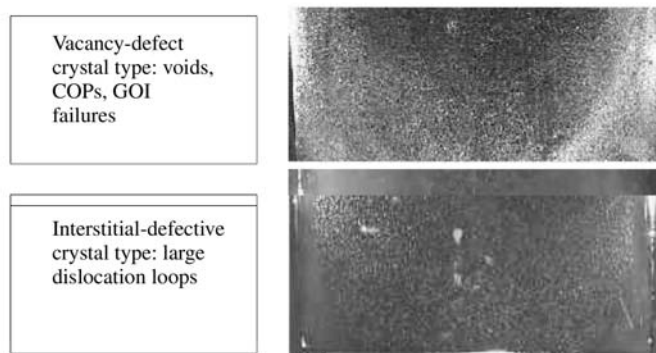


Figure 11.2 Images of silicon crystal cross sections after copper decoration and etching.

11.3 THE CONTROL OF OXYGEN PRECIPITATION THROUGH THE ENGINEERING OF VACANCY CONCENTRATION IN SILICON WAFERS: MAGIC DENUDED ZONE™ WAFERS

In the discussion above, it was noted that there exists a region of vacancy concentration accessible through crystal-growth in which no microdefects are formed but in which the clustering of oxygen is significantly enhanced. It is also possible to achieve such levels of vacancy concentration in thin wafers through the proper control of their heating and cooling. By doing so, it is possible to strongly affect the subsequent precipitation behaviour of the wafer. In fact, it is possible, through the judicious control of point-defect generation, injection, diffusion and recombination to install vacancy-concentration profiles into silicon wafers that result in the ideal precipitation performance for internal gettering (IG) purposes.

While high concentration of vacancies enhance oxygen clustering, it is found that there is a lower bound on vacancy concentration for which clustering is 'normal'. This is quite a sharp transition and lies around about $5 \times 10^{11} \text{ cm}^{-3}$. Installing a vacancy concentration profile that rises from the wafer surface into the bulk of the wafer crossing the critical concentration at some desired depth from the surface results in a wafer with a surface region of 'normal' silicon and a bulk of vacancy-enhanced precipitation. This is the basis underlying the 'magic denuded zone™' (or MDZ™) wafer (Falster *et al.* 1998a).

11.3.1 'TABULA RASA' SILICON AND THE SUPPRESSION OF OXYGEN PRECIPITATION IN LOW-VACANCY-CONCENTRATION MATERIAL

In modern low-vacancy silicon, oxygen precipitation is suppressed if grown-in pre-existing clusters are dissolved by simple high-temperature heat treatments. Such material is known as 'Tabula Rasa' silicon (Falster *et al.* 1997).

The dissolution of grown-in clusters is an integral part of the thermal treatments necessary to install the required vacancy concentration profile. From the 'Tabula Rasa' state, re-nucleation of stable oxygen clusters at low temperatures (approximately 450–700 °C) is inhibited in almost all practical cases by the requirement of relatively long incubation times, even though the oxygen concentration remains high. Thus 'normal' precipitating material actually means the suppression of precipitation in most practical situations. In the high vacancy concentration regions, the incubation times are reduced over a wide temperature range to very small values (Falster *et al.* 1998a). It is this very large difference in incubation times between high and low vacancy concentrations that is primarily responsible for the creation of the denuded zone effect.

Through control of process temperature, ambient and cooling rate a wide variety of precipitate profiles can be installed in thin silicon wafers. An example of the precipitate profiles achieved from two different installed vacancy-concentration profiles along with the resulting oxygen precipitate profiles is shown in Figure 11.3. Vacancy-concentration profiles were measured by a

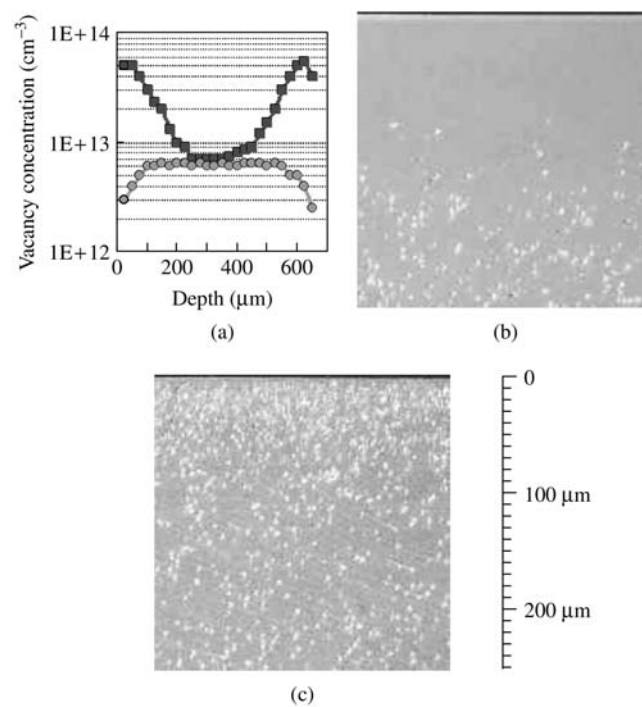


Figure 11.3 Vacancy concentration profiles (a) from Pt diffusion results on two samples heat treated at 1250 °C for 30 s in a nitrogen (squares) and argon (circles) ambient. Following this the wafers were given a precipitation test treatment (4 h, 800 °C + 16 h, 1000 °C); (b) argon treatment; (c) nitrogen treatment. The bulk precipitate densities in both cases are approximately $5 \times 10^{10} \text{ cm}^{-3}$.

Pt-diffusion technique (Jacob *et al.* 1997). In low vacancy concentration surface regions, the Pt technique is not very accurate due to competition with the kick-out mechanism for platinum incorporation.

11.3.2 MATERIAL 'SWITCHING' AND TRANSFER FUNCTIONS

The transition in vacancy concentration between 'normal' and 'enhanced' precipitation is very sharp indeed. Figure 11.4 is a plot of current estimates of the density of oxygen precipitates produced by a simple 'test' heat treatment (4 h at 800 °C followed by 16 h at 1000 °C) as a function of vacancy concentration at the outset of the treatment. The width of the bar represents some uncertainty in the determination of vacancy concentration. Such a sharp transition represents a kind of material-switching action and the curve a kind of material-transfer function that is nearly binary in nature. This switching action can be used to effectively 'program' silicon wafers to produce sharply defined zones of precipitation behaviour.

11.3.3 COMPARISON OF CONVENTIONAL AND VACANCY-ENGINEERED CONTROL OF OXYGEN PRECIPITATION

Conventionally, denuded zones are prepared through the out-diffusion of oxygen by long, high-temperature heat treatments prior to the 'normal' (low vacancy concentration) very slow nucleation of oxygen precipitates. It relies on the very strong (typically 20-th order (Falster *et al.* 1998a)) oxygen concentration, dependence

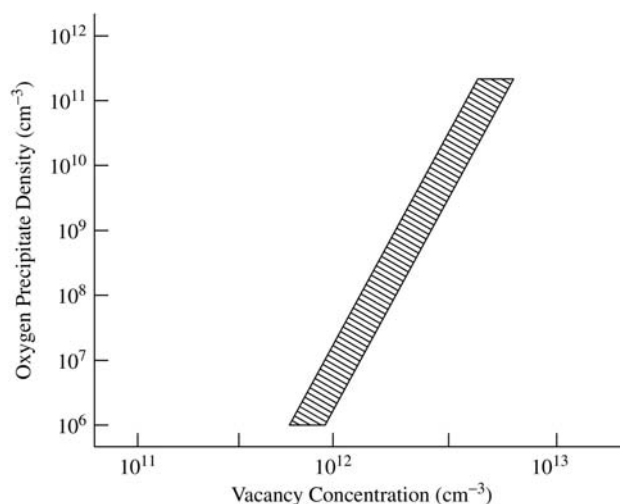


Figure 11.4 Oxygen precipitate density dependence on vacancy concentration.

of the nucleation processes. This very strong dependence on oxygen concentration while responsible for a denuded zone effect is, in fact, one of the major weaknesses of the conventional approach; it necessitates extremely tight controls on the concentration of oxygen in silicon crystal growth. A further difficulty is that with modern low thermal budget IC processing the times and temperatures required to produce sufficient out-diffusion of oxygen simply no longer exists. Another difficulty is the strong coupling of the 'normal' nucleation behaviour of the details of the crystal-growth process and the thermal cycles of the IC process to which it is submitted. The problem of the 'normal' nucleation of oxygen precipitation in silicon has proven to be an extraordinarily difficult one and has yet to be satisfactorily resolved. No models exist that can predict the outcome of this highly coupled problem. Thus the problem of precipitation control in 'normal' silicon remains a largely and unsatisfactorily empirical exercise in which silicon materials are 'tailored' to meet the needs of specific applications adding undesired costs and rigidity to the process.

In vacancy-engineered oxygen-precipitation control these problems are circumvented. The two-zoned precipitation required for internal gettering action is achieved by the installation of a vacancy concentration profile that rises from a low value at the wafer surface and crosses the vacancy-threshold concentration at some desired point below the surface defining the depth of the denuded zone. The two processes for the creation of denuded zones are schematically illustrated and compared in Figure 11.5.

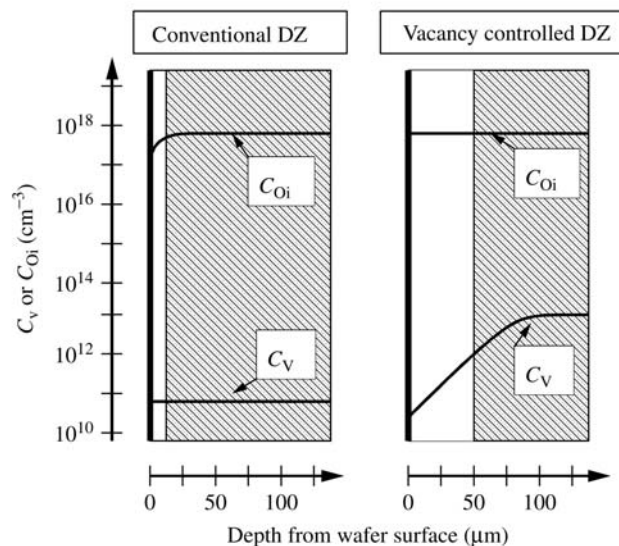


Figure 11.5 Schematic comparison of conventional and the vacancy-controlled denuded zone formation of the MDZTM wafer. The shaded areas represent the locations of the precipitated regions.

11.3.4 THE INSTALLATION OF VACANCY CONCENTRATION PROFILES IN THIN SILICON WAFERS

The installation of appropriate vacancy-concentration profiles in a thin silicon wafers is a three-step process, all of which occur in a single rapid thermal processing (RTP) step (Falster *et al.* 1998a). (1) When silicon is raised to high temperatures, vacancies and interstitials are spontaneously produced in equal amounts through Frenkel pair generation, a very fast reaction. At distances far removed from crystal surfaces we thus have $C_I = C_V = \{C_{Ieq}(T)C_{Veq}(T)\}^{1/2}$, where T is the process temperature. Were the sample to be cooled at this point the vacancies and interstitials would merely mutually annihilate each other in the reverse process of their generation. (2) In thin wafers, however, the surfaces are not far away and this situation changes very rapidly. Assuming equilibrium boundary conditions (not oxidizing or nitriding) leads to coupled fluxes of interstitials to the surface and vacancies from the surface ($C_{Ieq}(T) < C_{Veq}(T)$ for the temperature ranges of interest (see below)) and the rapid establishment of equilibrium conditions throughout the thickness of the wafer. Experiments suggest that this occurs very rapidly – in a matter of seconds or even less. This equilibration is primarily controlled by the diffusivity of the fastest component, the self-interstitials, since the concentrations are roughly equal. (3) Upon cooling, two processes are important: direct recombination of vacancies and interstitials, and surface recombination and the resulting fluxes toward the surfaces. The slower vacancies are now the dominant species of the coupled diffusion ($C_V > C_I$) and hence the equilibration processes toward the equilibrium state at the surface is not as fast as the interstitial-dominated initial equilibration. It is thus possible to freeze-in excess vacancies at not unreasonable cooling rates. For samples cooled rapidly, the residual bulk concentration of vacancies following recombination with interstitials, C_V , is the initial difference $C_{Ve} - C_{Ie}$ (at the process temperature, T). Closer to the surfaces C_V is lower due to diffusion (again now primarily controlled by the dominating vacancies) toward the decreasing equilibrium values at the wafer surface. The relatively rapid cooling rates achievable (50–100 °C/s) in RTP systems insure that sufficiently high concentrations of vacancies can be frozen in the bulk of the wafer to achieve the desired effect. In general, the level of bulk precipitation is controlled by the value of C_V (determined by the process temperature) while the depth of the denuded zone is controlled by the diffusion of vacancies during cooling. Such information, coupled with numerical simulation of the coupled diffusion process, can be very important points of reference in analysing the parameters of the native point defects in silicon. For example, critical vacancy concentrations ($= C_{Ve}(T) - C_{Ie}(T)$) for precipitation enhancement (approximately $5-8 \times 10^{11} \text{ cm}^{-3}$), is achieved at about 1175 °C, while at about 1250 °C, much higher vacancy concentration is found, to be between about $2-5 \times 10^{12} \text{ cm}^{-3}$. The uncertainty in these numbers reflect our uncertainty in the platinum-diffusion technique. Further experiments with various cooling rates and subsequent relaxation rates of an installed profile during a second RTP process

at a different temperature give insight into the diffusivity of vacancies at various temperatures. Such information gained from MDZ experiments is coupled with information gleaned from crystal growth experiments to compile a unified picture of the point-defect parameters. This is discussed below.

11.3.5 ADVANTAGES OF THE USE OF VACANCIES TO CONTROL OXYGEN PRECIPITATION IN WAFERS

The use of MDZ wafers is a very powerful tool for the resolution of the problem of oxygen precipitation control in silicon wafers. The installation of an appropriate vacancy-concentration profile effectively programs a silicon wafer to behave in a well-defined and ideal way. Essentially all the difficulties associated with the robust engineering of IG structures are removed at a stroke. At sufficiently high vacancy concentration levels the control of the nucleation reactions is decoupled from the oxygen concentration over the entire practical CZ range ($4\text{--}10 \times 10^{17} \text{ cm}^{-3}$) thus eliminating the need for tight oxygen control in CZ crystal growth. The 'Tabula Rasa' character of the heat treatments that produce the MDZ wafer erase all details of oxygen clustering during crystal-growth. Finally, the extraordinarily rapid incubation of clusters at low temperatures insures that the installed vacancy 'template' is 'fixed' essentially as wafers are loaded into their first high-temperature heat treatment. The vacancies are consumed in this process and only the clusters in their well-defined distribution are left behind to grow. No further nucleation takes place, except in extraordinary circumstances. In short, an MDZ™ wafer is a generic high-performance IG wafer decoupled from the need to tailor a specific material to a specific process. Our goal of simplicity is thus achieved.

11.3.6 THE MECHANISM OF THE VACANCY EFFECT ON OXYGEN PRECIPITATION

At low T , oxygen clusters are nucleated to high density even without vacancies but there is a long incubation (several hours at 650°C) before a subsequent high-temperature anneal results in an appreciable precipitate density, 10^9 cm^{-3} or higher. This incubation, most likely, is not related to a lag in the time-dependent nucleation rate but rather to the problem of subsequent survival of nucleated oxygen clusters. The clusters formed without volume accommodation (without assistance of vacancies) would inevitably dissolve at higher T since the strain energy per oxygen atom becomes larger than the oxygen chemical potential. The only way to survive is to relieve the strain energy by emitting enough self-interstitials, to acquire some space in the lattice. The emission rate is expected to be strongly size dependent. It becomes appreciable only if the cluster size is above some critical limit. To achieve this size, some incubation time is required. However, with vacancies present, the clusters will relieve the strain simply by

absorbing vacancies. The vacancy species at low T exist predominantly as O_2V complexes (bound vacancies – see below). The O_2V species may be of high enough mobility, even at low T , to be absorbed by the clusters at the nucleation stage. Even if this is not the case, vacancies will be absorbed during the subsequent ramp-up of the temperature since the effective vacancy diffusivity (averaged over O_2V and V species) is a rapidly increasing function of T . Either way, at the beginning of the precipitation stage (for example at 1000°C) each cluster will contain m vacancies ($m = C_v/N$ where N is the cluster density). The critical vacancy number m^* – for clusters in equilibrium with the equilibrium solution of point defects – is estimated to be about 100 at 1000°C (it is slightly dependent on the oxygen concentration). This important estimate comes from the oxide/silicon interfacial energy fitted to account for the microdefect formation (Voronkov, to be published). If the actual value of m exceeds m^* then the cluster-controlled point-defect concentrations correspond to interstitial supersaturation (and vacancy undersaturation). Under such conditions, all the clusters can grow simultaneously since self-interstitials are removed to the sample surface thus providing more space for the clusters. This means that m will increase, and the number of oxygen atoms in each cluster (n) will follow the increase in m . However, if the starting value of m is below m^* (a much more likely situation), the point-defect solution in equilibrium with clusters corresponds to interstitial undersaturation; then the interstitials diffuse from the sample surface into the bulk decreasing m – and thus inducing the cluster dissolution. Along with this (presumably slow) process there will be fast coalescence with respect to the size m : the clusters of smaller m will lose vacancies, while the clusters of larger m will gain those vacancies. In this way the total cluster density N will decrease, while the average size m will increase, until it becomes larger than m^* . After that, all the remaining clusters can grow simultaneously. This consideration results in a simple rule for the final precipitate density N_p . It is on the order of C_v/m^* (about 10^{10} cm^{-3} for $C_v = 10^{12}\text{ cm}^{-3}$). It is remarkable that though the initial (nucleated) cluster density N may strongly depend on the oxygen content, the final precipitate density N_p is almost independent of the oxygen content: it is controlled by the vacancy concentration C_v . When the vacancy concentration is low, the starting size $m = C_v/N$ will be accordingly small. The clusters of small m would simultaneously lose the vacancies to the vacancy solution, and will be completely dissolved.

Another mechanism of vacancy-enhanced precipitation is direct agglomeration of the vacancy species (O_2V) during the nucleation stage. The production of this new cluster population – by agglomeration not of oxygen but of O_2V – goes in parallel with the nucleation of oxygen-only clusters considered above. Attachment of the O_2V species to a cluster may proceed either by direct migration of these species or by the dissociation with subsequent fast migration of a released free vacancy to a cluster followed by attachment of oxygen atoms. For both ways the nucleation rate is not very sensitive to the oxygen content but controlled primarily by the species concentration, C_v . If the vacancy size of clusters,

$m = C_v/N$, is below m^* , the precipitation anneal will result in a coalescence process (described above), and the cluster density N will be reduced to the final value on the order of C_v/m^* . At low C_v the nucleation rate of O_2V -clusters would be negligible.

The two mechanisms of vacancy-enhanced oxygen precipitation share some common features: (a) the basic effect of vacancies is to supply the oxygen clusters with space necessary for the cluster survival during the precipitation anneal; (b) the vacancy concentration must be over some limit to enhance the precipitation; (c) the produced precipitate density is controlled by the vacancy concentration rather than by oxygen content. It is likely that the first mechanism is important at low T (at 650 °C or below). The second mechanism certainly operates at higher T (like 800 °C) – when the effective vacancy mobility is enough for vacancy-assisted nucleation of oxygen clusters. The first mechanism is not operative at all at such T since the nucleation rate of oxygen-only clusters becomes negligible.

11.4 CONCLUSIONS DRAWN REGARDING THE INTRINSIC POINT-DEFECT PARAMETERS TAKEN FROM THE COMBINATION OF CRYSTAL GROWTH AND MDZ EXPERIMENTS

Both the problems of microdefect formation in crystal-growth and the principles behind the MDZ wafer involve the properties of point defects at high temperatures. At high temperatures in lightly doped material, the analysis of the problem should be free of the complications of defect complexes. This section discusses conclusions drawn from the analyses of both problems taken together to present a coherent view of the properties of free, neutral point defects in silicon and the nature of complexing at lower temperatures.

11.4.1 RECOMBINATION RATE

The v/G rule for grown-in microdefect type (the type of incorporated native defect) implies that the balance between defect recombination and pair generation is achieved very rapidly. The characteristic equilibration time τ_r must be much shorter than the time spent within the near-interface region where major defect annihilation occurs (for float-zoned crystals this dwell time may be as short as 20 s). This conclusion is in line with the extremely short equilibration time observed in MDZ experiments in wafers at 1250 °C (on the order of 1 s). This result means that both equilibration processes (pair generation/recombination and diffusion) occur within this short time. The characteristic time τ_r is therefore on the order of 1 s (or less) at 1250 °C. Since τ_r is a rapidly decreasing function of T , It will be still much lower (several milliseconds or less) at the melting point.

11.4.2 SELF-INTERSTITIAL DIFFUSIVITY

The short equilibration at 1250 °C also means that the characteristic diffusion time, $(d/\pi)^2/D_i$ – where d is the wafer thickness (0.07 cm) – is on the order of 1 s. Accordingly, the interstitial diffusivity, D_i , is on the order of $5 \times 10^{-4} \text{ cm}^2/\text{s}$. The estimate for D_i at the melting point (resulting from quenched-in microdefect patterns) is the same number (Voronkov 1982). This coincidence implies that (a) the interstitial diffusivity is very high, (b) the temperature dependence of D_i is not significant (at least over 1250 °C). The interstitial migration energy E_{mi} is thus rather low. We adopt $E_{mi} = 0.2 \text{ eV}$ following the data of Watkins 1999.

11.4.3 VACANCY DIFFUSIVITY

This value was deduced (Voronkov and Falster 1999) from the observed density and size of voids: D_v is about $2 \times 10^{-5} \text{ cm}^2/\text{s}$ at the void formation temperature (around 1100 °C); a slightly higher number follows from the cavitation model of void production (Voronkov, to be published). Since the vacancy is mobile even at the room temperature (Voronkov and Falster 1999), the vacancy migration energy E_{mv} can be then deduced to be about 0.35 eV (Voronkov and Falster 1998). This is close to the number obtained by Watkins, 0.45 eV. On the other hand, the vacancy diffusivity is the parameter that largely controls the width of a denuded zone in the MDZ process: that zone is basically formed due to vacancy out-diffusion during fast cooling of wafers after the RTP anneal. Accordingly, a good estimate for D_v (assuming the above low migration energy) can be deduced from the observed quenched-in vacancy profiles under a variety of cooling-rate conditions. The deduced diffusivity at the reference temperature of 1100 °C is about $2 \times 10^{-5} \text{ cm}^2/\text{s}$, in excellent accord with the microdefect-based number for D_v .

11.4.4 THE DIFFERENCE OF EQUILIBRIUM VACANCY AND INTERSTITIAL CONCENTRATIONS

Both the world of grown-in microdefects and the world of MDZ are based on the inequality $C_{ve} > C_{ie}$. This inequality (at the melting point) insures the change-over from interstitial incorporation (at v/G below the critical ratio) to vacancy incorporation (at higher v/G). Incorporation of vacancies in the MDZ process is based on a similar inequality at the process temperature: the quenched-in vacancy concentration in the wafer bulk is equal to $C_{ve} - C_{ie}$ at the process temperature. This difference – for the two temperatures, 1250 and 1175 °C – was measured by the Pt technique with some uncertainty. The melting-point difference can be deduced from the amount of vacancies stored in voids (Saishoji *et al.* 1998) calculated from the LST data on the void density on size, in dependence of v/G . This difference lies within rather narrow limits, $(2-3) \times 10^{14} \text{ cm}^{-3}$. The ranges

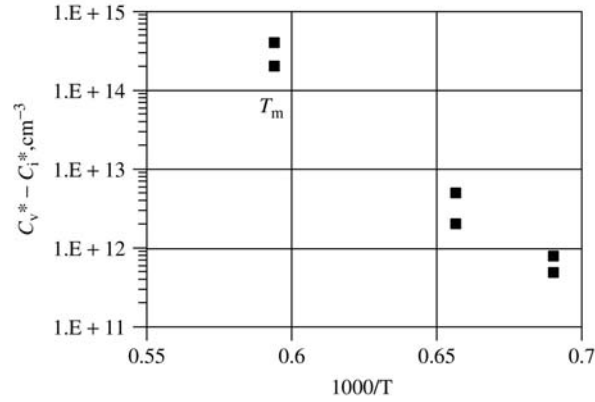


Figure 11.6 The range of the solubility difference for vacancy and self-interstitial. The melting point (T_m) range is based on the measured amount of vacancies in voids. The range for the two other temperatures (1250 and 1175 °C) comes from RTA-treated wafer measurement data.

for $C_{ve} - C_{ie}$ are thus available for the three temperatures; these are shown in Fig. 11.6.

11.4.5 FORMATION ENERGIES

The plot of Figure 11.6 imposes strong constraints on the values of formation energies, E_v for vacancy and E_i for self-interstitial. The melting-point value for the equilibrium interstitial concentration, C_{im} , is fixed by the estimated diffusivity D_i and the value of the $D_i C_{ie}$ product (2.3×10^{11} cm²/s at the melting point) known from self-diffusion and zinc-diffusion data (Bracht 1999). Making allowance for some uncertainty in both D_i and $D_i C_{ie}$, a reasonable range for C_{im} is $(5-15) \times 10^{14}$ cm⁻³. If one specifies the formation energies, then the temperature dependence of $C_{ve} - C_{ie}$ can be plotted for various C_{vm} and C_{im} within the fixed ranges for C_{im} and $C_{vm} - C_{im}$. If none of these curves falls within the ranges of Figure 11.6, the chosen energies E_v and E_i are rejected. Otherwise they are considered as consistent with the data of Figure 11.6. This procedure shows that acceptable energies are very close one to the other. The acceptable range for the average energy $E = (E_i + E_v)/2$ and for (very small and negative) energy difference $E_i - E_v$ is shown in Figure 11.7. Both formation energies are over 4.3 eV. To be consistent with self-diffusion data, E_i must be lower than the activation energy for the $D_i C_{ie}$ product, 4.9 eV (Bracht 1999). Since the interstitial migration energy is thought to be 0.2 eV (or perhaps somewhat larger), the actual estimate for the interstitial formation energy is $E_i \leq 4.7$ eV. The final range for E_i is then from 4.3 to 4.7 eV. The vacancy formation energy E_v is within the same range. An important implication of these estimates is that the

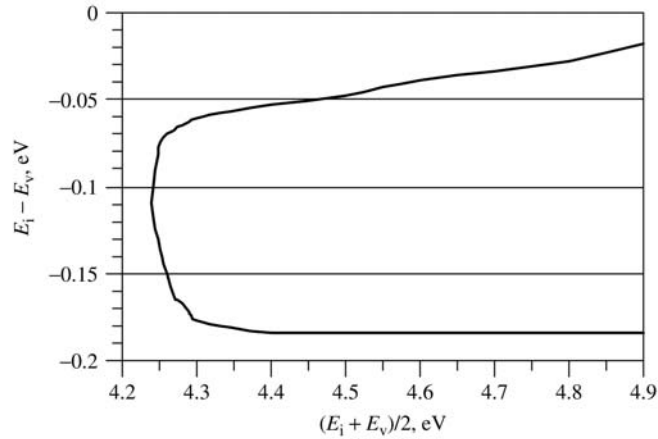


Figure 11.7 The values of average formation energy and the energy difference consistent with the data shown in Fig. 11.6. These values are in the area inside the curve.

activation energy for the vacancy contribution into the self-diffusivity, $E_v + E_{vm}$, lies within the range 4.7–5 eV. It is thus comparable to that for the interstitial contribution, $E_i + E_{im} = 4.9$ eV. The interstitial contribution to self-diffusivity prevails at high T (Bracht 1999). It will then prevail over the whole temperature range, with no cross-over to vacancy-dominated self-diffusivity at lower T . A presumed cross-over point is indeed refuted by recent data (Bracht 1999).

11.4.6 CRITICAL v/G RATIO

This is expressed (Voronkov 1982) through the average formation energy E , the $D_i C_{im}$ product and the concentration difference $C_{vm} - C_{im}$ – the same parameters that are relevant in the above analysis of the formation energies. On substituting the numerical values of these parameters one gets for $(v/G)_{cr}$ a rather narrow range consistent with the value found experimentally (Dornberger *et al.* 1996, Falster *et al.* 1998b) (about 2×10^{-5} cm²/s or 0.12 mm²/min K). This result shows the self-consistency of the present approach to the estimation of the point-defect parameters.

11.4.7 VACANCY BINDING BY OXYGEN

The reaction of vacancies with oxygen, to form a O_2V complex (a bound vacancy) must be invoked (Falster *et al.* 1998b) to account for nonzero residual concentration of vacancies in as-grown crystals. The residual vacancies are manifested in subsequent oxygen precipitation, which is strongly banded spatially,

due to a banded distribution of residual vacancies (Falster *et al.* 1998b, Voronkov and Falster, to be published). The binding (complexing) reaction is strongly dependent on temperature: there is some characteristic binding temperature, T_b , separating the higher-temperature region (where the free vacancies dominate) from the lower-temperature region (where the vacancies exist predominantly as O_2V , with only a small fraction of free vacancies). The binding temperature was estimated to be somewhat above 1000°C (1020°C or perhaps slightly higher). The basic implication of the binding reaction is that the effective vacancy mobility is rapidly reduced below T_b , and the vacancy loss to microdefects is thus strongly suppressed, giving an opportunity for some vacancies to survive – as O_2V complexes. The suppression of vacancy mobility below T_b is also of great importance in the processes that produce the MDZ wafer. If the quenched-in depth profile of vacancies is simulated without the binding reaction, the computed vacancy concentration is far lower than the measured value (for some cooling rates). Even if the computed concentration at the wafer centre is not low (at higher cooling rates) the profile shape is strongly different from that observed. When the vacancy binding is taken into account, the computed profiles are in accord with the experiment. The vacancy binding is also clearly manifested if the MDZ wafers are subjected to the second RTP process at a temperature T_2 lower than that of the first RTP anneal (at $T_1 = 1250^\circ\text{C}$). At $T_2 = 1100^\circ\text{C}$ (well above the binding temperature) the initially installed vacancy profile disappears within 20 s. At $T_2 = 1000^\circ\text{C}$ a similar relaxation occurs but within a much longer time scale (at 60 s it is not yet fully relaxed) indicating a considerably reduced effective vacancy diffusivity. At $T_2 = 900^\circ\text{C}$ the vacancy profile does not change at all within 15 min, indicating a strongly reduced effective vacancy mobility; therefore the temperature of 900°C is already well below T_b .

11.5 UNIFIED SCHEMATIC PICTURES OF VACANCY CONTROL FOR CRYSTAL GROWTH AND WAFER PROCESSING

The above discussion, which takes into account observations from both crystal-growth and wafer-processing experiments, can in part be summarized in a useful schematic graphical form illustrating the problem of vacancy-defect engineering. A similar set of schematics exists for the self-interstitial mode of growth and will be presented elsewhere. The vacancy schematics are illustrated in Figures 11.8–11.14.

Figure 11.8 illustrates the basic vacancy *reaction template*. Here is plotted the various important zones of vacancy reaction (void formation, O_2V binding and enhanced oxygen precipitation) in terms of temperature and vacancy concentration. As a main point of reference, the solubility of vacancies is also shown. Such a chart can be viewed as a kind of map through which the concentration of vacancies in a growing crystal or heat-treated wafer must be steered during the cooling of the crystal or wafer in order to achieve a desired result.

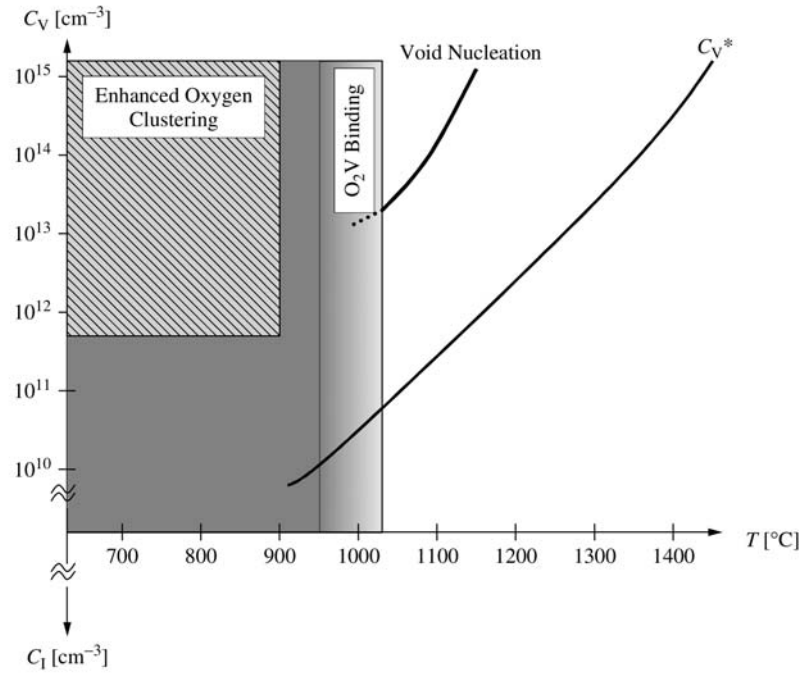


Figure 11.8 The basic vacancy reaction 'template'.

Figure 11.9 then uses this map to illustrate the first part of the crystal-growth problem: that of the incorporation of vacancies into a growing crystal. Starting at the equilibrium concentration at the melt temperature, the vacancy concentration is reduced as the crystal cools through a transient phase in which vacancy and self-interstitial fluxes compete with each other via mutual annihilation. Eventually this stops when the concentration of one or the other point-defect species becomes exhausted. At this point an essentially constant concentration of the surviving species is obtained. It is the residual vacancy (or self-interstitial) concentration, set at high temperature by the v/G rule, which is then launched into the possible reactions at lower temperatures. The reference value of the ratio of the actual to critical v/G value is given on the right-hand scale for several examples. The value for each example corresponds to the value at the vacancy-concentration saturation value. At the normalized V/V_t value of 0.8 the illustrated incorporated vacancy concentration drops below the equilibrium concentration. The crystal is at this point 'interstitial type'.

Figure 11.10 illustrates the most usual case in commercial CZ crystal-growth, that of void reaction. At a temperature of typically around 1100°C the vacancies incorporated in the growing crystal become sufficiently supersaturated to drive the void reaction. Very shortly after this starts, a sufficiently large number of vacancies are consumed, thus shutting the reaction off. The resulting density of

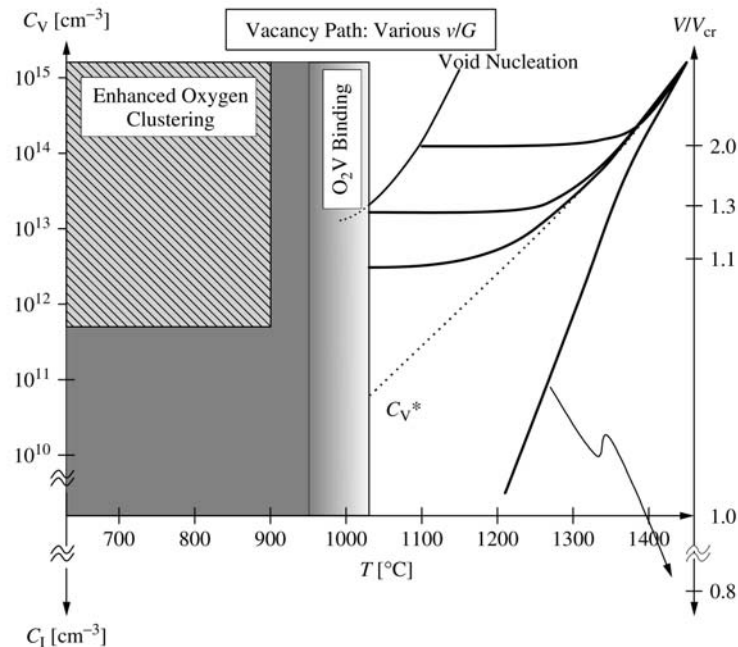


Figure 11.9 An illustration of the incorporation of vacancies into a growing crystal at various values of v/G relative to the critical value.

voids depends on the concentration of vacancies entering the reaction barrier and the cooling rate while the reaction proceeds. Upon further lowering of the crystal temperature no more voids are produced but vacancies continue to be consumed by the existing voids until the vacancies are fully bound in the relatively immobile O_2V complex. The residual concentration of vacancies (now in the form of O_2V complexes) is, however, usually below the critical concentration level for precipitation enhancement. If, however, the crystal is cooled rapidly through the growth phase, such as can happen when fast pull rates are used to produce crystal end cones, the residual vacancy concentration can be larger than the transition level to enhanced oxygen precipitation and regions of ‘anomalously’ high levels of precipitation can be observed. This is often the case in the tail-end regions of CZ crystals. Figure 11.11 illustrates this effect within the framework of the vacancy diagrams.

At lower values of v/G and in particular at values of v/G approaching the critical value, the concentration of incorporated vacancies is reduced. It is at these levels of vacancy concentration that strong defect banding effects are observed. Figure 11.12 illustrates the conditions for ‘p-band’ or OSF-ring formation. The consumption rate of vacancies is larger than the void case due to the typically 2 orders of magnitude higher density of the p-band particles (the vacancy ‘sinks’) than voids.

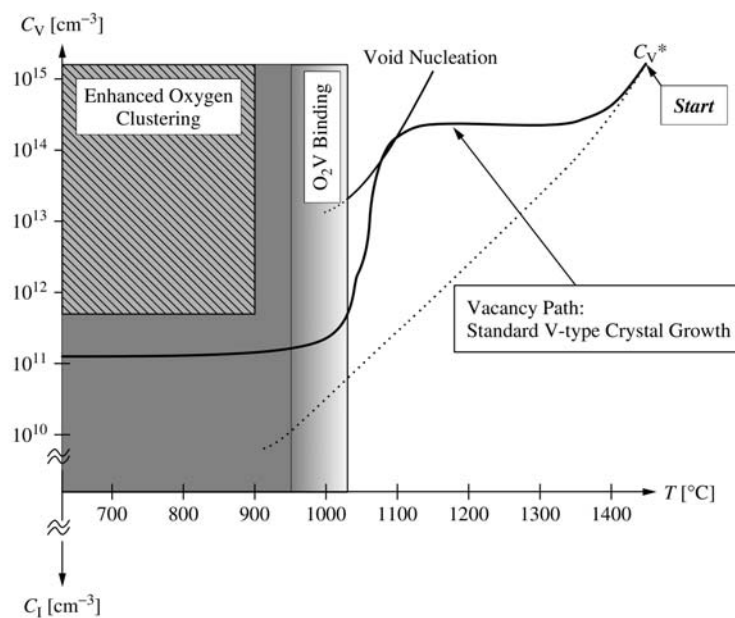


Figure 11.10 An illustration of the production of voids in a growing crystal in the most usual case.

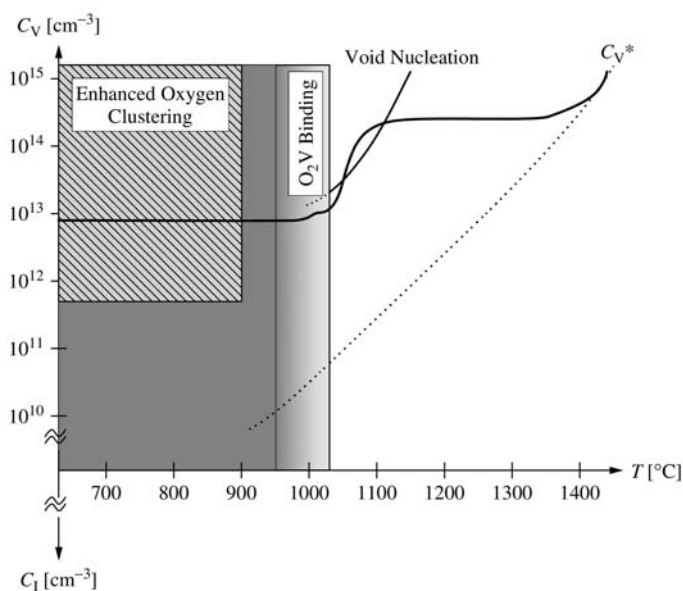


Figure 11.11 An illustration of the effect of more rapid cooling through the void growth regime resulting in 'anomalously' high values of oxygen precipitation.

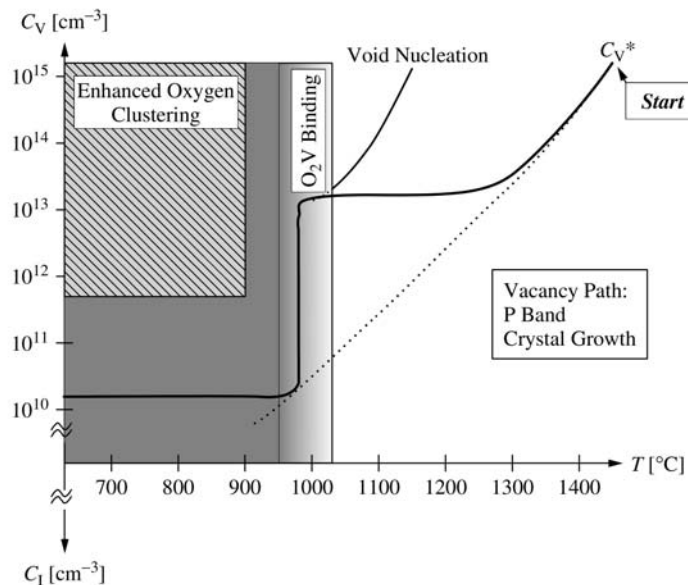


Figure 11.12 An illustration of the conditions under which the ‘P-band’ or OSF-ring is formed during crystal growth.

Figure 11.13 shows the case for ‘L-band’ formation. In this case the vacancy concentration goes underneath the void reaction and enters directly into the O_2V binding as illustrated in Figure 11.13. No voids can form as the process is now kinetically limited. The usual case is for the vacancies to enter the ‘enhanced precipitation’ condition at lower temperature giving rise to the precipitation peaks observed in the L-band region. Material grown under these conditions is ‘vacancy perfect’-type material.

Finally, the same vacancy schematic used above for crystal-growth can be used to explain the incorporation of vacancies during the heat treatment of thin silicon wafers leading to the MDZ™ wafer. Figure 11.14 illustrates this. Here our starting point is not at the melt temperature of silicon but usually substantially lower. As a result, the maximum vacancy concentrations achievable are substantially lower than that of crystal-growth from the melt (unless point defects are additionally injected from the wafer surfaces). Initially, in the bulk of the wafer, the concentration of vacancies is somewhat less than equilibrium as a result of the fact that the only possible source of vacancies is Frenkel pair generation and mass action. Shortly after this, however, due to the close proximity of the wafer surfaces, the equilibrium vacancy concentration is rapidly reached throughout the bulk of the wafer primarily through interstitial in-diffusion coupled to IV recombination/generation. At the wafer surfaces, equilibrium conditions are always maintained. As the sample cools, the vacancy concentration

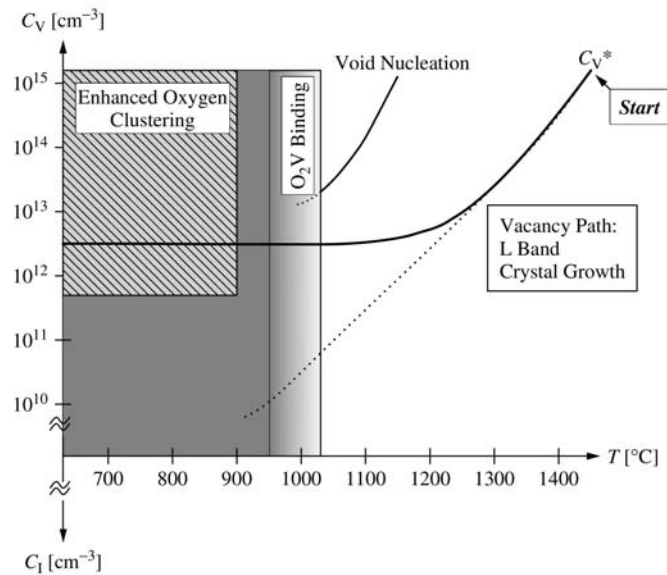


Figure 11.13 An illustration of the conditions under which the ‘L-band’ or ‘vacancy-perfect’ type material is formed during crystal growth.

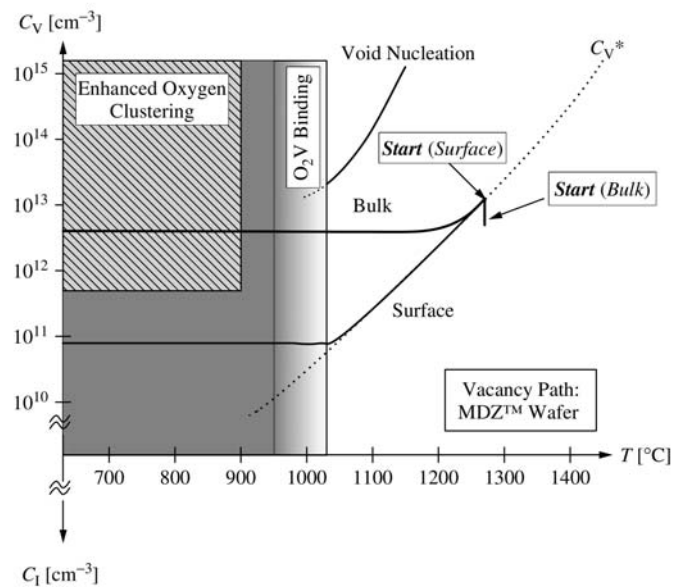


Figure 11.14 An illustration of the use of the vacancy template to illustrate the creation of dual-zoned precipitation effects in thin silicon wafers (the MDZ™ wafer) by means of high-temperature rapid thermal processing.

drops, following equilibrium at the surfaces, while the decrease in the bulk, far (relatively speaking) from the surfaces is limited to recombination with existing self-interstitials. These are rapidly exhausted, leaving behind a 'residual' vacancy concentration (which is equal to $C_{ve}(T) - C_{le}(T)$ where T is the process temperature). If the cooling of the wafer is sufficiently rapid such that the expanding vacancy-diffusion profile does not penetrate into the wafer centre prior to reaching the O_2V binding temperatures, then this concentration is maintained. If this residual concentration is sufficiently large to be greater than the critical vacancy concentration for precipitation enhancement, then the desired two-zoned precipitation effect is created.

ACKNOWLEDGMENTS

Measurements of vacancy concentration by the platinum-diffusion technique were performed by Fabian Quast and Peter Pichler of the Fraunhofer Institut, Erlangen. Computer programs for the simulation of point-defect dynamics during MDZ treatments were developed by Marco Pagani. We also wish to acknowledge the contributions of Daniela Gambaro, Max Olmo, Marco Cornara, Harold Korb, Jeff Libbert, Joe Holzer, Bayard Johnson, Seamus McQuaid, Lucio Mule' Stagno, and Steve Markgraf of MEMC Electronic Materials to this work.

REFERENCES

- Abe, T. 1999 in *ECS Proc.*, **99-1**, 414.
 Bracht, H. 1999 in *ECS Proc.*, **99-1**, 357.
 de Kock, A. J. R. 1973 *Philips Res. Repts Suppl.*, **1**, 1.
 Dornberger, E. and W. von Ammon, W. 1996 *J. Electrochem. Soc.*, **143**, 1648.
 Falster, R., Fisher, G. R. and Ferrero, G. 1991, *Appl. Phys. Lett.*, **59**, 809.
 Falster, R., Cornara, M., Gambaro, D., Olmo, M. and Pagani, M. 1997, *Solid State Phenom.*, **57-58**, 123.
 Falster, R., Gambaro, D., Olmo, M., Cornara, M. and Korb, H. 1998a *Mater. Res. Soc. Symp. Proc.*, **510**, 27.
 Falster, R., Voronkov, V. V., Holzer, J. C., Markgraf, S., McQuaid, S. and MuleStagno, L. 1998b in *ECS Proc.*, **98-1**, 468.
 Foell, H. and Kolbesen, B. O. 1975, *Appl. Phys.*, **8**, 319.
 Jacob, M., Pichler, P., Ryssel, H. and Falster, R. 1997, *J. Appl. Phys.*, **82**, 182.
 Nishimura, N., Yamaguchi, Y., Nakamura, K., Jablonski, J. and Watanabe, M. 1998, in *ECS Proc.*, **98-13**, 188.
 Park, J. G., Lee, G. S., Park, J. M., Chon, S. M. and Chung, H. K., 1999, *ECS Proc.*, **99-1**, 324.
 Petroff, P. M and de Kock, A. J. R. 1975, *J. Appl. Phys.*, **30**, 117.
 Puzanov, N. I and Eidenzon, A. M. 1992, *Semicond. Sci. Technol.*, **7**, 406.
 Roksnoer, P. J. and van den Boom M. M. B. 1981, *J. Cryst. Growth*, **53**, 563.

- Saishoji, T., Nakamura, K., Nakajima, H., Yokoyama, T., T. Ishikawa, T. and Tomioka, J. 1998, in *ECS Proc.*, **98-13**, 28.
- Ueki, T., Itsumi, M. and Takeda, T. 1997, *Appl. Phys. Lett.*, **70**, 1248.
- Veselovskaya, N. V., Sheyhet, E. G., Neymark, K. N. and Falkevich, E. S. 1977, in *Growth and Doping of Semiconductor Crystals and Films (in Russian)*, Part 2 (Nauka: Novosibirsk) 284.
- Voronkov, V. V. 1982, *J. Cryst. Growth*, **59**, 625.
- Voronkov, V. V. and Falster, R. 1998, *J. Cryst. Growth*, **194**, 76.
- Voronkov, V. V. and Falster, R. 1999, *J. Cryst. Growth*, **198/199**, 399.
- Voronkov, V. V., Voronkova, G. I., Veselovskaya, N. V., Milvidski, M. G. and Chervonyi, I. F. 1984, *Sov. Phys. Crystallogr.*, **29**, 688.
- Watkins, G. D. 1999, in *ECS Proc.*, **99-1**, 38.

12 The Formation of Defects and Growth Interface Shapes in CZ Silicon*

TAKAO ABE

*Shin-Etsu Handotai, Isobe R&D Center, Isobe 2-13-1, Annaka, Gunma
379-0196 Japan*

ABSTRACT

The thermal distributions near the growth interface of 150 mm Czochralski (CZ) crystals were measured by three thermocouples installed at the centre, middle (half-radius) and edge (10 mm from surface) of the crystals. The results show that larger growth rates produced smaller thermal gradients (G) similar as reported for FZ crystals. The results seem not to contradict the balance equation because temperature distributions continue through the growth interface to the bulk of crystal. The growth rate (v) in Voronkov's theory does not effect directly the point-defect formation. Finally, it is proposed that the shape of the growth interface is also determined by the distribution of G across the interface. That is, small G and large G in the centre induce concave and convex interfaces to the melt, respectively.

12.1 INTRODUCTION

Investigations on native point defects in silicon crystals may be classified into three categories, depending on the temperature ranges at which they are formed.

* Note of the editor: The interesting measurements reported here are not yet fully understood and require further studies and interpretation. Generally one would assume that the thermal gradient in the crystal at the growth interface increases with increasing growth rate in order to remove the latent heat. Alternatively, in specific growth arrangements, the latent heat may be compensated by a decreasing thermal gradient in the liquid (near the interface) with increasing growth rate as postulated by Voronkov and in this work by T. Abe. In these latter cases the temperature gradient in the solid is either constant or even slightly decreasing with increasing growth rate. The effective temperature distribution at the growth interface and the thermal history of the crystal determine the interface shape, defect formation, and defect distribution HJS.

The electron paramagnetic resonance (EPR) is carried out at cryogenic temperature in order to study the lattice vacancies and the silicon interstitials produced by electron irradiation. This investigation was extensively performed by Watkins *et al.* [1] in the 1960s. The second category of investigations is devoted to two phenomena: (i) the enhanced and retarded impurity diffusion induced by oxidation and nitridation, and (ii) the kick-out and dissociative diffusion of metals such as Au, Pt and Zn in the temperature range 44 to 1388 °C [2].

The third category concerns the secondary point defects produced during the crystal-growth process, from the melting point down to 1000 °C. These secondary defects form as a result of nonequilibrium phenomena, that is, the crystal-growth and subsequent cooling, which are characterized by the presence of thermal gradients. Up to now measuring procedures or parameters obtained with the investigations of the first and second type could not be applied in order to fully understand and then prevent the grown-in defect formation near the melting point.

When float-zone (FZ) silicon crystals were first grown without dislocations, the layer structure of defects perpendicular to the growth axis [3] and the so-called 'shallow pits' distributed in a swirl-like pattern [4] could be clearly observed. De Kock [5] first proposed that the shallow pits were agglomerates of vacancies. However, Foell and Kolbesen [6] later found by direct TEM observations that shallow pits are produced by excess interstitials that give rise to interstitial-type dislocation loops. Currently, such defects are commonly named A defects. Following this evidence, many researchers proposed their own models [7–13] as shown in Table 12.1. Foell *et al.* [7] and Petroff and de Kock *et al.* [8] assumed interstitial silicon to be in equilibrium and in nonequilibrium, respectively. Van Vechten [9] and Chikawa and Shirai [10] suggested that the vacancies are predominant at equilibrium. However, even when vacancies are assumed to be predominant, Chikawa's droplet model does not exclude the occurrence of A defects. The equilibrium model in which vacancy and interstitial concentrations are equal at the growth interface is accepted by many researchers. Sirtl [11] suggested that pair annihilation and creation is kept with the local equilibrium. Hu [12] and de Kock *et al.* [13] proposed that the A defects are generated due to the energy differences of recombination and agglomeration energies between interstitials and vacancies. Roksnoer *et al.* [14] reported another type of defects named D defects, consisting of excess vacancies created by growing FZ crystals with extremely large growth rate. Based on this observation, Voronkov [15] developed a theory according to which the species of intrinsic point defects created during growth depends upon the ratio of growth rate (v) and thermal gradient (G) near the growth interface. He defined a critical value of this ratio (C_{crit}), and suggested that when $v/G < C_{crit}$, interstitials are dominant, whilst if $v/G > C_{crit}$, vacancies are dominant. Tan and Goesele [16] tried to modify this theory introducing a new concept of 'local equilibrium', but this was not yet proven experimentally.

In 1990, Ryuta *et al.* [17] found the crystal-originated particles (COP) which are the result of the D defects in Czochralski (CZ) crystals, by using a particle

Table 12.1 Proposed models on the origin of point defects

$C_1 \gg C_v$		$C_1 \ll C_v$		$C_1 = C_v$	
Equilibrium	<div>1975 Foell et al: Interstitials [6]</div> <div>1977 Foell, Goesele Kolbesen: In equilibrium [7]</div>	<div>1973 de Kock: Vacancies [5]</div> <div>1978 Van Vechten: Cavity model [9]</div>	<div>1965 Plaskett: Microdefects [3]</div> <div>1977 Sirtl: Local equilibrium [11]</div> <div>1977 Hu: Recombination energy [12]</div> <div>1981 Roksnoer et al: D defect [14]</div> <div>1982 Voronkov: Thermomdiffusion [15]</div> <div>1985 Tan et al.: Local equilibrium [16]</div> <div>1990 Ryuta et al: COP [17]</div> <div>1995 Itsumi et al: Voids [18]</div> <div>1994 Habu: Uphill diffusion [20]</div> <div>1994 Brown: Thermomdiffusion [21]</div> <div>1995 Ammon: Voronkov's parameter [23]</div> <div>1980 de Kock/van de Wijgert [13]</div>	<div>1976 Petroff/de Kock: Impurity clustering [8]</div> <div>1976 Chikawa/Shirai: Interstitials by local remelting [10]</div> <div>1983 Abe, Harada/Chikawa: Thermal gradient (stress)</div> <div>1984 Roksnoer: Carbon [29]</div>	Nonequilibrium

counter based on light scattering techniques. Later, Itsumi *et al.* [18] reported that COPs are twinned structures of octahedral voids covered with thin oxide on inside (111) planes. After those two findings, many numerical simulations were started with the aim of explaining the generation of the A and D defects; see, for example, Wijaranakula [19], Habu *et al.* [20], and Brown *et al.* [21], who postulate almost equal concentrations of interstitials and vacancies at the growth interface. They calculated the flux of point defects using the gradient of chemical potentials. However, the parameters used for the computation were varied in a wide range: Habu *et al.* [20] postulated that both species of point defects at the growth interface are controlled by G and v but characterized by uphill diffusion [22] of vacancies. The conclusion resulted opposite to that of Voronkov who stated that if v is large enough, vacancies are predominant and uphill diffusion is negligible. However, the experimental results [29, 30] obtained by detaching the crystal from the melt, showed that the solid near the growth interface is filled with vacancies. On the other hand, it is experimentally known that the dominant species outside and inside of R-OSF (ring-likely distributed oxidation-induced stacking fault) are interstitial silicon and vacancy, respectively. Ammon *et al.* [23] and Hourai *et al.* [24] determined the value of v/G on the R-OSF to be $0.13 \text{ mm}^2/\text{min K}$ [25] and $0.22 \text{ mm}^2/\text{min } ^\circ\text{C}$ [24], respectively. The former used the commercially available finite element codes FEMAG [25] for the global heat transfer analysis, and the latter calculated the temperature distribution in the crystals by ABAQUS [24]. However, the present author and his coworkers measured the temperature distributions near the growth interface of growing FZ crystal surfaces by a two-colour thermometer [26]. The results clearly showed that larger v values induce smaller G values. Recently, we measured the temperature distributions [31] near the growth interface of growing CZ crystals using thermocouples buried in 150 mm crystals. From these results we have proposed that the generation of point defects only depends on G near the growth interface, but not explicitly on v , which just contributes to change G and to agglomeration of these defects during cooling.

In this chapter, we first discuss three points based on the G values actually measured on growing CZ crystals: first is the traditional balance equation used for the computer simulation, second is the meaning of Voronkov's theory, and third is the formation of growth-interface shape.

12.2 EXPERIMENTS

As schematically shown in Figure 12.1, two previously grown dislocation-free crystals of lengths of 250 mm and 350 mm with 150 mm diameter, having a conical shoulder but not a conical tail, were prepared for measuring temperature distributions during crystal-growth. Thermocouples were installed at the flat tail end. To avoid the radiation effects and to measure the temperatures in the crystal interior, three thermocouples at the centre, middle (half-radius) and edge

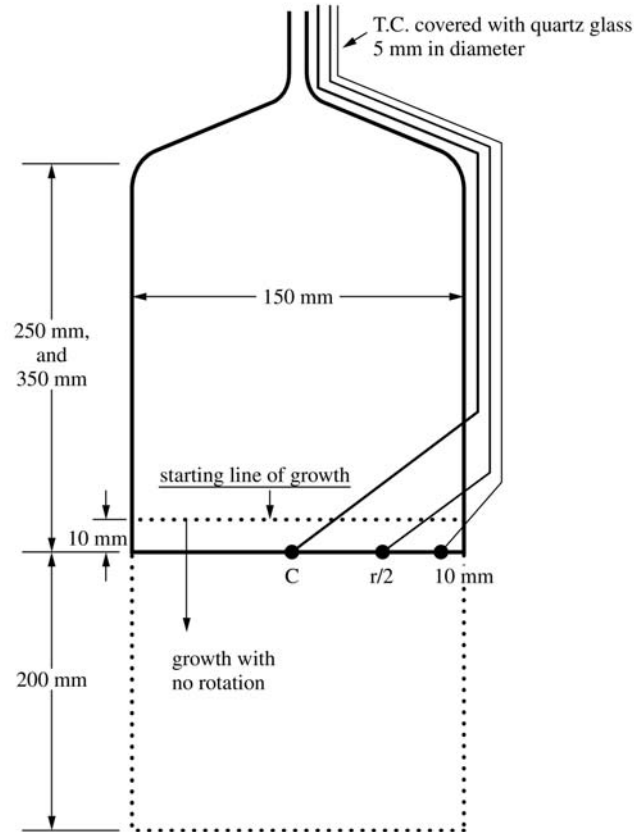


Figure 12.1 Schematic of test crystals installed with three thermocouples at the end surface.

(10 mm from edge) positions were inserted into the crystals. The diameter of the thermocouples is 1 mm and the outer diameter of their quartz cover is 5 mm. The test crystals were supported by multiple tungsten wires as if real crystals were growing. The weight of melted silicon was adjusted depending on the test crystal length to simulate an initial silicon melt weight of 40 kg. The test crystal was first melted to 10 mm from the tail end of the crystal by dipping a few mm into the melt at a time and waiting for melting to occur, achieving an average melting speed of 0.7 mm/min. Finally, the crystal-growth was started with a growth rate of 1.2 mm/min but no rotation. When the length of the newly grown crystal reached 210 mm from the re-melted position, the temperature measurement was halted and the re-melting with the above average melting speed was done again to the point 10 mm over the thermocouple positions. In the same manner, the temperature measurements were done for the other three cases of growth rates; 1.0 mm/min, 0.6 mm/min and 0.3 mm/min. The temperature distributions

of other test crystals of 350 mm length were also measured in the same manner. A standard CZ puller was used, but was equipped with a hot zone that cools crystals strongly, in order to observe the crystal length effects on G .

12.3 RESULTS

Figure 12.2 shows, for four different growth rates, the temperature distributions recorded at the centre, middle and edge thermocouple positions in the 250-mm crystal. However, all these profiles are intentionally adjusted to normalize the melting temperature to 1412 °C because they showed lower temperatures than 1412 °C at the point assumed as the growth interface. The actual position of the thermocouples may include a few mm errors around the 0-mm position in Figure 12.2. Since it is known from other experiments that the growth interface height with growth rate is postulated as concave to the melt as shown in Table 12.2, the thermocouple positions passing through the interface are also adjusted in Figure 12.2 according to Table 12.2. In the experiments on the stopping of growth of FZ crystal [26] and the decreasing growth rate of CZ crystals [27], secondary defects consisting of interstitials were observed in both crystals, and the effective region for defect generation as measured from the growth interface were several to several tens of millimeters depending on whether it is FZ or CZ growth. In this chapter, as we defined the effective length as 10 mm from the growth interface, the axial temperature gradient G is $G = (T_{\text{int}} - T_{10}) / \text{cm}$. The G at the centre is the smallest and the G at the edge is the largest in the case of 1.2 mm/min growth rate as shown in Figure 12.2(a). On the other hand, in the case of the 0.3 mm/min growth rate the G values in all three positions are almost equal as shown in Figure 12.2(d). The temperature distributions shown in Figure 12.2 can be transferred to the isotherms as shown in Figure 12.3, if we postulate an axial symmetry of temperature distribution. When v is large, the temperature in the centre is higher than that at the edge. On the other hand, when v is small, a uniform temperature distribution in the cross section of the crystals is obtained. Concerning the interface height in Table 12.2, it can be said that our supposition is reasonable for Figure 12.2 and Figure 12.3 based on the following considerations. The smallest G in the centre of the crystal with 1.2 mm/min growth rate causes the deepest concave interface shape.

The axial temperature distributions for each thermocouple position, as it depends on the growth rate, are collected in Figure 12.4. A larger growth rate v produces a smaller G in the centre and middle positions, but at the edge the differences of G values are small for all growth rates. This means that the surface temperature distribution may be largely determined by the type of hot zone within 1.2 mm/min.

Previously reported papers concerning point-defect generation have not mentioned the crystal-length effects, although some have discussed the thermal-history effects caused by the seed end of the crystal having a longer thermal

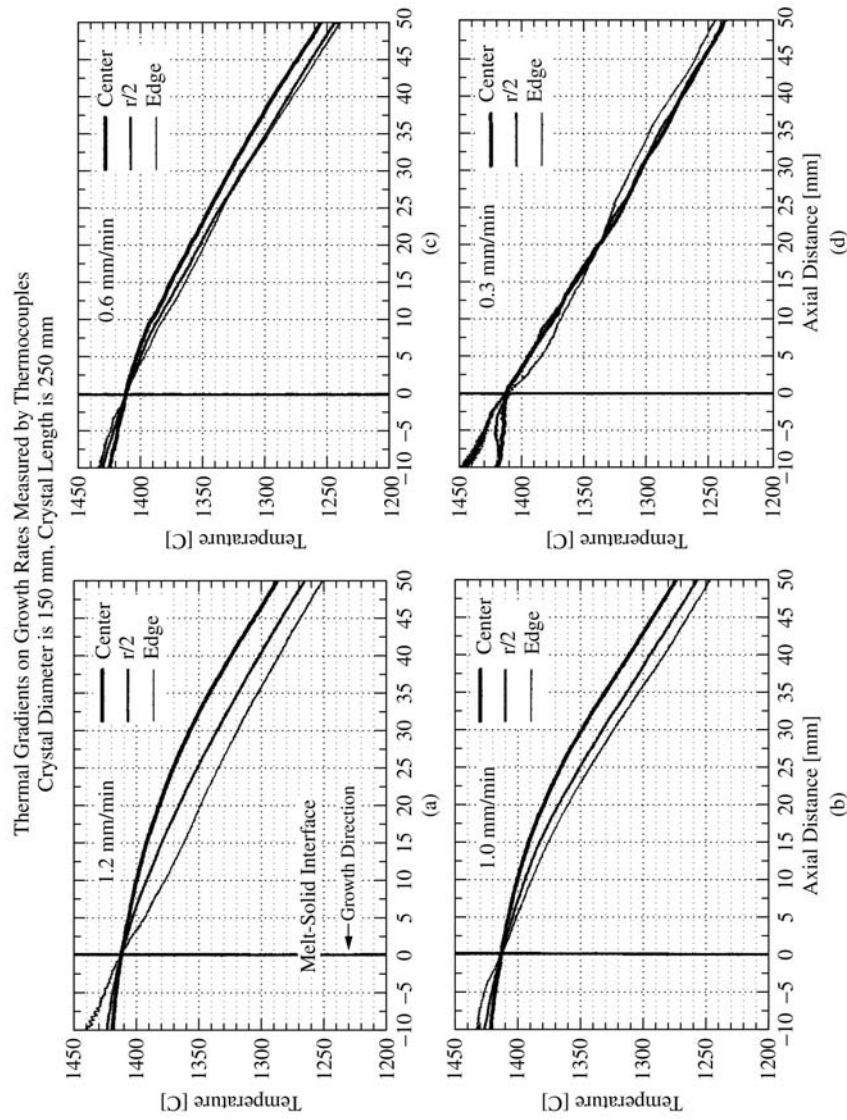


Figure 12.2 Axial temperature distributions of 250-mm crystals for four different growth rates: (a) 1.2 mm/min; (b) 1.0 mm/min; (c) 0.6 mm/min and (d) 0.3 mm/min.

Table 12.2 Postulated interface height (concave)

Growth rate (mm/min)	Center (mm)	Middle ($r/2$) (mm)	Edge surface (mm)
1.2	6	5	0
1.0	5	4	0
0.6	3	2	0
0.3	1.5	1	0

history than the tail of the crystal. In FZ crystal growth, both G and the thermal history do not vary with crystal length, due to rapid cooling effects. However, in CZ crystal growth, it is anticipated that the crystal length has a direct influence on G because of the large contribution of heat conduction through the crystal interior. So we also measured the temperature distributions of the 350-mm crystal in addition to the 250-mm crystal. The order of G values of the 350-mm crystal on growth rates is the same as that of the 250-mm crystal, although in the region far from the growth interface an anomaly in the temperature distributions is observed in the case of the 0.6-mm/min growth rate.

In order to consider the length effect, G values are collected as shown in Figure 12.5. It is first concluded that smaller v produces larger G in all positions in both Figure 12.5(a) and (b), independent of crystal length, with an exception in the case of a 1.2-mm/min growth rate for the 250-mm crystal. On the other hand, in actual crystal-growth when the melt level is descending, after-heating from the heater increases. As a result the G value at the edge becomes small. So to keep the same G , the v must be lowered. In a comparison of Figure 12.5(a) and (b), it is noted that the cross-sectional distribution of G changes with crystal length. The G at the edge is larger than that at the centre in Figure 12.5(a), but a flat distribution of G and a larger G at the centre are seen in Figure 12.5(b). This is a length effect.

12.4 DISCUSSION

12.4.1 BALANCE EQUATION

The balance equation is widely used as the boundary condition of heat transfer at a growth interface. If the thermal gradients in the solid and liquid at the interface are G_s and G_l then the continuity of heat flux requires

$$K_s G_s - K_l G_l = Lv \quad (12.1)$$

where K_s and K_l are the thermal conductivities of solid and liquid, L is the latent heat of solidification per unit volume, and v is the growth rate.

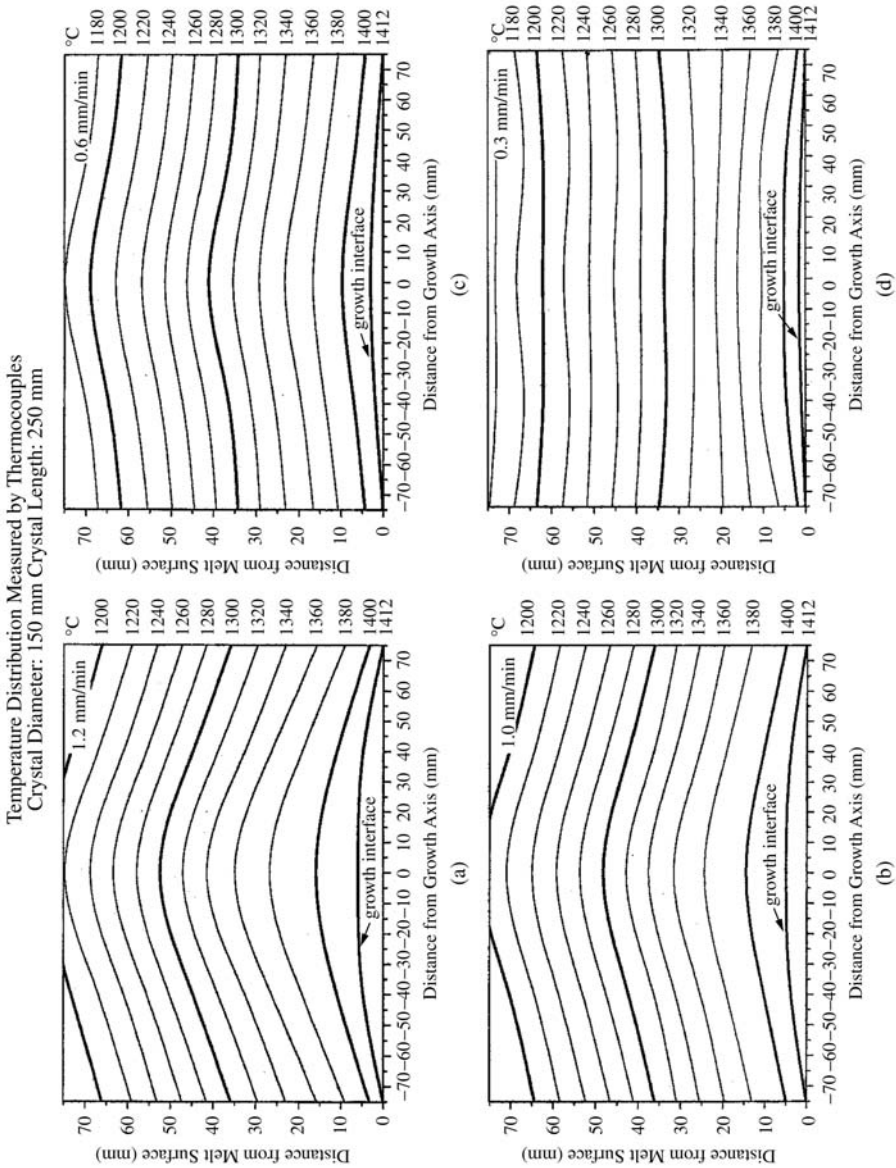


Figure 12.3 Isotherms near growth interfaces obtained from Figure 12.2. (a) 1.2 mm/min; (b) 1.0 mm/min; (c) 0.6 mm/min and

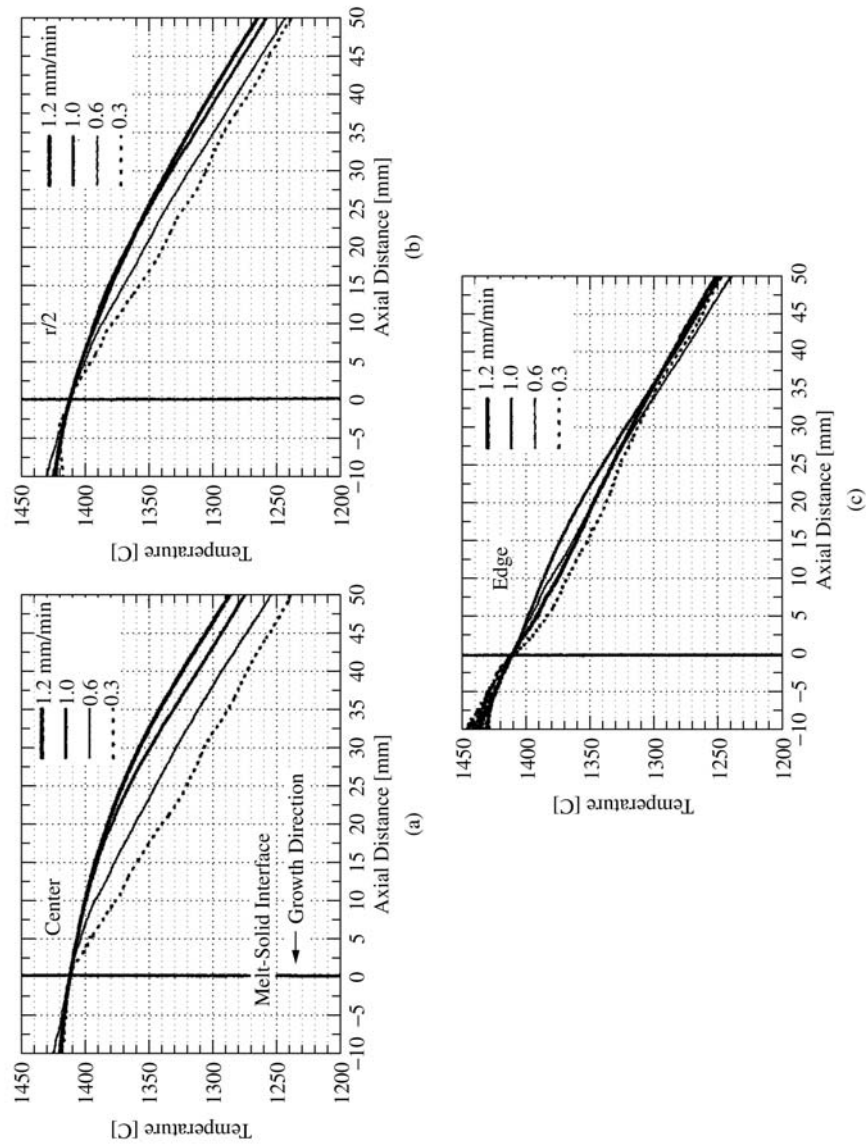


Figure 12.4 Axial temperature distributions of 250-mm crystal on (a) center; (b) middle and (c) edge positions obtained from Figure 12.2.

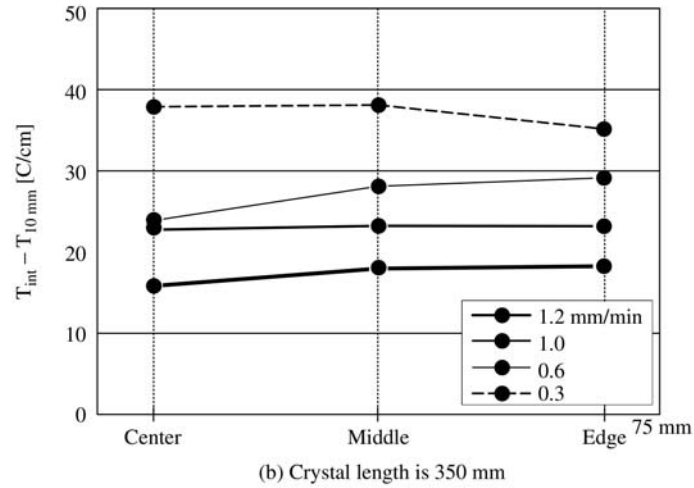
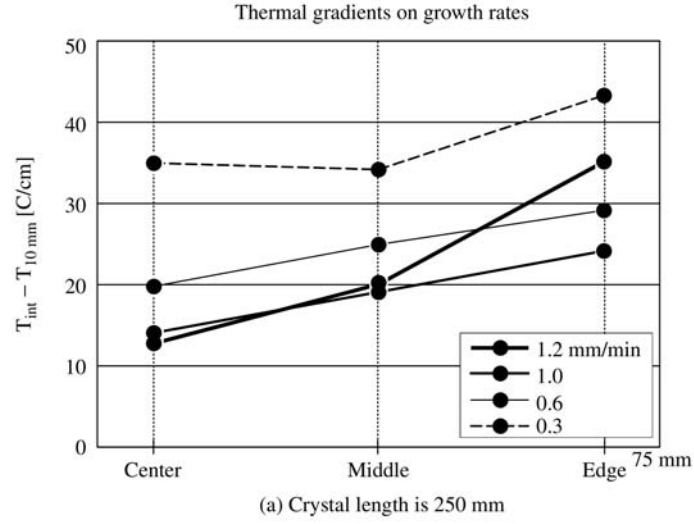


Figure 12.5 Temperature gradient G on center, middle and edge depending on growth rates. Crystal length (a) 250 mm and (b) 350 mm.

This equation satisfies the following four cases as seen in Figure 12.6. As there is no reason for G_1 to increase with increasing v , Figure 12.6(a) may be excluded. Most researchers in their simulations suppose that the larger v produces the larger G_s with constant G_1 as seen in Figure 12.6(b). However, both cases seem unrealistic although the latent heat term Lv becomes infinite with increasing v . In addition, Equation (12.1) is only valid in the vicinity of the interface and cannot be applied far from the interface. Voronkov proposes the case of Figure 12.6(c) based on the experimental results of Puzanov *et al.* in which G_s is independent

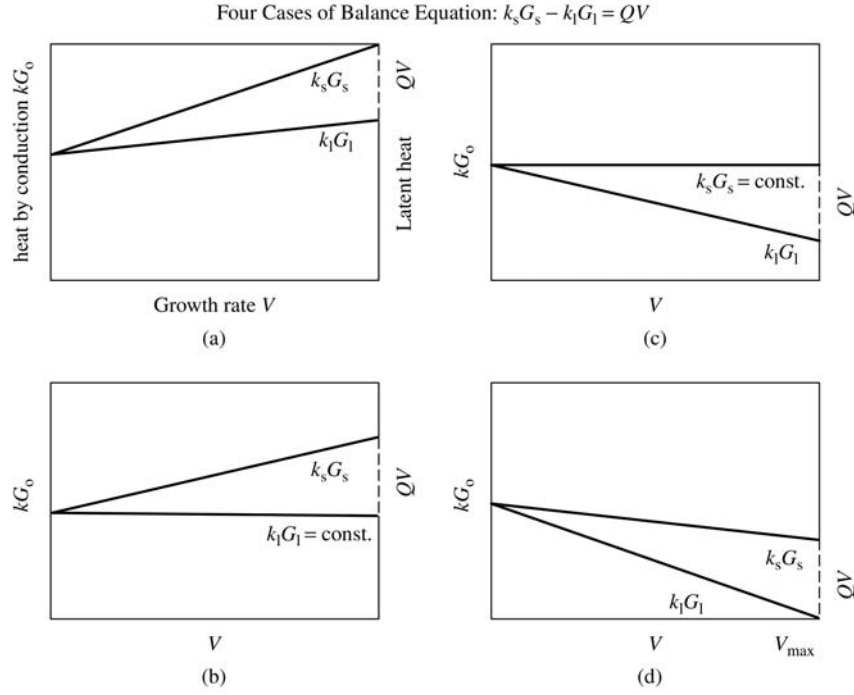


Figure 12.6 Four cases of the balance equation as discussed in the text.

of v . He speculates that the decreasing G_l is caused by the interface being lifted from the melt level. We propose the case of Figure 12.6(d), i.e. both G_s and G_l decrease with increasing v . Although this condition might only be valid in the case of transient phenomena during the re-solidification process in our experiment, we tend to believe the relationship shown in Figure 12.6(d).

12.4.2 DISCUSSION OF VORONKOV'S RELATION

G_s in Voronkov's relation is assumed as a constant value (independent of v) which is determined by the design of the hot zone. The relation is applied to the macroscopic range and thus is not limited to the interface. However, from our experimental results the thermal gradient G' in the crystal is slightly inverse of v . So the critical value C_{crit} for formation of R-OSF is written as

$$C_{\text{crit}} = v/G \sim a/G'G \quad (12.2)$$

where a is constant. When we use a hot zone with large G we have to achieve a small G' and a large v to compensate for the large G in order to obtain C_{crit} .

The occurrence of D-defects by Roksnoer may be interpreted by the very small G value in pedestal pulling of small-diameter (23 mm) crystals in combination with the very large v (>6 mm/min) and small G' : vacancy-rich crystals are obtained with $C_{\text{crit}} > a/G'G$.

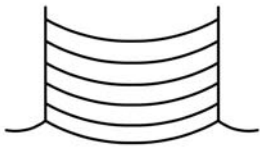
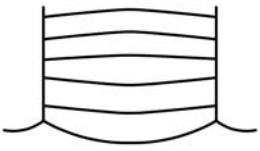

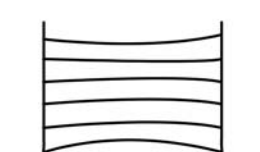
Von Ammon *et al.* maintain C_{crit} with the relationship between v and G , and the formation of R-OSF is explained by the above concept that large v induces small G' .

In growth experiments using a hot zone with very small G no R-OSF are formed even when C_{crit} is reached by small v . Thus it seems that G' is the important parameter and not v or G .

12.4.3 INTERFACE-SHAPE FORMATION

Macroscopic interface-shape formation has not been fully understood in silicon crystal-growth. In fact when the hot zone and the crystal diameter are constant, a small v creates a convex interface to the melt, and large v produces a concave interface. Our experimental results are shown in Figure 12.7(a) and (b). When v is small, as thermal conduction is dominant in the center, G' becomes large, whereas at large v a reduced G' is observed. The concave interface is formed

INTERFACE SHAPES AND THERMAL GRADIENTS

	Experiments	Macro balance equation
Low Growth Rate Interstitials R-OSF	 (a)	 (c)
High Growth Rate Vacancies AOP	 (b)	 (d)

Surface temperature distributions are constant.

Figure 12.7 Interface shapes and thermal gradients. (a) and (b) Experimental results, (c) and (d) traditional interpretation.

due to a reduced growth rate as explained by Figure 12.6(a). The growth rate v_{\max} in the centre is limited by $G_1 = 0$, which is caused by increasing Lv . On the other hand, near the edge of the crystal heat is effectively removed from the surface so that large G values allow crystal-growth with large v .

Numerous researchers reported temperature distribution/growth rate dependences as shown in Figure 12.7(c) and (d), which differ from Figure 12.7(a) and (b). In the case of Figure 12.7(c) there is no reason for a convex interface when G' is small. It is concluded that the interface shape is determined by the distribution of G' across the interface. Small or large G' in the center of the crystal lead to concave or convex interfaces, respectively.

12.5 CONCLUSIONS

The thermal distributions near the growth interface of 150-mm CZ silicon crystals were measured by three thermocouples installed at the centre, middle (half-radius) and edge of the crystals. The results show that larger v produced smaller G' in analogy to a report for FZ crystals. The results do not contradict the heat balance equation because temperature distributions continue through the growth interface into the bulk crystal. Finally, it is proposed that the shape of the growth interface is also determined by the distribution of G' across the interface. It is evident that the knowledge of the actual G distributions across the interface is essential to understand the formation mechanism of grown-in defects and to predict the shape of the interface.

REFERENCES

- [1] G. Watkins, Defects and Diffusion in Silicon Processing, eds. T. Diaz, de la Rubia, S. Cofa, P. A. Stalk and C. S. Rafferty, *Mater. Res. Soc. Symp. Proc.* **469** (1997) 139.
- [2] H. Bracht, E. E. Haller, K. Eberl, M. Cardona, and R. Clark-Phelps, *Mater. Res. Soc. Symp. Proc.* **527** (1998) 335.
- [3] T. S. Plaskett, *Trans. AIME* **233** (1965) 809.
- [4] T. Abe, T. Samizo and S. Maruyama, *Jpn. J. Appl. Phys.* **5** (1966) 458.
- [5] A. J. R. de Kock, *Appl. Phys. Lett.* **16** (1970) 100.
- [6] H. Foell and B. O. Kolbesen, *Appl. Phys.* **8** (1975) 319.
- [7] H. Foell, U. Goesele and B. O. Kolbesen, *Semiconductor Silicon 1977*, eds. H. R. Huff and E. Sirtl (Electrochem. Soc., Princeton, 1977) p. 565.
- [8] P. M. Petroff and A. J. R. de Kock, *J. Cryst. Growth* **30** (1975) 117.
- [9] J. A. Van Vechten, *Phys. Rev. B* **17** (1978) 3179.
- [10] J. Chikawa and S. Shirai, *Jpn. J. Appl. Phys.* **18**, Suppl. **18-1** (1979) 153.
- [11] E. Sirtl, *Semiconductor Silicon 1977*, eds. H. R. Huff and E. Sirtl (Electrochem. Soc., Princeton, 1977) p. 4.
- [12] S. M. Hu, *J. Vac. Sci. Technol.* **14** (1977) 17.
- [13] A. J. R. de Kock and W. M. Van de Wijgert, *J. Cryst. Growth* **49** (1980) 718.

- [14] P. J. Roksnoer and M. M. B. Van Den Moom, *J. Cryst. Growth* **53** (1981) 563.
- [15] V. V. Voronkov, *J. Cryst. Growth* **59** (1982) 625.
- [16] T. Y. Tan and U. Goesele, *J. Appl. Phys. A* **37** (1985) 1.
- [17] J. Ryuta, E. Morita, T. Tanaka and Y. Shimanuki, *Jpn. J. Appl. Phys.* **29** (1990) L1947.
- [18] M. Itsumi, H. Akiya and T. Ueki, *J. Appl. Phys.* **78** (1995) 5984.
- [19] E. Wijaranakula, *J. Electrochem. Soc.* **139** (1992) 604.
- [20] R. Habu, I. Yunoike, T. Saito, and A. Tomiura, *Jpn. J. Appl. Phys.* **32** (1993) 1740.
- [21] R. A. Brown, D. Maroudas, and T. Sinno, *J. Cryst. Growth* **137** (1994) 12.
- [22] W. W. Webb, *J. Appl. Phys.* **33** (1962) 1961.
- [23] W. v. Ammon, E. Dornberger, H. Oelkrug, and H. Weidner, *J. Cryst. Growth* **151** No. 3/4 (1995) 273.
- [24] M. Hourai, E. Kajita, T. Nagashima, H. Fujiwara, S. Ueno, S. Sadamitsu, S. Miki and T. Shigematsu, *Mater. Sci. Forum* **196–201** (1995) 1713.
- [25] F. Dupret, P. Nicodeme, Y. Ryckmans, P. Wouters, and M. J. Crochet, *Int. J. Heat Mass Transfer* **33** (1990) 1849.
- [26] T. Abe, H. Harada and J. Chikawa, *Physica* **116B** (1983) 139.
- [27] T. Abe and K. Hagimoto, *Solid State Phenom.* **47–48** (1996) 107.
- [28] N. Puzanov, A. Eidenson and D. Puzanov. Abstract of ICCG 12/ICVGE 10, July 1998, Jerusalem p. 342.
- [29] P. J. Roksnoer, *J. Cryst. Growth* **68** (1984) 596.
- [30] H. Harada, T. Abe and J. Chikawa, *Semiconductor Silicon 1986*, eds. H. R. Huff, T. Abe and B. O. Kolbesen (Electrochem. Soc. Pennington, 1986) p. 76.
- [31] T. Abe, *J. Korean Assoc. Cryst. Growth* **9** (1999) 402.

13 Silicon Crystal Growth for Photovoltaics

T. F. CISZEK

National Renewable Energy Laboratory, Golden, CO 804 01-3393, USA

13.1 INTRODUCTION

Unlike silicon crystals used in the electronics industry, crystal perfection, purity, and uniformity are not necessarily highest on the list of desirable attributes for crystalline Si incorporated into commercial photovoltaic (PV) modules. Tradeoffs are routinely made, weighing these attributes against cost, throughput, energy consumption, and other economic factors. In fact, such tradeoffs for PV use have spawned far more alternative growth methods for silicon than has the many decades of semiconductor technology development. Semiconductor applications use the well-known Czochralski (CZ) technique almost exclusively, with a small contribution (on the order of 10 % to 15 %) from float-zone (FZ) growth.

Of course, some FZ material is used in the PV industry, and the highest recorded silicon solar cell efficiency (ratio of cell-output electrical power to solar power incident on the cell), 24 %, has been achieved for devices fabricated on FZ wafers (Zhao *et al.*, 1995). But the device-processing procedures needed to achieve the high efficiencies are expensive and time consuming. So, as in the semiconductor industry, more CZ wafers than FZ wafers are used for PV. What may be surprising though, is that more multicrystalline silicon than single-crystal material is currently used in PV modules. Some of this multicrystalline Si is not wafers from ingots, but rather ribbons or sheets of silicon solidified in a planar geometry.

Of the 152 peak megawatts (MW_p) of PV modules sold throughout the world in 1998, 132 MW_p , or 87 %, were crystalline Si. Comprising this 87 % was ~39 % fabricated from single-crystal Si ingots, ~44 % made from multicrystalline-Si ingots, and ~4 % based on multicrystalline-Si ribbons or sheets (Maycock, 1999). The other 13 % of modules sold are largely amorphous silicon or nonsilicon thin films, which will not be discussed in this chapter. There is an increasing PV research effort focused on thin-layer polycrystalline Si deposited on foreign substrates. These approaches have not yet reached a commercialization stage.

An issue common to all the Si PV growth approaches is the availability of low-cost polycrystalline Si feedstock. The PV industry has in the past relied

on reject silicon from the electronics industry for use as feedstock. But the PV industry has been growing at an average rate of 20 % over the last five years, which is faster than the growth rate of the electronics industry, and the point has been reached where the supply of reject silicon is insufficient.

13.2 BASIC CONCEPTS

The criteria for crystalline silicon used in PV are somewhat different from those for silicon used in integrated circuits. In this section, the photovoltaic effect is described as a basis for understanding the importance of minority-carrier lifetime in PV device operation. Crystal-growth parameter effects on lifetime are discussed. The light absorption of silicon is relatively low because of the indirect bandgap. This limits how thin a crystalline-Si PV device can be and has some implications for thin-layer Si crystal-growth approaches.

13.2.1 THE PHOTOVOLTAIC EFFECT

A silicon solar cell (shown schematically in Figure 13.1) converts sunlight energy into direct-current (DC) electrical energy by the photovoltaic effect. As sunlight impinges on the top surface, some of the light is reflected off the cell's grid structure and some is reflected by the surface of the cell. The grid reflection loss can range from 3 % for advanced cell designs to as much as 20 % for some screen-printed cells. Antireflection coatings and texturing of the silicon surface can be used to minimize the surface reflection losses. Some light (long-wavelength

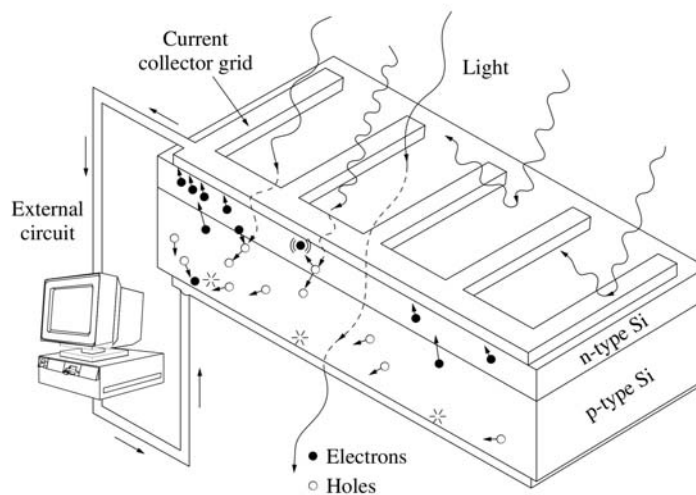


Figure 13.1 Operation of a Si solar cell.

infrared) does not have the threshold energy needed to free electrons from the Si atoms and passes through the cell without interacting. Some light (short-wavelength ultraviolet) has more than enough energy to create the electron–hole pairs. The excess energy transferred to the charge carriers is dissipated as heat. About 40 % of the incident light energy is effectively used in freeing electrons from silicon atoms so that they can wander in the crystal lattice. They leave behind holes, or the absence of electrons, which also wander. The solar cell has a p/n junction, like a large-area diode. The n-type portion (typically near the front of the device) has a high density of electrons and few holes, so generated electrons can travel easily in this region. The opposite is true in the p-type region. There, holes travel easily. The electric field near this junction of n- and p-type silicon causes generated electrons to wander toward the grid on the surface, while the holes wander toward the back contact. If the electrons survive their trip across the cell thickness without recombining at defects or impurities, they are collected at the grid and flow through an external circuit as current that can operate an electronic instrument or appliance. After that, they re-enter the solar cell at the back contact to recombine with holes, and the process repeats.

13.2.2 MINORITY-CARRIER LIFETIME, τ

If some of the generated carriers recombine at defects, impurities, surface damage, etc., before reaching the contacts, the current output of the solar cell is diminished. Because it is a quantitative measure of such phenomena, minority-carrier lifetime (τ) characterization (ASTM, 1993) is frequently used to qualify the crystalline-Si material before it is used in device processing. Quality in a silicon photovoltaic material is nearly synonymous with τ . The parameters used in crystal growth have a direct bearing on τ , because they determine impurity levels and defect structures that give rise to carrier-recombination sites. Impurity incorporation, segregation, and evaporation during the crystal-growth process can be altered via ambient choice, growth rate, number of solidification steps, choice of container, heat-source characteristics, selection of source material, and other factors that vary from one process to another.

Heavy doping imposes an upper limit on lifetime according to $\tau_A = 1/C_A N^2$, where τ_A is the Auger-limit lifetime. C_A is the Auger coefficient, and N is the doping concentration. At the lower limit, $\tau < 2 \mu\text{s}$ is unlikely to be useful in most PV processes due to balance-of-systems costs. Poor-quality material cannot generate enough PV energy to justify the costs of the total PV system. Thus, the τ – N space available for photovoltaic applications is the nonhatched region in Figure 13.2, and the four labeled curves are ‘quality’ contours. In addition to the two limits, curves representing moderate τ (typical of Czochralski-grown, CZ, silicon) and high τ (typical of the best commercially available FZ silicon) are included. Note that there is a vast discrepancy between τ_A and the lifetime of the best available silicon. So there is potential for higher lifetimes and new

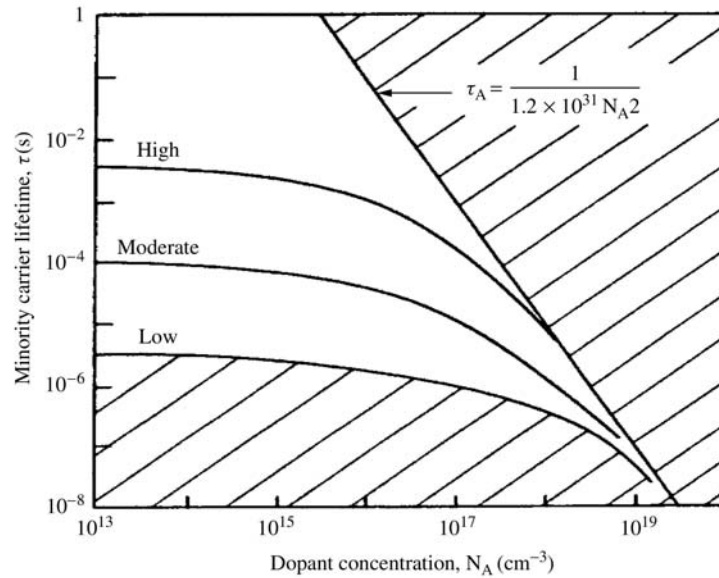


Figure 13.2 Material-quality contours of lifetime versus dopant concentration. The hatched region is not available or suitable for PV use.

device designs to take advantage of it. Transition-metal-impurity effects on τ and solar-cell efficiency as a function of their concentration levels are reasonably well understood from quantitative and detailed experimental studies (Davis *et al.*, 1980). Some metals such as titanium have a significant effect on τ even in concentrations as low as a few 100 ppta (parts per trillion, atomic). Others, such as copper, can be tolerated at a few ppma (parts per million, atomic). Fortunately, most of the detrimental impurities have small effective segregation coefficients, and their concentrations can be reduced during directional solidification (DS).

When no impurities are present in high enough concentration to affect τ , a myriad of structural defects can still act as recombination centers. Grain boundaries and their associated dislocation arrays usually constrain τ to $\leq 20 \mu\text{s}$. The lifetime of Si decreases with decreasing grain area as reported by Cizek *et al.* (1993) and illustrated in Figure 13.3. Even dispersed dislocations in a single crystal at a density $< 5 \times 10^4 \text{ cm}^{-2}$ can reduce τ to $30 \mu\text{s}$ in material that, when grown in the same way except dislocation-free, yields $\tau = 450 \mu\text{s}$. If grain boundaries, dispersed dislocations, and transition-metal impurities are present, as may be the case in ingots cast from low-grade silicon feedstock, it is not unusual to see $\tau < 10 \mu\text{s}$.

Si crystals that are free of transition-metal impurities, dislocations, and grain boundaries unveil second-order structural effects on lifetime. These are most easily seen in FZ material because O and C effects somewhat obscure the issue in CZ crystals. Types A and B swirl microdefects (Si interstitial cluster defects)

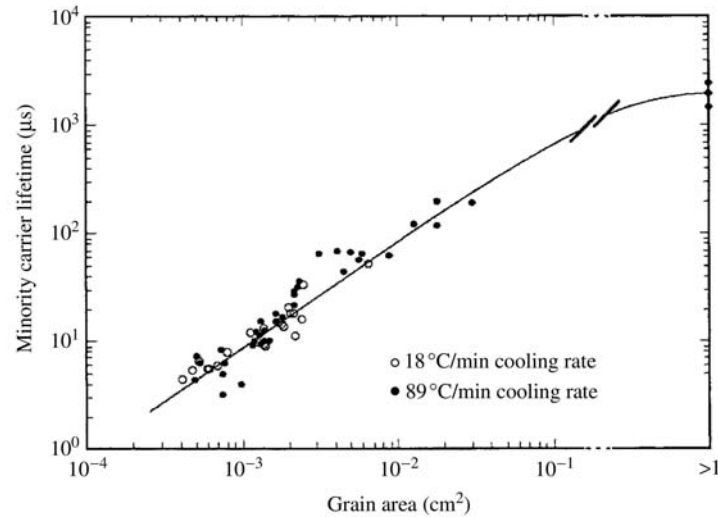


Figure 13.3 The effect of grain size on the minority-carrier lifetime of high-purity multicrystalline silicon.

are present in dislocation-free FZ crystals that are grown at a speed v that is too slow or in a temperature gradient G that is too large. Eliminating these defects allows $\tau > 1$ ms. When A and B swirls are eliminated, a third-order effect is unveiled – τ varies inversely with cooling rate, the product of $v \times G$, in swirl-free crystals. Thus v should be chosen just fast enough to eliminate swirls, if very high lifetimes are required. The physical nature of this ‘fast-cooling’ defect is not understood at the present time. By appropriate choice of v and G , Cizek *et al.* (1989) obtained $\tau > 20$ ms in lightly doped, p-type, high-purity silicon and were able to grow crystals on a quality contour an order of magnitude better than the one labeled ‘high’ in Figure 13.2.

13.2.3 LIGHT ABSORPTION

Besides variations in τ , another property of silicon that can impact solar-cell performance as a consequence of the growth method – in this case, because of the growth method’s effect on geometry – is the absorption coefficient, α , defined as the inverse distance in cm required for the intensity of incident light to fall to $1/e$ of its initial value. The absorption coefficient is a function of wavelength. Because Si is an indirect-bandgap semiconductor, the absorption edge is not sharp, and for some of the thin-layer growth methods, useful light passes through the silicon without being absorbed. The absorbed useable fraction of photons as a function of Si layer thickness is shown in Figure 13.4 for the typical light spectrum incident on the Earth (Wang *et al.*, 1996). While 100 % of the light is

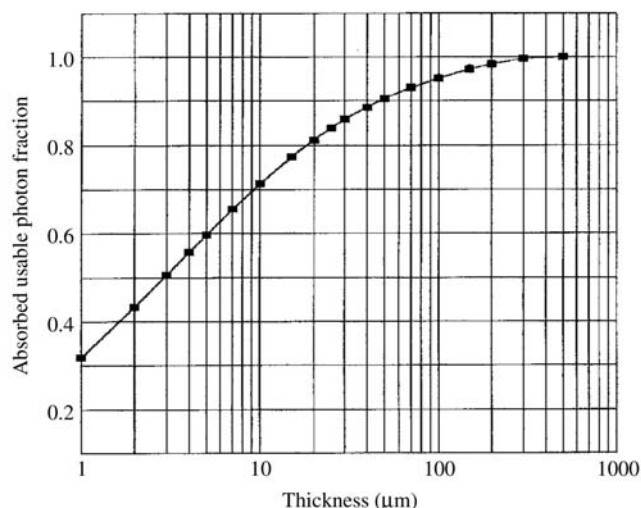
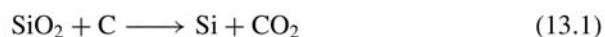


Figure 13.4 Fraction of solar photons absorbed, as a function of silicon thickness for air mass (AM) 1.5 illumination.

used in 300-μm wafers, this falls off to 90 % in 50-μm thin layers and 70 % in 10-μm thin layers. Thus if thin-layer Si solar cells are to be effective, it will be necessary to enhance the optical path length by appropriate surface coatings or texturing to cause multiple passes of the light in the thin structure. An advantage of thin Si layers is that shorter minority-carrier lifetimes can be tolerated because the generated carriers do not have as far to travel before reaching the contacts.

13.3 SILICON SOURCE MATERIALS

Silicon is the second most abundant element in the crust of the Earth (27 %), but it does not occur as a native element because SiO_2 is more stable. Many processing steps (Figure 13.5) are conducted to bring Si from its native ore, quartzite, to the crystalline substrates we use for solar cell fabrication or integrated circuit (IC) components. The starting silicon for both PV and IC applications is 99 % pure metallurgical-grade (MG) Si obtained via the carbon reduction of SiO_2 in an arc furnace. Although the overall reaction can be considered to be



there are a complex series of reactions that take place in different temperature regions of the arc furnace, with liquid Si finally forming from SiC. The Si liquid is periodically tapped from the furnace and typically allowed to solidify in shallow molds about 1.5×1 m in size. The major impurities are Fe, Al, and C. This

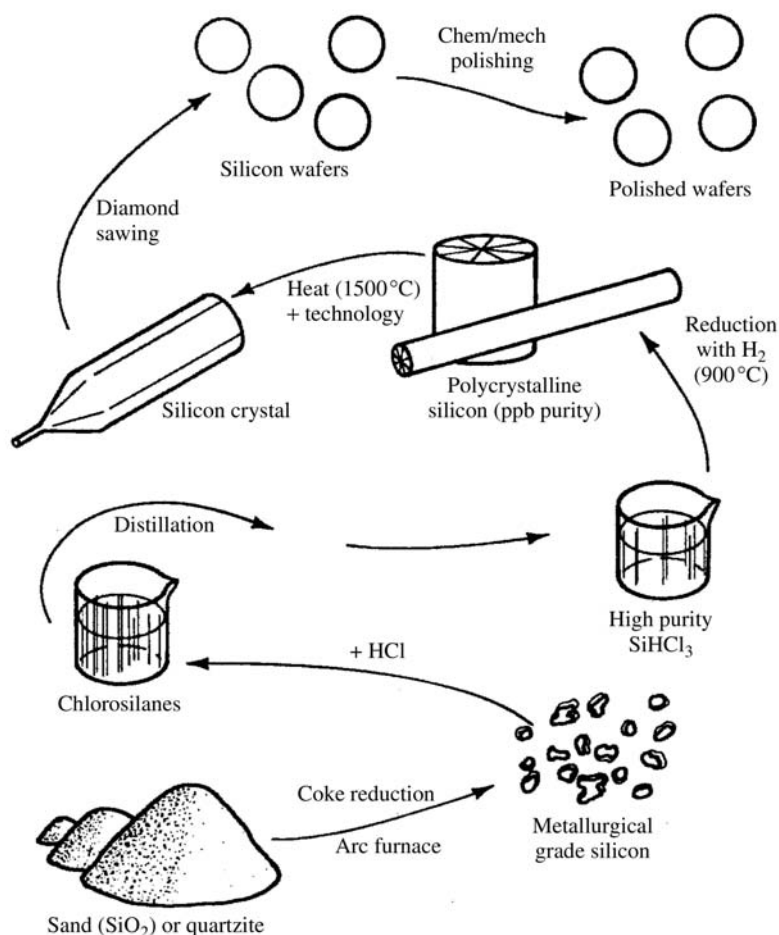


Figure 13.5 Stages in the transformation of silicon from quartzite to single-crystal wafers.

MG-Si material is inexpensive ($\sim \$1/\text{kg}$), but the residual impurities degrade τ to unacceptably low values and some, like B and Al, electronically dope it too heavily for PV devices. B is particularly bothersome because it neither segregates nor evaporates significantly during melt processing.

IC industry chlorosilane purification and deposition steps increase the purity to more than adequate levels for PV use (99.999999%), but also increase the cost to unacceptable levels for PV manufacturers. The current price of polysilicon from the chlorosilane IC process is about $\$50/\text{kg}$, while PV users have a target price of about $\$20$. So the Si PV industry has been using reject material from IC polysilicon and single-crystal production – material that is too impure for IC use but adequate for PV use. The IC industry now consumes about

20 000 metric tons of Si annually, and the PV industry uses about 3000 metric tons. But as production techniques improve and as the Si PV industry grows at a faster rate than the IC industry, the supply of reject material is becoming insufficient. New sources of polysilicon will be needed (Mauk *et al.*, 1997; Mitchell, 1998). Demand first exceeded supply of reject Si in 1996. The subsequent downturn in the IC industry temporarily relieved the PV feedstock shortage, but projections by one of the large polysilicon manufacturers indicate that the PV demand for reject Si will exceed the supply (8000 metric tons/yr) by a factor of 2 to 4 by the year 2010 (Maurits, 1998). This does not represent a fundamental material shortage problem, because the technology, quartzite, and coke needed to make feedstock are in abundant supply. The issue is to supply feedstock with necessary but only sufficient purity ($\sim 99.999\%$) at an acceptable cost.

The trichlorosilane (SiHCl_3) distillation method is used to purify Si for more than 95% of polysilicon production (even if converted to other chlorosilanes or silane for reduction), but is very energy intensive. It produces large amounts of waste, including much of the starting silicon and a mix of environmentally damaging chlorinated compounds. In addition, the feedstock produced by reduction following this distillation method exceeds the purity requirements of the PV industry, which are estimated to be:

- Electrical dopant impurities, iron, and titanium, each $< \sim 0.1$ ppma (they will be reduced further in the crystal-growth process by impurity segregation)
- Oxygen and carbon concentrations below the saturation limits in the Si melt (i.e., no SiC- or SiO_2 -precipitate formation)
- Total other nondopant impurities $< \sim 1$ ppma.

Fresh approaches are needed to originate novel separation technologies that can extract B, Al, P, transition metal impurities, and other impurities from MG silicon, to meet the purity requirements listed above – but in a simpler process. Examples of new approaches that are in the early stages of investigation are: (i) use of electron-beam and plasma treatments with several DS steps to remove impurities from MG-Si (Nakamura *et al.*, 1998); (ii) directly purifying granular MG-Si using repeated porous-silicon etching, subsequent annealing, and surface impurity removal (Menna *et al.*, 1998); (iii) a method that uses MG-Si and absolute alcohol as the starting materials (Tsuo *et al.*, 1998); (iv) vacuum and gaseous treatments of MG-Si melts coupled with directional solidification (Khattak *et al.*, 1999) guided by thermochemical calculations (Gee *et al.*, 1998); and (v) use of impurity partitioning when silicon is recrystallized from MG-Si/metal eutectic systems (Wang and Cizek, 1997). Approaches like these or other yet-to-be-determined innovative methods could have a major impact on the continued success and growth of the Si PV industry – especially if one is discovered that is intrinsically simpler than current technology, yet yields adequate Si purity.

13.4 INGOT GROWTH METHODS AND WAFERING

Basically, four methods are used to grow Si ingots for commercial PV use. These techniques are shown schematically in Figure 13.6. Two methods produce single-crystal material (FZ and CZ techniques shown in Figures 13.6(a) and 13.6(b),

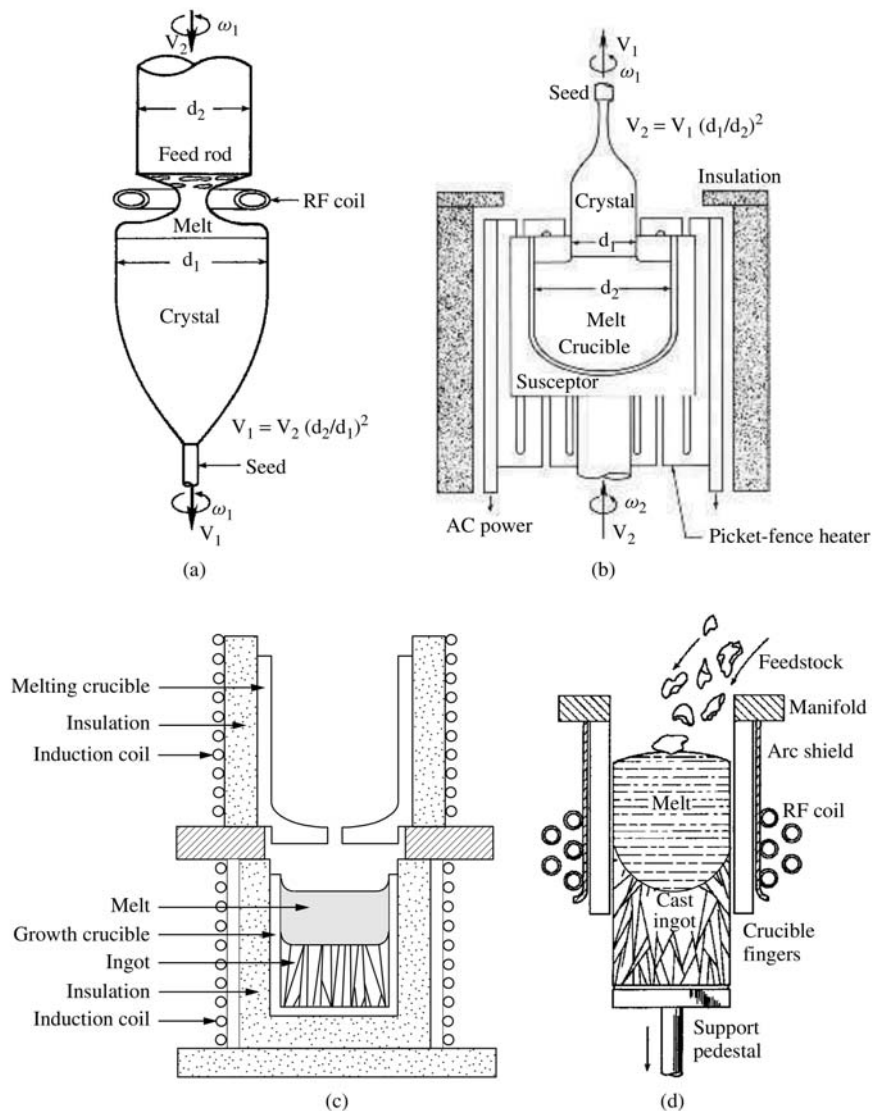


Figure 13.6 Schematic drawings of the four principal methods used to produce Si ingots for PV use: (a) float-zoning; (b) Czochralski growth; (c) directional solidification, and (d) electromagnetic semicontinuous casting.

respectively). Two others make large-grain (mm-to-cm grain size) multicrystalline silicon (directional solidification in square crucibles as shown in Figure 13.6(c), and electromagnetic semicontinuous casting shown in Figure 13.6(d)).

13.4.1 SINGLE-CRYSTAL GROWTH

The single-crystal growth methods, FZ and CZ, are relatively well known, and only some aspects pertinent to PV applications will be addressed here. Table 13.1 compares the characteristics of the FZ and CZ methods. There are two principal technological advantages of the FZ method for PV Si growth. The first is that large τ values are obtained due to higher purity and better microdefect control, resulting in 10 % to 20 % higher solar-cell efficiencies. The second is that faster growth rates and heat-up/cool-down times, along with absences of a crucible and consumable hot-zone parts, provide a substantial economic advantage. The main technological disadvantage of the FZ method is the requirement for a uniform, crack-free cylindrical feed rod. A cost premium (100 % or more) is associated with such poly rods. At the present time, FZ Si is used for premium high-efficiency cell applications and CZ Si is used for higher-volume, lower-cost applications.

Electrical power requirements for these two methods are on the order of 30 kWh/kg for FZ growth and 60 kWh/kg for CZ growth in the IC industry. The more cost-conscious PV industry has been achieving 35–40 kWh/kg for CZ growth, and some recent experiments indicate that levels on the order of 18 kWh/kg may be achieved for 150-mm diameter crystals by using improved insulation materials and lower argon gas-flow rates (Mihalik *et al.*, 1999). Not

Table 13.1 Comparison of the CZ and FZ growth methods

Characteristic	CZ	FZ
Growth speed (mm/min)	1 to 2	3 to 5
Dislocation-free?	Yes	Yes
Crucible?	Yes	No
Consumable Material Cost	High	Low
Heat-up/cool-down times	Long	Short
Axial resistivity uniformity	Poor	Good
Oxygen content (atoms/cm ³)	$>1 \times 10^{18}$	$<1 \times 10^{16}$
Carbon content (atoms/cm ³)	$>1 \times 10^{17}$	$<1 \times 10^{16}$
Metallic impurity content	Higher	Lower
Bulk minority charge carrier lifetime (μ s)	5–100	100–20 000
Mechanical strengthening	10^{18} oxygen	10^{16} nitrogen
Production diameter (mm)	150–200	100–150
Operator skill	Less	More
Polycrystalline Si feed form	Any	Crack-free rod

only were energy requirements reduced, but also argon consumption was reduced from 3 m³/kg of Si to 1 m³/kg of Si. Also, oxygen content in the crystals was reduced by 20 %, crystal growth rate was increased from 1.28 kg/h to 1.56 kg/h, and relative solar-cell efficiency increased by 5 %.

In CZ Si PV technology, approximately 30 % of the costs are in the crystal ingot, 20 % in wafering, 20 % in cell fabrication, and 30 % in module fabrication. High-speed wire saws that can wafer one or more entire ingots in one operation have greatly improved the throughput of the wafering process. A wire saw can produce about 500 wafers/h compared to about 25 wafers/h for older inside-diameter (ID) saw technology. Furthermore, it creates shallower surface damage (10 μ m) than the ID saws (30 μ m), and allows thinner wafers to be cut, thus increasing the number of wafers per ingot. Currently about 20 wafers are obtained from 1 cm of ingot. Efforts are underway to obtain 35 wafers/cm. Problems with increased breakage are seen with the thinner wafers – especially in the sawing process. At 20 wafers/cm and a wafer thickness >300 μ m, breakage is on the order of 15 %. This can rise to on the order of 40 % when the wafer thickness is decreased to 200 μ m. It is clear that wafer handling will be an important issue as wafers become thinner.

One clever way of dealing with the low fracture strength of thin (100) wafers from single-crystal CZ ingots is to deliberately introduce a controlled multicrystalline structure into the growing ingot. In particular, the tricrystalline structure described by Martinelli and Kibizov (1993) provides three grains propagating along the length of the ingot. Each has a $\langle 110 \rangle$ longitudinal direction. Two of the grain boundaries are first-order $\{111\}$ twin planes, and the third is a second-order $\{221\}$ twin plane. The three angles between boundaries are thus 125.27°, 125.27°, and 109.47°. The twins block any $\{111\}$ planes from crossing across the entire ingot, and improve the resistance to cleavage or propagation of defects that takes place on $\{111\}$ planes. Wafers from these tricrystals are observed to possess about 440 MPa fracture strength compared to about 270 MPa for (100) single-crystal wafers and 290 MPa for multicrystalline wafers (Endros *et al.*, 1997). The measurements were made on wafers after etching in KOH at 100°C to 310- μ m thicknesses. Breakage during wire sawing of tricrystal ingots at <200 μ m thickness is half of that for $\langle 100 \rangle$ ingots. The tricrystal ingots have been shown to maintain their structure for reasonably long lengths (150–400 mm at the present state of technology) with minimal degradation of minority-carrier-recombination properties (Wawer *et al.*, 1997).

13.4.2 MULTICRYSTALLINE GROWTH

A multicrystalline structure with grains on the order of mm to cm in width and approximately columnar along the solidification direction is characteristic of DS or casting in crucibles and also of electromagnetic semicontinuous casting. Casting of multigrain silicon was reported more than 80 years ago (Allen, 1913).

In 1960, large multicrystalline-silicon domes and plates 330 mm in diameter by 50 mm thick were formed via ambip casting. Early applications were for infrared optics and other nonsemiconductor uses. A summary of early silicon casting approaches was compiled by Runyan (1965). Si casting into graphite molds as an alternative to CZ growth for PV applications was reported by Fischer and Pschunder (1976).

DS can be carried out in a separate crucible after (or as) silicon is poured into it from a melting crucible, as indicated in Figure 13.6(c). This process is usually referred to as silicon casting. Or the silicon can be melted and directionally solidified in the same crucible (e.g., the bottom crucible in Figure 13.6(c)). This technique is referred to as directional solidification. It is simpler than casting, because no melt pouring is involved, but there are longer reaction times at high temperature between the melt and the crucible, and longer turnaround times. Because melting and solidification are decoupled in casting, higher throughputs are possible. But the process and equipment are more complex.

DS of silicon in the same quartz (fused silica) crucible used to melt it would seem to be a logical approach for large-grained ingot production, but sticking and thermal expansion mismatch between the solidified Si and the crucible lead to significant cracking problems. This was alleviated to some extent by deliberately weakening the inner wall of the quartz crucible (Khattak and Schmid, 1978). High-density graphite crucibles were introduced for DS as a way of avoiding the cracking (Ciszek, 1979). Most crucible-based commercial methods of growing multicrystalline-Si ingots for PV consumption use either the casting method or DS in the melting crucible. The crucibles are either graphite or quartz (often coated with Si_3N_4 or other compounds to discourage sticking and cracking or enable reuse). The actual growth process is DS in either method.

Multicrystalline ingots as large as 690 mm \times 690 mm in cross section and weighing as much as 240 kg are grown in total cycle times of 56 h. The resultant throughput is 4.3 kg/h. Thus the larger area, compared to CZ crystals, more than offsets the somewhat lower linear growth rates leading to higher throughputs for DS by a factor of ~ 3 . Both induction heating, as shown in Figure 13.6(c), and resistance heating can be used. The energy consumption for DS is in the range of 8–15 kWh/kg. Unlike CZ growth, the solid/liquid interface is submerged in DS, and precipitates or slag at the melt surface do not disrupt growth. DS is a simpler process requiring less skill, manpower, and equipment sophistication than CZ, which can make it a lower cost process. However, there are also drawbacks. There are numerous crystal defects (grain boundaries and dislocations) due to the multicrystalline structure. Impurity contents can be higher depending on the crucibles used, and portions of the bottom, sides, and top surface of the ingot are discarded. So the lower cost of DS is at the expense of solar-cell efficiency. DS solar cells are about 85 % as efficient as CZ cells. The best efficiency of small cells, with sophisticated processing, is 18.6 %. Typical large production cell efficiencies are 13–14 %, with good consistency.

Electromagnetic casting (EMC) has some similarities to the casting and DS methods described above, but also has several unique features that change the ingot properties and warrant a separate discussion. The method was first applied to semicontinuous silicon ingot casting by Ciszek (1985, 1986). EMC is based on induction-heated cold-crucible melt confinement, except that unlike the conventional cold crucible, there is no crucible bottom. A parallel, vertical array of close-spaced, but not touching, water-cooled, conducting fingers is attached at one end to a water-cooling manifold. The other end of each finger is closed. An internal distribution system carries cooling water to the tip and back again. The shape of the region enclosed by the close-spaced fingers determines the cross section of the cast ingot, and a wide variety of shapes are possible (circular, hexagonal, square, rectangular, etc.). Silicon is melted on a vertically moveable platform (typically graphite) located within the finger array. The melting is accomplished by induction heating after suitable preheating. The induction coil, placed outside the finger array (Figure 13.6(d)), induces a current to flow on the periphery of each finger, around the finger's vertical axis. Like a high-frequency transformer, each finger in turn induces a current to flow in the periphery of the silicon charge, about its vertical axis. The silicon is heated by its resistance to the current flow. There is a Biot–Savart-law repulsion between the current flowing in the periphery of the silicon melt and the currents flowing in the fingers, because they are induced to flow in opposite directions at any particular instant in the RF cycle. Thus, the melt is repulsed from the water-cooled fingers. The open-bottom arrangement allows the platform to be withdrawn downward, solidifying the molten silicon, while new melt is formed by introducing feed material from the top. In this way, a semicontinuous casting process can be carried out.

A variety of feed silicon geometries can be used (melts, rods, pellets, scrap, etc.). Because the interface is submerged, feed perturbances or slag at the melt surface do not affect the solidification front. Ingot lengths of nearly 3 m have been demonstrated. The cross section of the ingots has evolved over years of development and is currently about 350 mm × 350 mm. The cold fingers allow steep thermal gradients and fast growth speeds ($\sim 1.5\text{--}2$ mm/min), even in ingots with large cross sections. But they also cause a steeply curved interface that is concave toward the melt. Thus, grains are neither as columnar nor as large as in conventional DS. The average grain size is on the order of 1.5 mm in large ingots. This decreases τ , but the relatively high purity and freedom from oxygen and carbon impurities ($O < 6 \times 10^{15}$; $C < 8 \times 10^{16}$) largely offset the grain-size effect, so that solar-cell efficiencies of about 14–15 % are obtained on 15 cm × 15 cm cells. The throughput of EMC is the highest of any ingot growth technique – up to approximately 30 kg/h. The power consumption can be as low as 12 kWh/kg.

13.5 RIBBON/SHEET GROWTH METHODS

More than a dozen techniques have been introduced over the years for growing silicon ribbons or sheets. Only the ones currently in use for commercial

PV substrates will be addressed here. For a description of the others, see Ciszek (1984). The four methods being developed commercially are dendritic web growth, shown in Figure 13.7(a), growth from a capillary shaping die (Figure 13.7(b)), growth with edge supports or 'strings' (Figure 13.7(c)), and growth on a substrate (Figure 13.7(d)). These methods can be placed in two categories: (i) those pulled perpendicular to a solid/liquid interface with the same shape as the ribbon cross section (web growth, capillary die growth, and edge-supported growth), and (ii) those pulled at a large angle to a solid/liquid interface that is much greater in area than the cross section of the sheet (growth on a substrate). There is a large difference in the limiting pulling rate v between type (i) and type (ii). For type (i) growth,

$$v_I = \frac{1}{L\rho_m} \left(\frac{\sigma \varepsilon (W + t) K_m T_m^5}{Wt} \right)^{1/2} \quad (13.2)$$

where L is latent heat of fusion, ρ_m is density at the melting temperature, σ is the Stefan-Boltzmann constant, ε is emissivity, K_m is the thermal conductivity at the melting temperature T_m , W is the ribbon width, and t is the ribbon thickness (Ciszek, 1976). For type (ii) growth,

$$v_{II} = \frac{4\alpha K_m b}{(2K_m - \alpha t)t L\rho_m} \Delta T \quad (13.3)$$

where α is the effective coefficient of heat transfer, b is the length of the solid/liquid interface (in the pulling direction), and ΔT is the temperature gradient between melt and substrate (Lange and Schwirtlich, 1990). For the case of a 250- μm thick ribbon, Equation (13.2) predicts a maximum type (i) growth rate of ~ 8 cm/min. Experimentally, rates closer to 2 cm/min are realized. Equation (13.3) predicts a 6-m/min growth rate at $\Delta T = 160^\circ\text{C}$, and experimental pulling speeds near that value were realized. The indication is that type (ii) growth speeds can be hundreds of times faster than type (i) vertical pulling approaches, especially if b and ΔT are maximized.

Dendritic web growth, the oldest Si ribbon growth method, was introduced by Dermatis and Faust (1963). The technique arose from the observation that long, thin, flat dendrites with a (111) face and $\langle 2\bar{1}\bar{1} \rangle$ growth direction could be pulled from Ge and Si melts. As Figure 13.7(a) indicates, one such dendrite is used as a seed and a thermally defined 'button' is grown laterally from it. Then upward pulling is commenced with appropriate melt-temperature adjustments such that a dendrite of the same orientation propagates from each end of the button. A web of crystalline silicon solidifies between the dendrites. It is a single crystal except for an odd number (1, 3, 5, etc.) of twin planes in the central region. Web ribbons are currently grown at about 1.5 to 2 cm/min pulling rates, with a width of ~ 5 cm, a thickness of 100 μm , and in lengths up to 100 m with continuous melt replenishment (~ 0.25 g/min). Furnace runs are typically one week in duration, and produce

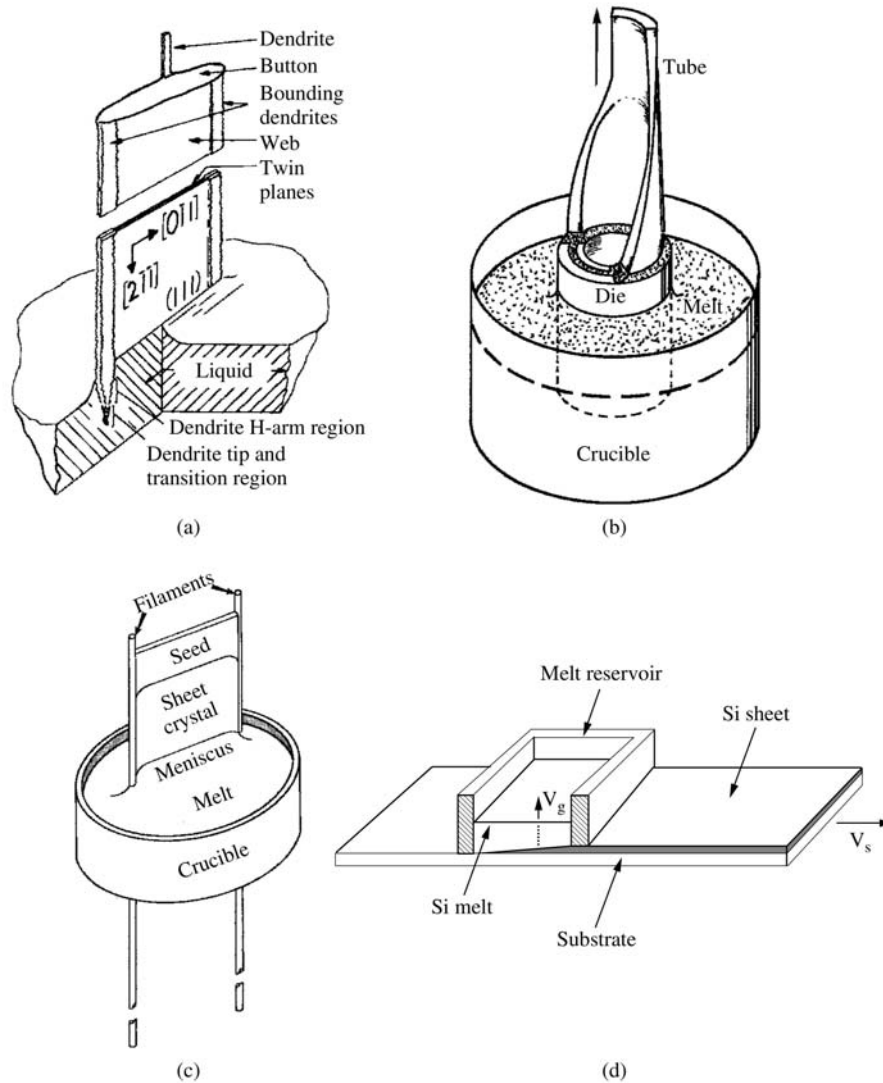


Figure 13.7 Schematic drawings of the four Si ribbon or sheet-growth methods currently under commercial development: (a) dendritic web growth; (b) growth from a capillary shaping die; (c) growth with edge support strings, and (d) growth on a substrate.

more than $1 \text{ m}^2/\text{day}$. Material properties do not degrade over 100-m lengths. Dislocation etch pit densities are about $10^4/\text{cm}^2$, and τ is on the order of $100 \mu\text{s}$ or less. Growth is conducted from an 8-mm-deep melt contained in a shallow, rectangular quartz crucible. Thermal control is very important, not just for initiating the web, but also to maintain steady growth with proper dendrite propagation

characteristics at the ribbon edges, low thermal stresses in the ribbon region, and continuous melt replenishment without disturbing the growing web ribbon. Edge dendrite thickness stability is an excellent indicator of melt-temperature stability. Both induction heating with molybdenum hot zones and resistance heating with graphite heaters and hot zones have been used. The electrical energy used for growth is about 200–300 kWh/m². The thin material is particularly well suited for PV applications that require some bending flexibility, or for bifacial solar-cell applications. Since the material is nearly single crystalline, relatively high cell efficiencies can be achieved. The best reported value is 17.3 % for a 4-cm² cell. Initial production cell efficiencies are expected to be ~13 %. One growth furnace can produce web for about 50 kWp/y cell production.

Growth of crystals from the tips of capillary shaping dies was introduced for sapphire growth using molybdenum dies by LaBelle *et al.* (1971), and was first applied to silicon ribbons using graphite shaping dies by Ciszek (1972) and later to silicon tubes (Ciszek, 1975). As shown in Figure 13.7(b), liquid Si rises by capillarity up a narrow channel in the shaping die and spreads across the die's top surface, which defines the base of the meniscus from which the shaped crystal solidifies. The meniscus base is typically wider than the wall thickness of the crystal. Commercial development first concentrated on flat ribbons as wide as 100 mm, but edge-stability issues led to a preference for the tubular geometry (i.e., edges are eliminated). Octagonal tubes with 100-mm-wide flat faces are now used for production of PV substrates. Pulling rates are comparable to those used in web growth, but the 800-mm effective width increases the throughput to about 20 m²/day. A graphite crucible and graphite shaping dies are used with induction heating. The electrical energy consumption for this method is approximately 20 kWh/m². After growth, rectangular 100-mm-wide 'wafers' are laser-cut from the tube faces. They provide 275- μ m thick multicrystalline substrates with longitudinal grains that routinely make 14 % efficient solar cells. The best efficiency attained on a 10-cm² cell is 15.5 %. The capillary-die method is somewhat more susceptible to impurity effects from solar-grade feedstock than other methods, because the narrow channel impedes mixing of segregated impurities back into the melt and thus increases the effective segregation coefficient.

Edge-supported pulling of 'string ribbons' was introduced by Ciszek and Hurd (1980). This technique is similar to dendritic web growth with foreign filaments or strings replacing the edge-stabilizing role of the dendrites (Figure 13.7(c)). This greatly relaxes the temperature-control requirements and makes the technique easier to carry out than dendritic web growth. Simpler equipment can be used. A variety of carbon- and oxide-based materials were investigated for use as the filaments, with carbon-based filaments generating a higher density of grains at the edges of the ribbons than oxide-based filaments, but having a better thermal expansion match to silicon. The filaments are introduced through small holes in the bottom of either quartz or graphite crucibles. Ribbons as wide as 8 cm have been grown, with the standard commercial size now being 5.6 cm wide \times 300 μ m thick. The ribbons are grown at about 1–2 cm/min pulling rates, giving

a throughput of about $1 \text{ m}^2/\text{day}$, which is comparable to that obtained with web growth. Furnaces can be kept in continuous operation for weeks at a time by replenishing the melt. Ribbon sections of a desired length are removed by scribing while pulling is in progress. Continuous growth of more than 100 m of ribbon has been achieved, and lengths greater than 300 m have been obtained from a single furnace run (with successive seed starts). Dislocation densities are $\sim 5 \times 10^5/\text{cm}^2$ and τ is in the range $5\text{--}10 \mu\text{s}$. The highest cell efficiency obtained is 16.3 %, although production efficiencies are $<13 \%$. The steady-state grain structure contains longitudinal grains of about 1 cm^2 area, predominantly with coherent boundaries, in the central portion of the ribbons, and newly generated grains at the ribbon edges. The electrical energy used is about 55 kWh/m^2 .

The first application of type (ii) sheet growth to a semiconductor material was by Bleil (1969), who pulled ice and germanium sheet crystals horizontally from the free surface of melts in a brim-full crucible. Many approaches have been considered for applying type (ii) growth to photovoltaic silicon, including horizontal growth from the melt surface. The ones currently under commercial development move a substrate through a hot zone tailored in such a way that a long region of molten silicon in contact with the upper surface of the substrate solidifies with a long wedge-shaped crystallization front. The front grades from 0 thickness at the tip to the sheet thickness t (where the sheet leaves the melt), over a distance b . An example of one such approach is shown in Figure 13.7(d). As indicated in Equation (13.3), the pulling speed is proportional to b/t and to ΔT . It is feasible to make b very large, on the order of tens of centimeters. Coupled with moderate ΔT values (160°C), $250\text{-}\mu\text{m}$ thick sheets can then be grown with pulling speeds V_s as high as 6 m/min as mentioned earlier (Lange and Schwirtlich, 1990). If W is also tens of centimeters, extremely high throughputs can be achieved – in the vicinity of $1\,500 \text{ m}^2/\text{day}$. Heat removal is facilitated by the fact that the surface in which heat of crystallization is generated is nearly parallel to, and in close proximity to, the surface from which it is to be removed. The solid/liquid interface's growth direction V_g is essentially perpendicular to the pulling direction V_s . So, as grains nucleate at the substrate surface, their growth is columnar across the thickness of the sheet. This is in contrast to longitudinal grains aligned along the pulling direction obtained in the type (i) techniques in which V_g and V_s are 180° apart, pointing in opposite directions. The grains tend to be smaller in type (ii) growth methods, but are on the order of t . Production solar cell-efficiencies as high as 12 % are attainable at the present time, and the best small-cell efficiency is 16 %. The substrate does not have to remain with the grown sheet, and may be engineered for clean separation at some point after solidification.

13.6 THIN-LAYER GROWTH ON SUBSTRATES

Thin-layer Si is considered to be $<50\text{-}\mu\text{m}$ thick silicon deposited on a foreign substrate. Potential advantages of thin-layer approaches include less Si usage,

lower deposition temperatures relative to melt growth, monolithic module construction possibilities, and a tolerance for lower τ (the distance charge carriers have to travel is shorter). Disadvantages include incomplete light absorption (see Figure 13.3) and the probable need for light-trapping, a likelihood that grain sizes will be small, and difficulty in making rear contacts if the substrate is an insulating material.

The R&D challenge for successful thin-layer Si is to produce a 10–50- μm silicon layer of sufficient electronic quality with a diffusion length greater than the layer thickness and a grain size comparable to the thickness. A fast deposition rate of $>1\text{ }\mu\text{m}/\text{min}$ on a low-cost substrate such as glass is needed. There is not yet any significant quantity of thin-layer crystalline Si in commercial production for PV because only partial successes have been achieved in meeting the challenge. What has been accomplished is:

- Fast epitaxy ($1\text{ }\mu\text{m}/\text{min}$) of high-quality Si layers at intermediate temperatures ($700\text{--}900^\circ\text{C}$), e.g., by liquid-phase epitaxy (LPE) but on Si substrates
- Low- T ($<600^\circ\text{C}$) epitaxial growth of high-quality Si layers (e.g., by chemical vapor deposition (CVD)), but at low growth rates ($<0.05\text{ }\mu\text{m}/\text{min}$) and on Si substrates.
- Low- T poly/microcrystalline 10 % cells, but at slow growth rates
- Low- T micro/amorphous direct-gap 13 % cells, but at slow growth rates
- Fast CVD at intermediate T on foreign substrates, but with submicrometer grain size
- Fast CVD of $>1\text{-}\mu\text{m}$ grain-size layers on foreign substrates, but at high T ($\sim 1200^\circ\text{C}$) and with contamination
- Smooth Si at intermediate T by solid-state crystallization, but at slow rates, from slowly grown a-Si layers, and highly stressed.

A new approach to iodine vapor transport growth (Wang and Cizek, 1999) shows considerable promise, and has achieved 5–20- μm -thick Si layers with 5–10- μm grain size at 1–10- $\mu\text{m}/\text{min}$ growth rate directly on hi- T glass at $850\text{--}950^\circ\text{C}$. The layers have $5\text{ }\mu\text{s}$ effective minority-carrier lifetime, which implies diffusion length \gg layer thickness and a low impurity content. A scanning electron microscopy (SEM) photomicrograph of a layer is shown in Figure 13.8.

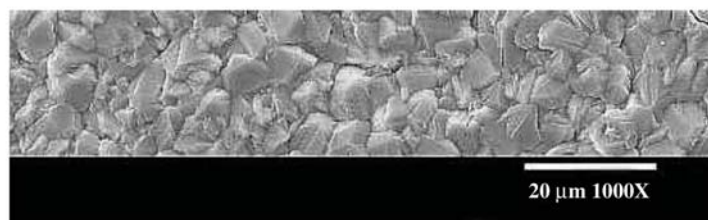


Figure 13.8 SEM micrograph showing the grain size of a 20- μm -thick poly-Si layer grown directly on a glass substrate at 900°C for 10 min ($2\text{ }\mu\text{m}/\text{min}$ deposition rate).

13.7 COMPARISON OF GROWTH METHODS

Table 13.2 summarizes some of the technological characteristics of the methods used to grow silicon crystals for photovoltaic applications. A variety of approaches have viability for further development, which is a strong point for Si PV commercial growth. As mentioned in the introduction, cost-driven tradeoffs are made in Si PV crystal-growth technology. This is evident in both the ingot and sheet-growth approaches. For example, the highest throughput ingot method, electromagnetic casting, yields lower cell efficiencies because of smaller grain sizes. A similar situation is seen in ribbons and sheets, where substrate melt shaping has tremendous throughput potential. Again, the grain size and cell efficiency are smaller than for some of the lower-throughput ribbon methods. The diversity and redundancy in approaches is healthy for the industry and increases the probability that further reductions in PV module cost will be achieved.

13.8 FUTURE TRENDS

The PV industry is expected to continue to grow at an annual rate of about 20 %. The well-established technology base and ready availability, proven performance, and salubrity of silicon, coupled with economies of scale in larger factories, will likely allow Si to remain the dominant PV material for the foreseeable future. The demand for off-specification polycrystalline silicon feedstock for PV use is likely to exceed the available supply by a factor of at least 2 within the next 10 years, and this will probably be an impetus for development of alternative feedstock material with adequate but not excessive purity levels.

In ingot growth, the trend for single crystals will be away from the smaller 100- and 125-mm diameter sizes with more focus on 200-mm diameters. Despite the potential advantages of FZ material, it is unlikely that its role in PV will increase significantly because of higher costs for the crack-free, long cylindrical feedstock it requires and difficulty in producing the larger FZ diameters. In CZ growth, we are likely to see an increased effort to make hot zones more energy efficient, to grow larger diameters, and to achieve continuously melt-replenished long growth runs. An effort will continue to evaluate trocrystalline growth or other means of strengthening the ingots so as to improve breakage yields for thin wafers. There will be a continuing effort to achieve more wafers per length of ingot, and to take advantage of potentially higher cell efficiencies afforded by thinner wafers when back surface fields are used in the cell design. Multicrystalline casting, directional solidification, and electromagnetic casting are commanding an increasing share of the Si PV market (53 % of all ingot-based modules sold in 1998 were multicrystalline). This trend is likely to continue because the processes and equipment are simpler and the throughputs are higher (especially for electromagnetic casting) by a factor of 2.5 to 20.

In the ribbon- and sheet-growth technologies, a challenge for dendritic web growth and edge-supported pulling will be to increase areal throughput via wider

Table 13.2 Comparison of the silicon crystal-growth techniques used for photovoltaics

Method	Width (cm)	Weight (kg)	Growth rate (mm/min)	Growth rate (kg/h)	Throughput (m ² /day)*	Energy use (kWh/kg)	Energy use (kWh/m ²)**	Efficiency (typical %, best %)
Float-zone	15	50	2–4	4	80	30	36	<18,24
Czochralski	15	50	0.6–1.2	1.5	30	18–40	21–48	<15,20
Directional solidification	69	240	0.1–0.6	3.5	70	8–15	9–17	<14,18
Electromagnetic casting	35	400	1.5–2	30	600	12–20	14–24	<13,16
Dendritic web	5	–	12–20	–	1	–	200	<15,17
Capillary die growth	80	–	15–20	–	20	–	20	14,16
Edge-supported pulling	8	–	12–20	–	1.7	–	55	<13,16
Substrate melt shaping	20	–	1000–6000	–	>1000	–	–	<12,16
Thin-layer Si	2	–	10 ^{–3} ⊥	–	–	–	–	– 13

*Areal throughput for ingots assumes 20 wafers/cm

– indicates data are not available or not appropriate

** Only the energy for growth is included

⊥ deposition rate perpendicular to the substrate

ribbons, multiple ribbons, or other approaches. Even though these methods have the advantage of minimal silicon consumption and elimination of wafering, it is unlikely that they can effectively compete with their current throughput of 1–2 m²/day. This is because the effective areal throughputs of ingot growth range between 30 and 600 m²/day, and other sheet technologies produce 20 m²/day to >1000 m²/day. While capillary die growth of octagons produces about 20 m²/day, experimentation is underway to grow large-diameter, thin-walled circular tubes (as depicted in Figure 13.7(b)) a meter in diameter and much thinner than current octagonal tubes. This would increase throughput to more than 75 m²/day. So far, tubes with 0.5-m diameter have been made, effectively doubling the current octagon areal throughput (Roy *et al.*, 1999). We will probably see continued progress in horizontally pulled, large-area solid/liquid interface sheets by some variant of the method shown in Figure 13.7(d), because the throughput potential is enormous and one growth furnace could easily generate material for 35 MWp/year or more of solar-cell production.

The future is expected to bring continued exploration of thin-layer Si growth approaches, in search of ones that have significant economic advantages over the best ingot and sheet techniques. Successful ones will have fast deposition rates, large grain sizes, high efficiencies (at least 14 % production efficiency) compatibility with low-cost substrates, and amenability to low-cost cell-fabrication schemes. It is not likely that production of thin-layer Si PV modules will be a significant fraction of the mainstream PV market for at least 10 years, although they, like the ingot and sheet approaches, would have substantial advantages over many other thin-film PV approaches. These include the simple chemistry and relative abundance of the Si starting material. The Earth's crust contains 27.7 % Si, in contrast to 0.00002 % Cd, 0.00001 % In, 0.000009 % Se, and 0.0000002 % Te (commonly used thin-film elements). In addition, crystalline Si benefits from an extremely well-established technology base, compatibility with SiO₂ surface passivation, relative salubrity with respect to toxicity, and stability under light exposure.

REFERENCES

- Allen, T. B. (1913) U.S. Patent 1,073,560.
- ASTM (1993) F28-91 Standard. *1993 Annual Book of ASTM Standards*, Vol. **10.05**, Philadelphia, American Society for Testing and Materials, 30.
- Bleil, C. E. (1969) *J. Cryst. Growth* **5**, 99.
- Ciszek, T. F. (1972) *Mater Res. Bull.* **7**, 731.
- Ciszek, T. F. (1975) *Phys. Stat. Sol. (a)* **32**, 521.
- Ciszek, T. F. (1976) *J. Appl. Phys.* **47**, 440.
- Ciszek, T. F. (1979) *J. Cryst. Growth* **46**, 527.
- Ciszek, T. F. (1984) *J. Cryst. Growth* **66**, 655.
- Ciszek, T. F. (1985) *J. Electrochem. Soc.* **132**, 963.
- Ciszek, T. F. (1986) U.S. Patent 4,572,812.

- Ciszek, T. F., and Hurd, J. L. (1980) in: *Proceedings of the Symposia on Electronic and Optical Properties of Polycrystalline or Impure Semiconductors and Novel Silicon Growth Methods* (K. V. Ravi and B. O'Mara, eds) p. 213. The Electrochemical Soc., *Proceedings Volume* 80-5, Pennington, NJ.
- Ciszek, T. F., Wang, Tihu, Schuyler, T., and Rohatgi, A. (1989) *J. Electrochem. Soc.* **136**, 230.
- Ciszek, T. F., Wang, T. H., Burrows, R. W., Wu, X., Alleman, J., Tsuo, Y. S., and Bekkedahl, T. (1993) *23rd IEEE Photovoltaic Specialists Conf. Record*, Louisville (IEEE, New York), 101.
- Davis, J. R., Jr., Rohatgi, A., Hopkins, R. H., Blais, P. D., Rai-Choudhury, P., McCormick, J. R., and Mollenkopf, H. C. (1980) *IEEE Trans. Electron. Devices* **ED-27**, 677.
- Dermatis, S. N., and Faust Jr., J. W. (1963) *IEEE Trans. Commun. Electron.* **82**, 94.
- Endros, A. L., Einzinger, R., and Martinelli, G. (1997) *14th European Photovoltaic Solar Energy Conference Proceedings*, Barcelona, 112.
- Fischer, H., and Pschunder, W. (1976) *IEEE 12th Photovoltaic Specialists Conf. Record*, IEEE, New York, 86.
- Gee, J. M., Ho, P., Van Den Avyle, J., and Stepanek, J. (1998) in: *Proceedings of the 8th NREL Workshop on Crystalline Silicon Solar Cell Materials and Processes*, ed: B. L. Sopori (August 1998 NREL/CP-520-25232), 192.
- Khattak, C. P., Joyce, D. B., and Schmid, F. (1999) in: *Proceedings of the 9th NREL Workshop on Crystalline Silicon Solar Cell Materials and Processes*, ed: B. L. Sopori (August 1999 NREL/BK-520-26941), 2.
- Khattak, C. P., and Schmid, F. (1978) *IEEE 13th Photovoltaic Specialists Conf. Record*, IEEE, New York, 137.
- LaBelle, H. E., Mlavsky, A. I., and Chalmers, B. (1971) *Mater. Res. Bull.* **6**, 571, 581, 681.
- Lange, H., and Schwirtlich, I. A. (1990) *J. Cryst. Growth* **104**, 108–112.
- Martinelli, G. and Kibizov, R. (1993) *Appl. Phys. Lett.* **62**, 3262.
- Mauk, M. G., Sims, P. E., and Hall, R. B. (1997) *Am. Ins. of Phys. Conf. Proc.* **404**, 21.
- Maurits, J. (1998) in: *Proceedings of the 8th NREL Workshop on Crystalline Silicon Solar Cell Materials and Processes*, ed: B. L. Sopori (August 1998 NREL/CP-520-25232), 10.
- Maycock, P. D., ed. (1999) *PV News*, February.
- Menna, P., Tsuo, Y. S., Al-Jassim, M. M., Asher, S. E., Matson, R., and Ciszek, T. F. (1998) *Proc. 2nd World Conf. on PV Solar Energy Conversion*, 1232.
- Mihalik, G., Fickett, B., Stevenson, R., and Sabhapathy, P. (1999) Presentation at the 11th American Conference on Crystal Growth & Epitaxy, Tucson August 1–6. To be published, *J. Cryst. Growth*.
- Mitchell, K. M., (1998) *Am. Ins. Phys. Conf. Proc.* **462**, 362.
- Nakamura, N., Abe, M., Hanazawa, K., Baba, H., Yuge, N., and Kato, Y. (1998) *Proc. 2nd World Conf. on PV Solar Energy Conversion*, 1193.
- Roy, A., Chen, Q. S., Zhang, H., Prasad, V., Mackintosh, B., and Kalejs, J. P. (1999) Presentation at the 11th American Conference on Crystal Growth & Epitaxy, Tucson August 1–6. To be published in, *J. Cryst. Growth*.
- Runyan, W. R. (1965) *Silicon Semiconductor Technology* McGraw-Hill Book Company, New York.
- Tsuo, Y. S., Gee, J. M., Menna, P., Strebkov, D. S., Pinov, A., and V. Zadde (1998) *Proc. 2nd World Conf. on PV Solar Energy Conversion*, 1199.

- Wang, T. H., and Cizek, T. F. (1997) *J. Cryst. Growth* **174**, 176.
- Wang, T. H., and Cizek, T. F. (1999) Presentation at the 11th American Conference on Crystal Growth & Epitaxy, Tucson, August 1–6. To be published.
- Wang, T. H., Cizek, T. F., Schwerdtfeger, C. R., Moutinho, H., and Matson, R. (1996) *Solar Energy Mater. Solar Cells* **41/42**, 19.
- Wawer, P., Irmscher, S., and Wagemann, H. G., (1997) 14th *European Photovoltaic Solar Energy Conference Proceedings*, Barcelona, 38.
- Zhao, J., Wang, A., Altermatt, P., and Green, M. A. (1995) *Appl. Phys. Lett.* **66**, 3636.